Chapter 1
Introduction

This chapter gives an introduction to the magnetostrictive active line-of-sight (LOS)-stabilization of a vehicle-mounted optical instrument. A formulation of the problem, i.e. the LOS-angular disturbance sensitivity of optical instruments and the wide-band vibration problem in vehicles, is given in section 1.1. Two possible stabilization methods, viz passive and active stabilization, are compared in section 1.2 and the need for active stabilization is pointed out. The performance of hydraulic, electrodynamic, piezo-electric and magnetostrictive actuator types is compared in section 1.3 and the use of magnetostrictive actuation is motivated. Section 1.4 covers a literature survey on magnetostriction and highlights the applicability and limitations of each literature item in solving the stabilization problem. Section 1.5 gives an outline of the rest of the thesis.

1.1 Problem formulation

A moving vehicle is subjected to two sources of vibration, i.e. onboard disturbance systems and the movement of the vehicle over the terrain. The propulsion system is the most dominating source of all the onboard disturbance systems. Each vehicle type is equipped with its own unique type of propulsion system and is thus exposed to a different kind of environment. Vibrations which originate from the propulsion systems of ground vehicles, for instance, can be attributed to moving parts in internal combustion engines, gearboxes and drivelines, while gas turbines and propellers are responsible for vibrations in aircraft and helicopters. Environmentally, or externally induced vibrations are caused by terrain irregularities in road and off-road vehicles, aeroelastic effects in aircraft and hydrodynamic forces in ships.

Vehicle vibrations are transmitted to the vehicle structure, passengers and vehicle systems and may have several undesirable consequences, e.g. the vehicle structure may fail due to fatigue, hydraulic systems may fail due to broken pipes and passengers may experience discomfort and loss of concentration. Furthermore, any fragile onboard equipment such as computers, radios and optical systems, will suffer costly performance losses if exposed to excessive vibration levels. Optical instruments like high resolution imaging television, infrared and laser sensors, periscopes and reconnaissance cameras, are particularly sensitive to vibration environments. A periscope mounted in the turret of an army tank, for example, will not track its target accurately if the mounting base of the periscope vibrates relative to the gun platform. This will lead to incorrect aiming, missed shots and eventually to loss of the tank and its personnel.

Incorrect aiming of an optical instrument can mainly be attributed to an angular disturbance of the mounting base of the instrument. This causes a pitching or yawing rotation of the instrument relative to the desired line of sight (LOS) and results in a pointing error at the target (see figure 1.1). Pitch is more susceptible to external or environmental disturbances.

The pointing error depends on the disturbance angle and the distance between the optical instrument and the target, and can be mathematically expressed as follows:

$$e = \theta D \tag{1.1.1}$$

where e is the pointing error, θ is the disturbance angle and D is the distance between the instrument and the target.

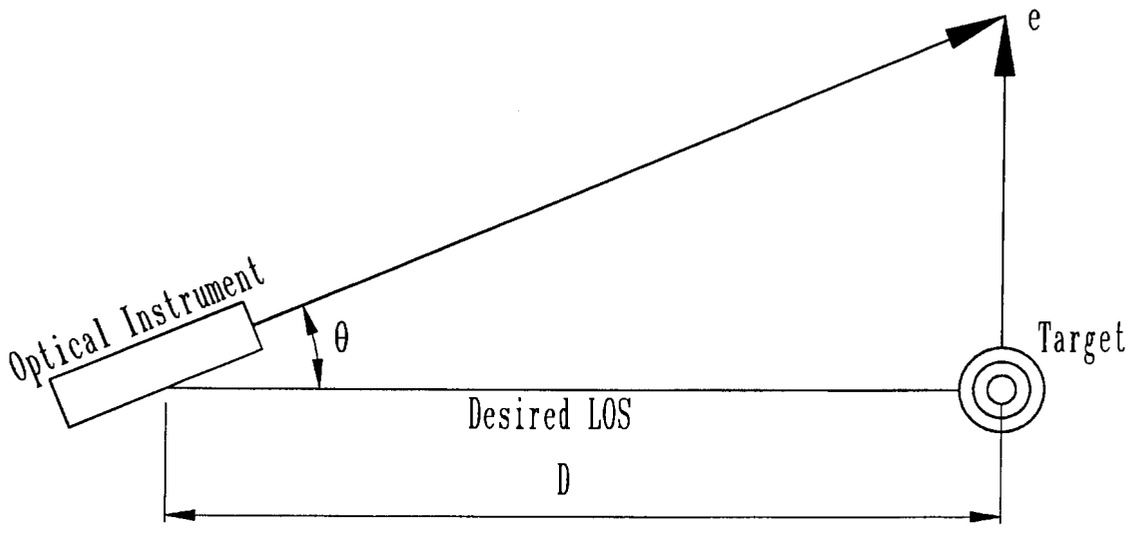

Figure 1.1.1: Line of sight angular disturbances and pointing errors

The pointing error problem is further complicated by the fact that the disturbance angle fluctuates due to vibrations in the mounting base of the optical instrument, and that vehicle vibrations are generally wide-band in nature. The frequency band of aircraft vibrations, for instance, is 15 Hz to 2 kHz, while the frequency band of road vehicle vibrations is 5 Hz to 500 Hz [MIL 810 E, 1988]. Wide-band angular disturbances such as these may cause blurred images, which will make target visibility and recognition extremely difficult.

In order to improve target visibility, it is essential to isolate the instrument from the base vibrations. Although it may be desirable to totally eliminate the LOS error, this may be difficult to achieve due to the high sensitivity of optical instruments. Instead, the effect of the base disturbance must be attenuated to such an extent that the remaining LOS error will minimize target blur. For this reason, minimum LOS errors are usually specified. The specified LOS accuracy for a shipboard electro-optical platform, for example, is less than 0,1 mrad RMS over a frequency band of 0,5 Hz to 200 Hz [Stockum & Carroll, 1984].

The topic of this study is the isolation of a lightweight commercial video camera, mounted on a vibrating platform next to the gun of a tracked vehicle (tank). The isolation system will be specifically designed and implemented to solve the particular problem. A vibration signal with a given frequency spectrum, bandwidth, RMS angular displacement and acceleration, measured on the instrument mounting base of an existing vehicle, will serve as the disturbance. The disturbance will be simulated and excited in a laboratory, where the isolation system will be implemented, tested

and evaluated. The instrument will be represented by a dummy load with the same mass and length.

The objective is to limit the LOS displacement amplitude of the optical instrument to 0,1 mrad peak-to-peak (p-p). The length of the instrument is 250 mm and its mass, together with that of its support structure, is 1,24 kg. The maximum angular displacement of the base is 0,7 mrad p-p and the maximum angular acceleration is 39,48 rad/s^2 p-p. The base RMS angular displacement is 0,181 mrad and the RMS angular acceleration is 9,12 rad/s^2. The frequency band is 2,5 Hz to 500 Hz. The maximum acceleration amplitude occurs at 96 Hz and the maximum displacement amplitude occurs at 24 Hz. The base angular acceleration and displacement signals are shown in figure 1.1.2, and the frequency spectra of the base angular acceleration and displacement are shown in figure 1.1.3.

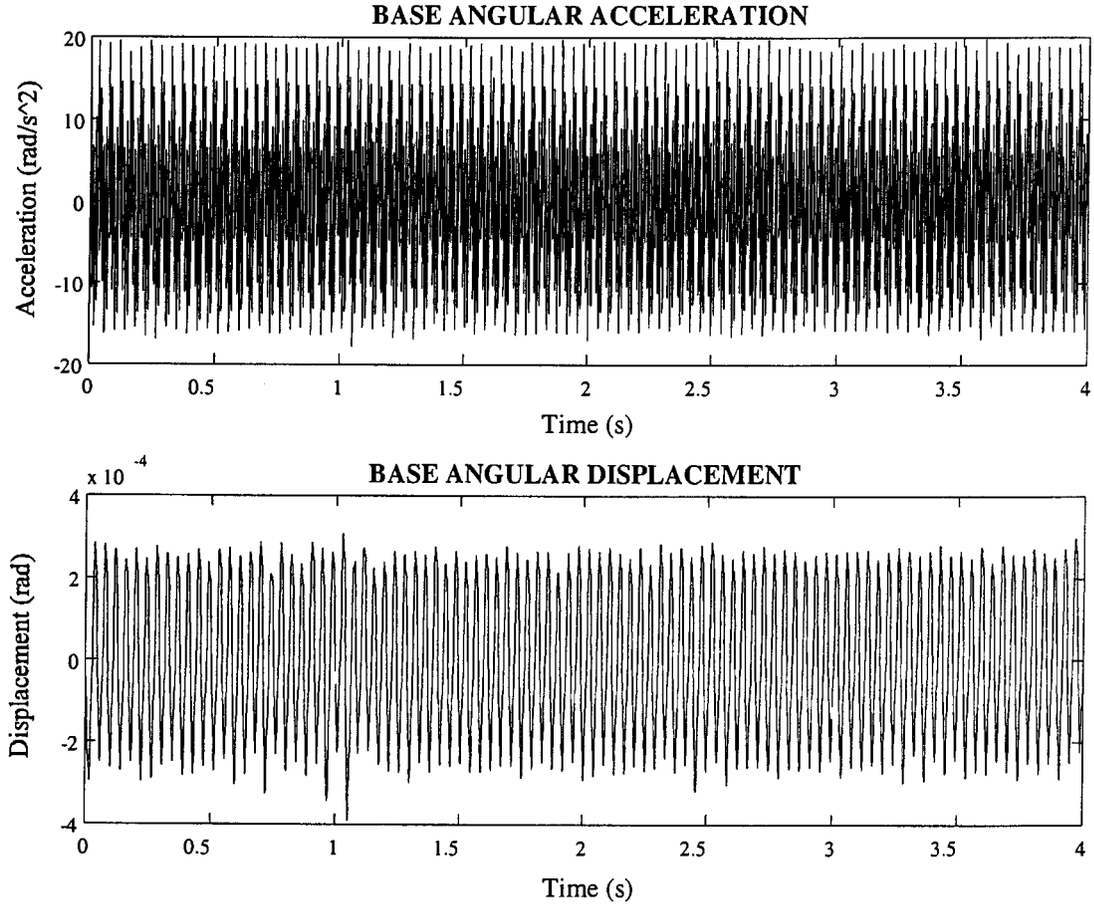

Figure 1.1.2: Base angular acceleration and displacement

It can be seen from figure 1.1.3 that the vibration spectrum is wide-band. This complicates the isolation problem because a limitation is placed on the choice of available stabilization methods, such as passive, semi-active and active vibration isolation. On the one hand, it will be desirable to use an isolator with zero energy consumption, such as a passive isolator, but on the other hand wide-band isolation capabilities are required, which may necessitate an active isolator. The next section will give a more complete comparison between passive and active stabilization systems. It

will be shown by means of mathematical equations and graphs that active isolation is required to stabilize the optical instrument.

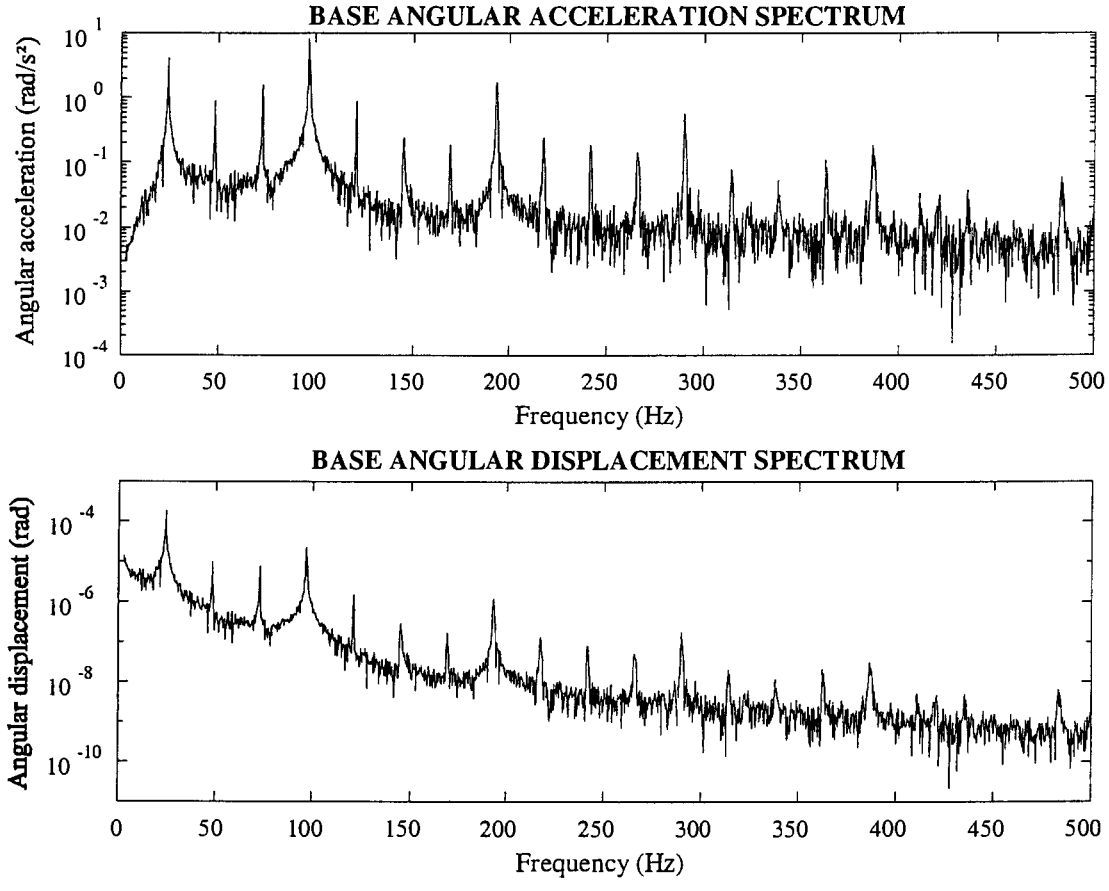

Figure 1.1.3: Base angular acceleration and displacement frequency spectra

1.2 Comparison between passive and active isolation

The previous section gave a background on the vibration sensitivity of vehicle-mounted optical instruments. It was shown that angular disturbances of the mounting base cause pointing errors at the target and that vibration isolation of the instrument is essential to improve target visibility. It was also shown that vehicle vibrations are wide-band in nature, which places a limitation on the choice of a suitable isolator, such as passive, semi-active and active isolators.

This section will discuss three different types of stabilization methods for broadband isolation of the optical instrument, i.e. passive, semi-active and active isolation. The section starts with a basic philosophy of vibration isolation, after which the different methods will be compared by means of mechanical models, equations of motion and damping forces. The performance of each isolation type will be discussed in terms of vibration transmissibility and wide-band isolation ability and the advantages and disadvantages of each method will be pointed out.

Lastly, it will be shown that an active isolation system will be required to reduce the LOS error of the optical instrument to 0,1 mrad p-p over a frequency band of 2,5 Hz to 500 Hz.

The basic philosophy of vibration isolation is to attenuate unwanted disturbances before the disturbances reach the instrument [Crawley & Hall, 1991]. This can be achieved by isolating components at the most suitable locations, e.g. at the source of the disturbance or at major substructure interfaces. In the case of the optical instrument, isolation is essential at locations that have a significant effect on attenuating vibrations in the relevant degree of freedom (DOF). The important DOF in the stabilization of the optical instrument LOS is the pitching rotation DOF, since it directly affects the LOS accuracy of the instrument (see figure 1.1.1). Suitable locations for isolators to reduce pitching motion may for instance be at the front and rear ends of the instrument, where the isolator can exercise a maximum resisting moment to attenuate the rotational motion of the optical instrument, thereby improving visibility of the target.

The ability of an isolator to attenuate vibrations is normally expressed in terms of vibration transmissibility. Transmissibility can be defined as the nondimensional ratio of the response amplitude of a system in steady state harmonic vibration to the excitation amplitude [Harris, 1988]. The ratio may be one of forces, displacements, velocities or accelerations. In the case of the optical instrument, the transmissibility TR can be defined as the ratio of the angular displacement amplitude $\theta(\omega)$ of the instrument, to the angular displacement amplitude $\theta_b(\omega)$ of the base:

$$TR = \frac{\theta(\omega)}{\theta_b(\omega)} \tag{1.2.1}$$

where ω is the angular excitation (or disturbance) frequency in rad/s. A transmissibility of less than one is required for isolation purposes, in other words the angular displacement of the instrument must be less than that of the base. The lower the transmissibility, the better the isolation. If the isolator transmissibility exceeds unity, the base disturbance will be amplified instead of being attenuated. A discussion is provided by Crawley & Hall [1991].

Three isolator types, i.e. passive, semi-active and active isolators can be considered for LOS stabilization of the optical instrument. Firstly, passive isolation works on the principle of attenuating vibrations by means of internal forces, such as isolator stiffness, inertia and damping forces. No external force, with the exception of the base disturbance, acts on the system. The advantages of passive isolation are mechanical simplicity and zero energy consumption, since no external energy sources like hydraulic pumps are required. It is for these reasons that passive isolators have traditionally been the most popular isolator type in use. Unfortunately the absence of an external energy source also creates certain problems, e.g. the transmissibility of the system cannot be altered at high frequencies without affecting static system behaviour. This shortcoming practically rules out the possibility of using passive isolation for broadband disturbance rejection.

Two types of passive vibration isolators can be distinguished, i.e. band-pass filters and low-pass filters. The application of band-pass filters is generally limited to narrow-band vibrations, and therefore cannot be considered suitable for wide-band isolation. Low-pass filters can be used for isolation purposes if the undamped natural frequency of the system is lower than the disturbance

frequency band [Crawley & Hall, 1991]. This can be accomplished by using an isolator with a low spring stiffness.

However, a low spring stiffness may yield an undesirably large static deflection, which cannot be corrected due to the absence of an external force. If, for instance, a low-pass filter is used to isolate an optical instrument against the disturbance shown in figure 1.1.2, a natural frequency of less than 2,5 Hz is required. The spring stiffness required to bring about this natural frequency may be so low that all efforts to stabilize the LOS over a wide frequency band, will result in large static pointing errors which will make the stabilization effort futile. The static error can only be corrected by means of a force that is independent of the natural frequency of the system, such as an active force.

An active isolator makes use of an external energy source to generate forces which oppose the base motion, thereby reducing the vibrations transmitted to the optical element. Examples of active isolators are hydraulic, electrodynamic, piezo-electric, and magnetostrictive actuators. The purpose of active isolation is to modify the passive transmissibility of an isolator in three different ways, i.e. to increase mass, to increase damping near the natural frequency or to reduce the static stiffness of the isolator [Crawley & Hall, 1991]. The advantage of active isolation is the possibility of supplying the correct force to stabilize the optical instrument at any frequency inside the disturbance band, but the main disadvantage is the necessity of an external energy source like hydraulic pressure or electric power. Furthermore, an electronic control system is required to ensure the desired actuator closed loop response. Active isolation is therefore less energy efficient, more bulky and more costly.

The third isolator type, i.e. a semi-active isolator, contains controllable passive damping elements. The control system changes the damping force according to the direction and magnitude of the relative speed between the damper attachment points to ensure the correct damping force at a given frequency. As in the case with passive isolators, the mechanism of removing energy is internal to the system. The advantage is that, except for a small actuator to change the passive damping coefficient, no energy source is required, but the disadvantage is that no energy can be added to the system. No further attention will be paid to semi-active isolation, but instead, the differences between passive and active isolation will be pointed out in the next few paragraphs. The two system types will be compared for damping force, vibration transmissibility and isolation ability.

In order to obtain a better understanding of passive and active system behaviour, consider the two simple single degree of freedom (SDOF) translational systems as shown in figure 1.2.1. The system on the left hand side of figure 1.2.1 consists of a moving base which is attached to a mass m via a linear spring with stiffness k and a viscous damper with damping coefficient c. The absolute displacement of the base is x_b and the absolute displacement of the mass is x. The system on the right hand side of figure 1.2.1 consists of a moving base, which is attached to a mass m via a linear spring with stiffness k. A viscous damper with damping coefficient c connects the mass to an inertial earth via a viscous damper with damping coefficient c. The absolute displacement of the base is x_b and the displacement of the mass is x. The system shown on the left hand side of figure 1.2.1 is a passively damped system (or passive system for short) while the system shown on the right hand side is an active system.

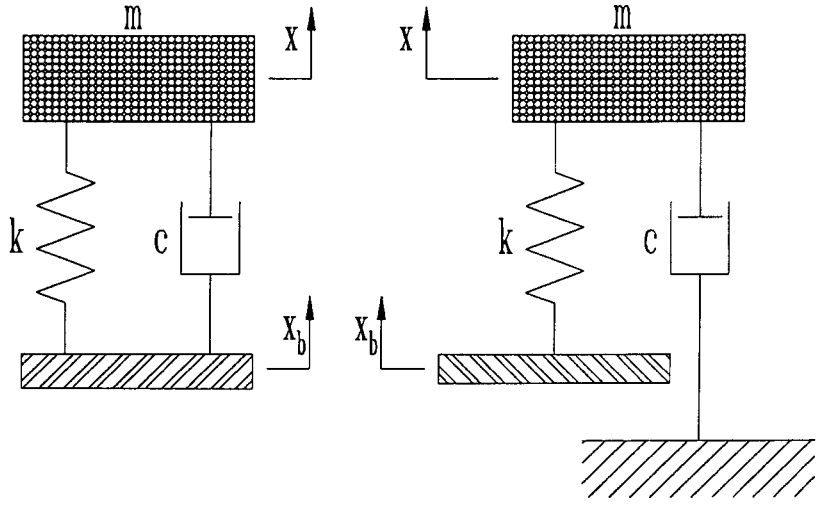

Figure 1.2.1: **Base-excited dynamic system with passive damping (left) and active damping (right)**

The difference between the passive and active systems can best be analyzed by comparing the damper forces of the two systems. The passive damper force F_{DP} is given by the following equation:

$$F_{DP} = c(\dot{x}_b - \dot{x}) \tag{1.2.2a}$$

and the active damper force F_{DA} can be expressed as:

$$F_{DA} = -c\dot{x} \tag{1.2.2b}$$

where $\dot{x}_b$ is the speed of the base and $\dot{x}$ is the speed of the mass.

Equations 1.2.2a and 1.2.2b highlight the important difference between the force characteristics of the two systems. The passive damper force is proportional to the relative speed between the base and the mass, while the active damper force is proportional to the absolute speed of the mass. This difference will inevitably lead to a difference in the vibration transmissibilities of the two systems. The transmissibility TR_P of the passive system in figure 1.2.1 is given by:

$$TR_P = \sqrt{\frac{1+\left(2\xi\frac{\omega}{\omega_n}\right)^2}{\left(1-\left(\frac{\omega}{\omega_n}\right)^2\right)^2+\left(2\xi\frac{\omega}{\omega_n}\right)^2}} \tag{1.2.3a}$$

The transmissibility TR_A of the active system is:

$$TR_A = \frac{1}{\sqrt{\left(1-\left(\frac{\omega}{\omega_n}\right)^2\right)^2 + \left(2\zeta\frac{\omega}{\omega_n}\right)^2}} \qquad \textbf{(1.2.3b)}$$

where ω is the angular frequency of the base disturbance in rad/s, ω_n is the undamped natural angular frequency given by:

$$\omega_n = \sqrt{\frac{k}{m}} \qquad \textbf{(1.2.4)}$$

and ζ is the dimensionless damping ratio:

$$\zeta = \frac{c}{2m\omega_n} \qquad \textbf{(1.2.5)}$$

The transmissibilities of the two systems as given by equations 1.2.3a and 1.2.3b are graphically illustrated in figure 1.2.2. The damping ratios are arbitrarily selected as 5% and 50%, while the undamped natural frequency is 10 Hz and the disturbance frequency band is 1 to 100 Hz.

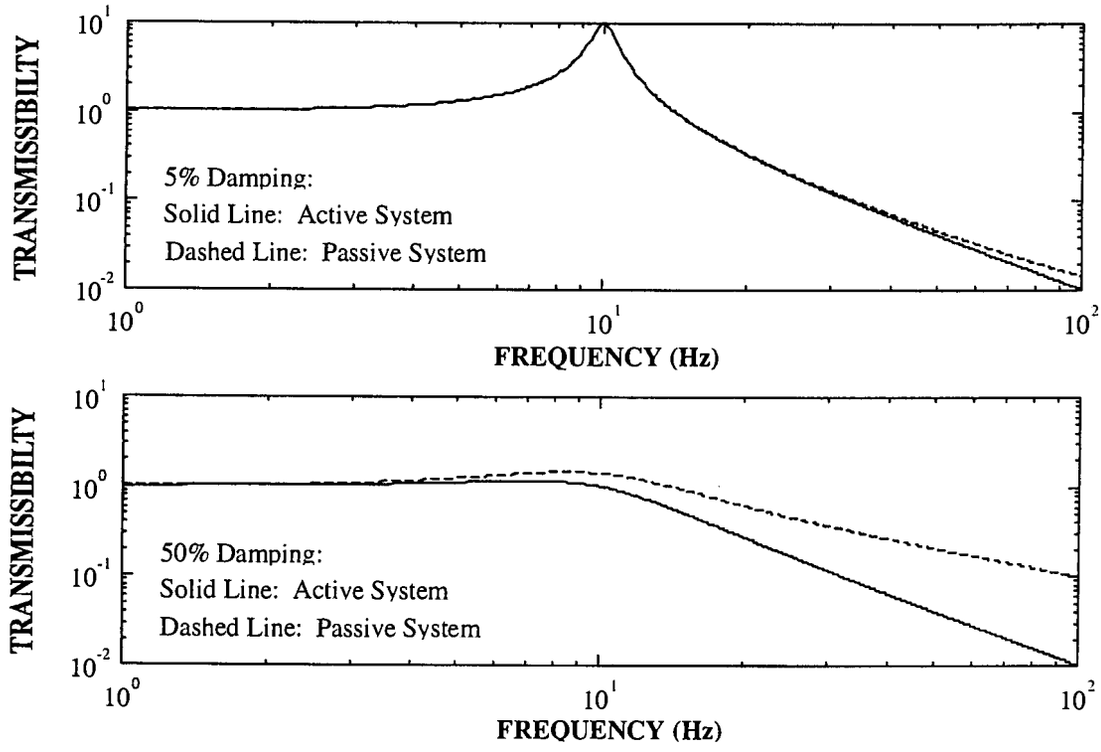

Figure 1.2.2: Passive and active system transmissibilities for a natural frequency of 10 Hz and damping ratios of 5% and 50%

Figure 1.2.2 shows that, in the case of 5% damping, the transmissibilities of the passive and active systems are virtually identical for excitation frequencies from 1 Hz to approximately 30 Hz, but for frequencies above 30 Hz, the transmissibility of the active system is slightly lower. It can therefore be concluded that, at higher frequencies, the active system provides slightly better isolation than the passive system. However, neither system succeeds in lowering the transmissibility peak at resonance (10 Hz).

In the case of 50% damping, there is a significant difference in the transmissibilities of the two systems at frequencies above 3 Hz, and this difference increases with frequency. It can also be seen that the active system gives a lower peak at resonance than the passive system. Furthermore, the active system isolates from 10 Hz upwards, while the passive system only manages to isolate above 14 Hz. Lastly, it can be concluded from figure 1.2.2 that, in order to obtain superior isolation characteristics over a broad frequency band, an active damper with a high damping factor is required.

The above example indicates the differences between passive and active damping. Active damping can be employed to alter the transmissibility of the system, and higher damping factors produce better isolation over a wide frequency band. However, the scope of altering the dynamic behaviour of the system by means of active damping alone is limited because the static transmissibility is constant and cannot be altered to any other desired value (see figure 1.2.2).

Modifying the static transmissibility can for instance be accomplished by applying an external force that is proportional to both the absolute speed and the absolute displacement of the mass, which would necessitate an additional active spring force. The system has the advantage that the transmissibility can be lowered over a wide frequency band without the necessity of a very low isolator spring stiffness. This method is generally applied in active isolation systems. An actuator is used to supply the necessary relative motion between the base and the instrument, thereby adjusting the dynamic characteristics of the system to give the desired isolation.

Judging by the wide-band nature of the disturbance given in figure 1.1.3, passive isolation must be ruled out in favour of active isolation. The latter can be accomplished by various means, i.e. by using hydraulic, electrodynamic, piezo-electric and magnetostrictive actuators. In the next section, four different active isolation methods as possible candidates for LOS stabilization of the optical instrument will be considered and compared. The use of magnetostrictive actuators will be motivated on the basis of performance criteria such as stroke length, frequency response and force output.

1.3 Magnetostrictive active LOS stabilization

It was indicated in the previous section that active vibration isolation is required to stabilize the line of sight of vehicle-mounted optical instruments, which will require actuators powered by an external source. Different types of actuators can be considered for this purpose, such as hydraulic, electrodynamic, piezoelectric and magnetostrictive actuators. Each actuator type works on a different principle and has its own application, advantages and disadvantages. The principles of operation and application of each actuator type will be discussed and compared in this section and

the advantages and disadvantages will be mentioned. The use of magnetostrictive actuators will be motivated for LOS stabilization of the optical instrument.

A hydraulic actuator works on the following principle: A pump supplies hydraulic fluid at a high pressure to an actuator consisting of a cylinder and piston. The fluid exerts a force on the piston and displaces it. The actuator displacement and force are controlled by a hydraulic servovalve which regulates the fluid flow to the cylinder. The actuator performance, expressed in terms of frequency, stroke length and force output, depends on the pump power, the pipe length and diameter, valve inertia, load mass and actuator dimensions such as plunger length and diameter.

An electrodynamic actuator contains a magnetic core and a drive coil wound around the piston of a moving table. A signal generator provides the excitation signal, which is amplified to supply the desired voltage to the coil. The coil induces a magnetic field in the piston and generates a magnetomotive force, which displaces the table. A permanent magnet may be used to provide the magnetic field for excitation forces of up to 200 N, while for higher force requirements an electromagnetic stator assembly is used [Broch, 1984].

Piezoelectric actuators make use of asymmetrical crystalline materials, such as polyvinilidene fluoride (PVDF) and piezoelectric ceramic (PZT), to produce a strain when subjected to an external electric field [Harris, 1988]. For small electrical fields, the strain is proportional to the field, but for larger fields, the strain reaches a saturation point, where an increase in field strength will produce no further increase in strain.

Magnetostrictive actuators require a magnetic field to produce a strain in a ferromagnetic material. The field is supplied by a coil, wound concentrically around a magnetostrictive active rod. When the field is applied, small magnetic domains in the material rotate, causing the rod to expand in the direction of the field [Butler, 1988]. For small fields, the strain is proportional to the field, but when all the domains are aligned, the material becomes magnetically saturated and no further expansion of the rod is possible. However, the saturation strain can be enhanced, by applying a compressive stress to the material. Stresses of up to 65 MPa can be applied [Kvarnsjö, 1993], giving theoretical saturation strains of up to 2000 $\mu\varepsilon$ or 0,2%.

Magnetostrictive materials are mainly rare earth materials, oxides, intermetallic compounds and rapidly quenched amorphous metals. One class of alloys of iron and the rare earth materials terbium (Tb) and dysprosium (Dy) which has become very attractive given its high magnetostriction at room temperatures and above, is $Tb_xDy_{1-x}Fe_{1.9-2}$. This material is better known as Terfenol-D in the commercial market and is currently the most widely used material in magnetostrictive applications. Two versions of Terfenol-D are $Tb_{.27}Dy_{.73}Fe_{1.9-1.95}$ and $Tb_{.3}Dy_{.7}Fe_{1.9-1.95}$, the latter giving higher strains for magnetic field strengths below 1 kOe [Butler, 1988]. The strain versus field strength relationship of $Tb_{.27}Dy_{.73}Fe_{1.9}$ for compressive prestresses of 6,9 MPa to 24,1 MPa is shown in figure 1.3.1.

The range of stroke lengths available from hydraulic actuators is 5,5 μm to 1 m, while that of electrodynamic actuators is 0,3 nm to 20 mm [Broch, 1984]. Magnetostrictive actuator stroke lengths depend on the magnetostrictive strain as well as on the length of the magnetostrictive active rod. A magnetostrictive rod with a length of 100 mm, for instance, can produce a stroke length of 0,2 mm. Piezoelectric actuators deliver strains of 0,02% to 0,06% of their lengths [Van Schoor & Bester, 1992], which is only 10% to 30% of the strains available from magnetostrictive actuators.

Furthermore, piezoelectric actuators may require biasing voltages of up to 300 volts to produce these strains. Magnetostrictive actuators, which may be biased by means of permanent magnets, require 10% or less of the excitation voltage of piezoelectric actuators. However, the high voltage requirement of piezoelectric actuators is not the limiting factor in the choice of a suitable actuator type. (The required voltage increase may for instance be achieved by means of a transformer or a power amplifier). High supply voltages are undesirable in vehicles, mainly due the danger of electrical shock and fires. Therefore, in the interest of safety, supply voltages in vehicle electrical systems are limited to relatively low levels. In the case of military vehicles, for example, the maximum allowable supply voltage is 28 V. Whereas magnetostrictive actuators may meet this safety requirement, piezoelectric actuators may be illegal.

Both magnetostrictive and piezoelectric actuators deliver relatively short stroke lengths compared to those of hydraulic and electrodynamic actuators. Some means of extending the stroke lengths of the former two actuator types is therefore required. Piezoelectric actuators make use of piezostacks to increase the effective actuator length, while magnetostrictive actuators can be equipped with gain mechanisms such as hydraulic or mechanical displacement amplification devices. However, although these measures will give significant improvements, hydraulic and electrodynamic actuators will still deliver far superior stroke lengths.

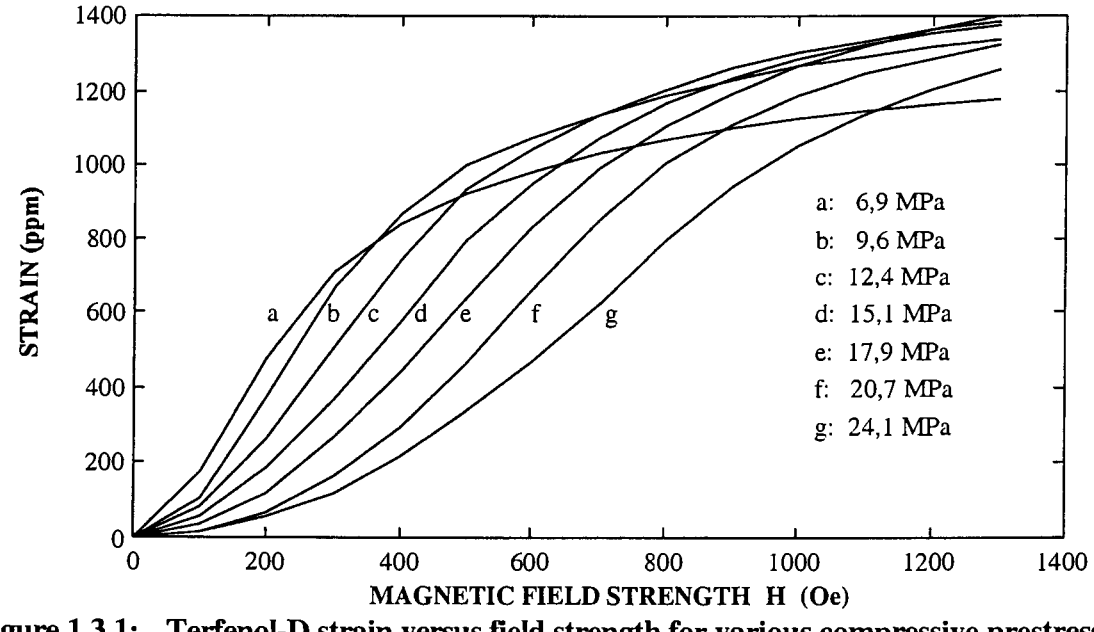

Figure 1.3.1: Terfenol-D strain versus field strength for various compressive prestresses [Butler, 1988]

The frequency range of electrodynamic actuators is 5 Hz to 20 kHz, while hydraulic actuators can be used for frequencies of 0 Hz to 1 kHz [Broch, 1984]. Electrodynamic actuators are generally not recommended for frequencies of lower than 5 Hz because of a danger of coil burnout, while hydraulic actuators are not suitable for frequencies above 70 Hz because hydraulic control valve inertia places a limitation on the reaction speed of the actuator.

The frequency range of magnetostrictive actuators is 0 Hz to 5 kHz, depending on the rod diameter. Larger diameters limit the frequency range due to eddy current losses, but the rods can

be laminated to extend the frequency range [Butler, 1988]. Piezo-electric actuators are capable of very high frequency responses. If the actuator is made up of a single piezofilm, frequencies of up to 1 GHz are attainable, but if piezostacks are used, the increase in actuator mass reduces the natural frequency, thereby narrowing the band significantly. However, frequencies of up to 20 kHz are attainable with piezoelectric actuators.

Another criterion by which the performance of actuators is judged, is output force. Hydraulic, piezoelectric and magnetostrictive actuators are capable of generating larger forces than electrodynamic actuators. Hydraulic actuators rely on the relatively low compressibility of hydraulic fluids to produce a hydrostatic force, while the output forces of piezoelectric and magnetostrictive actuators depend on the cross-sectional area of the actuator, the strain and the elastic modulus of the material.

To summarize the performance capabilities of the different actuator types, figure 1.3.2 gives a simple diagrammatical comparison of the stroke lengths, frequency responses and force outputs of the different actuator types.

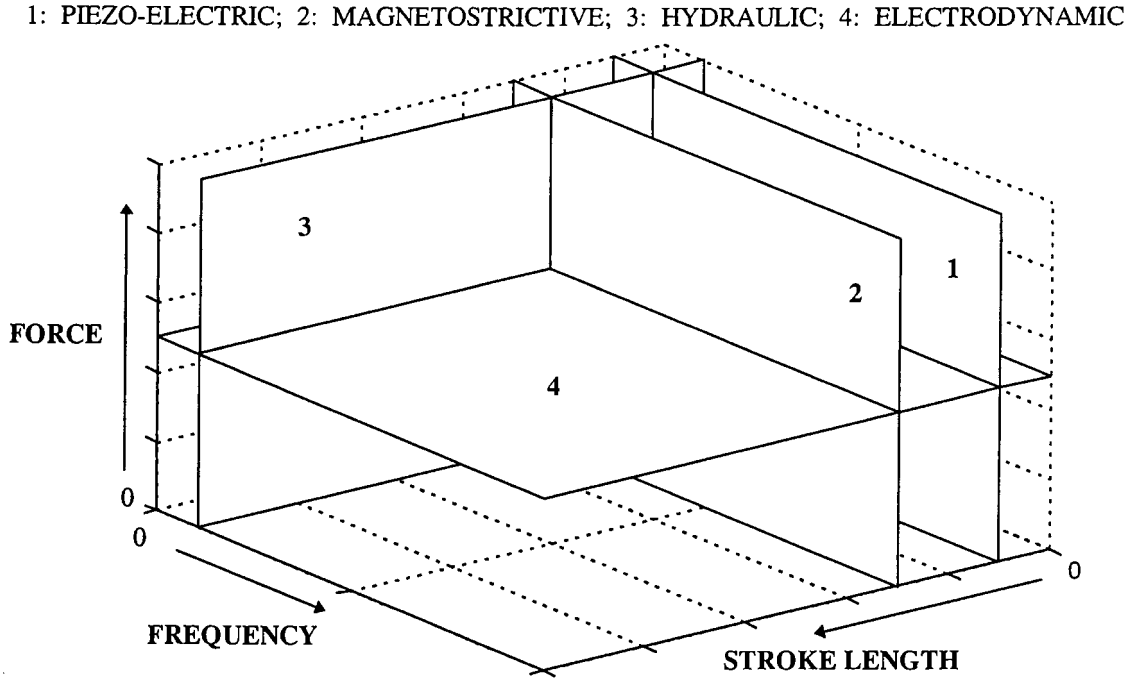

Figure 1.3.2: Comparison of piezoelectric, magnetostrictive, hydraulic and electro-dynamic actuators in terms of stroke length, frequency and force

The information given above can be used to select a suitable actuator type for stabilization of the optical instrument. Firstly, electrodynamic actuators can be ruled out due to their poor low-frequency response. The minimum disturbance frequency is 2,5 Hz (see section 1.1), while the lowest frequency attainable with electrodynamic actuators is 5 Hz.

Secondly, hydraulic actuators are generally not suitable for frequencies above 70 Hz, which are lower than the maximum disturbance frequency, i.e. 500 Hz. Furthermore, hydraulic

actuators require bulky external equipment like pumps, filters, piping and control valves to operate. Due to high pressures, fluid leakage may occur, necessitating periodic replenishment. Periodic flushing and cleaning may also be necessary.

Thirdly, piezoelectric actuators require large amplification (or gain) factors to produce reasonable stroke lengths. A disadvantage of a high gain factor is a reduction in the fundamental natural frequency of the isolation system, which may result in an insufficient isolation bandwidth and an accompanying reduction in actuator stroke at higher frequencies. Furthermore, high gains may cause high stresses in mechanical gain mechanisms. These shortcomings disqualify piezoelectric actuators as a suitable actuator type for LOS stabilization of the optical instrument.

Lastly, magnetostrictive actuators respond over a wide frequency range (0 Hz to 5kHz) and do not require the high excitation voltages of piezoelectric actuators. The stroke length may need amplification, but the gain factor will be smaller than would be required for piezo-electric actuators.

The magnetostrictive gain factor G can be calculated as follows:

$$G = \frac{l\theta}{2\varepsilon_{max} l_T} \tag{1.3.1}$$

where l is the length of the optical instrument, i.e. 250 mm (see section 1.1), θ is the difference between the disturbance angle and the desired LOS angle, i.e. 0,6 mrad, ε_{max} is the maximum magnetostrictive strain and l_T is the active length of the Terfenol-D rod. If the rod length is arbitrarily selected as 35 mm and the maximum allowable strain in the magnetostrictive active rod is 800 $\mu\varepsilon$, which is a conservative value if compared to a theoretical saturation strain of 2000 $\mu\varepsilon$, then the required amplification G, from equation 1.3.1, is 2,7. This is a reasonable gain factor, which can be relatively easily attained.

It can be concluded that magnetostrictive actuators are suitable for LOS stabilization of the optical instrument. The frequency band of the disturbance is within the actuator frequency band and a reasonable gain factor is required to produce the necessary attenuation of the disturbance. In this study, two Terfenol-D actuators will be used to isolate the optical instrument from the base disturbances. The active isolation mechanism is shown in figure 1.3.3.

Figure 1.3.3 shows the vibrating base, the optical element and two actuators, one at each end of the optical element and mounted between the base and the element. Each actuator consists of two Terfenol-D rods, with a coil wound around each rod, a flexible mechanism with a relatively low spring stiffness to act as a mechanical gain mechanism in order to multiply the output displacement of the actuator and, lastly, two coil springs to provide the desired prestress in the rods in order to enhance the saturation strain of the rods. An electronic control system will be used to measure the angular acceleration of the instrument and to control the output force of the actuator accordingly.

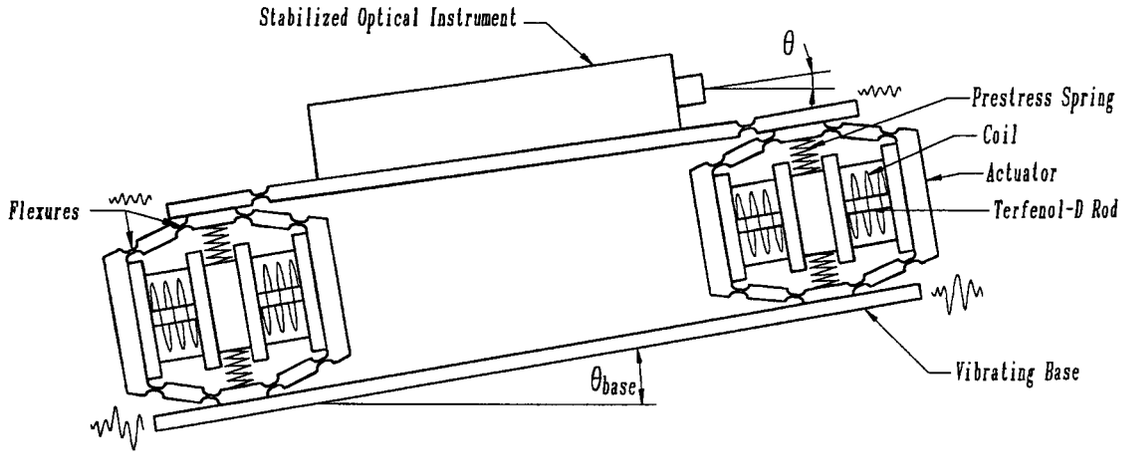

Figure 1.3.3: Magnetostrictive active isolation mechanism

The isolation approach consists of the following four steps: Firstly, a theoretical model, necessary to calculate the desired design input parameters, e.g. actuator size, frequency response and power consumed, is developed. Secondly, the isolators will be built and experimentally validated, and thirdly, the theory will be refined to match the experimental results as closely as needed. Lastly a magnetostrictive system, together with a validated mathematical model, will be demonstrated. To facilitate the work, contributions from related literature by other researchers will be used. The next section is devoted to literature in the field of magnetostriction.

1.4 Magnetostriction literature survey

This section summarizes the relevant work of other researchers in the field of magnetostriction and magnetostrictive applications. The literature survey is done to determine the contribution of these researchers to providing a better understanding of magnetostrictive behaviour, especially as far as the analysis, modelling and design of the magnetostrictive vibration isolation systems are concerned. The applicability of the different literature items to LOS stabilization of the optical instrument will be discussed in short below and the shortcomings will be pointed out.

For the purpose of this study, the available literature in the field of magnetostriction can broadly be classified in two groups, i.e. magnetostrictive material characteristics and magnetostrictive applications. Firstly, literature on material characteristics adresses the dependence of strain and magnetization on the applied field strength, mechanical prestress and temperature, nonlinearities like saturation and hysteresis, mechanical and magnetic biasing and eddy current losses. Secondly, literature on magnetostrictive applications describes, inter alia, vibration and shock isolation, noise cancellation and the design of micropositioners, actuators, resonators and shakers. Literature on magnetostrictive material characterization is discussed in section 1.4.1 and literature on applications in section 1.4.2.

1.4.1 Literature on magnetostrictive material characterization

The characterization, modelling and application of highly magnetostrictive materials are described in the PhD thesis of Kvarnsjö [1993]. A background on the relationship between magnetism and magnetostriction is given in the first chapter. In the second chapter, highly magnetostrictive materials are discussed and special attention is paid to the crystal structure of Terfenol-D, its mechanical properties and temperature dependence of magnetostrictive strain. Static material characterization is done in chapter 3 and linear and nonlinear one-dimensional models are derived in chapter 4. These models are expanded to include multidimensional behaviour and are verified in chapter 5. Chapter 6 is devoted to magnetic circuits, while chapter 7 discusses the application of highly magnetostrictive materials. Conclusions and recommendations on further work are made in chapter 8. A list of 83 references is included. Kvarnsjö's work is particularly useful for the characterization of Terfenol-D and is a valuable tool for the static and dynamic analysis and design of magnetostrictive actuators.

Clark et al [1983] address the influence of stress on magnetostriction and magnetization in rare-earth $Fe_{1.95}$ alloys. Five materials are analyzed over a stress range of 6,9 to 48,3 MPa. It is shown that the shape of the magnetostriction and magnetization curves depend on the relative concentrations of terbium, dysprosium and holmium. Schulze et al [1992] analyze the stress dependence of mechanical coupling, permeability and magnetostriction in $Tb_{0.3}Dy_{0.7}Fe_{1.95}$. The work was done to show how the simultaneous responses of these parameters change with stress and provides guidelines for the design of actuators which retain optimum performance under variable loading.

A finite element analysis of magnetomechanical coupling in magnetostrictive materials is described by Besbes et al [1996]. The finite element method is applied to calculate the magnetic field and mechanical deformation by minimizing the energy functional, which is the sum of the magnetic energy, mechanical energy and work done by external forces. Weak and strong coupling models are discussed in short. The weak coupling model solves the nonlinear magnetic and mechanical equations using an iterative technique, while the strong coupling model solves the nonlinear magnetic and mechanical equations simultaneously using the Newton-Raphson method. Magnetic force is calculated by means of the virtual work principle. The strong coupling model is applied to a simple two-dimensional example and the results are compared with those of the weak coupling model.

A large number of articles on hysteresis modelling of magnetic materials are available. Most of these articles concentrate on Preisach hysteresis models, such as those by Adly et al [1991], Bergqvist & Engdahl [1991], Doong & Mayergoyz [1985], Ossart et al [1995], Restorff et al [1990] and Vajda & Della Torre [1995]. A hysteresis model which makes use of Bessel functions, is presented by Sablik & Jiles [1988], while Rizzoli & Masotti [1995] model the simultaneous effect of hysteresis and saturation using the harmonic balance technique. Leonard et al [1995] describe finite element modelling of hysteresis, while Hall & Flatau [1992] give a much simpler model which makes use of a harmonic function superimposed on the strain curve to include the effect of hysteresis. These models aid in predicting the hysteresis losses during one cycle of static and dynamic excitation.

Clark [1993] investigates the influence of temperatures ranging from 50 K to 250 °C, on the magnetostriction of Terfenol-D and Tb_xDy_{1-x}. Magnetostriction curves are given for two prestresses and for field strengths ranging from 250 Oe to 2000 Oe. It is shown that, for high field

strengths, magnetostriction drops almost linearly with temperature. This article makes the designer aware of the fact that high temperatures must be avoided in magnetostrictive actuators and also quantifies the expected losses.

Sewell and Kuhn [1988] compared different magnetic biasing techniques for Terfenol-D. A magnetic field analysis program utilizing finite element techniques provided solutions that yielded good agreement with measured data. Emphasis was placed on the sensitivity of Terfenol-D to the variation in material properties that can occur under changing conditions of bias field, prestress and drive field. The article provides the designer with different options for magnetic biasing of the magnetostrictive rod.

In a very short article, Butler & Lizza [1987] developed an Eddy current loss factor series for magnetostrictive rods from Kelvin functions of zero order and their derivatives. This model can be used to predict the Eddy current losses for the applicable excitation frequency and rod diameter.

Additional articles on magnetostrictive materials which deserve to be mentioned, discuss magnetostriction in ferromagnetic composites in an elastomer matrix [Bednarck, 1999] and the modelling of large magnetostriction in ferromagnetic shape memory alloys [Likhachev & Ullakko, 2000]. The combination of magnetostrictive characteristics with those of other materials, such as plastics, which display large deformations, and alternative smart materials, which can be used for actuation, are described.

This concludes the discussion of literature on magnetostrictive material characterization. The next section will be devoted to literature on magnetostrictive applications.

1.4.2 Literature on magnetostrictive vibration isolation applications

Five important articles on active vibration and shock isolation are available in the literature. Bryant et al [1993] describe the use of Terfenol with feedback and/or neural network controllers for active vibration control in structures. Tests were performed on a three-legged table, with Terfenol actuators acting as the table legs. The actuators were used to attenuate the vibrations transmitted to the tabletop via the legs. The actuator forces were controlled by a PID controller and a neural network controller. The latter operated on the principle of adaptive back-propagation, which is a fast learning and adaptation algorithm.

Secondly, Hiller et al [1989] describe the attenuation and transformation of vibration through active control of magnetostrictive Terfenol. Experimental results indicate that, if properly controlled, vibration isolation that exhibits significant low-frequency performance and small static deflection can be obtained with magnetostriction.

Reed [1989] reports on the construction of a vibrator using a highly magnetostrictive material. The performance of the vibrator is modelled and verified experimentally. The control system makes use of acceleration feedback to reduce amplification at the mechanical resonance frequency.

In another publication, Reed [1988] describes shock isolation using an active magnetostrictive element. The actuator was modelled and tested and a controller was designed to demonstrate the ability of the actuator to reduce shock levels.

Hall & Flatau [1992] report on the development of a broadband magnetostrictive shaker with a size and mass of only 10% of that of a normal electrodynamic shaker. The frequency band is 300 Hz to 10 kHz and the shaker is capable of producing acceleration amplitudes in excess of 1960 m/s^2 at frequencies greater than 4 kHz with a load mass of 24 gram.

Compact magnetostrictive actuators and linear stepper motors are discussed by Joshi [2000]. Various magnetostrictive materials, together with their saturation strains and Curie temperatures, are listed. Results of strain measurements in TbDyZn (a magnetostrictive alloy) at cryogenic temperatures of 4,2 K and 77 K, are given. A method of obtaining linear motion actuation, by means of a magnetic rod surrounded by an electrical coil, is presented. Applications of linear actuators, such as precision positioning of large adaptive optical surfaces, vibration control, switch and valve operation, are mentioned. Typical response of a small actuator is shown. A digitally controlled, two-mode operation stepper motor with a stroke length of several millimeters, consisting of three magnetostrictive actuators, is discussed and its operation is described.

Certainly one of the most comprehensive publications is the Application Manual for the Design of Etrema Terfenol-D Magnetostrictive Transducers [Butler, 1988]. The manual gives fundamental magnetostrictive relations, like the magnetostrictive coupling coefficient and the eddy current critical frequency, as well as the thermal, mechanical and magnetic properties of Terfenol-D. Design considerations are discussed in full and examples are given for the design of a micropositioner, an actuator, a resonator and an acoustic transducer.

Bond graph models for linear motion magnetostrictive actuators are described by Bryant [1996]. Constitutive equations for strain and magnetic flux density, in terms of field and stress, are given. The Bond graph structure and derivation of the state equations, frequency-domain transfer functions and response, are described. Modelled transfer function spectra are compared with experimentally-determined spectra. Equations for modal vibrations of a magnetostrictive rod are derived in an appendix. The coil voltage to actuator displacement transfer function that is derived, is particularly applicable to this study.

A concise summary of magnetostriction, its principle of operation, modelling of the phenomenon, applications, properties and cost of Terfenol-D are given by Van Schoor et al [1999]. Magnetostrictive actuator modelling techniques are discussed and coil design information is given, together with an SDOF model of an actuator exciting a load mass. Active vibration isolation, passive-active damping and sensor applications are discussed in short. Advantages and disadvantages to be taken into consideration in magnetostrictive actuator design are mentioned.

Additional publications on magnetostrictive applications that also deserve to be mentioned, are the articles on the design and analysis of a self-sensing Terfenol-D actuator [Pratt, 1993], the use of magnetostrictive rods in mechanical applications [Dyberg, 1986], the impedance analysis of an acoustic vibration element [Wakiwaka et al, 1993], the development of a hybrid magnetostrictive and piezo-electric Tonpilz transducer [Butler et al, 1993], the development of an underwater sound transducer [Meeks & Timme, 1977], the silencing of aircraft cabin noise using "antinoise" actuators [Machine Design, April 4, 1994] and magnetostrictive actuation to adjust the shape of an aircraft wing [Ashley, 1998].

The above research provides essential information for the design of a magnetostrictive vibration isolation system. The first five articles in particular cover the control aspect in detail and the models, transfer functions and block diagrams will be necessary aids in the development of a magnetostrictive LOS stabilization system. The Etrema design manual gives indispensible practical and empirical design information, which will be employed in the analysis and design stages of the LOS isolation device. The information given by Van Schoor et al [1999] will serve as a guide to derive the equation of motion and coil current equation of a magnetostrictive actuator. (These equations will be required to investigate the influences of various actuator and coil parameters on actuator performance in the design stage). However, there is one shortcoming in all the articles, namely that no mention is made of any method to stabilize the line of sight of optical instruments.

A current method of sightline stabilization is by means of gyroscopes, as described by Stockum & Carroll [1984]. Gyroscopes make use of gimbals, driven by motors to run at high rotational speeds, to increase the inertia of the system. Unfortunately, gyroscopes are expensive and sensitive instruments, which may not operate smoothly, due to gimbal stiction. The latter phenomenon causes highly nonlinear behaviour, which complicates controller design. The magnetostrictive active LOS stabilization method is a cheaper alternative, which, as will be shown in this study, can be satisfactorily controlled by means of a relatively simple linear controller.

The next section gives a systematic layout of the research and gives an outline of the rest of the thesis.

1.5 Thesis outline

The behaviour of the magnetostrictive active stabilization system is modelled and simulated in chapter 2. The model will serve as a design input and also as an aid in identifying system parameters from experimental test results. The chapter starts with linear and nonlinear models of the magnetostrictive and magnetization characteristics of Terfenol-D, after which a hysteresis model is presented. The equations of motion and coil current equations will subsequently be derived and written in state-space form. A simulation of the behaviour of the actuator will be carried out, which will be followed by a simulation of the behaviour of the system, consisting of the two actuators and optical instrument.

Chapter 3 will be devoted to the design and manufacture of the magnetostrictive actuators, consisting of the Terfenol-D rods, field coils, prestress springs, gain mechanism and support structure of the optical instrument. The information obtained in chapter 2 will serve as design input. Design requirements will be given and design concepts will be generated. The most suitable design concept will be selected. Design calculations will be done for the different system components and safety checks will be included. Design drawings will be made and the actuators and system will be built and assembled.

Experimental evaluation of the stabilization system will be described in chapter 4. The purpose of the tests will be to experimentally determine the system static and dynamic characteristics and to validate and update the model that was developed in chapter 2. The test procedure will be described and test equipment will be discussed. The tests will comprise static and dynamic tests. Static test results will be used to determine the saturation voltages of

the actuators and their linear ranges of operation. Dynamic tests will be carried out to obtain transfer functions between coil input voltage and output angular acceleration of the optical instrument.

Chapter 5 will cover the adjustment of certain model parameters such as natural frequencies, damping factors, input forces and coil current-to-voltage ratios. The purpose will be to generate an improved validated model which can be used with confidence to predict the behaviour of the system and which can be employed to design a suitable controller for the plant. The adjusted parameters will be used to remodel the system behaviour and the results will again be compared with the experimental results.

In chapter 6, a control strategy will be formulated for the plant. Control theory will be discussed, after which optimal and sub-optimal controllers will be designed. Control system stability will be investigated. Control hardware will be described. The controller will be implemented and tested. The test results will be processed, presented and discussed. Isolation system transmissibility will be shown graphically for the disturbance frequency range.

Conclusions which can be derived from the results of this study, will be made in chapter 7 and recommendations will be given about future work in the field of magnetostrictive active stabilization of optical elements.

Chapter 2
Modelling and simulation of magnetostrictive line of sight stabilization system

2.1 Background

In this chapter, the characteristics and behaviour of the magnetostrictive LOS stabilization system, consisting of the two Terfenol-D actuators, the optical instrument and its support structure, are modelled and simulated. The objective of a system model is firstly to obtain a tool for predicting system behaviour before manufacture. The model will give valuable insight into the influence of the linear and nonlinear characteristics of the magnetostrictive active material, i.e. Terfenol-D, on the dynamic properties of the system. Once the material characteristics are known, the linear and nonlinear equations of motion and the coil current equations will be derived. These equations will express the dynamic system behaviour in terms of system parameters such as the Terfenol-D rod diameter and length, actuator displacement gain factor, resistance and inductance of the field coils, mass and damping factors of the actuators and optical instrument.

The model will further be required to write the dynamic equations in state-space form, which is a powerful method of analyzing the coupled mechanical and electrical behaviour of the system. Both linear and nonlinear state-space equations will be derived. In order to facilitate Laplace and frequency domain analysis of the system behaviour, the characteristics will be linearized. The transfer functions (*TF*'s) of the system will subsequently be obtained from the state-space model. A particularly important *TF* which will be derived, is the ratio between the actuator input voltage and instrument angular displacement. In addition, system natural characteristics, such as the natural frequencies, damping factors and resistance to induction ratios of the actuator coils, will be calculated by means of the state-space method. Furthermore, the model will make it possible to simulate system behaviour for arbitrary actuator coil input voltages, like wide-band random voltages.

The model which will be derived in this chapter, will be used in chapter 3 to do a detailed system design. The model will provide a tool to investigate the influences of various design parameters on system performance. The model will for instance be applied to analyze the influence of the number of coil turns and wire thickness on the resistance to inductance ratio of the coil, and also to calculate the effect of different displacement gain factors on the output displacement of the optical instrument.

A further reason for modelling the system characteristics and behaviour, is to obtain a model with which system parameters can be extracted, or identified, from measured data during the experimental evaluation phase. The test data will typically contain measured spectra between coil input voltage and instrument angular acceleration. From these results, natural frequencies and damping factors, as well as coil characteristics will be determined by matching the measured values with the parameters in the model. The extracted parameters will then indicate the degree of accuracy of the initial model, and will also provide an indication of how the model can be adjusted and updated to give a closer representation of the measured behaviour. Identification and updating of the system parameters will be done in chapter 5.

Lastly, the model will be required for control system design purposes. In order to design a suitable controller, *TF* and state-space models of the uncontrolled system (plant) are required to predict the behaviour and characteristics of the controlled system. The models will be applied to determine, inter alia, feedback and feedforward gain matrices. Once the gains are known, behaviour of the controlled system will be simulated and experimentally evaluated. Control system design and testing will be done in chapter 6.

Modelling and simulation of the system characteristics and behaviour will be systematically done in the following sections of this chapter. The magnetostrictive and magnetization characteristics of Terfenol-D will be modelled in sections 2.2 and 2.3. In this study, material characteristics are classified in two groups, i.e. saturation characteristics and hysteresis characteristics. Saturation characteristics will be covered in detail in section 2.2, while section 2.3 will cover hysteresis characteristics.

The equation of motion of a magnetostrictive actuator, in isolation of the rest of the system, will be derived from first principles in section 2.4. This will be done for both linear and nonlinear material properties. For the sake of simplicity, it will be assumed that the actuator has only one degree of freedom. The coil current equation, a differential equation (DE) which expresses the current in the coil wire in terms of the actuator output speed and input voltage, will also be derived from first principles.

In section 2.5, the equation of motion and the coil current equation of the actuator will be coupled to give a single set of dynamic actuator equations in state-space form. The linear and nonlinear state and output equations will be derived in detail. The Laplace and frequency domain transfer functions will be obtained from the linear state-space model.

Natural vibration behaviour of the actuator will be covered in section 2.6. The natural characteristics, i.e. the natural frequency, damping factor and effective resistance to inductance ratio of the coil will be expressed in terms of the eigenvalues of the state-space model and poles of the Laplace-domain transfer function.

Forced behaviour of the actuator will be simulated in section 2.7. Nonlinear behaviour will be simulated first, whereafter the average values of the magnetostrictive parameters will be calculated from the nonlinear solution. These parameters will then be employed to do a linear frequency domain simulation of the actuator behaviour.

In the last section of the chapter, section 2.8, behaviour of the entire system, consisting of the two actuators, the optical instrument and its support structure, will be modelled. The linear actuator model developed in section 2.7, will be coupled to those of the optical instrument and its support structure by means of the Rayleigh-Ritz method. The system state-space model and *TF*'s will be derived. Frequency domain *TF* magnitudes and phase angles will be shown graphically.

2.2 Magnetostrictive and magnetization characteristics of Terfenol-D

This section covers the linear and nonlinear magnetostrictive and magnetization characteristics of Terfenol-D. A background on the sources of nonlinear behaviour in Terfenol-D, i.e. saturation and hysteresis, is given. The nonlinear strain and flux density characteristics are shown graphically, and the influence of stress and field on the saturation properties is discussed. Regression equations are given which closely represent the characteristics. The need for linearization is pointed out and the characteristics are linearized. The linear magnetostrictive and magnetization parameters, i.e. Young's Modulus, the strain constant, piezomagnetic cross-coupling constant and permeability are defined, expressed mathematically and shown graphically. An inverse characteristic, with stress as a function of field, is also presented.

Terfenol-D displays magnetostrictive and magnetization saturation and hysteresis characteristics. When a magnetic field is applied to a Terfenol-D rod, small domains in the material rotate, causing the rod to expand in the direction of the field. For small fields, the strain is proportional to the field, but when all the domains are aligned, the material is magnetically saturated and no further elongation of the rod is possible. A similar phenomenon occurs in the magnetization characteristic of Terfenol-D. When a small field is applied, the increase in magnetic flux density will initially be proportional to the increase in field strength, but when the material becomes magnetically saturated, any further increase in field strength will produce no further increase in flux density.

Magnetostrictive hysteresis in Terfenol-D is explained as follows: If an increasing magnetic field is applied to a demagnetized Terfenol-D rod, the rod will produce an increase in strain. The strain versus field characteristic for the increasing field is known as the loading characteristic. If the field is subsequently removed, the strain will be reduced. However, the rod remains partially magnetized. The characteristic for a decreasing field, or the unloading characteristic, therefore differs from the loading characteristic. If a cyclic field is applied to the rod, an energy loss occurs during every cycle. The magnitude of the loss depends on the initial field and strain, mechanical stress and field strength.

In general, nonlinear systems display phenomena which are not encountered in linear systems, like amplitude-dependent natural frequencies and damping factors, and sub- and superharmonics. As a result, special mathematical techniques are required to describe nonlinear system behaviour, such as the perturbation method, the method of slowly varying amplitude and phase and the describing function method. The mathematical analysis is further complicated if a nonlinearity is discontinuous, because the characteristic is not differentiable at reversal points between loading and unloading characteristics. This type of nonlinearity is appropriately known as a "hard nonlinearity" [Slotine & Li, 1991]. Examples of a hard nonlinearities are hysteresis, backlash, Coulomb friction and dead bands.

Only a few mathematical methods can be applied to analyze the behaviour of systems with hard nonlinearities. One method that is often used for the design of nonlinear control systems, is the describing function (DF) method [Gelb & Vander Velde, 1968]. This method can predict, inter alia, the response of nonlinear systems to sinusoidal inputs. Only the first harmonic component of the system behaviour is taken into account and superharmonics are neglected.

Linear system analysis, on the other hand, is comparatively simple. Characteristics of linear systems, like eigenvalues, eigenvectors, natural frequencies, damping factors and Laplace- and frequency domain transfer functions, are mostly relatively easy to obtain. For this reason, linearization of nonlinear systems is recommended in order to simplify the mathematical analyses.

However, the application of linear system analysis to nonlinear system behaviour may be inadequate. Although linearization may be accurate in a limited working range, it may be inaccurate in the nonlinear or saturation range [Slotine & Li, 1991]. Furthermore, if a control system is designed with parameters obtained from a linear system analysis, poor control performance and system instability may result. In order to design a system which will perform equally well in its linear and nonlinear ranges, it will be necessary to take the effects of nonlinearities into account.

This can be done in more than one way. Firstly, a purely nonlinear analysis can be done where the magnetostrictive and magnetization properties are evaluated at each input field strength. The change in strain per unit change in field strength will not be constant, but will be a function of the momental field. The advantage of this method is that behaviour can be described with a high degree of accuracy. The disadvantage, however, is that the analysis can become extremely complex.

Secondly, the analysis can be carried out by assuming linear behaviour over the excitation range, i.e. the slope of the strain versus field characteristic is assumed constant over the applicable range of behaviour. If the range changes, the slope of the characteristic changes. Nonlinearities are therefore described as range-dependent linearities. This approach is favoured for the advantages it offers in terms of simplified mathematical operations, but may not be as accurate as the nonlinear analysis, due to the fact that sub- and superharmonics are neglected.

In order to analyze and design the system, it is clear from the above paragraphs that both the linear and nonlinear magnetostriction and magnetization characteristics of Terfenol-D are required. These characteristics will enable the designer to obtain the saturation field and proportionality constant between field and strain, to determine to what extent hysteresis will affect actuator performance and to determine whether the input field strength will be sufficient to produce the desired stroke length. The magnetostrictive and magnetization characteristics of Terfenol-D are discussed next.

Strains in magnetostrictive materials are produced by two sources, i.e. a magnetic field and a mechanical stress. A magnetic field rotates the magnetic domains in the material to produce a strain, while a mechanical stress causes an elastic deformation of the material. When both a magnetic field and a mechanical stress are applied, the resultant strain is a combined effect of those of field and stress. Mathematically, strain can be expressed as follows:

$$\varepsilon = \varepsilon(\sigma, H) \qquad \textbf{(2.2.1)}$$

where ε is strain, σ is mechanical stress and H is field strength.

Magnetostriction is also a phenomenon where the combined effect of the application of a mechanical stress and a magnetic field causes a change in magnetic induction (or magnetic flux, magnetization) of a ferromagnetic material [Harris, 1988].

Flux density can therefore, as in the case with material strain, be mathematically expressed as a function of stress and field strength:

$$B = B(\sigma, H) \tag{2.2.2}$$

where B is flux density.

The magnetostrictive and magnetization characteristics will respectively be discussed in sections 2.2.1 and 2.2.2. In both sections, the general nonlinear characteristics will be given first, followed by the linear characteristics. Hysteresis effects on the magnetostrictive and magnetization characteristics will be discussed in section 2.3.

2.2.1 Magnetostrictive characteristics of Terfenol-D

This section covers the linear and nonlinear magnetostrictive characteristics of Terfenol-D. The nonlinear strain characteristics are shown graphically, and the influence of stress and field on the saturation properties is discussed. A two-dimensional regression equation is given which closely represents published characteristics. The characteristics are linearized and the linear magnetostrictive parameters, i.e. Young's Modulus and the strain constant are defined, expressed mathematically and shown graphically. An inverse characteristic, where stress is a function of field, is also presented.

There have been many efforts by researchers to obtain the linear and nonlinear characteristics of Terfenol-D. Consequently, a vast number of applicable data sources exist, such as those by Kvarnsjö [1993], Clark & Savage [1983], Clark et al [1983], Clark et al [1990] and Schulze et al [1992]. Kvarnsjö [1993] gives a complete set of strain versus field strength curves for 10 constant compressive stresses. Clark & Savage [1983] discuss the magnetostriction of rare earth-Fe_2 compounds under compressive stress, while Clark et al [1983] describe the effect of stress on the magnetostriction and magnetization of rare-earth $Fe_{1.95}$ alloys. Schulze et al [1992] analyze the stress-dependence of mechanical coupling, permeability and magnetostriction in $Tb_{0.3}Dy_{0.7}Fe_{1.95}$, while Clark et al [1990] characterize the magnetomechanical coupling in Bridgman-grown $Tb_{0.3}Dy_{0.7}Fe_{1.9}$ at high drive levels.

The magnetostrictive characteristics which will be used in this study, will be obtained from data supplied by Kvarnsjö [1993] and Clark & Savage [1983]. Kvarnsjö [1993] gives a complete set of strain vs mechanical stress and magnetic field curves. The stress range is -65 MPa to -1 MPa and the field strength range is 0 to 2600 Oe (207 kA/m). These strain curves supply a powerful tool for the mathematical analysis of the magnetostrictive characteristics. Two-dimensional interpolation can be applied to the data to obtain functional relationships between stress, field and strain. Furthermore, the mathematical function thus obtained can be differentiated with respect to field and stress to give the strain constant and Young's Modulus respectively.

The data supplied by Clark & Savage is particularly useful for studying the saturation properties of Terfenol-D for various compressive stresses. Although not as complete as the data supplied by Kvarnsjö, the strain curves facilitate the comparison of the saturation characteristics for different stresses. This is accomplished by normalizing the strain curves with respect to stress at zero field strength, in other words, at zero field, the strain is zero for all the stresses. The strain characteristics as supplied by Kvarnsjö [1993] and the normalized strain characteristics as supplied by Clark & Savage [1983] are shown in figure 2.2.1.1 and figure 2.2.1.2 respectively.

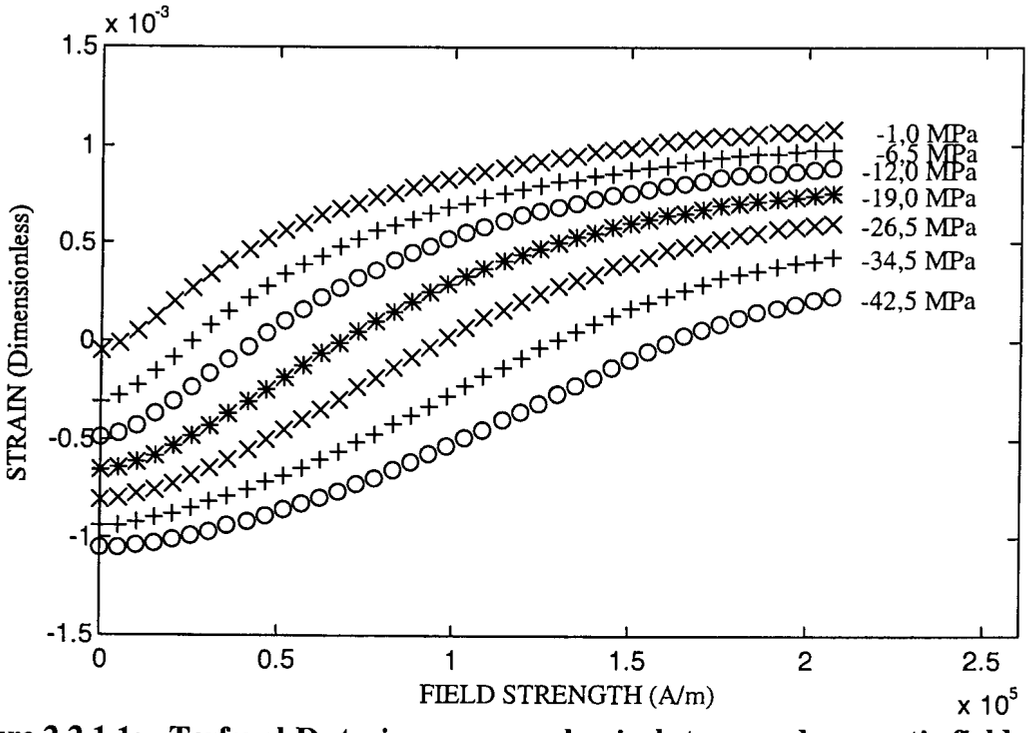

Figure 2.2.1.1: Terfenol-D strain versus mechanical stress and magnetic field strength [Kvarnsjö, 1993]

Figure 2.2.1.1 shows strain versus magnetic field for seven constant compressive stresses. The stresses range from -42,5 MPa to -1 MPa and the field strengths range from 0 to 207 kA/m. It can be seen from figure 2.2.1.1 that strain increases with magnetic field strength and also with mechanical stress. For low compressive stresses, the strain curves initially rise sharply with field, but saturate at relatively low fields and strains. As the compressive stress is increased, the curves do not initially rise as sharply as in the case of low compressive stresses, which implies that higher compressive stresses necessitate larger field strengths to produce the same strain. Also, at higher compressive stresses, the strains saturate at higher field strengths. Although a qualitative analysis of the saturation characteristics of Terfenol-D can be done by means of figure 2.2.1.1, a more complete quantitative analysis can be done by means of figure 2.2.1.2.

Figure 2.2.1.2 shows the normalized strain versus magnetic field for seven constant compressive stresses. The compressive stresses range from 6,9 MPa to 24,1 MPa and the field strengths range from 0 to 1250 Oe (approximately 100 kA/m). The strains at zero field strength are zero for all the stresses. Figure 2.2.1.2 is mainly used to study the magnetostrictive saturation properties of Terfenol-D. It can be seen that, for low stresses, the

strain curves initially rise sharply with field, but saturate at relatively low fields. It can also be seen that the strain curves do not reach sudden saturation points, but that the slopes of the curves gradually drop and eventually decay to zero. The saturation fields and strains are therefore not clearly demarcated.

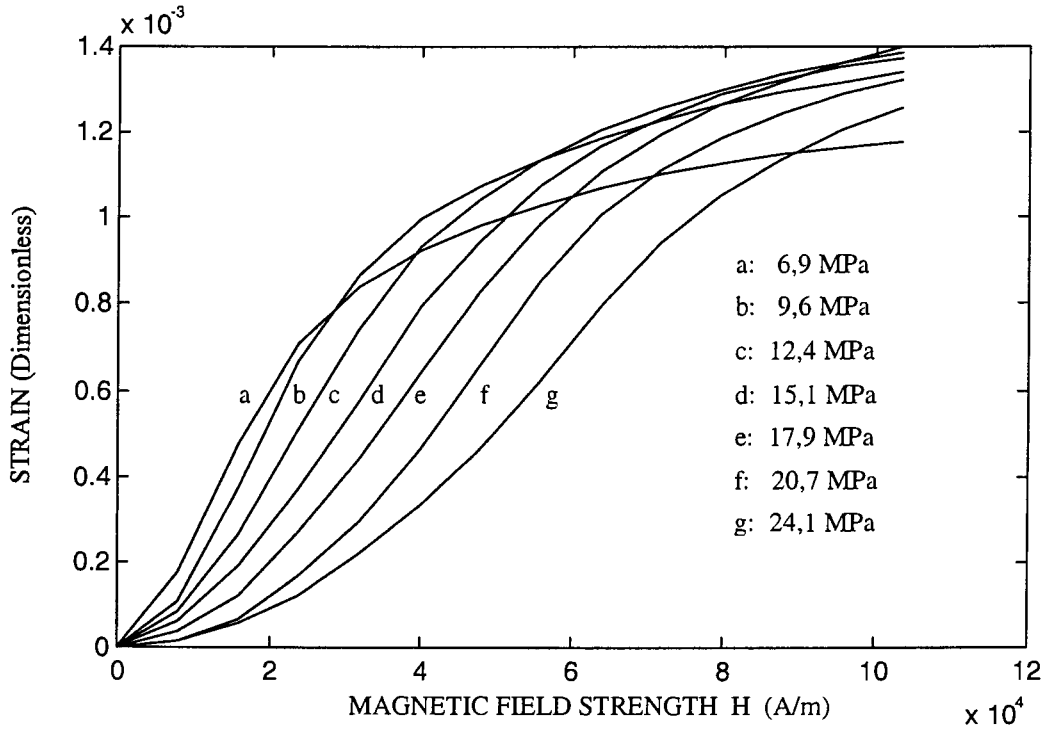

Figure 2.2.1.2: Normalized Terfenol-D strain versus mechanical stress and magnetic field strength [Clark & Savage, 1983]

In order to determine the particular saturation strain and field for a given stress, subjective judgment is needed. Consider, for example, the strain curve for a 6,9 MPa compressive stress (curve a). It can be judged that saturation sets in at 30 kA/m, where the corresponding strain is $0{,}8.10^{-3}$, and that full saturation is reached at a field strength of 100 kA/m, where the strain is $1{,}15.10^{-3}$. As another example, consider the strain curve for a 17,9 MPa compressive stress (curve e). Saturation sets in at 60 kA/m, where the strain is 1.10^{-3}, while at 100 kA/m, where the strain is $1{,}4.10^{-3}$, full saturation has not yet been reached. It can be concluded that the saturation strain can be greatly enhanced by applying higher compressive stresses, but that higher field strengths are required to produce the higher saturation strains. Generally speaking, the higher the compressive stress, the higher the saturation strain. According to Kvarnsjö [1993], a saturation strain of up to 2.10^{-3} is possible with a compressive stress of 65 MPa.

The magnetostrictive strain and saturation characteristics of Terfenol-D have been presented in graphical form in the foregoing paragraphs. The need however also exists for a mathematical function which will express the strain in terms of the mechanical stress and magnetic field. The function will enable the designer of a magnetostrictive actuator and LOS stabilization system to calculate the strain in a Terfenol-D rod for any given stress and field. Furthermore, the function will make it possible to simulate the behaviour of the actuator and system for continuously varying stresses and field strengths. To obtain this function, a

technique is required which will transform the graphical data to a mathematical equation. Such techniques are known in mathematical terms as data regression or data fitting methods.

Several regression techniques can be employed to obtain the desired mathematical function. Firstly, a one-dimensional least-squares nonlinear function can be fitted to the data to obtain strain in terms of field strength for a constant stress. A large number of function types can be used for this purpose, such as polynomial functions, piecewise linear functions and saturating functions. An example of a saturating function for strain in terms of field is given in equation 2.2.1.1:

$$\varepsilon(H)\Big|_{\sigma=const} = \sum_{i=0}^{m} a_i \left[\tanh\left(\frac{\pi H}{H_{sat}} \right) \right]^i \qquad \textbf{(2.2.1.1)}$$

where ε is the strain, H is the field, H_{sat} is the saturation field and σ is the stress. a_i are polynomial constants which depend on the order m of the data fit, as well as on the value of σ. The advantage of this method of data regression is that a high degree of accuracy can be obtaned with a relatively low order of m. The disadvantage is that strain is expressed as a function of field only, and no account is taken of the effect of stress. In order to describe the simultaneous relationship between strain, stress and field, a functional relationship for a_i in terms of stress is required. The one-dimensional nonlinear function is therefore not as simple to apply as was initially intended, and it becomes clear that an alternative technique of data regression will have to be considered.

One such technique is a two-dimensional polynomial data fit. This data regression technique is described in more detail by, inter alia, Hayes [1970]. The method is simpler to apply due to the fact that strain can be expressed as a single function of stress and field. This will facilitate the strain calculation, as well as the derivation of the magnetostrictive constants, i.e. Young's Modulus and the strain constant. The disadvantage of the method is that higher order polynomials are generally required to represent the data fairly accurately. However, this method is preferred to the one-dimensional data fit because of its simplicity of use. The following equation expresses strain as a two dimensional polynomial function of stress and field:

$$\varepsilon(\sigma, H) = \sum_{i=0}^{m} \sum_{j=0}^{n} p_{ij} \sigma^j H^i \qquad \textbf{(2.2.1.2)}$$

where ε is strain, σ is mechanical stress and H is magnetic field strength. m is the order of the polynomial for strain as a function of field and n is the order of the polynomial for strain as a function of stress. p_{ij} are the two-dimensional polynomial coefficients which will give the most accurate approximation to the data for the applicable values of m and n.

Note that in equation 2.2.1.2, stress is of the order of 10^6 Pa, and field is of the order of 10^5 A/m. Products of high order polynomials of stress and field, such as those in equation 2.2.1.2, may therefore be quite large quantities, which may be difficult to calculate and to handle numerically. To avoid the problem of having to deal with unnecessarily large numbers,

it is convenient to scale stress by a factor 10^6 Pa and field by a factor 10^5 A/m, as follows:

$$\varepsilon(\sigma,H)=\sum_{i=0}^{m}\sum_{j=0}^{n}p_{ij}\left(\frac{\sigma}{10^6}\right)^j\left(\frac{H}{10^5}\right)^i \qquad \textbf{(2.2.1.3)}$$

where σ is in Pa and H is in A/m. The order of the polynomial and its influence on the accuracy of the data fit deserve to be mentioned here. Generally, higher values of m and n will give higher accuracy. It was found that values of $m=8$ and $n=4$ gave sufficient accuracy for the strain data supplied by Kvarnsjö [1993]. The values of p_{ij} for $m=8$ and $n=4$ are shown in table 2.2.1.1. The coefficients are truncated after four digits.

Table 2.2.1.1: Two-dimensional polynomial coefficients p_{ij} for strain as a function of mechanical stress and magnetic field

j / *i*	0	1	2	3	4
0	$-1{,}6347.10^{-7}$	$5{,}7158.10^{-5}$	$1{,}7481.10^{-6}$	$3{,}5580.10^{-8}$	$2{,}8999.10^{-10}$
1	$5{,}9733.10^{-4}$	$1{,}2848.10^{-4}$	$1{,}0642.10^{-5}$	$3{,}4613.10^{-7}$	$3{,}7434.10^{-9}$
2	$6{,}2387.10^{-3}$	$-8{,}6155.10^{-4}$	$-1{,}1545.10^{-4}$	$-4{,}1127.10^{-6}$	$-4{,}5506.10^{-8}$
3	$-2{,}0391.10^{-2}$	$1{,}7893.10^{-3}$	$3{,}2207.10^{-4}$	$1{,}2486.10^{-5}$	$1{,}4402.10^{-7}$
4	$3{,}0809.10^{-2}$	$-1{,}9773.10^{-3}$	$-4{,}4307.10^{-4}$	$-1{,}8152.10^{-5}$	$-2{,}1542.10^{-7}$
5	$-2{,}6232.10^{-2}$	$1{,}3023.10^{-3}$	$3{,}4734.10^{-4}$	$1{,}4739.10^{-5}$	$1{,}7806.10^{-7}$
6	$1{,}2855.10^{-2}$	$-5{,}1776.10^{-4}$	$-1{,}5876.10^{-4}$	$-6{,}8867.10^{-6}$	$-8{,}4052.10^{-8}$
7	$-3{,}3814.10^{-3}$	$1{,}1583.10^{-4}$	$3{,}9542.10^{-5}$	$1{,}7379.10^{-6}$	$2{,}1320.10^{-8}$
8	$3{,}6962.10^{-4}$	$-1{,}1295.10^{-5}$	$-4{,}1571.10^{-6}$	$-1{,}8402.10^{-7}$	$-2{,}2615.10^{-9}$

The accuracy of the data fit can be evaluated by comparing the strains calculated with equation 2.2.1.3, with the strains given in figure 2.2.1.1. The strains are calculated for seven compressive stresses in a range of -42,5 MPa to -1 MPa and for a field strength range of 0 to 207 kA/m. The calculated strains and the data as supplied by Kvarnsjö [1993] are shown in figure 2.2.1.3.

Figure 2.2.1.3 shows that, for the tabulated values of p_{ij} in table 2.2.1.1, the strains calculated with equation 2.2.1.3 compare favourably with the data as supplied by Kvarnsjö [1993]. The root mean square (RMS) error of the regression equation is 3,03% for a stress range of -42,5 MPa to -1 MPa and for a field range of 0 to 207 kA/m. It can therefore be concluded that the regression equation closely represents the published data.

Thus far in section 2.2.1, extensive attention has been paid to the nonlinear magnetostriction characteristics of Terfenol-D. The above information can however only be applied to do nonlinear analyses of the behaviour of a magnetostrictive actuator and LOS stabilization system, but is insufficient to analyze linear behaviour. The questions that now arise are: How and to what extent can the magnetostrictive characteristics of Terfenol-D be linearized, and how can the linear magnetostrictive parameters, i.e. Young's Modulus and the strain constant, be calculated. These questions will be answered in the following paragraphs.

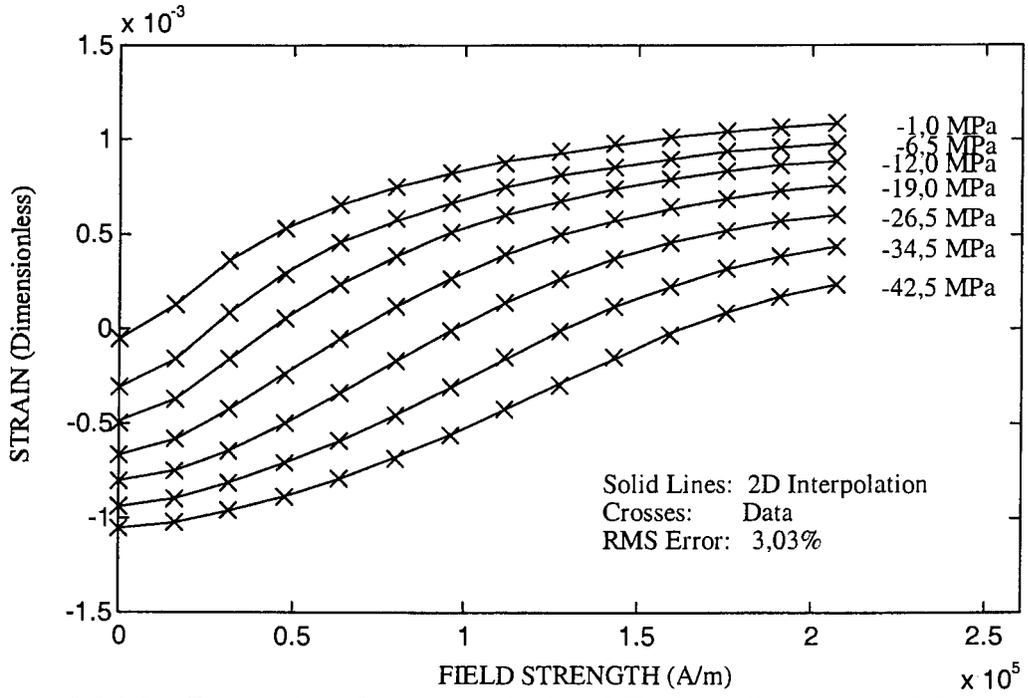

Figure 2.2.1.3: Comparison between calculated Terfenol-D strain and data

Linear magnetostrictive characteristics of Terfenol-D

Equation 2.2.1.3 expressed strain as a nonlinear, two-dimensional polynomial function of stress and field and table 2.2.1.1 gave the polynomial coefficients. The linear characteristics are much simpler in the sense that strain is assumed to be directly proportional to both stress and field. Mathematically, the strain characteristic can be expressed as follows as a linear combination of stress and field:

$$\varepsilon(\sigma, H) = \frac{\sigma}{E} + d^H H \qquad \textbf{(2.2.1.4)}$$

where E is Young's modulus and d^H is the piezomagnetic cross-coupling constant, also known as the magnetostrictive strain constant. The first term on the right hand side of equation 2.2.1.4, i.e. σ/E, describes the linear relationship between strain and stress at a constant field strength, while the second term $d^H H$, gives the linear relationship between strain and field strength at a constant stress.

In order to do a proper analysis of the linear behaviour of a magnetostrictive actuator and LOS stabilization system, mathematical expressions and graphs of Young's Modulus and the strain constant will be required. Mathematical expressions for E and d^H will subsequently be derived and shown graphically.

Young's Modulus can be defined as the change in mechanical stress per unit change in strain, at a constant magnetic field strength. Mathematically, E can be described as the reciprocal of

the partial derivative of strain with respect to stress, at a constant field:

$$E(\sigma,H)=\frac{1}{\left.\frac{\partial\varepsilon(\sigma,H)}{\partial\sigma}\right|_{H=const}}=\frac{10^6}{\sum_{i=0}^{m}\sum_{j=1}^{n}p_{ij}j\left(\frac{\sigma}{10^6}\right)^{j-1}\left(\frac{H}{10^5}\right)^{i}} \qquad \textbf{(2.2.1.5)}$$

where $\varepsilon(\sigma,H)$ is given by equation 2.2.1.2 and p_{ij} are the polynomial coefficients as given by table 2.2.1.2. Young's Modulus versus stress and field is shown graphically in figure 2.2.1.4. The stress range is -26,5 MPa to -1 MPa and the field range is 0 to 100 kA/m.

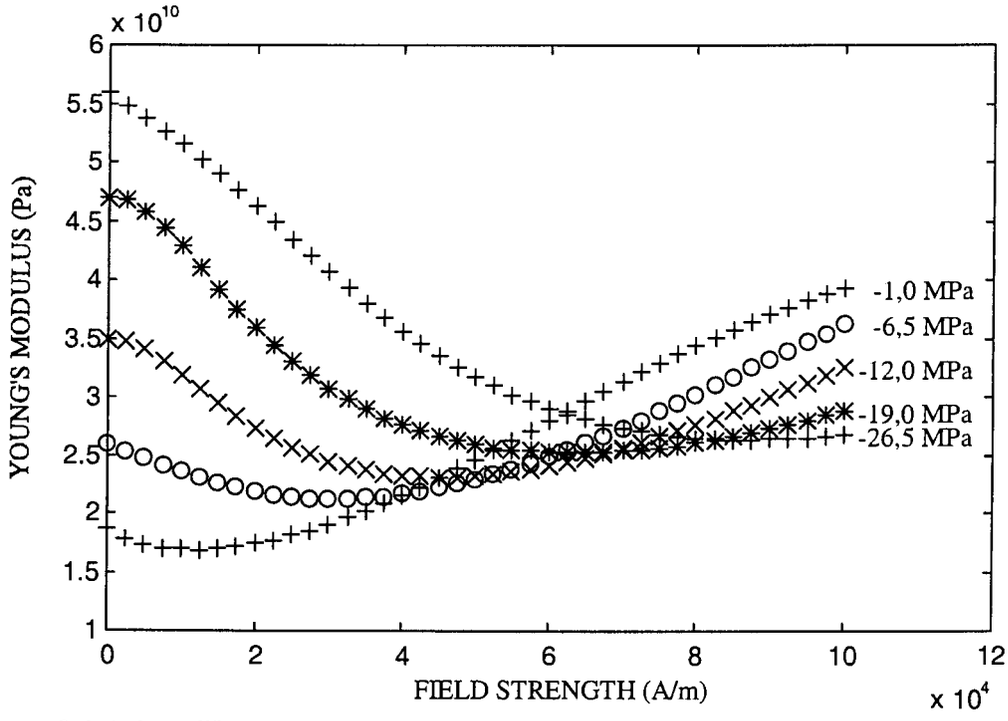

Figure 2.2.1.4: Young's Modulus of Terfenol-D versus mechanical stress and magnetic field strength

The following observations can be made from figure 2.2.1.4: At low field strengths, Young's Modulus increases with a decrease in stress, and the variation in E is relatively high. At zero field strength E varies from approximately 18 GPa for a compressive stress of 1 MPa, to approximately 56 GPa for a compressive stress of 26,5 GPa. As the field increases, the variation in E diminishes. At a field strength of 60 kA/m, the variation in E is at a minimum, i.e. approximately 5 to 6 GPa, and at this field strength it can be assumed that E is relatively independent of stress. As the field is increased beyond 60 kA/m, Young's Modulus increases with an increase in stress, and the variation in E reaches a maximum of approximately 14 GPa at a field of 100 kA/m.

A mathematical expression for Young's Modulus has been obtained by means of partial differentiation of strain with respect to stress. E has been shown graphically for a stress

variation of -26,5 MPa to -1 MPa and a field variation of 0 to 100 kA/m. A similar procedure can be followed to obtain the strain constant in terms of stress and field.

The strain constant d^H can be defined as the change in strain per unit change in magnetic field strength at a constant mechanical stress. Mathematically, d^H can be described as the partial derivative of strain with respect to field at a constant stress:

$$d^H(\sigma,H)=\left.\frac{\partial\varepsilon(\sigma,H)}{\partial H}\right|_{\sigma=const}=10^{-5}\sum_{i=1}^{m}\sum_{j=0}^{n}p_{ij}i\left(\frac{\sigma}{10^6}\right)^j\left(\frac{H}{10^5}\right)^{i-1} \qquad \textbf{(2.2.1.6)}$$

where $\varepsilon(\sigma,H)$ is given by equation 2.2.1.2 and p_{ij} are the polynomial coefficients as given by table 2.2.1.2. The strain constant versus stress and field, according to equation 2.2.1.6, is shown graphically in figure 2.2.1.5. The stress range is -26,5 MPa to -1 MPa and the field range is 0 to 100 kA/m.

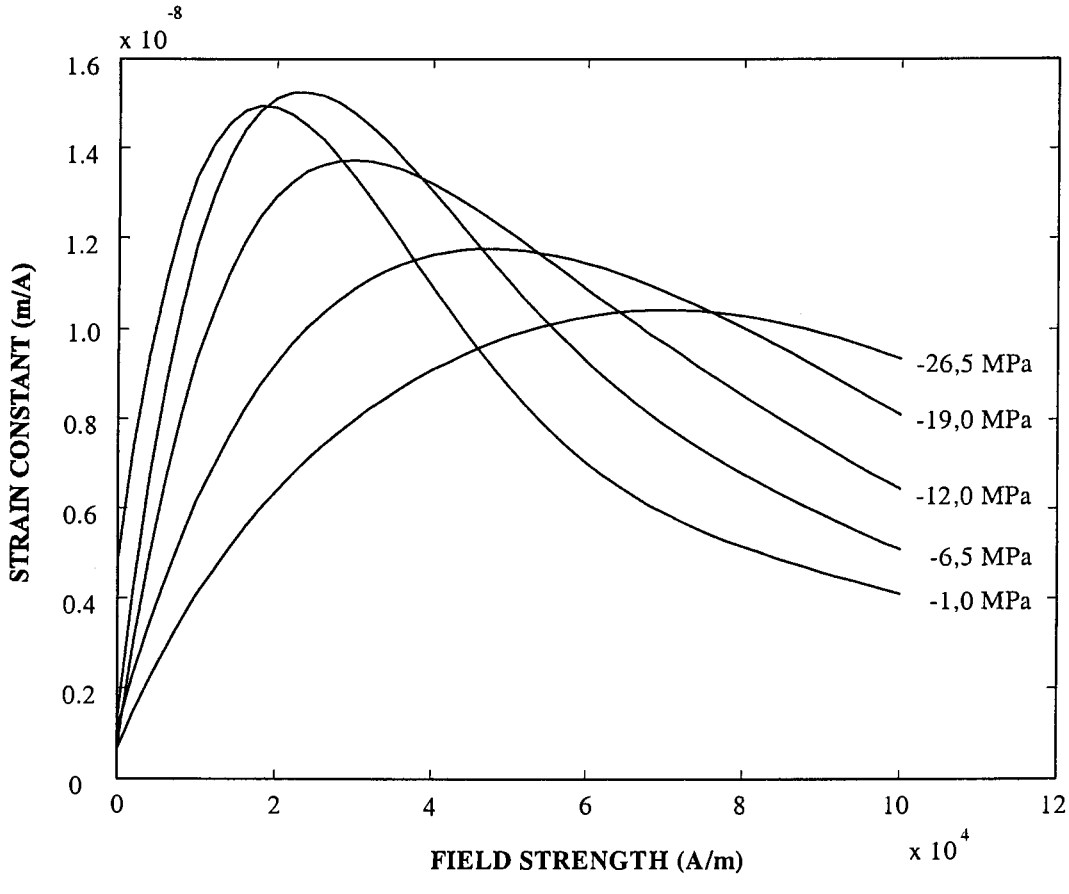

Figure 2.2.1.5: Terfenol-D strain constant versus mechanical stress and magnetic field strength

Figure 2.2.1.5 shows that, for any given constant stress, d^H is initially low, and increases with field until a peak is reached. After the peak, d^H gradually drops off to zero as the material becomes magnetically saturated. The peak value of d^H not only depends on the field, but also

on the stress. The peak value is generally higher for low stresses. Furthermore, for higher stresses, higher field strengths are required to produce the peak value of d^H.

It was shown in equations 2.2.1.5 and 2.2.1.6, as well as in figures 2.2.1.4 and 2.2.1.5, that the linear magnetostrictive parameters, i.e. E and d^H, are dependent on both mechanical stress and magnetic field strength. For small stress and field amplitudes, E and d^H can be assumed constant, but if stresses and field strengths with large amplitudes are applied, the values of E and d^H will vary. In a linear analysis, large amplitude constant values of the linear magnetostrictive parameters are required. It will therefore be necessary to force the changing parameters by means of large amplitude linearization to assume constant values. These values of E and d^H will depend on the reference stress and field, stress amplitude and field amplitude. Large amplitude linearization of the magnetostrictive characteristics of Terfenol-D will be covered in more detail in the next section.

Large amplitude linear magnetostrictive characteristics of Terfenol-D

This section covers the large amplitude linear magnetostrictive characteristics of Terfenol-D. Equations for the large amplitude average values of E and d^H will be given for simultaneous variations in stress and field. It will be shown that the equations can be simplified for the special cases of constant stress and constant field. An example will be done where the average value of d^H and the linear strain versus field characteristic will be calculated. The linear and nonlinear characteristics will be compared and the saturation region will be identified.

A study was carried out by Clark et al [1990] to investigate the influence of different stress and field amplitudes on E and d^H. In the first part of the study, five different field amplitudes were applied, while the compressive stress was held constant. The reference stress and field were 32,3 MPa and 80 kA/m respectively and the field amplitudes were 20, 30, 40, 50 and 60 kA/m. In the second part of the study, five different stress amplitudes were applied, while the field was held constant. The reference stress and field were unchanged from the first part of the study. The stress amplitudes varied from 7,5 MPa to 37,9 MPa in increments of approximately 7,5 MPa. The values of E and d^H were tabulated for each field and stress amplitude. The results of the study are useful for the calculation of E and d^H for large amplitude mechanical and magnetic excitation of Terfenol-D for the given reference stress and field. However, these results are only usable for the abovementioned reference stress and field, and if E and d^H are required for arbitrary reference stresses and fields, the study will have to be repeated.

An alternative method can be applied to determine the large amplitude linear values of E and d^H. The method is analytical, and makes use of the mathematical relationships for E and d^H in equations 2.2.1.5 and 2.2.1.6, as well as the peak-to-peak stresses and fields.

For given peak-to-peak values of stress and field, the average large amplitude values of E and

d^H can be calculated by means of the following equations:

$$\overline{E} = \frac{1}{(\sigma_2 - \sigma_1)(H_2 - H_1)} \int_{\sigma_1}^{\sigma_2} \int_{H_1}^{H_2} E(\sigma, H) dH d\sigma \qquad \textbf{(2.2.1.7a)}$$

$$\overline{d^H} = \frac{1}{(\sigma_2 - \sigma_1)(H_2 - H_1)} \int_{\sigma_1}^{\sigma_2} \int_{H_1}^{H_2} d^H(\sigma, H) dH d\sigma \qquad \textbf{(2.2.1.7b)}$$

where $\overline{E}$ and $\overline{d^H}$ are the average values of E and d^H respectively, σ_2–σ_1 is the peak-to-peak stress and H_2–H_1 is the peak-to-peak field strength. $E(\sigma,H)$ and $d^H(\sigma,H)$ are given by equations 2.2.1.5 and 2.2.1.6 respectively.

The above equations give E and d^H for simultaneous variations in stress and field. The equations can however be simplified if either stress or field is held constant. In the case of a constant stress, for example, the average values of E and d^H for a peak-to-peak field of H_2–H_1 can be calculated as follows:

$$\overline{E}_{\sigma=const} = \frac{1}{H_2 - H_1} \int_{H_1}^{H_2} E(\sigma, H) dH \qquad \textbf{(2.2.1.8a)}$$

$$\overline{d^H}_{\sigma=const} = \frac{1}{H_2 - H_1} \int_{H_1}^{H_2} d^H(\sigma, H) dH \qquad \textbf{(2.2.1.8b)}$$

Equations 2.2.1.8 are useful for the calculation of linear strain versus field characteristics of Terfenol-D at constant stress, and are applicable to any arbitrarily selected reference field, stress and field amplitude. Similar equations to the above can also be derived for the average values of E and d^H, for different stress amplitudes at a constant field strength.

An example of the application of equation 2.2.1.8b will subsequently be done, where the average value of d^H and the linear strain versus field characteristic will be calculated. The linear and nonlinear characteristics will be compared and the saturation region will be identified. To this end, consider the d^H-curve for a 12 MPa compressive stress shown in figure 2.2.1.5. The reference field and field amplitude are arbitrarily selected as 50 kA/m and 32 kA/m respectively. If the integration in equation 2.2.1.8b is carried out, and the numerical value of the peak-to-peak field, i.e. 64 kA/m, is substituted into the resulting equation, the calculated value of $\overline{d^H}$ is $1{,}192.10^{-8}$ m/A. Note that this value of $\overline{d^H}$ is constant, therefore the linear strain characteristic will be a straight line in the strain versus field plane, with a slope of $\overline{d^H}$. The linear strain versus field characteristic, together with the nonlinear characteristic, is shown in figure 2.2.1.6.

The circle in figure 2.2.1.6 indicates the reference point, at a field strength of 50 kA/m and a corresponding strain of 566 $\mu\varepsilon$. For field strengths below 50 kA/m, the slope of the nonlinear strain versus field characteristic curve increases with field, and for field strengths above 50 kA/m, the slope of the curve decreases. In this region, there is a gradual decline in the slope of the curve, which makes it difficult to identify a single point on the curve where the strain saturates. Therefore, subjective judgment of the linear and saturation regions will have

to be made here. By inspection of figure 2.2.1.6, the characteristic for field strengths below 100 kA/m can be considered as the linear region, where the linear characteristic gives reasonable accuracy compared with the nonlinear characteristic. Field strengths above 100 kA/m can be considered as the saturation region. It is clear that, in this region, the linear characteristic becomes highly inaccurate, and is therefore not recommended.

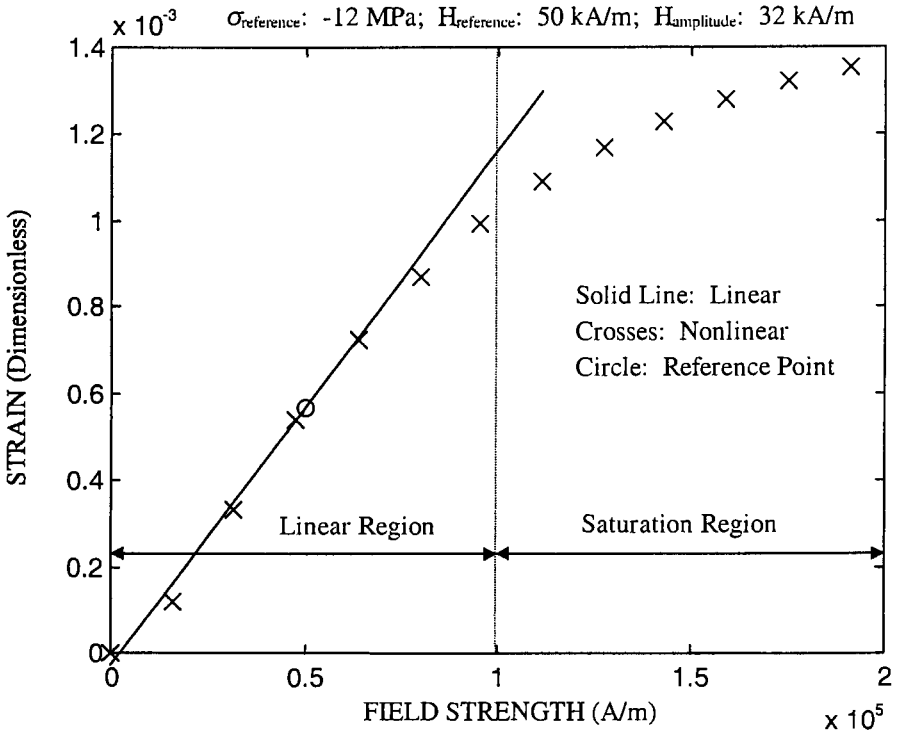

Figure 2.2.1.6: Terfenol-D linear and nonlinear strain versus field characteristics for a constant stress

To summarize, the linear and nonlinear magnetostrictive characteristics were discussed in detail this section. Strain was expressed as a function of stress and field and the characteristics were linearized. Equations for the large amplitude average values of E and d^H were derived. An example was done where $\overline{d^H}$ was calculated for a given reference stress, reference field and field amplitude. The large amplitude linear and nonlinear characteristics were compared graphically and the linear and saturation regions were identified.

The next section will present an alternative magnetostrictive characteristic, with stress as a function of field and strain.

Inverse magnetostrictive characteristic of Terfenol-D

In this short section, an inverse characteristic, where stress is a function of field and strain, will be presented. The inverse characteristic is required because it will be needed to derive the equations of motion of the magnetostrictive actuator and LOS stabilization system in later sections of this chapter. A regression equation will be given to represent the data. Stress will be expressed as a two-dimensional polynomial function of field and strain. The stress characteristic and the data fit will be shown graphically.

The following equation expresses mechanical stress as a two dimensional polynomial function of magnetic field and strain:

$$\sigma = \sigma(\varepsilon, H) = 10^6 \sum_{i=0}^{m} \sum_{j=0}^{n} s_{ij} \left(\frac{\varepsilon}{10^{-3}} \right)^j \left(\frac{H}{10^5} \right)^i \qquad \textbf{(2.2.1.9)}$$

where σ is the stress in Pa, ε is the dimensionless strain and H is the field strength in A/m. The two-dimensional polynomial coefficients s_{ij} for $m = 7$ and $n = 3$ are given in table 2.2.1.2.

Table 2.2.1.2: Two-dimensional polynomial coefficients s_{ij} for mechanical stress as a function of strain and magnetic field

j / *i*	0	1	2	3
0	-0,1334	14,937	-15,741	7,798
1	-8,921	26,12	100,92	32,83
2	-101,9	-3,804	-422,5	-115,9
3	-219,9	-79,86	939,7	103,92
4	-240,9	145,2	-1111,1	35,98
5	142,6	-105,8	703,8	-98,71
6	-43,29	34,22	-223,2	48,45
7	5,297	-4,007	27,70	-7,513

The accuracy of the data fit can be evaluated by comparing the stresses calculated with equation 2.2.1.9 with the data. The stresses are calculated for fourteen field strengths in a range of 0 to 2600 Oe (207 kA/m) and for a strain range of $-1{,}2.10^{-3}$ to $1{,}2.10^{-3}$. The data is obtained by inverting the graphical strain characteristics as supplied by Kvarnsjö [1993], so that stress becomes the dependent variable and field and strain become the independent variables. The RMS error of the data fit is 5,14% for the above field and strain ranges. Figure 2.2.1.7 shows the stresses as calculated with equation 2.2.1.9, together with the data.

Figure 2.2.1.7 shows that, for low field strengths, the stress curves initially rise sharply with strain, but as the strain is increased, the slopes of the curves decrease (see for instance curve a). This type of characteristic is known in mechanical engineering terms as a "softening characteristic". This implies that the required change in stress per unit change in strain decreases. For higher fields (see curve h), the slope of the stress versus strain curve initially decreases with strain until a minimum slope is reached. As the strain is further increased, the slope increases again until a maximum slope is reached at maximum stress. For high field

strengths (see for instance curve n), the slope of the stress versus strain curve increases with strain for all strains. This type of characteristic is known as a "stiffening characteristic".

For low fields, the curves are closely spaced, but as the field increases, the curves are further apart. In the vicinity of the maximum field strength of 2600 Oe, the curves are closely spaced again, which indicates that the strain will not increase significantly with an increase in field. At this field strength, the material is magnetically saturated. This phenomenon was discussed in more detail in previous sections.

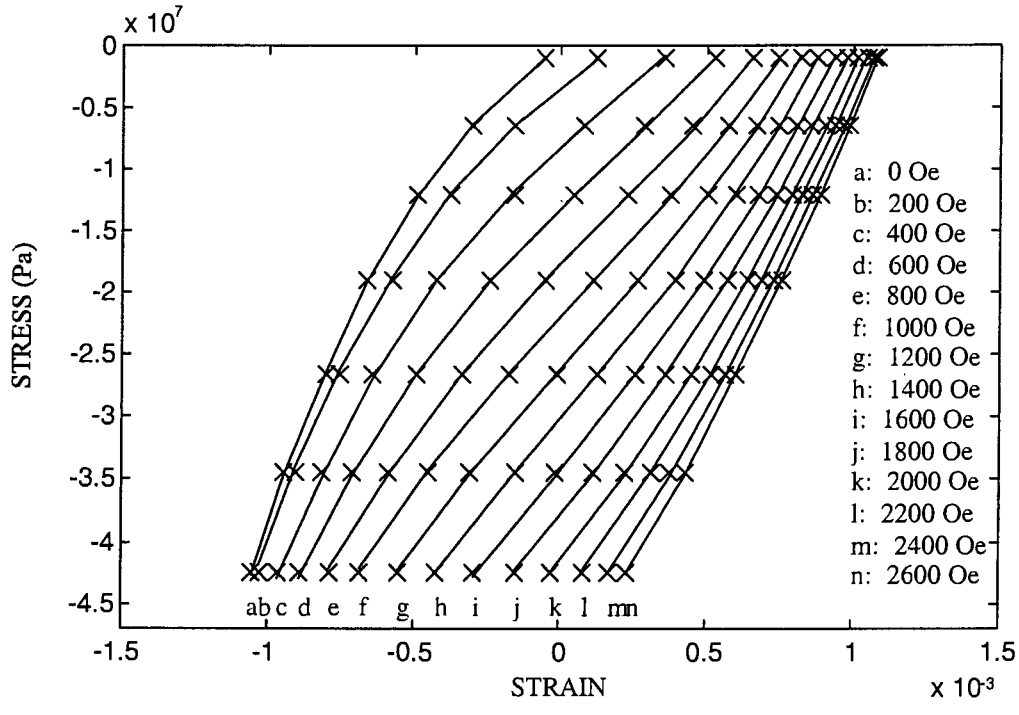

Figure 2.2.1.7: Terfenol-D mechanical stress versus magnetic field and strain: Interpolated two-dimensional polynomial and original data

To summarize section 2.2.1, the magnetostrictive characteristics of Terfenol-D, i.e. the strain, Young's Modulus and the magnetostrictive strain constant were expressed in terms of the mechanical stress and the magnetic field strength. Mathematical equations were obtained by means of least squares fits to data supplied in the literature. The equations were also represented graphically. Section 2.2.2 will cover the magnetization characteristics of Terfenol-D.

2.2.2 Magnetization characteristics of Terfenol-D

This section discusses the linear and nonlinear magnetization characteristics of Terfenol-D. A graph of magnetic flux density versus mechanical stress and magnetic field strength is shown. The influence of stress and field on the saturation flux density is discussed. A two dimensional regression equation is given which closely represents the data. The flux density characteristic is linearized and the linear magnetization parameters, i.e. the piezomagnetic cross-coupling constant d^{σ} and the permeability μ^{σ}, are defined, expressed mathematically and shown graphically.

In section 2.2 magnetostriction was defined as the phenomenon wherein ferromagnetic materials experience an elastic strain when subjected to an external magnetic field. Magnetostriction is also the converse phenomenon in which mechanical stresses cause a change in the magnetic induction, or flux density, of a ferromagnetic material [Harris, 1988]. The magnetization characteristics of all magnetic materials are usually expressed in terms of magnetic flux density versus field strength, but in the case of magnetostrictive materials, flux density is also a function of the applied mechanical stress.

The magnetization characteristics of Terfenol-D are required to calculate the electrical current in the field coil of a magnetostrictive actuator and the magnetic field strength in the active rod, for a given input voltage. The field strength is of particular importance since it produces the magnetostrictive strain in the rod, as well as the actuator force. Once the field strength is known, the strain in the rod can be obtained by means of the magnetostrictive characteristics as given in section 2.2.1.

The magnetization characteristics of Terfenol-D which will be used in this study, are obtained from data supplied by Kvarnsjö [1993]. The flux density of Terfenol-D versus mechanical stress and magnetic field strength for a stress range of -42,5 MPa to -1 MPa and a field range of 0 to 150 kA/m is shown in figure 2.2.2.1.

Figure 2.2.2.1 shows that flux density increases with both stress and field strength. For low field strengths, flux density initially increases sharply, but the increase diminishes as soon as the field exceeds 25 kA/m. Also, the initial increase in flux density is higher for higher stresses. The maximum flux density for the above stress and field range is approximately 1,2 tesla (T).

The flux density curves as shown in figure 2.2.2.1 can be used to do a mathematical analysis of the magnetization characteristics of Terfenol-D. A functional relationship between flux density, stress and field can be obtained by means of two-dimensional interpolation of the data. The mathematical function thus obtained can be differentiated with respect to stress and field to give the piezomagnetic cross-coupling constant d^{σ} and the permeability μ^{σ} respectively. A suitable two-dimensional polynomial equation, which closely represents the data, will subsequently be given, after which d^{σ} and μ^{σ} will be derived.

Flux density can be expressed as follows as a two-dimensional function of stress and field:

$$B(\sigma,H)=\sum_{i=0}^{m}\sum_{j=0}^{n}b_{ij}\left(\frac{\sigma}{10^{6}}\right)^{j}\left(\frac{H}{10^{5}}\right)^{i} \qquad \textbf{(2.2.2.1)}$$

where B is the magnetic flux density in T, σ is the mechanical stress in Pa and H is the magnetic field strength in A/m. Note that the field and stress are scaled by factors of 10^5 A/m and 10^6 Pa respectively. m is the order of the polynomial for flux density as a function of field and n is the order of the polynomial for flux density as a function of stress. b_{ij} are the two-dimensional polynomial coefficients. Values of b_{ij} for $m=8$ and $n=3$ are given in table 2.2.1.1.

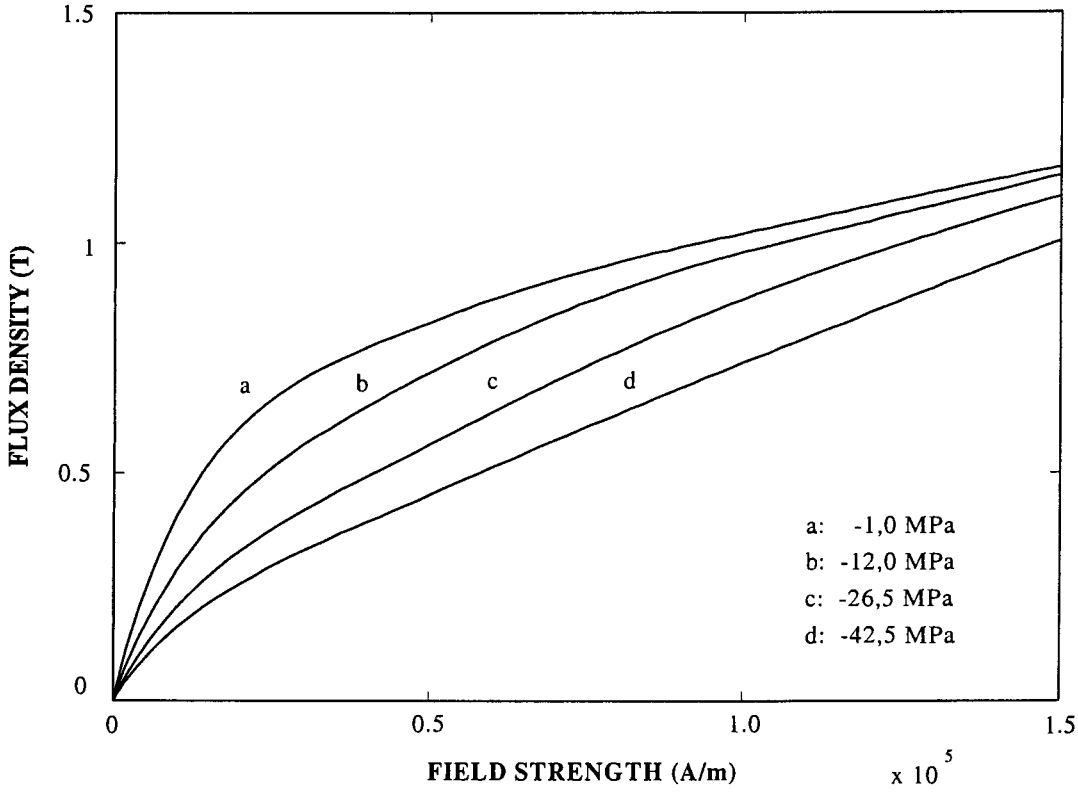

Figure 2.2.2.1: Terfenol-D flux density versus mechanical stress and magnetic field strength [Kvarnsjö, 1993]

The accuracy of the data fit can be evaluated by comparing the flux densities calculated with equation 2.2.2.1 with the flux densities given by Kvarnsjö [1993]. The flux densities are calculated for four compressive stresses in a range of -42,5 MPa to -1 MPa and for a field strength range of 0 to 150 kA/m. The calculated flux densities and the data as supplied by Kvarnsjö [1993] are shown in figure 2.2.2.2.

Table 2.2.2.1: Two-dimensional polynomial coefficients b_{ij} for magnetic flux density as a function of mechanical stress and magnetic field

j / *i*	0	1	2	3
0	$3{,}465.10^{-4}$	$-1{,}535.10^{-5}$	$-1{,}145.10^{-6}$	$-1{,}384.10^{-8}$
1	-5,959	0,2403	$5{,}792.10^{-3}$	$5{,}343.10^{-5}$
2	-21,96	-1,231	$-3{,}54.10^{-2}$	$-3{,}548.10^{-4}$
3	49,44	2,936	$8{,}447.10^{-2}$	$8{,}139.10^{-4}$
4	-67,07	-4,125	-0,1137	$-9{,}994.10^{-4}$
5	55,34	3,575	$9{,}534.10^{-2}$	$7{,}642.10^{-4}$
6	-27,09	1,859	$-4{,}901.10^{-2}$	$-3{,}685.10^{-4}$
7	7,214	0,527	$1{,}394.10^{-2}$	$1{,}013.10^{-4}$
8	-0,8037	$-6{,}227.10^{-2}$	$-1{,}663.10^{-3}$	$-1{,}191.10^{-5}$

Figure 2.2.2.2 shows that, for the values of b_{ij} in table 2.2.1.1, the flux densities calculated with equation 2.2.2.1 compare favourably with the data supplied by Kvarnsjö [1993]. The root mean square error of the regression equation is 0,31% for a stress range of -42,5 MPa to -1 MPa and for a field range of 0 to 150 kA/m.

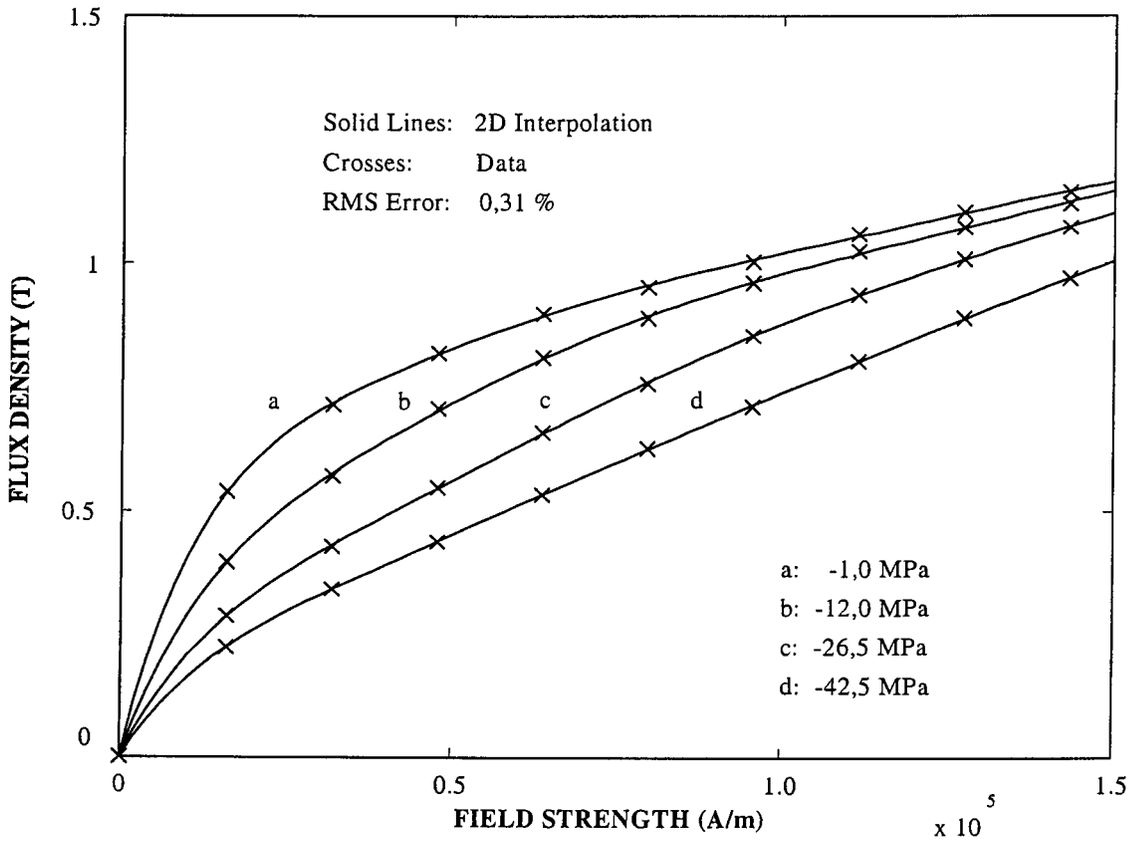

Figure 2.2.2.2: Comparison between calculated Terfenol-D flux density and data

The nonlinear magnetization characteristics of Terfenol-D have been covered in detail in this section. The flux density characteristics have been shown graphically, the saturation properties have been discussed and a regression equation has been given which closely represents the data. Whereas the nonlinear magnetization characteristics are an accurate tool for calculating the coil current of a magnetostrictive actuator and the field in the Terefnol-D rod, the linear characteristics are required to simplify the calculations. The linear magnetization characteristics will be discussed next.

Linear magnetization characteristics of Terfenol-D

Equation 2.2.2.1 expressed the magnetic flux in Terfenol-D as a nonlinear, two-dimensional polynomial function of stress and field. The linear magnetization characteristics of Terfenol-D will be covered in this section. The linear magnetization parameters, i.e the permeability and the piezomagnetic cross-coupling constant, will be derived and shown graphically.

A linear analysis of the magnetization characteristics is simpler than a nonlinear analysis due to the fact that, in the linear case, flux density is assumed to be directly proportional to both stress and field. Mathematically, the flux density can be expressed as follows:

$$B(\sigma, H) = d^{\sigma}\sigma + \mu^{\sigma} H \qquad \textbf{(2.2.2.2)}$$

where d^{σ} is the piezomagnetic cross-coupling constant and μ^{σ} is the permeability. The first term on the right hand side of equation 2.2.2.2, i.e. $d^{\sigma}\sigma$, describes the linear relationship between flux density and stress at a constant field strength, while the second term, $\mu^{\sigma}H$, gives the linear relationship between flux density and field strength at a constant stress.

In order to do a proper analysis of the linear behaviour of a magnetostrictive actuator and LOS stabilization system, the piezomagnetic strain constant and permeability will be required as functions of stress and field. These functions will enable the designer of the plant to calculate d^{σ} and μ^{σ} for any given mechanical stress and magnetic field strength. Mathematical expressions for d^{σ} and μ^{σ} will subsequently be derived and shown graphically.

The piezomagnetic cross-coupling constant can be defined as the change in magnetic flux per unit change in mechanical stress, at a constant magnetic field strength. Mathematically, d^{σ} can be described as the partial derivative of flux density with respect to stress at a constant field, as given by equation 2.2.2.3:

$$d^{\sigma}(\sigma, H) = \left.\frac{\partial B(\sigma, H)}{\partial \sigma}\right|_{H=const} = 10^{-6} \sum_{i=0}^{m} \sum_{j=1}^{n} b_{ij}\, j \left(\frac{\sigma}{10^{6}}\right)^{j-1} \left(\frac{H}{10^{5}}\right)^{i} \qquad \textbf{(2.2.2.3)}$$

where $B(\sigma,H)$ is given by equation 2.2.2.1 and the polynomial coefficients b_{ij} are given in table 2.2.2.1. The cross-coupling constant, according to equation 2.2.2.3, is shown in figure 2.2.2.3. The field range is 0 kA/m to 100 kA/m and the stress range is -1,0 MPa to -26,5 MPa.

Figure 2.2.2.3 shows that, for any given constant stress, d^{σ} is initially low, and increases with field until a peak is reached. After the peak, d^{σ} gradually drops off to zero as the material becomes magnetically saturated. The peak value of d^{σ} not only depends on the field, but also on the stress. The peak value is generally higher for low stresses. Furthermore, for higher stresses, higher field strengths are required to produce the peak value of d^{σ}. Lastly, if figure 2.2.2.3 is compared with figure 2.2.1.5, it can be seen that d^{σ} follows the same trends as d^{H} and that the numerical values of the two parameters are comparable for the same values of stress and field strength.

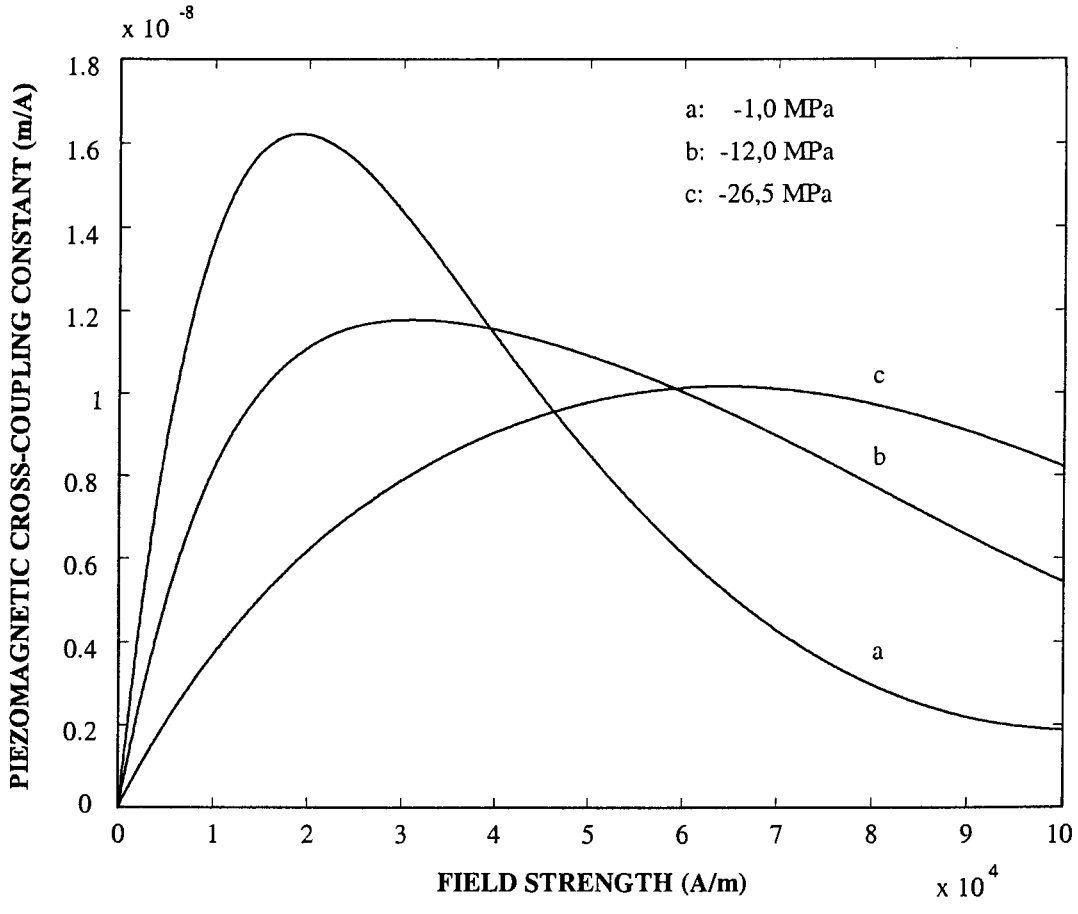

Figure 2.2.2.3: Terfenol-D piezomagnetic cross-coupling constant versus mechanical stress and magnetic field strength

A mathematical expression for the piezomagnetic cross-coupling constant has been obtained by means of partial differentiation of magnetic flux with respect to stress. d^{σ} has been shown graphically for a stress variation of -26,5 MPa to -1 MPa and a field variation of 0 to 100 kA/m. A similar procedure can be followed to obtain the permeability in terms of stress and field.

The permeability μ^{σ} can be defined as the change in magnetic flux per unit change in magnetic field strength, at a constant mechanical stress. Mathematically, μ^{σ} can be described as the partial derivative of flux density with respect to field at a constant stress:

$$\mu^{\sigma}(\sigma,H)=\left.\frac{\partial B(\sigma,H)}{\partial H}\right|_{\sigma=const}=10^{-5}\sum_{i=1}^{m}\sum_{j=0}^{n}b_{ij}i\left(\frac{\sigma}{10^{6}}\right)^{j}\left(\frac{H}{10^{5}}\right)^{i-1} \qquad \textbf{(2.2.2.4)}$$

where $B(\sigma,H)$ is given by equation 2.2.2.1 and the polynomial coefficients b_{ij} are given in table 2.2.2.1. The permeability, according to equation 2.2.2.4, is shown in figure 2.2.2.4. The field range is 0 kA/m to 100 kA/m and the stress range is -1,0 MPa to -26,5 MPa.

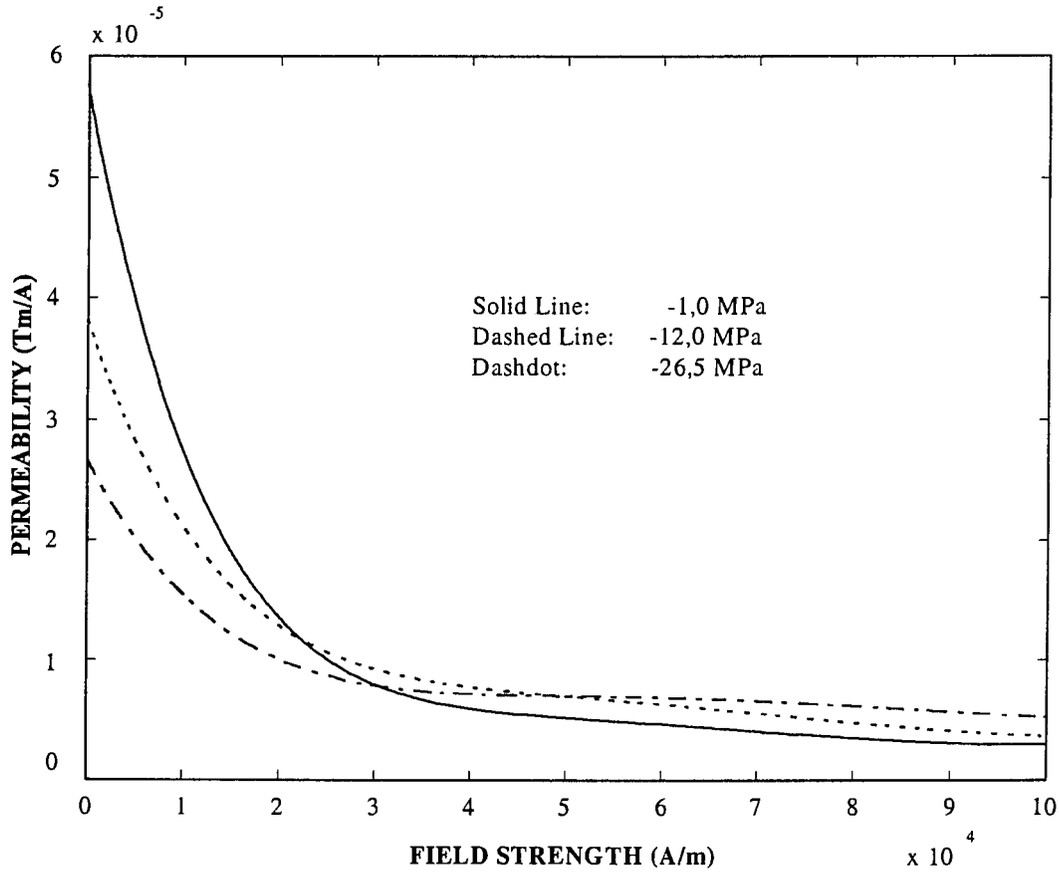

Figure 2.2.2.4: Terfenol-D permeability versus mechanical stress and magnetic field strength

Figure 2.2.2.4 shows that permeability decreases with an increase in field. For field strengths below 25 kA/m, permeability generally increases with stress. For field strengths above 25 kA/m, the material becomes magnetically saturated, permeability is weakly dependent on stress and eventually decays to zero.

It was shown in equations 2.2.2.3 and 2.2.2.4, that the linear magnetization parameters, i.e. d^{σ} and μ^{σ}, are dependent on both mechanical stress and magnetic field strength. For small stress and field amplitudes, d^{σ} and μ^{σ} can be assumed constant, but if large amplitude stresses and field strengths are applied, the values of d^{σ} and μ^{σ} will vary. A similar phenomenon was detected in the magnetostrictive parameters. However, in a linear analysis, large amplitude constant values of the magnetization parameters are required. It will therefore be necessary to force the changing parameters by means of large amplitude linearization to assume constant values. The values of d^{σ} and μ^{σ} will depend on the reference stress and field, the stress amplitude and the field amplitude.

The large amplitude values of d^{σ} and μ^{σ} can be obtained by means of the following equations:

$$\overline{d^{\sigma}} = \frac{1}{(\sigma_2 - \sigma_1)(H_2 - H_1)} \int_{\sigma_1}^{\sigma_2} \int_{H_1}^{H_2} d^{\sigma}(\sigma, H) dH d\sigma \qquad \textbf{(2.2.2.5a)}$$

$$\overline{\mu^{\sigma}} = \frac{1}{(\sigma_2 - \sigma_1)(H_2 - H_1)} \int_{\sigma_1}^{\sigma_2} \int_{H_1}^{H_2} \mu^{\sigma}(\sigma, H) dH d\sigma \qquad \textbf{(2.2.2.5b)}$$

where $\sigma_2 - \sigma_1$ is the peak to peak stress, $H_2 - H_1$ is the peak to peak field and $d^{\sigma}(\sigma,H)$ and $\mu^{\sigma}(\sigma,H)$ are respectively given by equations 2.2.2.3 and 2.2.2.4.

Equations 2.2.2.5 can be simplified if either stress or field is held constant. In the case of a constant stress, for example, equations 2.2.2.5a and 2.2.2.5b reduce to:

$$\overline{d^{\sigma}}_{\sigma=const} = \frac{1}{H_2 - H_1} \int_{H_1}^{H_2} d^{\sigma}(\sigma, H) dH \qquad \textbf{(2.2.2.6a)}$$

$$\overline{\mu^{\sigma}}_{\sigma=const} = \frac{1}{H_2 - H_1} \int_{H_1}^{H_2} \mu^{\sigma}(\sigma, H) dH \qquad \textbf{(2.2.2.6b)}$$

To conclude section 2.2, the linear and nonlinear magnetostrictive and magnetization characteristics of Terfenol-D were covered in detail. It was shown that magnetostrictive strain and magnetic flux saturate at high field strengths. Strain and flux density were expressed mathematically in terms of mechanical stress and magnetic field strength. The expressions were used to derive relationships for the cross-coupling constants, Young's Modulus and permeability. These characteristics are a valuable tool for the analysis of the dynamic behaviour of the Terfenol-D actuators and LOS stabilization system. The characteristics will be used in sections 2.4 to 2.8 to derive the linear and nonlinear equations of motion and coil current equations, the state-space models and transfer functions of the magnetostrictive actuators and system, as well as to simulate their behaviour.

Section 2.2 covered the influence of saturation on the magnetostrictive and magnetization characteristics of Terfenol-D. The effects of hysteresis will be covered in section 2.3.

2.3 The effects of hysteresis on the magnetostrictive and magnetization characteristics of Terfenol-D

This section describes the effects of hysteresis on the magnetostrictive and magnetization characteristics of Terfenol-D. A definition of hysteresis is given. The problems caused by hysteresis are mentioned. A number of magnetostrictive hysteresis models are discussed in short. The effects of hysteresis on the strain constant and permeability are described. A simplified model, which makes use of a hysteresis loss factor and an equivalent viscous damping coefficient, is presented.

When a magnetic material is magnetized with a magnetic field, and the field is subsequently removed, the flux density for the decreasing field will differ from that of the increasing field. The reason is that, during the reversal of the field, the material will not become fully demagnetized, as a portion of the field will remain in the material. This phenomenon is known as magnetic hysteresis. In the case of magnetostrictive materials, not only the flux density characteristic, but also the strain characteristic, exhibits hysteresis. In magnetostrictive hysteresis, the strain characteristic for an increasing field will differ from that of a decreasing field. The characteristic for an increasing field is known as the loading characteristic, while that for the decreasing field is known as the unloading characteristic.

The sequence of the loading and unloading fields has an important effect on the strain history of the material. The latter is determined by, inter alia, the application and usage of the magnetostrictive actuator. For instance, if sensitive equipment such as an optical instrument must be isolated against shock blasts, the field required to cancel the rapidly increasing forces, will be of a transient nature. On the other hand, if the optical instrument is to be isolated against steady-state harmonic base vibrations, the applied field will be cyclic. In the latter case, the loading and unloading curves form a closed loop, called a hysteresis loop. If the optical instrument is subjected to broadband random base vibrations, the required field will not be steady-state harmonic, but will consist of a spectrum of cyclic loadings.

The analysis of the dynamic behaviour of a magnetostrictive actuator and LOS stabilization plant of an optical instrument will necessarily have to make provision for the difference in loading and unloading magnetostrictive and magnetization characteristics. A number of problems arise in such an analysis. The first problem is that for a given excitation field, the strain can have many different values [Restorff et al, 1990]. Contrary to the saturation characteristics considered in section 2.2, the hysteresis strain and flux density cannot be described by single-valued functions of the applied field, as the direction of application of the field, i.e. whether the field is increasing or decreasing, must also be considered. Different characteristics for loading and unloading fields will therefore be required.

A second problem is that the value of magnetostrictive strain constant d^H is lowered if a cyclic excitation field is applied [Kvarnsjö, 1993] and [Pratt, 1993]. It was shown in section 2.2.1 that d^H is the slope of the strain versus magnetic field curve for a constant mechanical stress. However, this is only valid for a "dehysterized" characteristic, where the difference between the loading and unloading characteristics is ignored. Due to the multi-valued nature of hysteresis, the strain constant not only depends on the mechanical stress and magnetic field, but also on the difference between the loading and unloading fields and on the field amplitude.

For a small field amplitude, the hysteresis loop differs from that of a large field amplitude. The large amplitude loop is known as the major loop, while the small amplitude loop is known as the minor loop. Figure 2.3.1 shows an example of a magnetostrictive strain versus field characteristic, including the dehysterized characteristic, the loading and unloading curves, the major and minor hysteresis loops, and the hysteresis and dehysterized strain constants.

Lastly, hysteresis causes energy losses during excitation, necessitating larger field amplitudes to produce the same strain than in the dehysterized case. These energy losses cannot be predicted and must be experimentally measured. Hysteresis therefore also has a damping effect on the dynamic behaviour of the actuator and LOS stabilization plant, as it removes energy from the system. This effect may in some cases be desirable, such as at resonance frequencies where damping is required to suppress unduly high transmitted vibrations.

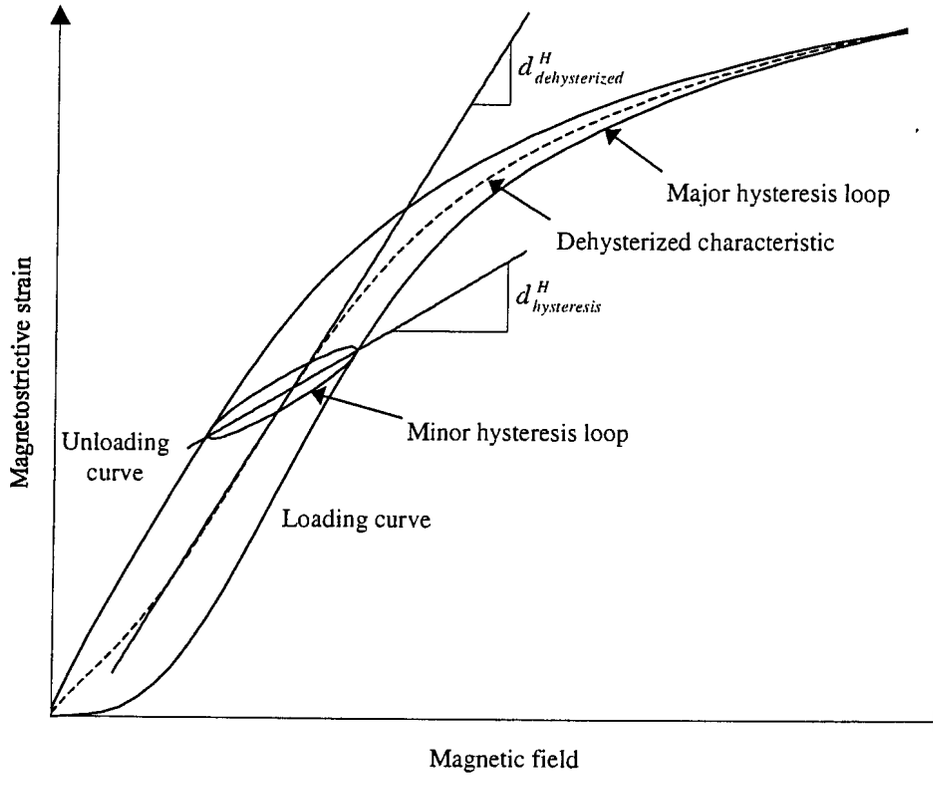

Figure 2.3.1: Hysteresis effects on the magnetostrictive strain versus field characteristic

In order to describe the magnetostrictive and magnetization hysteresis of Terfenol-D, mathematical models will be required to analyze its multi-valued nature, the effect of the lowered strain constant and energy losses. There have been many efforts to obtain mathematical hysteresis models, the most significant of which will be discussed in short in the next paragraphs. The application, advantages and disadvantages of each model will be mentioned. In addition, a linear model, which analyzes the strain constant and damping effect separately, will be presented and discussed in detail.

The Preisach model is arguably the most popular model for magnetic hysteresis. This model was developed in 1935 to describe general magnetic hysteresis, and was later adopted for

magnetostrictive materials by Adly et al [1991], Bergqvist & Engdahl [1991], Doong & Mayergoyz [1985], Ossart et al [1995], Restorff et al [1990] and Vajda & Della Torre [1995]. Other models which have been developed to describe magnetostrictive and magnetic hysteresis, include a Bessel function model [Sablik & Jiles, 1988] and a simplified model which superimposes a harmonic hysteresis function on the strain curve [Hall & Flatau, 1993].

The Preisach model is a general hysteresis model which is applicable to a broad range of phenomena that exhibit hysteresis [Restorff et al, 1990]. The model is widely used because of its computational efficiency. This feature also makes it desirable for the analysis of magnetostriction, where simultaneous changes in field and stress occur. The model takes cross-coupling between the two inputs, i.e. stress and field, into account.

Magnetostrictive and magnetization hysteresis is analyzed by means of an infinite number of generic hysteresis elements which have outputs of only ± 1. The sign is positive for an increasing input and negative for a decreasing input. In order to find the output value, the values of the different elements are summed with a weighting function. The model records a history of the inputs of all the elements in the form of two lists, which contain the local minima and maxima of the input. Since this list can grow without limit, it is truncated whenever a minimum lower than the lowest previous minimum or a maximum higher than the previous maximum is encountered.

The advantage of the Preisach model is that it can be used to predict magnetostrictive and magnetization hysteresis, including minor loops, fairly accurately [Restorff et al, 1990]. However, its application is limited to the time domain, which makes it unsuitable for frequency domain analyses of the behaviour of magnetostrictive actuators.

The Bessel function model [Sablik & Jiles, 1988], describes the simultaneous effects of saturation and hysteresis on the static magnetostrictive and magnetization characteristics of magnetostrictive materials, such as pure iron and Terfenol-D. The strain is expressed as a hyperbolic Bessel function of the effective field, which in turn is described in terms of the magnetization, applied field and its direction of application, stress and permeability.

The model is very powerful as it takes all the nonlinear magnetostrictive and magnetization characteristics into account, but does not provide a simple direct method of obtaining the strain constant. Furthermore, it is not a dynamic model, and can therefore not be used to investigate the effects of frequency on the damping coefficient. The model is more commonly known in the fields of magnetostriction and magnetism as the Jiles-Atherton (JA), or domain wall pinning model.

A model which simplifies the analysis of magnetostrictive hysteresis to a large extent, was developed by Hall & Flatau [1993]. The model describes magnetostrictive strain in terms of flux density for different harmonic coil input currents. The model considers both major and minor hysteresis loops of magnetic flux versus field strength. For major loops, flux density is described in terms of permeability, the maximum and minimum fields, input current, angular excitation frequency and time. A sinusoidal function of field is added to take the flux density saturation properties into account. The flux density hysteresis effects are described by means of a phase angle, which brings about a shift between the loading and unloading characteristics. For the minor loops, a parameter is included which controls the slope at either end of the loop. By setting this parameter to zero, elliptic minor loops are obtained.

The main advantage of the model is that, in contrast with the abovementioned JA model, it is a dynamic model, which takes the effects of the excitation frequency into account. Although the model is considerably simpler than the JA model, it also fails to provide a large amplitude strain constant and damping factor. However, since it was developed for harmonic coil input currents, it is a good starting point in the development of a simplified linear hysteresis model for vibration isolation problems.

The model which will be used in this study, is based on the assumption that all the hysteresis loops can be modelled as ellipses, i.e. the minor as well as the major loops are elliptic loops. This assumption is made in the interest of linearizing the hysteresis characteristics of the actuator and LOS stabilization system. Linearity is of essence in obtaining Laplace- and frequency domain transfer functions and will facilitate in the design of a suitable controller. The use of elliptic hysteresis loops will make it possible to linearize the nonlinear strain versus field strength characteristics, by means of large amplitude range-dependent average strain constants, hysteresis loss factors and viscous damping coefficients.

The effects of hysteresis on the large amplitude strain constant of Terfenol-D, are analyzed next, followed by the derivation of a hysteresis loss factor and a viscous damping coefficient.

The effects of hysteresis on the strain constant of Terfenol-D

The effects of hysteresis on the strain constant of Terfenol-D are modelled in this section. The loading, unloading and dehysterized magnetostrictive strain versus field strength characteristics, for a constant stress, are shown graphically. A mathematical equation is presented which expresses the different strain characteristics in terms of field strength. The hysteresis strain constant $d^H_{hysteresis}$ is defined and expressed mathematically by means of the loading and unloading strain characteristics. A sample calculation of $d^H_{hysteresis}$ is done for a given mechanical stress, reference field and a range of field amplitudes. The hysteresis strain constant is shown graphically and compared with the dehysterized strain constant. The effect of hysteresis on the strain constant are discussed.

The hysteresis characteristics of Terfenol-D, as supplied in graphical form by Kvarnsjö [1993], will be used in this study. For the sake of simplicity, the effects of stress on the hysteresis strain constant will not be discussed here. Instead, the strain constant will be calculated for an arbitrarily selected constant stress, as this method of analysis will also be applicable to other stresses. The loading and unloading strain versus field strength characteristics of Terfenol-D for a selected compressive stress of 12 MPa and a maximum applied field of 207 kA/m are shown in figure 2.3.2, together with the dehysterized characteristic.

A data regression technique will subsequently be used to obtain a mathematical function, which will express the hysteresis strain characteristics, i.e. the loading, unloading and dehysterized strains, in terms of the magnetic field. The function must accurately represent the different characteristics, and must be relatively easy to apply. For the sake of simplicity, it is further desirable to use the same function type for all three the characteristics. In order to distinguish between the loading, unloading and dehysterized characteristics, different numerical values of the function parameters will be used.

A function which satisfies the abovementioned requirements, can be fairly easily obtained by expressing strain ε as a polynomial of function of field strength H:

$$\varepsilon(H)\big|_{\sigma=const} = \sum_{i=0}^{n} p_i \left(\frac{H}{10^5}\right)^i \qquad (2.3.1)$$

where n is the order of the polynomial and p_i are the polynomial coefficients for the respective characteristic cases. Note that in equation 2.3.1, field strength is scaled by a factor of 10^5 A/m to avoid having to deal with unnecessarily large numbers.

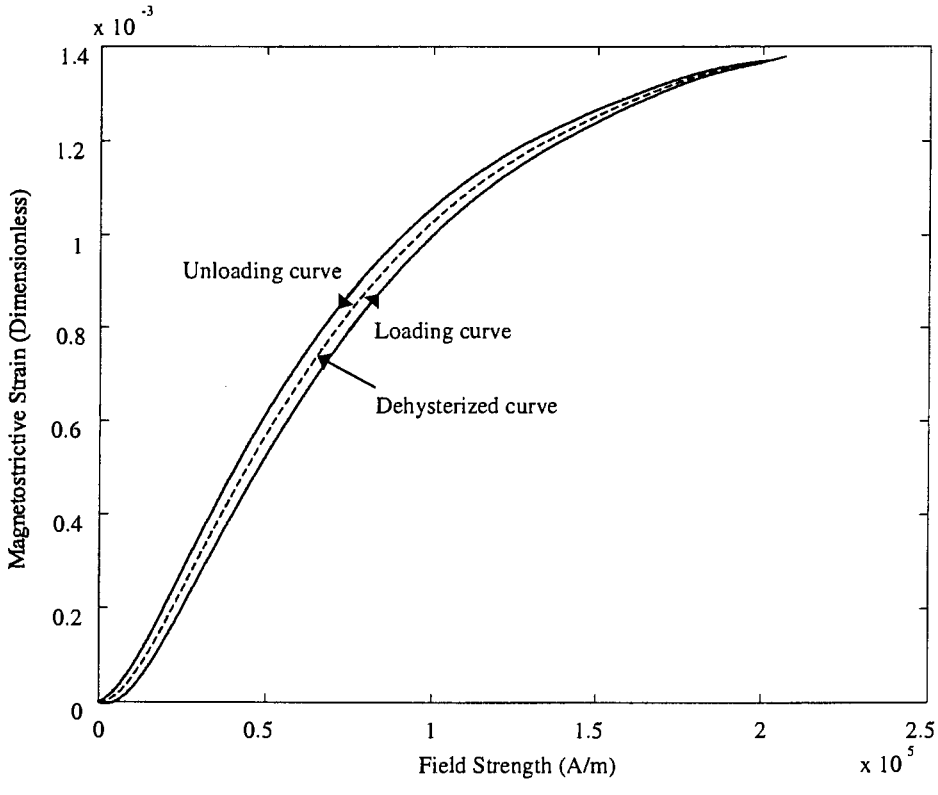

Figure 2.3.2: Loading, unloading and dehysterized strain versus field characteristics of Terfenol-D for a 12 MPa compressive stress [Kvarnsjö, 1993]

The accuracy of the function can be enhanced by using a high order n of the polynomial. However, it was found that sufficient accuracy is obtained if a value of n = 8 is used. The polynomial coefficients p_i for the loading, unloading and dehysterized strain characteristics of Terfenol-D for a compressive stress of 12 MPa are shown in table 2.3.1.

Table 2.3.1: Polynomial coefficients p_i for loading, unloading & dehysterized strain versus field characteristics of Terfenol-D for a 12 MPa compressive stress

Characteristic: i	Loading	Unloading	Dehysterized
0	$-1{,}6324.10^{-7}$	$-1{,}2071.10^{-7}$	$-1{,}4197.10^{-7}$
1	$-3{,}2056.10^{-4}$	$2{,}9977.10^{-4}$	$-1{,}1425.10^{-5}$
2	$8{,}1102.10^{-3}$	$6{,}2320.10^{-3}$	$7{,}1711.10^{-3}$
3	$-1{,}9974.10^{-2}$	$-1{,}6397.10^{-2}$	$-1{,}8185.10^{-2}$
4	$2{,}7567.10^{-2}$	$2{,}2879.10^{-2}$	$2{,}5223.10^{-2}$
5	$-2{,}3164.10^{-2}$	$-1{,}9256.10^{-2}$	$-2{,}1210.10^{-2}$
6	$1{,}1555.10^{-2}$	$9{,}6124.10^{-3}$	$1{,}0584.10^{-2}$
7	$-3{,}1260.10^{-3}$	$-2{,}6032.10^{-3}$	$-2{,}8646.10^{-3}$
8	$3{,}5218.10^{-4}$	$2{,}9357.10^{-4}$	$3{,}2288.10^{-4}$

Having obtained an equation, which expresses the loading and unloading strain versus field strength characteristics of Terfenol-D for a constant stress, the hysteresis strain constant can be defined and calculated. The hysteresis strain constant $d^{H}_{hysteresis}$ is defined as the slope of the major axis of the strain versus field hysteresis loop, and can be calculated by means of the following equation:

$$d^{H}_{hysteresis} = \frac{\varepsilon(H_2)_{loading} - \varepsilon(H_1)_{unloading}}{2\mathrm{H}_A} \qquad \textbf{(2.3.2)}$$

where H_2 is the maximum applied field, H_1 is the minimum applied field and H_A is the field amplitude, given by:

$$\mathrm{H}_A = \frac{H_2 - H_1}{2} \qquad \textbf{(2.3.3)}$$

The strains $\varepsilon(H_1)_{unloading}$ and $\varepsilon(H_2)_{loading}$ are calculated by means of equations 2.3.4a and 2.3.4b:

$$\varepsilon(H_1)_{unloading} = \sum_{i=0}^{8} p_{i\,unloading}\left(\frac{H_1}{10^5}\right)^i \qquad \textbf{(2.3.4a)}$$

$$\varepsilon(H_2)_{loading} = \sum_{i=0}^{8} p_{i\,loading}\left(\frac{H_2}{10^5}\right)^i \qquad \textbf{(2.3.4b)}$$

where the polynomial coefficients p_i for the unloading and loading characteristics are respectively given by the "loading" and "unloading" columns in table 2.3.1. For clarification purposes, the hysteresis loop parameters, i.e. the reference field and strain, minimum and maximum fields and their corresponding strains, field amplitude and hysteresis strain constant, are shown in figure 2.3.3.

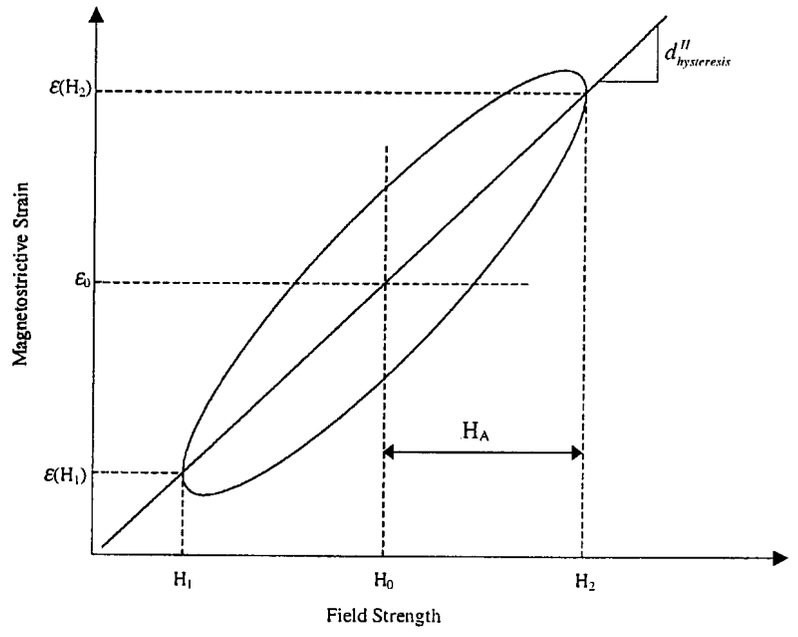

Figure 2.3.3: Magnetostrictive strain versus field strength hysteresis loop parameters and the hysteresis strain constant

Equations 2.3.2 to 2.3.4 provide a simple mathematical tool to calculate the hysteresis strain constant. A graph of the hysteresis strain constant for a stress of 12 MPa, a reference field of 50 kA/m and a field amplitude range of 4 kA/m to 47 kA/m is shown in figure 2.3.4. For comparison purposes, the dehysterized strain constant is also shown.

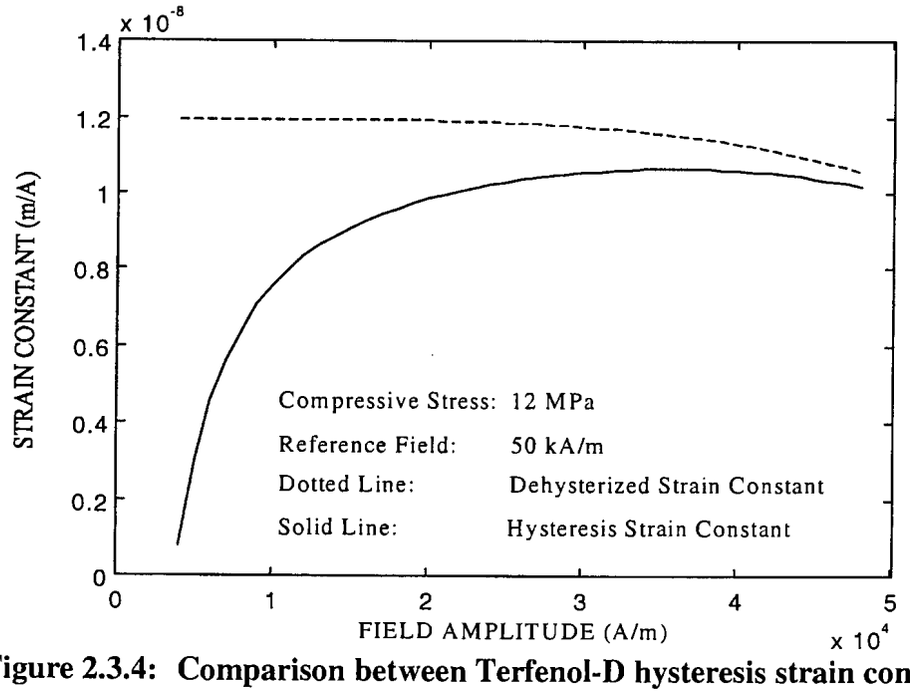

Figure 2.3.4: Comparison between Terfenol-D hysteresis strain constant and dehysterized strain constant for a 48 kA/m field amplitude range

Figure 2.3.4 shows that, for small field amplitudes, the hysteresis strain constant is relatively small in comparison with the dehysterized strain constant. As the field amplitude is increased, the hysteresis strain constant rises rapidly, until a peak is reached at approximately 35 kA/m. For field amplitudes larger than 35 kA/m, the hysteresis strain constant gradually drops and approaches the dehysterized strain constant.

The above example was done to indicate the effect of hysteresis on the strain constant for a given compressive stress, reference field and field amplitude range. Equations 2.3.1 to 2.3.4 are also valid for arbitrary stresses and fields, but the polynomial coefficients in table 2.3.1 are only applicable to a stress of 12 MPa. If the analysis is to be repeated for arbitrary stresses, different tables of polynomial coefficients will have to derived.

This concludes the section on the effects of hysteresis on the strain constant. The next section will be devoted to the hysteresis loss factor and damping coefficient.

Linear magnetostrictive hysteresis loss factor and viscous damping coefficient

This section models the magnetostrictive hysteresis losses of Terfenol-D by means of a linear dimensionless loss factor η and a linear damping coefficient c. An inverse field versus strain characteristic is presented, which is first expressed in dehysterized form, after which a strain rate dependent hysteresis loss term is added. The loss factor is defined in terms of excitation frequency, strain constant, applied field and strain rate. A complex field versus strain characteristic is derived for harmonic excitation and is shown graphically.

A method is presented to calculate η for nonlinear hysteresis loops. The steady-state harmonic damping coefficient is expressed in terms of the loss factor η, stiffness k of the Terfenol-D rod and the angular excitation frequency ω. A damping coefficient for wide-band random excitation is also derived and compared with the harmonic damping coefficient. A sample calculation of η and c is done for a constant stress and a large field amplitude.

An equation for the dehysterized linear strain in terms and the applied magnetic field and mechanical stress was given as follows by equation 2.2.1.4:

$$\varepsilon = \frac{\sigma}{E} + d^H H \tag{2.3.5}$$

where σ is the applied stress, E is Young's Modulus and d^H is the magnetostrictive strain constant. For the purpose of the analysis of the magnetostrictive hysteresis properties, it will be convenient to make use of an inverse characteristic, where the applied field is expressed in terms of strain for a constant stress:

$$H_{dehysterized} = \frac{\varepsilon}{d^H} - \frac{\sigma}{Ed^H} \tag{2.3.6}$$

The above equation describes field in terms of strain and stress in the absence of hysteresis. The equation can be easily extended to accommodate the effects of hysteresis, by adding a hysteresis loss term which contains a dimensionless hysteresis loss factor. The loss factor η

can be defined as the strain loss per cycle at an excitation frequency ω, and can mathematically be expressed as follows:

$$\eta = \frac{\omega d^H H_{loss}}{\dot{\varepsilon}} \tag{2.3.7}$$

where $\dot{\varepsilon}$ is the strain rate. The total field is the dehysterized field plus the hysteresis field loss:

$$H = H_{dehysterized} + H_{loss} \tag{2.3.8}$$

Substitution of equations 2.3.6 and 2.3.7 into equation 2.3.8 gives the following equation for the total magnetic field:

$$H = \frac{1}{d^H}\left(\varepsilon + \frac{\eta}{\omega}\dot{\varepsilon} - \frac{\sigma}{E}\right) \tag{2.3.9}$$

It can be seen from equation 2.3.9, that stress, strain and strain rate are required to obtain the total field. It will however be desirable to express field in terms of stress and strain only, as in the case of the dehysterized field. To this end, the strain rate must be eliminated by expressing it in terms of strain. This is easily accomplished by transforming equation 2.3.9 to the frequency domain, and analyzing the hysteresis characteristics for one cycle of harmonic excitation. The field and strain are then in the following form:

$$H = \mathrm{H}_A e^{j\omega t} \tag{2.3.10a}$$

$$\varepsilon = \mathrm{E}_A e^{j\omega t} \tag{2.3.10b}$$

where H_A is the field amplitude, E_A is the strain amplitude, $j = \sqrt{-1}$ and t is time.

Differentiation of equation 2.3.10b with respect to time, gives:

$$\dot{\varepsilon} = j\omega \mathrm{E}_A e^{j\omega t} = j\omega\varepsilon \tag{2.3.11}$$

Substitution of equation 2.3.11 into equation 2.3.9 gives:

$$H = \frac{1}{d^H}\left[(1 + j\eta)\varepsilon - \frac{\sigma}{E}\right] \tag{2.3.12}$$

Equation 2.3.12 gives the magnetic field strength in terms of mechanical stress and a complex strain.

At this stage of the derivation, it is convenient to analyze the field versus strain characteristic in isolation of the effects of stress. To this end, stress is treated as a constant, in which case field is expressed as follows, in terms of strain:

$$H\big|_{\sigma=const} = \left(\frac{1}{d^H} + j\frac{\eta}{d^H}\right)\varepsilon \tag{2.3.13}$$

Equation 2.3.13 gives the linear hysteresis field versus complex strain relationship at a constant stress. The graphic representation of equation 2.3.13 is an ellipse with a tilted major axis, as shown in figure 2.3.5. The slope of the major axis is $1/d^H$ and the ellipse intersects the field strength axis at a field of $\eta E_A/d^H$. The latter term gives an indication of the additional required field to overcome the losses and to produce the same strain amplitude as in the dehysterized case.

So far in this section it has been assumed that the hysteresis loops are elliptic. The assumption has made it possible to do linear analyses of the magnetostrictive characteristics of Terfenol-D. The assumption is reasonably accurate for minor loops, but in the case of major loops, the loading and unloading curves are distorted (see figure 2.3.2). However, the analysis of the behaviour of a magnetostrictive actuator and LOS stabilization system will be simplified considerably if the characteristics can be linearized. One way of achieving this is to obtain the equivalent elliptic loops of the nonlinear loops. This technique is popular in the field of mechanical engineering, where the force versus speed characteristic of a nonlinear damper, such as a quadratic, Coulomb or hysteretic damper, is expressed in terms of an equivalent viscous damping coefficient [Tse et al, 1978]. Figure 2.3.6 shows a nonlinear magnetostrictive hysteresis loop and its elliptic linear equivalent.

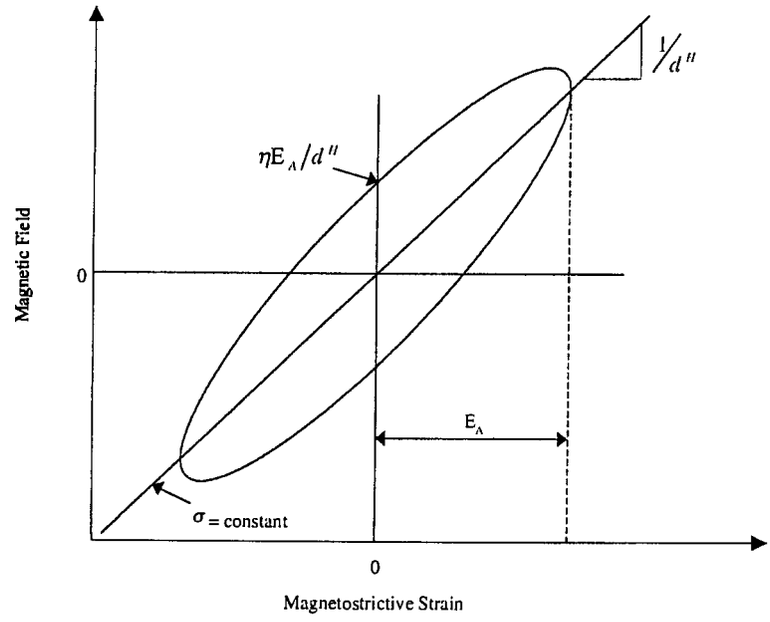

Figure 2.3.5: Magnetic field versus strain for a constant stress

In order to generate the equivalent elliptic loop, the loss factor η must be calculated from the nonlinear magnetostrictive characteristics. The loss factor is the ratio of the dissipated energy to the strain energy for a constant stress, where the dissipated energy is given by the included area of the nonlinear loop.

The loss factor can be obtained by means of the following equation:

$$\eta = \frac{\oint \varepsilon(H)\Big|_{\sigma=const} dH}{\pi \frac{1}{d^H} \mathrm{E}_A^2} \qquad \textbf{(2.3.14)}$$

The hysteresis strain constant d^H can be obtained by means of equations 2.3.2 to 2.3.4.

To summarize, magnetostrictive hysteresis was analyzed by means of a linear hysteresis loss factor in this section. The next section will explain a method to obtain the equivalent linear viscous damping coefficient if the loss factor is known.

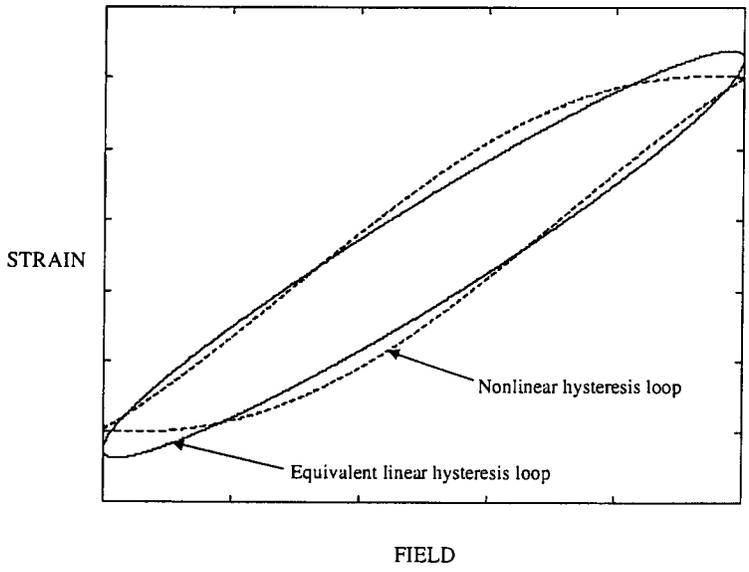

Figure 2.3.6: Nonlinear and equivalent linear magnetostrictive hysteresis loops

Viscous damping coefficient for magnetostrictive hysteresis

This section describes the magnetostrictive hysteresis losses in Terfenol-D in terms of a linear viscous damping coefficient. Mathematical expressions for the steady-state harmonic and wide-band random damping coefficients are given. A sample calculation of the damping coefficient is done for a given constant compressive stress and field amplitude.

The viscous damping coefficient is necessary to derive the linear equations of motion of the actuator and the LOS stabilization system. The equations are similar to that of a mechanical system, and will contain inertia, stiffness, damping and excitation force terms. The damping term is of particular importance in this section. In linear mechanical systems, the damping term may be expressed in a number of ways, e.g. in terms of a constant loss factor, as was done in the previous section, in terms of a viscous damping coefficient and in terms of a dimensionless constant damping factor. In this section, the viscous damping coefficient will be derived.

Whereas the loss factor of Terfenol-D could be expressed in terms of the magnetostrictive characteristics only (see equation 2.3.14), the damping factor also depends on the stiffness k of the Terfenol-D rod and the angular excitation frequency ω. The damping coefficient c can be expressed as follows in terms of k, η and ω:

$$c = \frac{k\eta}{\omega} \tag{2.3.15}$$

where the stiffness k is given by:

$$k = \frac{A_T E}{l_T} \tag{2.3.16}$$

A_T is the rod cross-sectional area, E is Young's Modulus of Terfenol-D and l_T is the rod length.

Closer inspection of equation 2.3.15 reveals that c is directly proportional to stiffness and loss factor, and inversely proportional to excitation frequency. For a constant k and η, the damping coefficient versus frequency characteristic will be a hyperbola. This phenomenon occurs in many hysteretic systems.

Equation 2.3.15 is suitable for the calculation of a damping coefficient at a constant excitation frequency. However, if a magnetostrictive actuator is excited over a wide range of frequencies, as is the case with wide-band random vibrations, c will vary over the frequency range, and will therefore not be constant. Although the analysis of linear systems, which display frequency-dependent damping coefficients, such as rubber isolators, can be carried out with relative ease in the frequency domain, time domain analyses of such systems are complicated. This is mainly due to the fact that the stiffness and damping terms in the equations of motion are time-dependent.

It will therefore be more desirable to obtain a constant c over a wide frequency range, which will facilitate the analysis of the random behaviour of the actuator and LOS stabilization system in both the time domain and the frequency domain. The wide-band average damping coefficient is given by:

$$c = \frac{1}{\Omega_f - \Omega_i} \int_{\Omega_i}^{\Omega_f} c(\omega) d\omega \tag{2.3.17}$$

where Ω_i is the minimum frequency of the disturbance band, Ω_f is the maximum frequency and $c(\omega)$ is given by equation 2.3.15.

Substitution of equation 2.3.15 into equation 2.3.17, gives the following relationship between c, k, η, Ω_f and Ω_i :

$$c = \frac{k\eta}{\Omega_f - \Omega_i} \ln\left(\frac{\Omega_f}{\Omega_i}\right) \tag{2.3.18}$$

The damping coefficient versus frequency relationship for a constant c can be compared with that for a constant η. A graphical comparison is shown in figure 2.3.7.

Equation 2.3.17 can be extended to obtain the damping coefficient if k and η are functions of ω. This may for instance happen in the vicinity of resonance, where the stroke length of the actuator may change dramatically relative to the low frequency stroke length, and due to the nonlinearities which occur at large amplitudes, the values of E and η will change. To accommodate frequency-dependent stiffnesses and loss factors, equation 2.3.17 is modified as follows:

$$c = \frac{1}{\Omega_f - \Omega_i} \int_{\Omega_i}^{\Omega_f} \frac{k(\omega)\eta(\omega)}{\omega} d\omega \qquad \textbf{(2.3.19)}$$

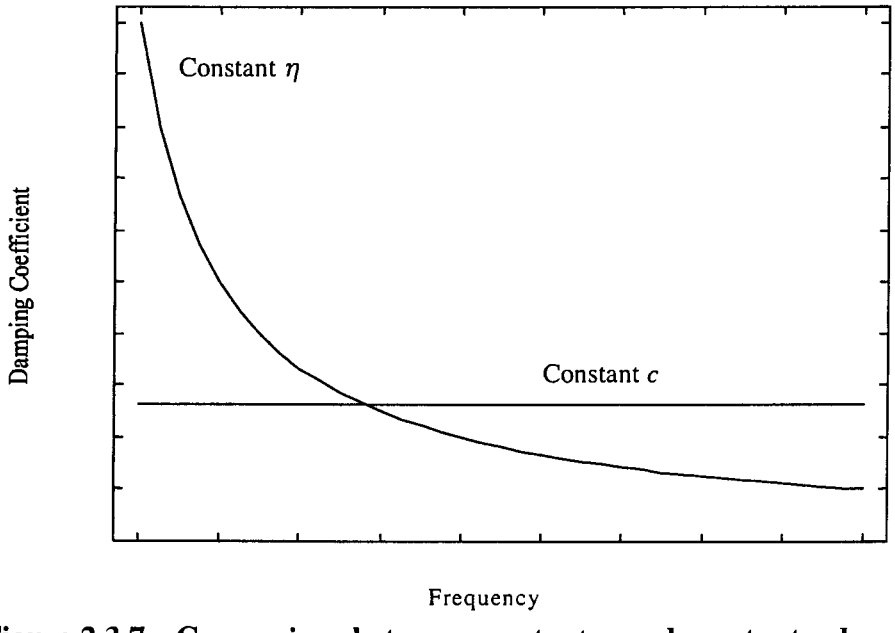

Figure 2.3.7: Comparison between constant η and constant c damping coefficients

A sample calculation of the loss factor and damping coefficient of a Terfenol-D rod is done next. Consider for example a rod with a length of 25 mm and a diameter of 5 mm, excited by a wide-band random (white noise) magnetic field with a reference (DC) value of 103,5 kA/m, a maximum field of 207 kA/m and a minimum value of 0 kA/m. The frequency band of the applied field is 2,5 Hz to 100 Hz. The stress is 12 MPa (compressive).

The parameters required to calculate the damping coefficient, are the large amplitude constant value of Young's Modulus, rod stiffness, strain amplitude, d^H and loss factor. From equations 2.2.1.5 and 2.2.1.8a, $\overline{E} = 36{,}95$ GPa, and from equations 2.3.1 to 2.3.4, $d^H = 6{,}67.10^{-9}$ m/A. By application of equation 2.3.16, k = 29,02 MN/m. The strain amplitude, from equations 2.3.4, is $6{,}9.10^{-4}$. Equation 2.3.14 gives the value of η as 0,0134, and finally, from equation 2.3.18, $c = 2{,}334.10^{3}$ Ns/m.

To summarize, the effects of hysteresis on the magnetostrictive characteristics of Terfenol-D have been discussed in detail in this section. A linear hysteresis loss factor has been defined and viscous damping coefficients have been derived for harmonic and wide-band random excitation.

Before proceeding to the next section, which will cover the effects of hysteresis on the magnetization characteristics of Terfenol-D, it deserves to be mentioned that damping is a phenomenon which is difficult to predict, and is more accurately assessed by means of experimental measurements. Predicted dynamic behaviour of a Terfenol-D actuator and LOS stabilization system will therefore have to be experimentally checked and corrected. The damping model derived above will only serve as a guideline to simulate the actuator and system behaviour in sections 2.7 and 2.8 and will be experimentally determined and corrected in chapters 4 and 5.

The effects of hysteresis on the magnetization characteristics of Terfenol-D

The loading, unloading and dehysterized flux density versus field strength characteristics of Terfenol-D, for a compressive stress of 12 MPa, are shown in figure 2.3.8.

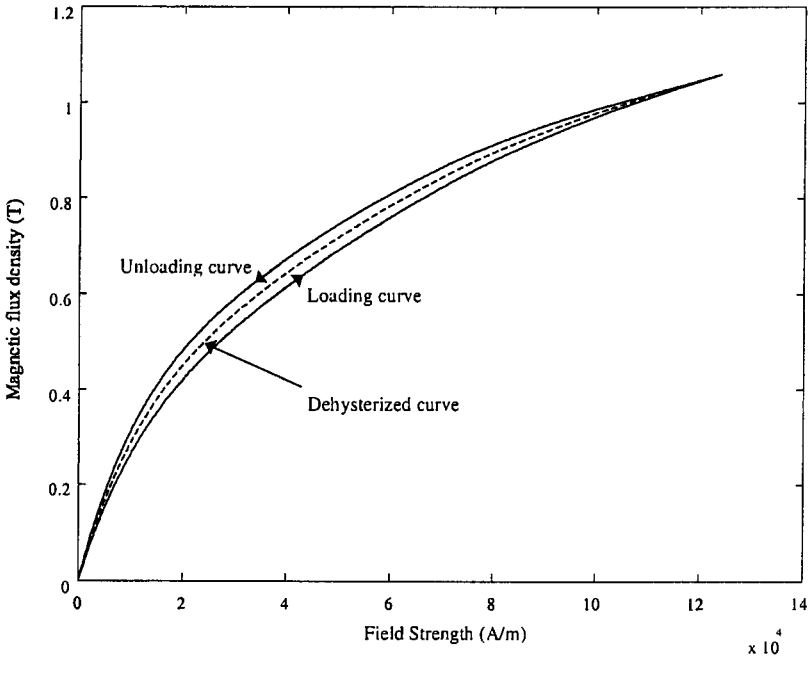

Figure 2.3.8: Loading, unloading and dehysterized flux density versus field strength characteristics of Terfenol-D for a 12 MPa compressive stress [Kvarnsjö, 1993]

Flux density can be expressed mathematically as:

$$B(H)\big|_{\sigma=-12MPa} = \sum_{i=0}^{8} b_i \left(\frac{H}{10^5}\right)^i \qquad \textbf{(2.3.20)}$$

The polynomial coefficients b_i for the loading, unloading and dehysterized flux density characteristics are given in table 2.3.2.

Table 2.3.2: Polynomial coefficients b_i for loading, unloading & dehysterized flux density vs field characteristics of Terfenol-D (12 MPa compressive stress)

Characteristic: i	Loading	Unloading	Dehysterized
0	$3{,}5792.10^{-4}$	$4{,}2134.10^{-4}$	$3{,}8963.10^{-4}$
1	3,4357	4,1987	3,8172
2	-9,8677	-13,49	-11,679
3	20,564	29,362	24,963
4	-26,015	-38,406	-32,210
5	19,742	29,94	24,841
6	-8,795	-13,603	-11,199
7	2,1209	3,3222	2,7216
8	-0,21376	-0,33699	-0,27538

The hysteresis permeability $\mu^{\sigma}_{hysteresis}$ can be calculated by means of the following equation:

$$\mu^{\sigma}_{hysteresis} = \frac{B(H_2)_{loading} - B(H_1)_{unloading}}{2H_A} \qquad \textbf{(2.3.21)}$$

where H_2 is the maximum applied field, H_1 is the minimum field and H_A is field amplitude, given by:

$$H_A = \frac{H_2 - H_1}{2} \qquad \textbf{(2.3.22)}$$

The flux densities $B(H_1)_{unloading}$ and $B(H_2)_{loading}$ are calculated by means of the following equations:

$$B(H_1)_{unloading} = \sum_{i=0}^{8} b_{i\,unloading} \left(\frac{H_1}{10^5}\right)^i \qquad \textbf{(2.3.23a)}$$

$$B(H_2)_{loading} = \sum_{i=0}^{8} b_{i\,loading} \left(\frac{H_2}{10^5}\right)^i \qquad \textbf{(2.3.23b)}$$

where the polynomial coefficients b_i for the unloading and loading characteristics are respectively given by the "loading" and "unloading" columns in table 2.3.2.

Equations 2.3.21 to 2.3.23 provide a simple mathematical tool to calculate the hysteresis permeability. A graph of the hysteresis permeability for a stress of 12 MPa, a reference field of 50 kA/m and a field amplitude range of 4 kA/m to 47 kA/m is shown in figure 2.3.9. For comparison purposes, the dehysterized permeability is also shown.

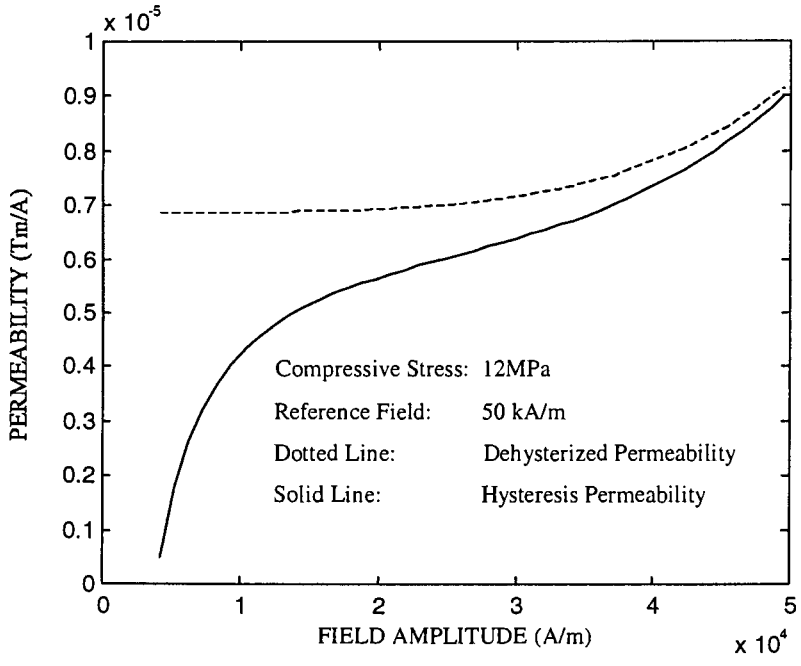

Figure 2.3.9: Comparison between Terfenol-D hysteresis permeability and dehysterized permeability for a 48 kA/m field amplitude range

Figure 2.3.9 shows that, for small field amplitudes, the hysteresis permeability is relatively small in comparison with the dehysterized permeability. As the field amplitude is increased, the hysteresis permeability rises sharply. As the field amplitude approaches the maximum value of 48 kA/m, the hysteresis permeability approaches the dehysterized permeability. It can be seen that hysteresis has a significant effect on the permeability of Terfenol-D, especially at low field amplitudes.

Section 2.3 covered the effects of hysteresis on the magnetostrictive and magnetization characteristics of Terfenol-D. The hysteresis strain constant and permeability, as well as a hysteresis loss factor and damping coefficient, were derived. This concludes the nonlinear characteristics of Terfenol-D. The information given in sections 2.2 and 2.3 will be used in section 2.4 to derive the nonlinear and linear equations of motion and coil current equation of a Terfenol-D actuator.

2.4 Linear and nonlinear equations of motion and coil current equations of a Terfenol-D actuator

The equation of motion and the coil current equation of a Terfenol-D actuator are derived in this section. A diagrammatical representation of the actuator is shown. Assumptions for which the model is valid, are given. The equation of motion is derived for both nonlinear and linear material characteristics. Equations are given for the actuator performance parameters such as displacement, acceleration, strain, stress, force and field strength. A differential equation describing the current in the coil, i.e. the coil current equation, is also derived for both linear and nonlinear material characteristics.

A magnetostrictive actuator is shown diagrammatically in figure 2.4.1. The actuator is mounted on a fixed base and consists of a Terfenol-D rod, a coil, an end cap, a piston and a displacement gain mechanism. The coil induces a field in the rod, which produces a strain and an accompanying compressive force in the rod. The force lifts the piston, whose displacement is amplified by the gain mechanism, thereby extending the stroke length of the actuator. The gain mechanism may operate hydraulically, pneumatically or mechanically. The walls of the actuator serve as magnetic couplers to form a closed circuit for the magnetic flux.

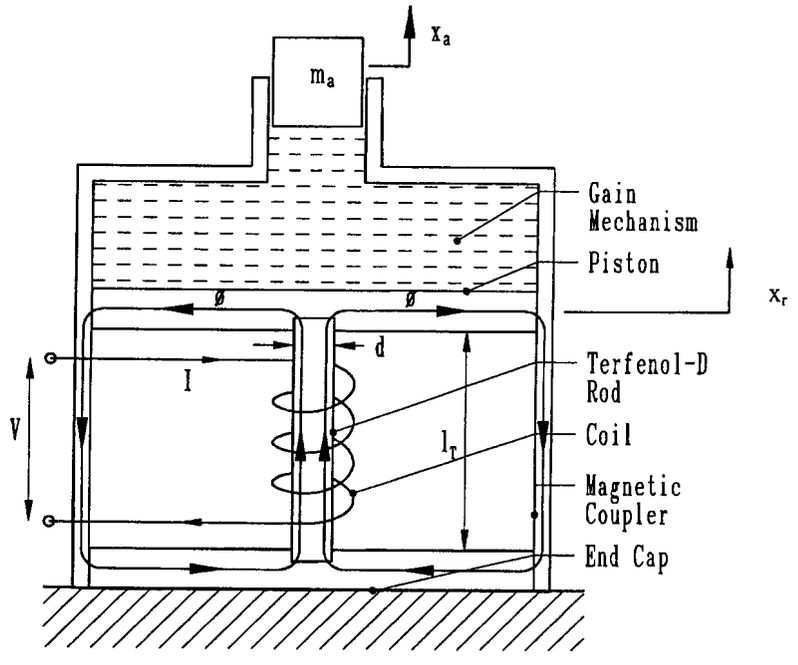

Figure 2.4.1: Diagrammatic representation of a Terfenol-D actuator

The concentrated mass of the actuator is m_a. The displacement of the mass is x_a and the displacement of the piston is x_r. The rod length is l_T and the rod diameter is d. R_c, I and V respectively represent the coil resistance, coil current and input voltage, while the flux in the rod is represented by ϕ.

The equation of motion and the coil current equation of the actuator will be derived from first principles. The equation of motion is a second order differential equation (DE), which

describes the acceleration $\ddot{x}_a$ of the mass in terms of the displacement x_a of the mass and the coil current I. The coil current equation is a first order DE, which describes the rate of change $\dot{I}$ of the coil current in terms of I, $\dot{x}_a$ and the actuator input voltage V.

A number of assumptions are made in order to derive the equations. The first assumption is that the actuator has only one degree of freedom (SDOF). The only displacement parameter that is of importance is the displacement of the mass. Secondly, it is assumed that the end cap and piston are rigid, i.e. there are no displacement losses due to resilience in the actuator. This implies that the elongation of the Terfenol-D rod, times the gain factor, equals the displacement of the mass. Similarly, in the derivation of the coil current equation, infinite permeability of the couplers is assumed, in other words the coupler reluctance, or resistance to magnetic flux, is zero. Lastly, it is assumed that the stiffness of the gain mechanism is zero. The actuator force equals the force produced by the rod, divided by the gain factor.

The nonlinear equation of motion of a Terfenol-D actuator is systematically derived in the next paragraphs. The gain factor is defined in terms of the displacement of the piston and the displacement of the mass. Equations are given for the strain and magnetic field strength in the rod. The stress in the rod is expressed as a nonlinear function of strain and field, which is then used to obtain expressions for the force produced by the rod and the actuator force. A force balance equation is written for the actuator, using Newton's second law. The stress, force produced by the rod, actuator output force and acceleration of the mass are also expressed in terms of the displacement of the mass and the coil current.

The displacement gain factor G of the actuator is defined as the ratio between the displacement of the mass and the elongation x_r of the Terfenol-D rod:

$$G = \frac{x_a}{x_r} \tag{2.4.1}$$

The strain ε in the rod is the displacement of the piston divided by the rod length:

$$\varepsilon = \frac{x_r}{l_T} \tag{2.4.2}$$

It is desirable to eliminate the displacement of the piston from equation 2.4.2, and to express the strain in terms of the displacement of the mass. This is done by substitution of equation 2.4.1 into equation 2.4.2:

$$\varepsilon = \frac{x_a}{G l_T} \tag{2.4.3}$$

The magnetic field H in the rod is given in terms of the coil current I by means of equation 2.4.4:

$$H = \frac{N}{l_T} I \tag{2.4.4}$$

where N is the number of coil turns.

From equation 2.2.1.9, the stress in the rod can be expressed as follows as a function of strain and magnetic field:

$$\sigma = \sigma(\varepsilon, H) \tag{2.4.5}$$

The stress in the rod can be used to derive equations for the force produced by the rod and the actuator output force. The force produced by the rod is the product of the stress in the rod and the cross-sectional area of the rod:

$$F_r = -A_T \sigma \tag{2.4.6}$$

Note the sign convention in equation 2.4.6: A compressive stress in the rod produces a positive force. The actuator output force is the force in the rod divided by the gain factor:

$$F_a = \frac{F_r}{G} \tag{2.4.7}$$

A force balance equation for the actuator is obtained from Newton's second law, i.e. the mass of the actuator times the acceleration of the mass equals the actuator output force:

$$m_a \ddot{x}_a = F_a \tag{2.4.8}$$

From equation 2.4.8, the acceleration of the mass is:

$$\ddot{x}_a = \frac{F_a}{m_a} \tag{2.4.9}$$

The performance parameters of the actuator, i.e. the stress in the rod, force produced by the rod, actuator output force and acceleration of the mass can be obtained from equations 2.4.3 to 2.4.9. It will however be more convenient to express these parameters as functions of displacement of the mass and coil current. This will facilitate the derivation of the equation of motion, coil current equation and state-space equations in section 2.5.

Firstly, the stress in the rod is expressed in terms of displacement and current by substitution of equations 2.4.3 and 2.4.4 into equation 2.4.5:

$$\sigma = \sigma\left(\frac{1}{Gl_T} x_a, \frac{N}{l_T} I\right) \tag{2.4.10}$$

Secondly, the force produced by th of displacement and current by substitution of equation 2.4.10 into equation 2.4.6:

$$F_r = -A_T \sigma\left(\frac{1}{Gl_T}x_a, \frac{N}{l_T}I\right) \tag{2.4.11}$$

Thirdly, the actuator output force is expressed in terms of displacement and current by substitution of equation 2.4.10 into equation 2.4.11:

$$F_a = -\frac{A_T}{G}\sigma\left(\frac{1}{Gl_T}x_a, \frac{N}{l_T}I\right) \tag{2.4.12}$$

Finally, the nonlinear equation of motion is obtained by substitution of equation 2.4.12 into equation 2.4.9:

$$\ddot{x}_a = -\frac{A_T}{m_a G}\sigma\left(\frac{1}{Gl_T}x_a, \frac{N}{l_T}I\right) \tag{2.4.13}$$

Equation 2.4.12 is a nonlinear, second order, ordinary DE which expresses the acceleration of the mass as a function of the displacement of the mass and coil current.

The equation of motion can subsequently be expressed in numerical terms by substitution of equations 2.4.3 and 2.4.4 into equation 2.2.1.9, and by substitution of the resulting equation into equation 2.4.13:

$$\ddot{x}_a = -10^6 \frac{A_T}{m_a G}\sum_{i=0}^{m}\sum_{j=0}^{n} s_{ij}\left(\frac{10^3}{Gl_T}x_a\right)^j\left(\frac{10^{-5}N}{l_T}I\right)^i \tag{2.4.14}$$

where the two-dimensional polynomial coefficients s_{ij} for $m = 7$ and $n = 3$ are given in table 2.2.1.2.

The nonlinear equation of motion of a Terfenol-D actuator has been derived in this section. The strain and stress in the rod, magnetic field, force produced by the rod and actuator output force have also been obtained as nonlinear functions of displacement and coil current. In the next section, the linear equation of motion will be derived using large amplitude constant values of the magnetostrictive parameters, i.e. Young's Modulus and the strain constant.

Linear equation of motion of a Terfenol-D actuator

The linear equation of motion of a Terfenol-D actuator is derived in this section. Average, large amplitude values of the magnetostrictive parameters, i.e. Young's Modulus and the strain constant, are used to express the stress in the rod in terms of the displacement of the mass and the coil current. It will be shown that, in contrast with the nonlinear system, the linear mechanical and magnetostrictive stress terms can be separated. A linear force balance equation is written for the actuator using Newton's second law. The equation of motion,

which gives the acceleration of the mass as a linear combination of the displacement of the mass and the coil current, is derived. The static and dynamic actuator characteristics, i.e. the spring stiffness, natural frequency, damping factor and forcing function are defined and incorporated into the equation of motion. All the terms in the equation of motion are explained.

The linear relationship between strain, mechanical stress and magnetic field, from equation 2.2.1.4, is:

$$\varepsilon = \frac{\sigma}{E} + d^H H \tag{2.4.15}$$

where E and d^H respectively represent the large amplitude average values of Young's Modulus and the strain constant, as given by equations 2.2.1.7a and 2.2.1.7b. From equation 2.4.15, the stress in the rod is expressed as follows as a linear combination of strain and field:

$$\sigma = E\varepsilon - Ed^H H \tag{2.4.16}$$

The first term on the right hand side of equation 2.4.16 is the stress due to the strain, and the second term is the stress due to the applied field. Comparing equations 2.4.16 and 2.4.5 shows that the linear stress equation has an advantage over the nonlinear stress equation, namely that the mechanical and magnetostrictive stress terms can be separated by means of constant factors.

For the purpose of the derivation of the linear equation of motion, it is desirable to express the stress in terms of the displacement of the mass and coil current. This is done by substitution of equations 2.4.3 and 2.4.4 into equation 2.4.16:

$$\sigma = \frac{E}{Gl_T} x_a - \frac{ENd^H}{l_T} I \tag{2.4.17}$$

The above equation will subsequently be used to write the force produced by the rod, the actuator output force and the acceleration of the mass in terms of the displacement of the mass and the coil current. The force produced by the rod is obtained by substitution of equation 2.4.17 into equation 2.4.6:

$$F_r = -\frac{A_T E}{Gl_T} x_a + \frac{A_T ENd^H}{l_T} I \tag{2.4.18}$$

The actuator output force is obtained by substitution of equation 2.4.18 into equation 2.4.7:

$$F_a = -\frac{A_T E}{G^2 l_T} x_a + \frac{A_T ENd^H}{Gl_T} I \tag{2.4.19}$$

The first term on the right hand side of the above equation gives the elastic, or spring force of the actuator, while the second term gives the force supplied by the coil current, or the input

force. The elastic term is negative because it resists the deflection x_a of the spring, while the input force, which forces the mass in the direction of x_a, is positive.

The linear equation of motion is obtained by substitution of equation 2.4.19 into equation 2.4.9:

$$\ddot{x}_a = -\frac{A_T E}{m_a G^2 l_T} x_a + \frac{A_T E N d^H}{m_a G l_T} I \tag{2.4.20}$$

Equation 2.4.20 is a linear, second order, ordinary DE, which gives the acceleration of the mass as a linear combination of the displacement of the mass and the coil current.

Equation 2.4.20 can be simplified by introducing the static and dynamic characteristics of the actuator, i.e. the mass, stiffness, angular natural frequency and input force. To this end, the equation of motion is written as follows:

$$\ddot{x}_a = -\omega_n^2 x_a + \frac{F_I}{m_a} I \tag{2.4.21}$$

where the angular natural frequency ω_n is:

$$\omega_n = \sqrt{\frac{k_a}{m_a}} \tag{2.4.22}$$

and the stiffness k_a is:

$$k_a = \frac{A_T E}{G^2 l_T} \tag{2.4.23}$$

F_I is the ratio of the input force to the input current, given by:

$$F_I = \frac{A_T E N d^H}{G l_T} \tag{2.4.24}$$

Equation 2.4.21 is the undamped linear equation of motion, since it contains no damping terms. Damping is introduced by defining a dimensionless damping factor ζ as:

$$\zeta = \frac{c}{2 m_a \omega_n} \tag{2.4.25}$$

where c is the viscous damping coefficient, which was described in more detail in section 2.3.

The addition of a damping term to equation 2.4.21 alters the equation of motion as follows:

$$\ddot{x}_a = -2\zeta\omega_n\dot{x}_a - \omega_n^2 x_a + \frac{F_l}{m_a} I \tag{2.4.26a}$$

or:

$$\ddot{x}_a + 2\zeta\omega_n\dot{x}_a + \omega_n^2 x_a = \frac{F_l}{m_a} I \tag{2.4.26b}$$

The individual terms in equation 2.4.26b are explained as follows: The first term on the left hand side is the inertia term, the second term is the damping term and the third term is the stiffness term. The term on the right hand side is the forcing term.

The equations for stress, force produced by the rod and actuator output force can be simplified in a similar manner as the equation of motion by introducing the natural frequency, damping factor and input force. The derivation of these equations will not be covered in full here. Instead, only the results will be given.

The stress in the rod, force produced by the rod and actuator output force, in terms of the dynamic characteristics of the actuator, are respectively given by:

$$\sigma = k_a \frac{G}{A_T} x_a + 2\frac{m_a G}{A_T}\zeta\omega_n\dot{x}_a - \frac{G}{A_T} F_l I \tag{2.4.27a}$$

$$F_r = -k_a G x_a - 2m_a G\zeta\omega_n\dot{x}_a + GF_l I \tag{2.4.27b}$$

$$F_a = -k_a x_a - 2m_a\zeta\omega_n\dot{x}_a + F_l I \tag{2.4.27c}$$

To summarize, the linear equation of motion was derived in detail in this section. The coil current equation will subsequently be derived. The nonlinear coil current equation will be derived first, and will be followed by the derivation of the linear coil current equation.

Nonlinear coil current equation of a Terfenol-D actuator

The nonlinear coil current equation of a Terfenol-D actuator is derived in this section. The input voltage of the coil is expressed in terms of the coil current and the rate of change of magnetic flux density. The nonlinear magnetization and magnetostrictive characteristics of Terfenol-D are used to write the coil voltage as a function of the speed of the mass, the coil current and the rate of change of the coil current. Finally, the nonlinear coil current equation is obtained from the coil voltage equation.

The fundamental relationship between the voltage input V to the actuator, the number of coil turns N, the flux density ϕ, the coil resistance R_c and the coil current I is:

$$V = N\dot{\phi} + R_c I \tag{2.4.28}$$

The magnetic flux is the product of the cross-sectional area A_T of the rod and the flux density B:

$$\phi = A_T B \tag{2.4.29}$$

The coil voltage can be expressed in terms of the flux density differentiation of equation 2.4.29 with respect to time, and by substitution of the resulting equation into equation 2.4.28:

$$V = A_T N\dot{B} + R_c I \tag{2.4.30}$$

Equation 2.4.30 expresses the actuator coil input voltage in terms of the flux density rate $\dot{B}$ and the coil current I. The next step is to express the flux rate in terms of the displacement of the mass and the coil current. To this end, the relationship between flux density, stress and field, as given by equation 2.2.2, are used. This relationship is:

$$B = B(\sigma, H) \tag{2.4.31}$$

Differentiation of equation 2.4.31 with respect to time, gives the following equation for the flux density rate $\dot{B}$:

$$\dot{B} = B_\sigma \dot{\sigma} + B_H \dot{H} \tag{2.4.32}$$

where B_σ is the partial derivative of the flux density with respect to mechanical stress at a constant magnetic field strength, which is also d^σ (see section 2.2.2), and B_H is the partial derivative of flux density with respect to field at a constant stress, which is the permeability μ^σ. Equation 2.4.32 can therefore be written as follows:

$$\dot{B} = d^\sigma \dot{\sigma} + \mu^\sigma \dot{H} \tag{2.4.33}$$

where d^σ and μ^σ are functions of stress and field:

$$d^\sigma = d^\sigma(\sigma, H) \tag{2.4.34a}$$
$$\mu^\sigma = \mu^\sigma(\sigma, H) \tag{2.4.34b}$$

The objective of this derivation is to obtain the coil current equation in terms of the same variables as the equation of motion, i.e. x_a and I. To this end, the stress rate and field rate must be eliminated from equation 2.4.33. This is done by differentiation of equation 2.4.16 with respect to time:

$$\dot{\sigma} = E\left(\dot{\varepsilon} - d^H \dot{H}\right) \tag{2.4.35}$$

where, from equations 2.2.1.5 and 2.2.1.6, E and d^H are functions of stress and field:

$$E = E(\sigma, H) \tag{2.4.36a}$$
$$d^H = d^H(\sigma, H) \tag{2.4.36b}$$

The strain rate $\dot{\varepsilon}$ is expressed in terms of the speed of the mass, i.e. $\dot{x}_a$, by differentiation of equation 2.4.3 with respect to time:

$$\dot{\varepsilon} = \frac{\dot{x}_a}{Gl_T} \tag{2.4.37}$$

The field rate $\dot{H}$ is expressed in terms of the rate of change of the coil current, i.e. $\dot{I}$, by differentiation of equation 2.4.4 with respect to time:

$$\dot{H} = \frac{N}{l_T}\dot{I} \tag{2.4.38}$$

After substitution of equations 2.4.37 and 2.4.38 into equation 2.4.35, and subsequent substitution of the resulting equation into equation 2.4.33, the flux density rate becomes:

$$\dot{B} = \frac{Ed^{\sigma}}{Gl_T}\dot{x}_a + \frac{N}{l_T}\left(\mu^{\sigma} - Ed^{\sigma}d^{H}\right)\dot{I} \tag{2.4.39}$$

The actuator coil input voltage is obtained by substitution of equation 2.4.39 into equation 2.4.30:

$$V = \frac{A_T ENd^{\sigma}}{Gl_T}\dot{x}_a + \frac{A_T N^2}{l_T}\left(\mu^{\sigma} - Ed^{\sigma}d^{H}\right)\dot{I} + R_c I \tag{2.4.40}$$

Equation 2.4.40 expresses the coil input voltage in terms of the speed of the mass, the coil current and the rate of change of the coil current. Finally, the coil current equation is obtained by isolating $\dot{I}$ in equation 2.4.40:

$$\dot{I} = \frac{l_T}{A_T N^2\left(\mu^{\sigma} - Ed^{\sigma}d^{H}\right)}\left(-\frac{A_T ENd^{\sigma}}{Gl_T}\dot{x}_a - R_c I + V\right) \tag{2.4.41}$$

Equation 2.4.41 is a nonlinear, first order, ordinary DE which gives the rate of change of the coil current in terms of the speed of the mass, the coil current and the input voltage. The magnetostrictive and magnetization parameters μ^{σ}, E, d^{σ} and d^{H} can be obtained in numerical terms from equations 2.2.1.5, 2.2.1.6, 2.2.2.3 and 2.2.2.4. It must be borne in mind that these equations give the parameters as functions of stress and field, and not as functions of displacement and coil current. However, by substitution of equations 2.4.4 and 2.4.5 into equations 2.4.34 and 2.4.36, the nonlinear functional relationships for the magnetostrictive and

magnetization parameters, in terms of actuator output displacement and coil current, become:

$$\mu^{\sigma} = \mu^{\sigma}\left(\sigma\left(\frac{1}{Gl_T}x_a, \frac{N}{l_T}I\right), \frac{N}{l_T}I\right) \tag{2.4.42a}$$

$$E = E\left(\sigma\left(\frac{1}{Gl_T}x_a, \frac{N}{l_T}I\right), \frac{N}{l_T}I\right) \tag{2.4.42b}$$

$$d^{\sigma} = d^{\sigma}\left(\sigma\left(\frac{1}{Gl_T}x_a, \frac{N}{l_T}I\right), \frac{N}{l_T}I\right) \tag{2.4.42c}$$

$$d^{H} = d^{H}\left(\sigma\left(\frac{1}{Gl_T}x_a, \frac{N}{l_T}I\right), \frac{N}{l_T}I\right) \tag{2.4.42d}$$

To summarize, the nonlinear coil current equation was derived in this section. The linear coil current equation will be derived in the next section. Equation 2.4.40 will form the basis of the derivation.

Linear coil current equation of a Terfenol-D actuator

The linear coil current equation of a Terfenol-D actuator is derived in this section. The average large amplitude constant values of the magnetostrictive and magnetization parameters are used in the derivation. The free inductance, coupling factor and clamped inductance of the coil are defined and employed to simplify the coil current equation. The rate of change of the coil current is written as a linear combination of the speed of the mass, coil current and input voltage.

For the purpose of this derivation, the nonlinear coil voltage equation given by equation 2.4.40 will be used. This equation is repeated here for convenience:

$$V = \frac{A_T E N d^{\sigma}}{Gl_T}\dot{x}_a + \frac{A_T N^2}{l_T}\left(\mu^{\sigma} - E d^{\sigma} d^{H}\right)\dot{I} + R_c I \tag{2.4.43}$$

In the nonlinear case, the magnetostrictive and magnetization parameters μ^{σ}, E, d^{σ} and d^{H} were expressed as functions of displacement and coil current in equations 2.4.42a to 2.4.42d, while in the linear case, these parameters are considered as constants. The linearization technique was covered in more detail in section 2.2.

Equation 2.4.43 is conveniently rewritten as follows in order to introduce the free inductance, the coupling factor and the clamped inductance of the coil into the voltage equation:

$$V = \frac{A_T E N d^{\sigma}}{Gl_T}\dot{x}_a + \frac{A_T N^2 \mu^{\sigma}}{l_T}\left(1 - \frac{E d^{\sigma} d^{H}}{\mu^{\sigma}}\right)\dot{I} + R_c I \tag{2.4.44}$$

The free inductance L_f, coupling factor cf and clamped induction L_0 of the coil are respectively given by:

$$L_f = \frac{A_T N^2 \mu^\sigma}{l_T} \tag{2.4.45}$$

$$cf = \sqrt{\frac{Ed^\sigma d^H}{\mu^\sigma}} \tag{2.4.46}$$

$$L_0 = L_f\left[1-(cf)^2\right] \tag{2.4.47}$$

By substitution of equations 2.4.45 and 2.4.46 into equation 2.4.47 and by substitution of the resulting equation into equation 2.4.44, the coil voltage equation is simplified as follows:

$$\underbrace{V}_{Input} = \underbrace{\frac{A_T ENd^\sigma}{Gl_T}\dot{x}_a}_{\text{"back emf"}} + \underbrace{L_0\dot{I}}_{inductive\ voltage} + \underbrace{R_c I}_{resistive\ voltage} \tag{2.4.48}$$

The first term on the right hand side of equation 2.4.48 gives the coil voltage due to the speed of the mass. This term is known as the "back-emf". The second term gives the coil voltage due to the rate of change of the coil current and is known as the inductive voltage of the coil. The last term gives the coil voltage due to the coil current. This term is the resistive voltage of the coil.

Finally, the linear coil current equation is obtained by isolating $\dot{I}$ in equation 2.4.48:

$$\dot{I} = -\frac{A_T ENd^\sigma}{Gl_T L_0}\dot{x}_a - \frac{R_c}{L_0}I + \frac{1}{L_0}V \tag{2.4.49}$$

To summarize, the linear and nonlinear equations of motion and coil current equations of a Terfenol-D actuator were derived in detail section 2.4. The equation of motion describes the mechanical behaviour of the actuator, while the coil current equation describes the electrical behaviour of the actuator. The two equations therefore describe the behaviour of two separate systems. The equation of motion can only be solved if the coil current is known, while the coil current equation can only be solved if the speed of the mass is known. In order to analyze the behaviour of the actuator as one integrated electromechanical system, the equation of motion and the coil current equation must be coupled into one system of equations. This can be done by means of the state-space method. The state-space equations of the actuator will be derived in section 2.5.

2.5 State-space model and transfer functions of a Terfenol-D actuator

The dynamic equations of the actuator are written in state-space form for the following reasons: Firstly, the equation of motion and the coil current equation can be coupled into one set of dynamic equations. Secondly, transfer functions between the input voltage and all of the actuator outputs, such as the displacement and acceleration of the mass, the rod strain, stress and field, the force producd by the rod and the actuator output force, can be obtained by means of the state-space method.

A third reason for writing the equations in state-space form is to obtain the natural vibration behaviour of the actuator, i.e. actuator behaviour in the absence of any coil voltage input. The actuator eigenvalues and their stability can be evaluated using the state-space method. In the fourth place, the state-space method can be employed to simulate the behaviour of the actuator for any arbitrary input in the time and frequency domains, using either the linear or the nonlinear models. Lastly, the state-space method, inter alia, can be used to design a controller for the LOS stabilization system.

The nonlinear and linear state-space equations, as well as the complex Laplace- and frequency domain *TF*'s of a Terfenol-D actuator, are derived in this section. The section is divided into three parts. The equation of motion and the coil current equation are combined into one set of dynamic actuator equations in section 2.5.1. Both the linear and nonlinear state-space equations are derived. Output equations for the different actuator performance parameters are also given.

The complex Laplace -domain *TF*'s are derived from the linear state and output equations in section 2.5.2. The *TF*'s for all the actuator parameters are given. An open-loop block diagram from the input voltage to the output displacement is shown. The Laplace-domain *TF*'s are transformed to the frequency domain in section 2.5.3. The general complex form of the *TF* is given, after which the magnitude and phase angle of the output displacement to input voltage are given in real form.

2.5.1 State-space model of a Terfenol-D actuator

A method of system representation developed since around 1960, has been the characterization of dynamic systems by means of state equations [Schwarzenbach & Gill, 1986]. The method involves the transformation of one or more sets of DE's with a total order of n into a number n of first order DE's. This requires the introduction of a set of variables, known as the state variables, or states for short, where the number of variables equals the number of DE's.

The state variables are not unique and may be chosen to suit a particular problem. The most suitable states, which describe the behaviour of a Terfenol-D actuator, will be chosen in this section and the state equations will be derived. It will be shown that, for the nonlinear material characteristics, the state derivatives are nonlinear functions of the states and inputs, while for the linear characteristics, the state derivatives are conveniently written as linear combinations of the states and inputs.

In addition to the state equations, a separate set of equations can be written to describe any number of variables, which may be required to analyze the system behaviour, in terms of the states and inputs. These equations are appropriately known as the output equations. A set of output variables will be chosen for the actuator in the following paragraphs, and the linear and nonlinear output equations will be derived. The equation of motion and the coil current equation, which were derived in section 2.4, will form the basis of the derivation of both the state and output equations.

The form of the state and output equations depends on the nature of the system, i.e. whether the system is nonlinear and time-dependent, nonlinear and time-independent, linear and time dependent, or linear and time-independent. The three forms that will be compared in short below, are the general nonlinear and time-dependent form, the nonlinear and time-independent form and the linear and time-independent form. The general nonlinear, time dependent form of the state and output equations is, according to Slotine & Li [1991]:

$$\dot{x} = f(x,u,t) \qquad \textbf{(2.5.1.1a)}$$
$$y = g(x,u,t) \qquad \textbf{(2.5.1.1b)}$$

where x is the state vector, u is the input vector and t denotes time. f is a vector of functions which describes the state derivatives $\dot{x}$ in terms of the states, inputs and time, and g is a vector of functions which describes the outputs in terms of the states, inputs and time.

If the system is time-independent and non-linear, equations 2.5.1.1a and 2.5.1.1b are modified as follows:

$$\dot{x} = f(x,u) \qquad \textbf{(2.5.1.2a)}$$
$$y = g(x,u) \qquad \textbf{(2.5.1.2b)}$$

It can be seen from equations 2.5.1.2a and 2.5.1.2b that the state and output vectors only depend on the states and inputs, and are independent of time.

If the system is time-independent and linear ("LTI"), the state and output equations are:

$$\dot{x} = Ax + Bu \qquad \textbf{(2.5.1.3a)}$$
$$y = Cx + Du \qquad \textbf{(2.5.1.3b)}$$

where A is a constant square matrix which relates the state derivatives to the states, known as the coefficient matrix. B is a constant matrix, which relates the state derivatives to the inputs, known as the driving matrix. C is a constant matrix, which relates the outputs to the states, known as the output matrix. D is a constant matrix, which relates the outputs to the inputs, known as the transmission matrix.

The states must be chosen in such a way that system behaviour can be described by a combination of the states and inputs, such as in equations 2.5.1.2 and 2.5.1.3. A suitable choice of states can for instance be the displacement x_a and speed $\dot{x}_a$ of the actuator mass, as well as the coil current I. This choice is in agreement with the variables chosen for the equation of motion and the coil current equation in section 2.4.

For this choice of states, the state vector can be written as follows:

$$x = \{x_a, \dot{x}_a, I\}^T \tag{2.5.1.4}$$

where the superscript T denotes the transpose of the state matrix.

The input u to the system can be chosen as the actuator coil input voltage V:

$$u = V \tag{2.5.1.5}$$

The outputs are chosen as the displacement x_a of the mass, coil current I, strain ε, field H and stress σ in the rod, the force F_r produced by the rod, the actuator force F_a and the acceleration $\ddot{x}_a$ of the mass:

$$y = \{x_a, I, \varepsilon, H, \sigma, F_r, F_a, \ddot{x}_a\}^T \tag{2.5.1.6}$$

Having chosen the most suitable states and outputs, the nonlinear and linear state and output equations can be derived from the linear and nonlinear equation of motion and the coil current equation. The nonlinear equation of motion was given by equation 2.4.13 and the nonlinear coil current equation was given by equation 2.4.41 and 2.4.42a to 2.4.42d. For the sake of completeness, the equation of motion and the coil current equation will be repeated below. The nonlinear equation of motion is:

$$\ddot{x}_a = -\frac{A_T}{m_a G}\sigma\left(\frac{1}{Gl_T}x_a, \frac{N}{l_T}I\right) \tag{2.5.1.7}$$

where σ is the mechanical stress as a function of displacement and current, as given by equation 2.4.14:

$$\sigma\left(\frac{1}{Gl_T}x_a, \frac{N}{l_T}I\right) = \sum_{i=0}^{m}\sum_{j=0}^{n} s_{ij}\left(\frac{10^3}{Gl_T}x_a\right)^j\left(\frac{10^{-5}N}{l_T}I\right)^j \tag{2.5.1.8}$$

The two-dimensional polynomial coefficients s_{ij} for $m = 7$ and $n = 3$ can be obtained from table 2.2.1.2 in section 2.2.1.

The nonlinear coil current equation, from equation 2.4.41, is:

$$\dot{I} = \frac{l_T}{A_T N^2\left(\mu^\sigma - Ed^\sigma d^H\right)}\left(-\frac{A_T ENd^\sigma}{Gl_T}\dot{x}_a - R_c I + V\right) \tag{2.5.1.9}$$

where the magnetostrictive and magnetization parameters μ^σ, E,d^σ and d^H are functions of the displacement and coil current state variables:

$$\mu^\sigma = \mu^\sigma\left(\sigma\left(\frac{1}{Gl_T}x_a, \frac{N}{l_T}I\right), \frac{N}{l_T}I\right) \quad \textbf{(2.5.1.10a)}$$

$$E = E\left(\sigma\left(\frac{1}{Gl_T}x_a, \frac{N}{l_T}I\right), \frac{N}{l_T}I\right) \quad \textbf{(2.5.1.10b)}$$

$$d^\sigma = d^\sigma\left(\sigma\left(\frac{1}{Gl_T}x_a, \frac{N}{l_T}I\right), \frac{N}{l_T}I\right) \quad \textbf{(2.5.1.10c)}$$

$$d^H = d^H\left(\sigma\left(\frac{1}{Gl_T}x_a, \frac{N}{l_T}I\right), \frac{N}{l_T}I\right) \quad \textbf{(2.5.1.10d)}$$

The nonlinear state equations can now be written in the state-space form as given by equation 2.5.1.2a. This is done by combining the equation of motion (equation 2.5.1.7) and the coil current equation (equation 2.5.1.9) into one vector of functions:

$$\dot{x} = f(x,u) \quad \textbf{(2.5.1.11)}$$

where f is given by:

$$f = \begin{Bmatrix} \dot{x}_a \\ -\frac{A_T}{m_a G}\sigma\left(\frac{1}{Gl_T}x_a, \frac{N}{l_T}I\right) \\ \frac{l_T}{A_T N^2\left(\mu^\sigma - Ed^\sigma d^H\right)}\left(-\frac{A_T ENd^\sigma}{Gl_T}\dot{x}_a - R_c I + V\right) \end{Bmatrix} \quad \textbf{(2.5.1.12)}$$

and the state vector x and input u are respectively given by equations 2.5.1.4 and 2.5.1.5.

The nonlinear output equations are written in the form equation of 2.5.1.2b, by making use of the nonlinear relations which were derived in section 2.4. The actuator output displacement, coil current, strain, field, stress, force produced by the rod, actuator output force and output acceleration, are given in terms of the states and inputs as:

$$y = g(x,u) \quad \textbf{(2.5.1.13)}$$

In equation 2.5.1.13, the output vector y is given by equation 2.5.1.6 and g is given by:

$$g = \begin{Bmatrix} x_a \\ I \\ \frac{1}{Gl_T} x_a \\ \frac{N}{l_T} I \\ \sigma\left(\frac{1}{Gl_T} x_a, \frac{N}{l_T} I\right) \\ -A_T \sigma\left(\frac{1}{Gl_T} x_a, \frac{N}{l_T} I\right) \\ -\frac{A_T}{G} \sigma\left(\frac{1}{Gl_T} x_a, \frac{N}{l_T} I\right) \\ -\frac{A_T}{m_a G} \sigma\left(\frac{1}{Gl_T} x_a, \frac{N}{l_T} I\right) \end{Bmatrix} \qquad \textbf{(2.5.1.14)}$$

An additional output, which is not incorporated in the output vector, is the coil power P. The coil power is omitted because it is not possible to describe P as a linear combination of states and inputs, since P is the product of the input voltage V and the coil current I:

$$P = VI \qquad \textbf{(2.5.1.15)}$$

The nonlinear state and output equations were derived in this section. The linear state and output equations will be derived next.

Linear state and output equations of a Terfenol-D actuator

The damped linear equation of motion of the actuator, (see equation 2.4.26), is:

$$\ddot{x}_a = -\omega_n^2 x_a - 2\zeta\omega_n \dot{x}_a + \frac{F_l}{m_a} I \qquad \textbf{(2.5.1.16)}$$

where F_l is given by equation 2.4.24 as:

$$F_l = \frac{A_T E N d^H}{Gl_T} \qquad \textbf{(2.5.1.17)}$$

The linear coil current equation, as given by equation 2.4.49, is:

$$\dot{I} = -\frac{A_T E N d^\sigma}{Gl_T L_0} \dot{x}_a - \frac{R_c}{L_0} I + \frac{1}{L_0} V \qquad \textbf{(2.5.1.18)}$$

The linear state and output equations are subsequently written in the state-space form as given by equations 2.5.1.3a and 2.5.1.3b:

$$\dot{x} = Ax + Bu \qquad \textbf{(2.5.1.19a)}$$
$$y = Cx + Du \qquad \textbf{(2.5.1.19b)}$$

where A, B, C and D are given by:

$$A = \begin{bmatrix} 0 & 1 & 0 \\ -\omega_n^2 & -2\zeta\omega_n & \dfrac{A_T ENd^H}{Gl_T} \\ 0 & -\dfrac{A_T ENd^\sigma}{Gl_T L_0} & -\dfrac{R_c}{L_0} \end{bmatrix} \qquad \textbf{(2.5.1.20a)}$$

$$B = \frac{1}{L_0}\begin{Bmatrix} 0 \\ 0 \\ 1 \end{Bmatrix} \qquad \textbf{(2.5.1.20b)}$$

$$C = \begin{bmatrix} 1 & 0 & 0 \\ 0 & 0 & 1 \\ \dfrac{1}{Gl_T} & 0 & 0 \\ 0 & 0 & \dfrac{N}{l_T} \\ k_a \dfrac{G}{A_T} & 2\dfrac{m_a G}{A_T}\zeta\omega_n & -\dfrac{ENd^H}{l_T} \\ -k_a G & -2m_a G\zeta\omega_n & \dfrac{A_T ENd^H}{l_T} \\ -k_a & -2m_a\zeta\omega_n & \dfrac{A_T ENd^H}{Gl_T} \\ -\omega_n^2 & -2\zeta\omega_n & \dfrac{A_T ENd^H}{m_a Gl_T} \end{bmatrix} \qquad \textbf{(2.5.1.20c)}$$

$$D = 0 \qquad \textbf{(2.5.1.20d)}$$

and the state vector x and input u are given by equations 2.5.1.4 and 2.5.1.5 respectively.

Equations 2.5.19 and 2.5.20 give the linear state and output equations. The only remaining output, which is not included in the above equations, because it cannot be written as a linear combination of states and inputs, is the coil power P. The coil power is given by:

$$P = VI \qquad \textbf{(2.5.1.21)}$$

To summarize, the nonlinear and linear state and output equations of the actuator were derived in sevtion 2.5.1. The linear state equations can be utilized to derive the complex Laplace domain transfer functions of the actuator, i.e. the ratios of each of the outputs in equation 2.5.1.6, to the input voltage V. This will be done in section 2.5.2.

2.5.2 Complex Laplace-domain transfer functions of a Terfenol-D actuator

The complex Laplace (s)-domain *TF*'s of a Terfenol-D actuator are derived from the linear state space equations obtained in section 2.5.1. The ratio's of the outputs, i.e. the actuator output displacement x_a, coil current I, strain ε, field H and stress σ in the rod, the force F_r produced by the rod, the actuator output force F_a and and the acceleration $\ddot{x}_a$ of the mass, relative to the coil input voltage V, are given in fractional form. The numerators and denominators of the *TF*'s are expressed as polynomial functions of s. The polynomial coefficients of the numerators of all the outputs are given. An open-loop block diagram is included to show the coupling between the mechanical and electrical subsystems.

The transfer functions can be obtained from the state-space model by means of the following equation [Crawley & Hall, 1991]:

$$G(s) = C[sI - A]^{-1} B + D \qquad \textbf{(2.5.2.1)}$$

where $G(s)$ is the transfer function matrix, whose size equals the product of the number of inputs and number of outputs. The derivation of equation 2.5.2.1 is given in appendix A.

Any particular transfer function $G(s)$ can be written in fractional form as:

$$G(s) = \frac{P(s)}{Q(s)} \qquad \textbf{(2.5.2.2)}$$

where $P(s)$ and $Q(s)$ are the numerator and denominator of $G(s)$ respectively.

Equations 2.5.2.1 and 2.5.2.1 can be applied to obtain all the *TF*'s of the actuator, i.e. $X_a(s)/V(s)$, $I(s)/V(s)$, $\varepsilon(s)/V(s)$, $H(s)/V(s)$, $\sigma(s)/V(s)$, $F_r(s)/V(s)$, $F_a(s)/V(s)$ and $\ddot{X}_a(s)/V(s)$.

Two *TF*'s of special importance, which are required for modelling actuator dynamic behaviour and which can also be relatively easily determined experimentally, are $X_a(s)/V(s)$ and $\ddot{X}_a(s)/V(s)$.

$X_a(s)/V(s)$, for instance, is obtained as follows: Substitution of equations 2.1.1.20a and 2.5.1.20b, the first row of the C matrix in equation 2.5.1.20c and equation 2.5.1.20d, into equation 2.5.2.1, gives:

$$\frac{X_a(s)}{V(s)} = \frac{\dfrac{A_T E N d^H}{m_a G l_T L_0}}{s^3 + \left[2\zeta\omega_n + \dfrac{R_c}{L_0}\right]s^2 + \left[\omega_n^2 + \left(\dfrac{A_T EN}{Gl_T}\right)^2 \dfrac{d^\sigma d^H}{m_a L_0} + 2\zeta\omega_n \dfrac{R_c}{L_0}\right]s + \left[\dfrac{R_c}{L_0}\omega_n^2\right]} \tag{2.5.2.3}$$

Similar equations can be derived for the other *TF*'s. For the sake of convenience, the *TF*'s are written in the following general form:

$$G(s) = \frac{P(s)}{Q(s)} = \frac{p_2 s^2 + p_1 s + p_0}{s^3 + q_2 s^2 + q_1 s + q_0} \tag{2.5.2.4}$$

where the polynomial coefficients p_0 to p_2 of the numerator are determined by the particular output and the denominator polynomial coefficients q_0 to q_2 are the same for all the outputs.

The denominator polynomial coefficients q_0 to q_2 are given by:

$$q_0 = \frac{R_c}{L_0}\omega_n^2 \tag{2.5.2.5a}$$

$$q_1 = \omega_n^2 + \left(\frac{A_T EN}{Gl_T}\right)^2 \frac{d^\sigma d^H}{m_a L_0} + 2\zeta\omega_n \frac{R_c}{L_0} \tag{2.5.2.5b}$$

$$q_2 = 2\zeta\omega_n + \frac{R_c}{L_0} \tag{2.5.2.5c}$$

The numerator coefficients for the different outputs are given in table 2.5.2.1.

An open-loop block diagram of the actuator for a coil voltage input and displacement output is shown in figure 2.5.2.1. The block diagram also shows the coupling between the mechanical and electrical subsystems.

This concludes the derivation of the Laplace-domain transfer functions of the actuator. The frequency domain transfer functions will be derived from the Laplace domain transfer functions in section 2.5.3.

Table 2.5.2.1: Numerator polynomial coefficients for the *TF*'s of a Terfenol-D actuator

TF	p_0	p_1	p_2
$\frac{X_a(s)}{V(s)}$	$\frac{A_T ENd^H}{m_a Gl_T L_0}$	0	0
$\frac{I(s)}{V(s)}$	$\frac{\omega_n^2}{L_0}$	$\frac{2\zeta\omega_n}{L_0}$	$\frac{1}{L_0}$
$\frac{\varepsilon(s)}{V(s)}$	$\frac{A_T ENd^H}{m_a L_0 (Gl_T)^2}$	0	0
$\frac{H(s)}{V(s)}$	$\frac{N\omega_n^2}{l_T L_0}$	$\frac{2\zeta\omega_n N}{l_T L_0}$	$\frac{N}{l_T L_0}$
$\frac{\sigma(s)}{V(s)}$	0	0	$\frac{-ENd^H}{l_T L_0}$
$\frac{F_r(s)}{V(s)}$	0	0	$\frac{A_T ENd^H}{l_T L_0}$
$\frac{F_a(s)}{V(s)}$	0	0	$\frac{A_T ENd^H}{Gl_T L_0}$
$\frac{\ddot{X}_a(s)}{V(s)}$	0	0	$\frac{A_T ENd^H}{m_a Gl_T L_0}$

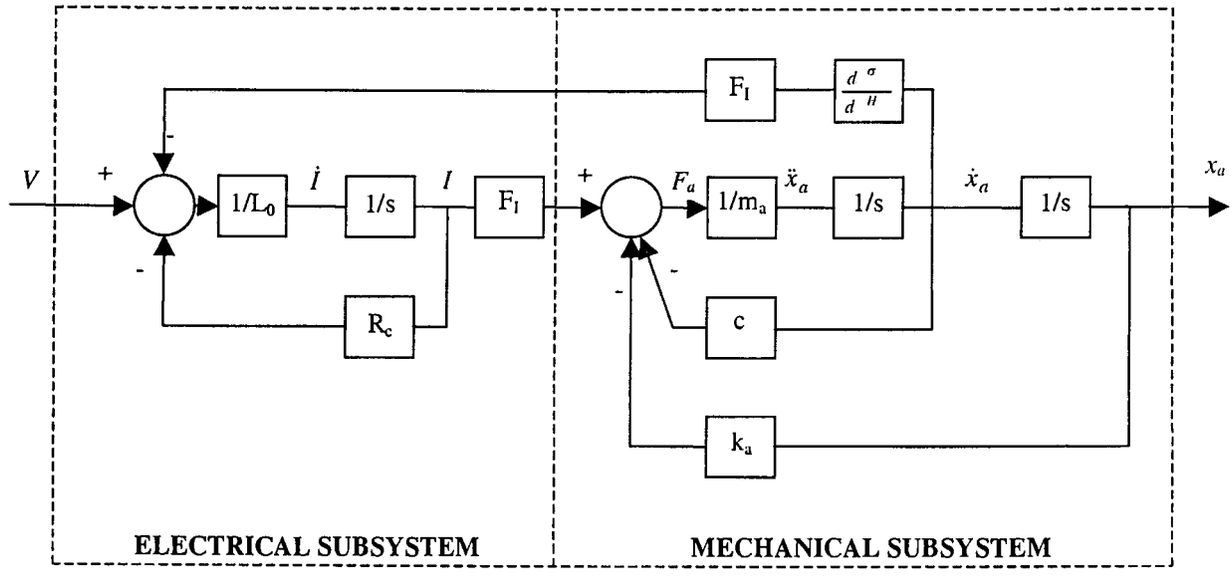

Figure 2.5.2.1: Block diagram of a Terfenol-D actuator

2.5.3 Actuator frequency domain transfer functions

In this section, the linear frequency *(ω)*-domain *TF*'s are obtained from the *s*-domain *TF*'s. Expressions for *ω*-domain *TF*'s are first written in a general complex form, after which the magnitude and phase angle will be expressed as real functions of frequency. It will be shown that all the *TF*'s can be written in the same complex form. The magnitude and phase angle of the actuator output displacement to coil voltage input ratio will be given as real functions of *ω*.

The frequency domain transfer function of the actuator is obtained from the Laplace-domain transfer function by setting $s \equiv j\omega$ in equation 2.5.2.2:

$$G(j\omega) = \frac{P(j\omega)}{Q(j\omega)} \tag{2.5.3.1}$$

where $j = \sqrt{-1}$ and $G(j\omega)$ is a complex function, which can be expressed as follows in terms of a magnitude $G_0(\omega)$ and phase angle $\varphi(\omega)$:

$$G(j\omega) = G_0(\omega) e^{j\varphi(\omega)} \tag{2.5.3.2}$$

The magnitude and phase angle are respectively given by the following real functions of ω:

$$G_0(\omega) = \sqrt{[\mathrm{Re}\{G(j\omega)\}]^2 + [\mathrm{Im}\{G(j\omega)\}]^2} \tag{2.5.3.3a}$$

$$\varphi(\omega) = \tan^{-1}\left[\frac{\mathrm{Im}\{G(j\omega)\}}{\mathrm{Re}\{G(j\omega)\}}\right] \tag{2.5.3.3b}$$

Re{ } and Im{ } are the real and imaginary parts of a complex function and $\tan^{-1}$ is the arctan function.

The general complex form of all the *TF*'s is obtained by substitution of $s \equiv j\omega$ into equation 2.5.2.4:

$$G(j\omega) = \frac{P(j\omega)}{Q(j\omega)} = \frac{(p_0 - p_2\omega^2) + j\omega p_1}{(q_0 - q_2\omega^2) + j\omega(q_1 - \omega^2)} \tag{2.5.3.4}$$

where p_0 to p_2 for the applicable *TF* are given in table 2.5.2.1 and q_0 to q_2 are given in equations 2.5.2.5a to 2.5.2.5c. The complex *TF* between the actuator output displacement and coil input voltage is given by:

$$G(j\omega) = \frac{p_0}{(q_0 - q_2\omega^2) + j\omega(q_1 - \omega^2)} \tag{2.5.3.5}$$

The magnitude and phase angle of the above *TF* are obtained in real form by substitution of equation 2.5.3.5 into equations 2.5.3.3a and 2.5.3.3b respectively:

$$G_0(\omega)=\sqrt{\frac{\left[p_0\left(q_0-q_2\omega^2\right)\right]^2+\left[\omega^3-q_1\omega\right]^2}{\left[q_0-q_2\omega^2\right]^2+\left[q_1-\omega^2\right]^2}} \qquad \textbf{(2.5.3.6a)}$$

$$\varphi(\omega)=\tan^{-1}\left[\frac{\omega^3-q_1\omega}{p_0\left(q_0-q_2\omega^2\right)}\right] \qquad \textbf{(2.5.3.6b)}$$

Equation 2.5.3.6a and 2.5.3.6b give the magnitude and phase angle of the ω-domain *TF* between the actuator output displacement and the coil input voltage. Similar equations can be derived for all the other *TF*'s.

To summarize section 2.5, the nonlinear and linear state and output equations of a Terfenol-D actuator were obtained from the equations of motion and the coil current equation. The linear complex Laplace-domain and frequency domain *TF*'s were also derived. The state-space equations and *TF*'s will be used in section 2.6 to analyze the natural vibration behaviour of the actuator, and in section 2.7 to simulate the forced linear and nonlinear behaviour of the actuator, in the time and frequency domains.

2.6 Natural vibration behaviour of a Terfenol-D actuator

This section describes the natural vibration behaviour of a Terfenol-D actuator. The importance of the analysis of the natural behaviour is mentioned. Two methods of obtaining the natural parameters are explained. The natural parameters are determined from the eigenvalues of the linear state-space model and from the poles of the *TF*'s. A closed form solution of the poles is given. It will be shown that two of the poles are complex conjugates and that the third pole is real. The effective angular natural frequency, damping factor and resistance to inductance ratio of the actuator coil are expressed in terms of the real and imaginary parts of the poles. A method of determining the stability of the poles is given.

It is essential to obtain the natural parameters of the actuator, for a number of reasons. In the first place, it will be important for the actuator designer to know what the maximum allowable load mass can be, before the natural frequency is lowered to such an extent that resonance will occur inside the disturbance band. If the natural frequency is too low, the isolation band of the actuator may not be wide enough to reject the disturbance. Secondly, the damping factor will significantly influence the displacement peak of the actuator at resonance: The higher the damping, the lower the peak. A third reason is that the dynamic displacement of the actuator will be 3 dB lower than the static displacement at a frequency corresponding to the resistance to inductance ratio (R_c/L_0) of the actuator coil. As is the case with the natural frequency, an R_c/L_0-value which exceeds the maximum frequency of the disturbance band, is preferable.

Furthermore, the natural parameters are required to analyze actuator stability. Stability solely depends on the sign of the real parts of the poles. If the real parts of all the poles are negative, the actuator is unconditionally stable. Lastly and most importantly, due to coupling between

the mechanical and electrical subsystems, which was described in more detail in section 2.5, the effective natural frequency, damping factor and resistance to inductance ratio of the coil will differ from those of the separate mechanical and electrical systems.

The natural parameters of the actuator can be determined by two methods, namely by means of the eigenvalues of the coefficient (A)-matrix of the state equations and by means of the poles of the TF, which are also the roots of the denominator $Q(s)$ of the TF. Both methods will be explained in short below. The eigenvalues of the A-matrix will be determined first, after which the poles of the TF will be obtained.

The linear state equation of the actuator, as given by equation 2.5.1.19a, is:

$$\dot{x} = Ax + Bu \tag{2.6.1}$$

where A is the coefficient matrix, x is the state vector, B is the driving matrix and u is the input vector. In the case of natural behaviour, the inputs are zero, therefore:

$$u = 0 \tag{2.6.2}$$

The state-space formulation of the natural behaviour of the actuator is obtained by substitution of equation 2.6.2 into equation 2.6.1:

$$\dot{x} = Ax \tag{2.6.3a}$$

or:

$$\dot{x} - Ax = 0 \tag{2.6.3b}$$

In order to obtain the eigenvalues, equation 2.6.3 must be transformed to the complex Laplace domain. The Laplace-domain equivalent of equation 2.6.3b is:

$$[sI - A]x = 0 \tag{2.6.4}$$

where s is the complex Laplace-domain differential operator and I is a unit matrix with the same size as A. The eigenvalues of A are obtained from equation 2.6.4 by setting the determinant of the $[sI - A]$ matrix equal to zero:

$$|sI - A| = 0 \tag{2.6.5}$$

The s-values for which equation 2.6.5 is valid, represents the eigenvalues. The number of eigenvalues equals the number of states.

Equation 2.6.5 provides a method of obtaining the natural parameters of the actuator by means of the state-space method. An alternative method which can be used, is to determine the poles of the transfer function. This method will be explained next.

The poles α are the roots of the denominator $Q(s)$ of the *TF*, or the values of s for which $Q(s)=0$:

$$\alpha = s\big|_{Q(s)=0} \tag{2.6.6}$$

where $Q(s)$ was given by equation 2.5.2.4 as:

$$Q(s) = s^3 + q_2 s^2 + q_1 s + q_0 \tag{2.6.7}$$

In equation 2.6.7, q_0 to q_2 are the polynomial coefficients of the denominator, which were given by equations 2.5.2.5a to 2.5.2.5c as:

$$q_0 = \frac{R_c}{L_0}\omega_n^2 \tag{2.6.8a}$$

$$q_1 = \omega_n^2 + \left(\frac{A_T EN}{Gl_T}\right)^2 \frac{d^\sigma d^H}{m_a L_0} + 2\zeta\omega_n \frac{R_c}{L_0} \tag{2.6.8b}$$

$$q_2 = 2\zeta\omega_n + \frac{R_c}{L_0} \tag{2.6.8c}$$

Either equation 2.6.5 or equation 2.6.6 can be used to obtain the natural parameters of the actuator, since the eigenvalues of A are equal to the roots of $Q(s)$.

The solutions of equations 2.6.5 and 2.6.6 can be mathematically obtained in closed form, or by means of numerical methods. A closed form solution for the roots α of a third order polynomial, such as in equation 2.6.7, is given by, inter alia, Spiegel [1968]. The poles of the actuator are:

$$\alpha_1 = -\frac{1}{2}(S+T) - \frac{1}{3}q_2 + \frac{1}{2}j\sqrt{3}(S-T) \tag{2.6.9a}$$

$$\alpha_2 = -\frac{1}{2}(S+T) - \frac{1}{3}q_2 - \frac{1}{2}j\sqrt{3}(S-T) \tag{2.6.9b}$$

$$\alpha_3 = S + T - \frac{1}{3}q_2 \tag{2.6.9c}$$

where S and T are given by:

$$S = \sqrt[3]{\frac{9q_1q_2 - 27q_0 - 2q_2^3}{54} + \sqrt{\left(\frac{3q_1 - q_2^2}{9}\right)^3 + \left(\frac{9q_1q_2 - 27q_0 - 2q_2^3}{54}\right)^2}} \tag{2.6.10a}$$

$$T = \sqrt[3]{\frac{9q_1q_2 - 27q_0 - 2q_2^3}{54} - \sqrt{\left(\frac{3q_1 - q_2^2}{9}\right)^3 + \left(\frac{9q_1q_2 - 27q_0 - 2q_2^3}{54}\right)^2}} \tag{2.6.10b}$$

Closer inspection of equations 2.6.9a to 2.6.9c indicates that the first two poles, i.e. α_1 and α_2, are complex conjugates, while α_3 is real.

A compact form of equations 2.6.9a to 2.6.9c is obtained by expressing the poles as follows in terms of the effective natural parameters, i.e. the effective damping factor, natural frequency and resistance to inductance ratio of the coil:

$$\alpha_1 = -\zeta_{eff}\omega_{neff} + j\omega_{neff}\sqrt{1-\zeta_{eff}^2} \tag{2.6.11a}$$

$$\alpha_1 = -\zeta_{eff}\omega_{neff} - j\omega_{neff}\sqrt{1-\zeta_{eff}^2} \tag{2.6.11b}$$

$$\alpha_3 = -\frac{R_c}{L_{0\,eff}} \tag{2.6.11c}$$

where ζ_{eff} is the effective damping factor, ω_{neff} is the effective angular natural frequency and $R_c/L_{0\,eff}$ is the effective resistance to inductance ratio.

The abovementioned natural parameters can be written in terms of the polynomial coefficients of the *TF* denominator by comparing the respective equations for the poles, as given by equations 2.6.9, with those given by equations 2.6.11:

$$\omega_{n\,eff} = \sqrt{S^2 - ST + T^2 + \frac{1}{3}(S+T)q_2 + \frac{1}{9}q_2^2} \tag{2.6.12a}$$

$$\zeta_{eff} = \frac{\frac{1}{2}(S+T) + \frac{1}{3}q_2}{\sqrt{S^2 - ST + T^2 + \frac{1}{3}(S+T)q_2 + \frac{1}{9}q_2^2}} \tag{2.6.12b}$$

$$\frac{R_c}{L_{0\,eff}} = -S - T + \frac{1}{3}q_2 \tag{2.6.12c}$$

where S and T were given by equations 2.6.10a and 2.6.10b.

The last purpose of the analysis of the natural behaviour is to determine the stability of the poles of the *TF*. As was mentioned before, this is done by investigating the sign of the real part of each pole. If the real part of each pole is negative, the actuator is unconditionally stable. If the real part of a pole is positive, that particular pole is unstable. If the real part of a pole is zero, the pole is marginally stable. It can be shown that the effective damping factor, angular natural frequency and resistance to inductance ratio of the actuator are positive, therefore, from equations 2.6.11, the real parts of all the poles are negative. It can be concluded that the linear behaviour of the actuator is unconditionally stable.

To summarize, the linear natural behaviour of a magnetostrictive actuator was analyzed in this section. Forced behaviour will be analyzed in the next section. Time and frequency domain simulations will be done to determine the output displacement, field, strain constant, Young's modulus, piezomagnetic cross-coupling constant and permeability for steady-state harmonic

and random coil input voltages. The state-space model and the frequency domain *TF*'s, which were respectively derived in sections 2.5.1 and 2.5.3, will be used to simulate the behaviour of the actuator.

2.7 Simulation of the characteristics and behaviour of a Terfenol-D actuator

In this section, the characteristics and behaviour of a magnetostrictive actuator are simulated. The results will be used in section 2.8 to calculate the linear LOS stabilization system parameters. Possible techniques for solving the nonlinear equations of motion and coil current equation are discussed and compared, and the most suitable technique is recommended. The solution technique is explained. Simulation and actuator input parameters are given. The simulations are carried out, after which the results are tabled, shown graphically and discussed.

2.7.1 Solution techniques for nonlinear equations of motion

A vast number of techniques exist for solving the equations of motion of nonlinear dynamic systems. These techniques can mainly be classified in two groups, i.e. time-domain techniques and frequency-domain techniques. In time-domain techniques, system parameters such as static (DC) output, rise-time, settling time, maximum displacement and maximum acceleration are obtained. If the system is written in state-space form, the states are also obtained.

In frequency-domain techniques, system parameters such as transfer functions (in magnitude and phase form), DC output, natural frequencies, anti-resonance frequencies and damping factors are obtained. For nonlinear systems, the transfer function dependence on input amplitude is also obtained.

Time-domain techniques include the method of slowly varying amplitude and phase, the perturbation method (also called the method of small parameters) and direct integration methods of the state equations. The latter are mainly the Euler method, Heun's method, 4^{th} and 5^{th} order Runge-Kutta methods, and predictor-corrector methods, such as the Adams-Bashforth and Adams-Moulton methods.

Frequency-domain techniques include, inter alia, the harmonic balance method and the Describing Function (DF) method. In the harmonic balance method, the output of the system to a harmonic input is obtained. Only the fundamental component of the output is retained and higher harmonics in the output are rejected. Using the DF method, the output can be calculated for higher harmonics, but at the cost of additional computational effort. The harmonic balance and DF methods can be considered equivalent if only the fundamental frequency component of the output is considered [Van Schoor, 1989].

Solution techniques considered in this study, are exact methods, the perturbation method, the method of slowly-varying amplitude and phase, statistical linearization, the DF method, Runge-Kutta methods and an iterative harmonic balance technique.

Exact methods

It is possible to obtain exact solutions for only a relatively few second order nonlinear equations of motion [Harris, 1988]. These methods are exact in the sense that the solution is given either in closed-form or in an expression that can be evaluated numerically to any desired degree of accuracy.

Exact solutions for forced vibration of nonlinear systems are virtually nonexistent [Harris, 1988], except if the system can be represented in a stepwise linear manner. Exact methods are discussed in more detail in appendix B.

The perturbation method and the method of slowly varying amplitude and phase

The perturbation method is based on the assumption that the equation of motion of a weakly nonlinear system can be written in the same form as that of a linear system, with an added term accounting for the nonlinearity. The time-domain solution is expressed as a linear series of time functions, whose coefficients are determined recursively. The perturbation method is described in short in appendix C.

The method of slowly varying amplitude and phase is based on the assumption that the solution of the equation of motion can be written as a harmonic function of time, whose amplitude and phase change with time. The method is described in short in appendix D.

Both the perturbation method and the method of slowly varying amplitude and phase can be used to solve the equations of motion of systems with weak nonlinearities. However, for systems with hard nonlinearities, such as Coulomb damping, hysteresis and dead-bands, the methods are, firstly, difficult to apply, and secondly, give highly inaccurate solutions. The behaviour of systems with hard nonlinearities is more easily analyzed with the statistical linearization-, harmonic balance- and DF methods.

The perturbation method and method of slowly varying amplitude and phase, are not easily applied to couple the equations of motion to the coil current equation. State methods, like the Runge-Kutta methods, are better suited for this purpose.

Statistical linearization

Three types of statistical methods for solving nonlinear equations of motion can be distinguished. These are the Fokker-Planck, perturbation and equivalent linearization methods [Atalik & Utku, 1976]. The perturbation method has already been discussed above. The Fokker-Planck method can be used to obtain exact solutions for white-noise inputs. Its disadvantage is that severe restrictions must be imposed on the nonlinearities and on the spectral density of the excitations.

Statistical linearization has a wide range of applicability for solving equations of motion of nonlinear systems under random excitation. The method is an extension of the method of slowly varying amplitude and phase. The method is discussed in appendix E.

The limitation of applying the method to the dynamic analysis of a magnetostrictive actuator, is that the strain characteristic of Terfenol-D is dependent on two variables, i.e. mechanical stress and magnetic field strength (see equation 2.2.1.2). This characteristic makes the statistical linearization method difficult to apply directly. The method can however be applied to obtain the natural frequency, damping factor and coil R_c/L_0 ratio if the time-domain solution of the actuator is known.

The Describing Function (DF) method

In a linear system, the output to a sinusoidal input is also sinusoidal. The output to input ratio is known as the transfer function (*TF*). For a spectrum of frequencies, the output to input ratio is known as the frequency response function (FRF). FRF's are often used for dynamic system modelling, simulation, characterization and control design purposes, because the *TF* at a particular frequency can be expressed in terms of two parameters only, i.e. a magnitude and a phase angle. Linear system analysis can therefore be simplified considerably using FRF's.

In a nonlinear system, the output to a sinusoidal input is non-sinusoidal. Generally, the output will contain more than one frequency component. A nonlinear system therefore cannot be characterized in terms of a transfer function, because its *TF* is undefined. However, if higher harmonics in the output can be neglected (albeit at the cost of accuracy) and only the fundamental component is retained, it is possible to express nonlinear system behaviour in terms of a *TF*. This *TF* is known in dynamics and control engineering as a Describing Function (DF).

In order to analyze a system in terms of its DF, the system must meet certain conditions [Slotine & Li, 1991]. The first is that the nonlinearity must be odd. If the nonlinearity is even, a DC shift will occur in the output. Secondly, the system must contain only one nonlinearity. If the system contains multiple nonlinearities, the nonlinearities must be lumped together, or only the dominant nonlinearity must be considered. Thirdly, the nonlinearity must be time-invariant. This condition is satisfied by a large variety of nonlinearities in practice, such as saturation, hysteresis, backlash and Coulomb friction.

The DF of any nonlinearity, which meets the above requirements, can be derived. A relatively simple method is given by Slotine & Li [1991]. The method is discussed in short in appendix F.

The DF method can also be extended to analyze nonlinear system behaviour to non-harmonic inputs, like two-sinusoid inputs, dual-inputs (e.g. DC plus sinusoid), transient and random inputs. *N* is tabled for a vast range of nonlinearities, for each of the above input types, by Gelb & Vander Velde [1968]. Examples of nonlinearities applicable to the analysis of Terfenol-D characteristics, are saturation and hysteresis. The DF's of these nonlinearities can be found in Gelb & Vander Velde [1968].

The main advantage of the DF method, is that it provides a frequency-domain linearization technique. System characteristics, such as input dependent natural frequency, damping factor and transfer functions, can be easily obtained.

Another advantage of the method is that it can be applied to describe the behaviour of a strongly nonlinear system in a relatively simple way. Hard nonlinearities, such as saturation, hysteresis, Coulomb damping, dead zones and backlash, are easily dealt with.

Depending on the cut-off and excitation frequencies of the system, the first-harmonic approach adopted by the DF method, can be highly accurate. This is particularly true of systems with low-pass filtering characteristics.

The DF method has a number of disadvantages. Firstly, systems which do not display low-pass filtering characteristics, are not necessarily accurately modelled by the DF technique. MDOF systems, for example, may require the inclusion of higher harmonics in the output series expansion for accurate modelling.

Secondly, nonlinearities depending on more than one system parameter, may be difficult to analyze. An example is Terfenol-D, whose strain depends on both field and stress (see equation 2.2.1.2). The problem is aggravated if the output contains a DC component. Terfenol-D, for example, requires a biasing (DC) field and stress to increase the saturation strain (see section 2.2.1).

Runge-Kutta (R-K) methods

In the R-K methods, the states and outputs are obtained in the time domain by direct integration of the state equations. The solution of each state equation is approximated by a polynomial. The order of the polynomial can vary from 1st order to 5th order and higher. The higher the order, the more accurate the solution for the same computational effort [Chapra & Canale, 1985]. For this reason, higher order methods are often preferred to lower order methods. The R-K methods are discussed in detail by Press et al [1992], Burden & Faires [1985], Chapra & Canale [1985], Gerald & Wheatley [1984] and Conte & de Boor [1972]. A 5th order method, also known as Butcher's method, is described mathematically in appendix G.

The advantages of the R-K methods are as follows: If time-domain solutions to nonlinear state equations are required, these methods are often used. The reasons for their popularity are high accuracy and simplicity of use. No prior knowledge of analytical solution methods to DE's is required to apply the R-K methods. All that is required, is relatively simple algebra.

Being state-space solution techniques, the R-K methods allow relatively easy coupling of other state equations to the equations of motion. In the analysis of a magnetostrictive actuator, coupling of the coil current equation to the equation of motion is required. The coil current equation (equation 2.5.1.9), was coupled to the equation of motion (equation 2.5.1.7) in section 2.5, resulting in the state equations 2.5.1.11 and 2.5.1.12.

For wide-band random and harmonic inputs, the R-K methods will give at least one output superharmonic for all frequencies up to half the Nyquist frequency. The lower the ratio between the excitation frequency and the sample frequency, the more superharmonics will be included.

The R-K methods are the only methods capable of describing the two-dimensional magnetostrictive and magnetization characteristics (i.e. stress and field-dependence) of

Terfenol-D in a relatively simple way. Stress and field are calculated using equations 2.4.10 and 2.4.4 respectively, after which the state equations (2.5.1.11 and 2.5.1.12) are solved as described in appendix G.

The R-K methods do also have a number of disadvantages. The first is that no insight into frequency-domain characteristics is provided. The transfer functions, natural frequency, damping factor and coil R_c/L_0 ratio cannot be directly obtained. However, if the time-domain solutions are transformed to the frequency domain, the linear characteristics can be "extracted" using data-fitting techniques. Unfortunately, this method is computationally expensive [Van Schoor, 1989].

For numerically stiff systems, the R-K methods can become numerically unstable if large time steps are used. The problem can be solved either by using smaller time steps, or by using adaptive time stepping. In the latter method, the time step is automatically adjusted according to the changing stiffness of the system. This technique in itself has another disadvantage, namely that the time-domain output will be unequally spaced. If the solution is transformed to the frequency-domain using the Fast Fourier Transform (FFT) technique, inaccurate amplitudes and phases will result. Data interpolation will be required to ensure equally spaced output data.

In the case of hysteretic systems, the state equations may contain discontinuous terms. During a simulation, the state derivative may jump from one level to another within a time-step, resulting in an inaccurate solution. The problem can be solved by adjusting the time increment in such a way that the jump occurs exactly at the end of the time step. This measure may however be clumsy to implement in a numerical solution procedure, since an additional conditional test must be implemented to check whether the jump has occurred.

Being time-domain techniques, the Runge-Kutta methods are initial value dependent. The methods may therefore be potentially dangerous to use if the system of equations is chaotic.

Iterative harmonic balance technique

In the iterative harmonic balance technique, a linear complex transfer function of the actuator is obtained, which takes account of the effects of hysteresis. The procedure is as follows: A number of discrete frequencies are defined in the excitation band. For each frequency, the field amplitude is obtained iteratively. A starting value of the field amplitude is assumed, which is used to calculate Youngs's modulus E, piezomagnetic cross-coupling constant d^{σ}, hysteresis strain constant d^{H}_{hyst}, hysteresis permeability μ^{σ}_{hyst} and equivalent damping coefficient c. The damping factor and R_c/L_0 ratio of the coil are then calculated. These parameters are substituted into the transfer function equations. The coil input voltage and voltage to field transfer function are used to calculate a new value of the field amplitude. The procedure is repeated until the field amplitude converges. The same procedure is applied to all the frequencies in the excitation band.

The iterative harmonic balance method explained above is in essence a DF technique. The advantages and disadvantages of the method are therefore the same as those of the DF method. An additional problem encountered with the harmonic balance method is that

convergence may be difficult to achieve at certain frequencies. At a notch frequency in the voltage amplitude to field *TF*, for instance, the field amplitude may be so low that the hysteresis strain constant and permeability can drop to zero. This will result in infinite values of certain *TF* numerator and polynomial coefficients.

2.7.2 Selection and description of a suitable solution technique for the actuator state equations

The advantages and disadvantages of the different nonlinear system solution techniques were discussed above. The most suitable technique is selected and described in this section. Methods not suitable for solving the state equations are eliminated.

Exact methods can be ruled out because they cannot be used to describe forced behaviour of the Terfenol-D actuator. The perturbation method is unsuitable because a high number of terms are required in the output to describe the discontinuous nature of hysteresis. The same applies to the method of slowly varying amplitude and phase, with the additional difficulty of coupling the coil current equation to the equation of motion.

The statistical linearization method can only be used if the time-domain behaviour of the actuator is known. The difficulty with the method is that the input voltage may contain a DC term to bias the field. Due to this DC offset, using the RMS values of μ^{σ}, E, d^{σ} and d^{H}, will result in inaccurate solutions to the state-space equations. However, fairly accurate results for dehysterized behaviour can be obtained if the average values of these variables, instead of the RMS values, are used.

The R-K methods are ideal for solving the state-space equations in the time-domain, because the dependence of both field and stress can be simultaneously addressed. The R-K methods can however not be considered to describe hysteresis behaviour, due to their inability to handle discontinuities.

The DF and harmonic balance methods can be considered if it can be shown that the magnetostrictive and magnetization parameters are dependent on field alone, instead of both field and stress. Fortunately, this proof can be obtained from the R-K solution.

The following procedure will be used to determine the actuator coil voltage to displacement *TF*. The time-domain solution for dehysterized behaviour will be obtained using the 5^{th} order R-K method. It will be shown that, for dehysterized behaviour, the average values of μ^{σ}, E, d^{σ} and d^{H} do not vary significantly with varying RMS values of input coil voltage. The frequency-domain solution to the state equations, with hysteresis taken into consideration, will be obtained using the iterative harmonic balance method. The *TF*'s for dehysterized behaviour will be compared with those including hysteresis effects. It will be shown that hysteresis has a significant effect on the magnitudes and phases of the *TF*'s.

Description of the iterative harmonic balance method

An algorithm for calculating the actuator parameters and *TF* using the iterative harmonic balance method is described stepwise as follows:

Step I: Specify the parameters of the actuator whose *TF* is required, i.e. mass m_a, displacement gain factor G, Terfenol-D rod length l_T, rod cross-sectional area A_T, coil resistance R_c, number of coil windings N, mechanical prestress σ_0 and coil input voltage amplitude V_A.

Step II: Define the desired frequency in the excitation band. For a wide-band spectrum, start with a low frequency, e.g. 0,01 Hz.

Step III: Estimate the field amplitude. For a starting value, use the following equation:

$$H_A = \frac{N}{l_T} I_A \qquad \textbf{(2.7.2.1)}$$

where H_A and I_A are the field and current amplitude respectively.

I_A is given by:

$$I_A = \frac{V_A}{R_c} \qquad \textbf{(2.7.2.2)}$$

where V_A is the coil input voltage amplitude and R_c is the coil resistance.

Step IV: Using H_A, calculate $\overline{E}$ and $\overline{d^{\sigma}}$ from equations 2.2.1.8a and 2.2.2.6a. Calculate d^{H}_{hyst} from equations 2.3.2 and 2.3.4. From equations 2.3.21 and 2.3.23, calculate μ^{σ}_{hyst}. Using equations 2.4.45 to 2.4.47, calculate L_f, cf and L_0. From equations 2.3.14 to 2.3.16, calculate η, k_a and c. Use equations 2.4.22 and 2.4.25 to calculate ω_n and ζ.

Step V: Substitute the above values of the dynamic parameters into the frequency domain transfer function equation 2.5.3.6a. The coil voltage to field *TF* numerator polynomial coefficients p_0 to p_2 are given in table 2.5.2.1, while the denominator coefficients q_0 to q_2 are given in equations 2.5.2.5a to 2.5.2.5c respectively. Calculate the field amplitude for the given coil voltage input amplitude.

Step VI: Use the new field amplitude and repeat steps IV and V until the field amplitude converges. Methods such as the secant and Newton-Raphson methods may be used to accelerate convergence.

Step VII: Calculate the coil voltage to displacement transfer function magnitude and phase using equations 2.5.3.6a and 2.5.3.6b, with the numerator polynomial coefficient p_0 given in table 2.5.2.1 and the denominator polynomial coefficients q_0 to q_2 given by equations 2.5.2.5a to 2.5.2.5c.

Step VIII: Return to step II and define a new frequency. Repeat steps III to VI until the field converges. Repeat step VII to obtain the *TF* magnitude and phase. Repeat steps I to VIII until the *TF*'s of all the desired frequencies in the excitation band have been solved.

2.7.3 Terfenol-D actuator simulation procedure and results

The simulation procedure and results of a Terfenol-D actuator are covered in this section. The simulations serve two purposes. In the first place, linear actuator characteristics are required to calculate the LOS system characteristics in section 2.8. In the second place, the results of the simulations will be used as inputs to the design of the actuators and LOS stabilization system in chapter 3.

The simulations are done in three steps. Firstly, nonlinear and linear simulations are carried out, using the 5^{th} order Runge-Kutta method, to obtain the dehysterized, nonlinear actuator characteristics. States and outputs are calculated for different coil input voltages. Transfer functions (*TF's*) between coil voltage and actuator displacement are obtained from the simulation results. The procedure and results are given in appendix H.

Secondly, average values of permeability, Young's modulus, piezomagnetic cross-coupling constant and strain constant are calculated from the nonlinear simulation results. These values are used to obtain the linear, dehysterized, characteristics. The characteristics are presented and discussed in appendix J.

Lastly, linear actuator characteristics, which include the effects of hysteresis, are calculated using the iterative harmonic balance technique. The RMS values of the inputs correspond with those of the time-domain simulations. The effects of hysteresis on field amplitude, permeability, strain constant and damping coefficient are calculated (see appendix K). The actuator characteristics are tabled. The actuator stiffness is calculated and the damping factor spectrum is shown graphically.

Actuator and simulation parameters

The actuator parameters required for simulation purposes are the concentrated mass, dimensionless displacement gain factor, Terfenol-D rod length, diameter and cross-sectional area, coil resistance, number of coil windings, coil bias voltage, bias field and bias stress. Mathematical equations, which describe the relationships between these parameters, were derived in section 2.4.

Time-domain simulation parameters are sample frequency, maximum time duration, minimum, maximum and RMS input voltages. Outputs are the actuator states (displacement, speed and coil current), stress and field, as well as the magnetostrictive and magnetization parameters, i.e. permeability, Young's modulus, piezomagnetic cross-coupling constant and strain constant. Nonlinear *TF* spectra are calculated from the input voltage and output displacement. Frequency-domain simulation outputs are field, permeability, strain constant and damping coefficient. Linear *TF* spectra are calculated using these outputs.

The actuator parameters are given in table 2.7.3.1. For the purpose of modelling the characteristics in this chapter, the parameters are fixed. A study will be done in chapter 3 to analyze the effects of varying parameters on actuator characteristics and to select the parameters in such a way as to meet the design criteria.

The sample frequency for time-domain simulations is 2,5 kHz. This frequency is 25 times the maximum frequency of the desired isolation band of the LOS stabilization system, i.e. 100 Hz. The reason for using such a high sample frequency is that the actuator mass is considerably lower than that of the entire system, resulting in a higher natural frequency. Maximum time duration is 40 s, in order to obtain statistically reliable data.

Table 2.7.3.1: Terfenol-D actuator parameters

Actuator parameter	Value
Actuator concentrated mass (m_a)	0,15 kg
Displacement gain factor (G)	5,4
Terfenol-D active rod length (l_T)	35 mm
Rod diameter (d)	6 mm
Rod cross-sectional area (A_T)	$2{,}827.10^{-5}$ m^2
Coil resistance (R_c)	3,2 Ω
Number of coil windings (N)	640
Coil input bias voltage (V_b)	8,75 V
Bias field (H_b)	50 kA/m
Mechanical bias stress (σ_b)	-12 MPa

Wide-band random (white noise) coil voltages are used as inputs for the time-domain simulations. In order to ensure positive field strengths, an input voltage with a minimum of zero and a maximum of 17,5 V (twice the bias voltage) is applied. The RMS value of this input (the full-scale input), is 2,18 V. In order to investigate the effects of nonlinearities, two additional inputs are applied, whose RMS values are 75% and 50% of the RMS value of the full-scale input, i.e. 1,63 V and 1,09 V. Harmonic inputs with the same RMS values as the random inputs are used for the frequency-domain simulations.

Actuator linear characteristics

A summary of the most important actuator characteristics, at 0,01 Hz and resonance, for a 2,18 V RMS input, is given in table 2.7.3.2.

The actuator linear stiffness, from equation 2.4.23, is given by:

$$k_a = \frac{A_T E}{G^2 l_T} \qquad \textbf{(2.7.3.1)}$$

Substitution of the applicable values in tables 2.7.3.1 and 2.7.3.2 into equation 2.7.3.1 gives the actuator stiffness as $6{,}5.10^5$ N/m.

Table 2.7.3.2: Actuator characteristics at 0,01 Hz and resonance for a 2,18 V RMS input

Parameter	0,01 Hz	Resonance (355 Hz)
Field amplitude H_A	17618 A/m	7946 A/m
Permeability μ^σ	$5{,}57.10^{-6}$ Tm/A	$3{,}63.10^{-6}$ Tm/A
Young's modulus E	23,46 GPa	23,46 GPa
Piezomagnetic cross-coupling constant d^σ	$1{,}088.10^{-8}$ m/A	$1{,}088.10^{-8}$ m/A
Strain constant d^H	$9{,}522.10^{-9}$ m/A	$6{,}338.10^{-9}$ m/A
Damping coefficient c	$1{,}31.10^{6}$ Ns/m	24,31 Ns/m
TF magnitude	10,2 μm/V	17,7 μm/V
TF phase	-0,1263 rad	-2,205 rad
Stroke length (17,5 V p-p)	178,5 μm	309,8 μm

The frequency spectrum of the damping coefficient, for a 2,18 V RMS input voltage, is shown in figure 2.7.3.1. The damping coefficient at 0,01 Hz is $1{,}31.10^{6}$ Ns/m. A sharp notch appears between 328 Hz and 332 Hz. At the latter frequency, the damping coefficient is 4,59 Ns/m. For a frequency range of 0,01 Hz to approximately 200 Hz, damping coefficient varies hyperbolically with frequency. In this range, the mathematical relationship between frequency and damping coefficient is:

$$c(f) = \frac{13076}{f} \qquad \textbf{(2.7.3.2)}$$

where f is frequency and c is damping coefficient.

The hyperbolic relationship between damping coefficient and frequency was discussed in section 2.3, where hysteresis models of Terfenol-D were derived (see also equation 2.3.15). On a logarithmic scale, the damping coefficient characteristic between 0,01 Hz and 200 Hz is a straight line, as shown in figure 2.7.3.1.

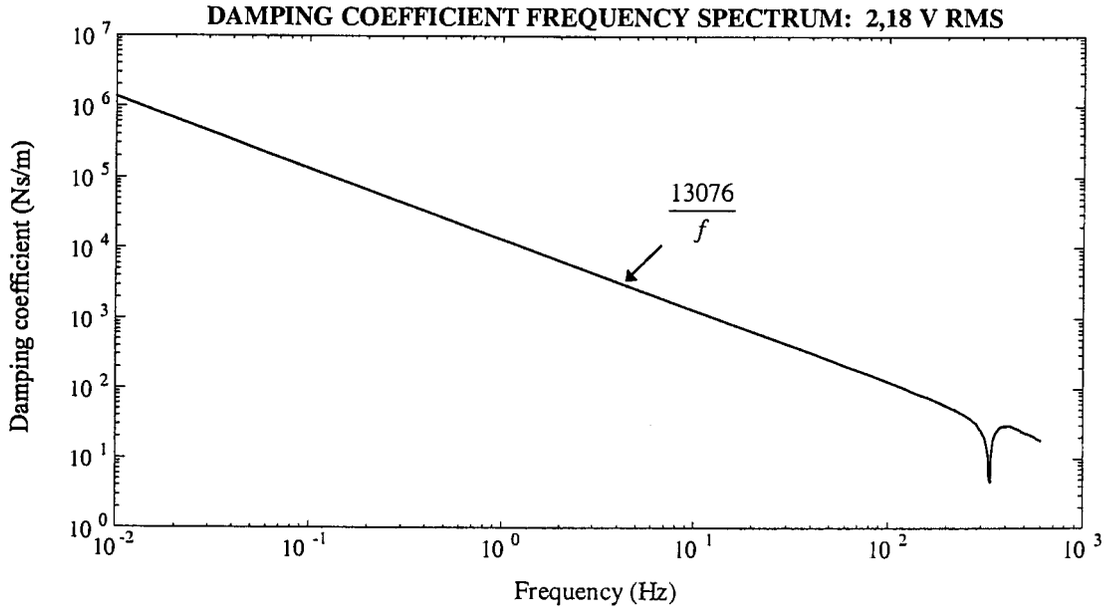

Figure 2.7.3.1: Damping coefficient frequency spectrum for a 2,18 V RMS input

The linear transfer functions, which include the effects of hysteresis, for 2,18 V, 1,63 V and 1,09 V RMS inputs, are shown in figure 2.7.3.2.

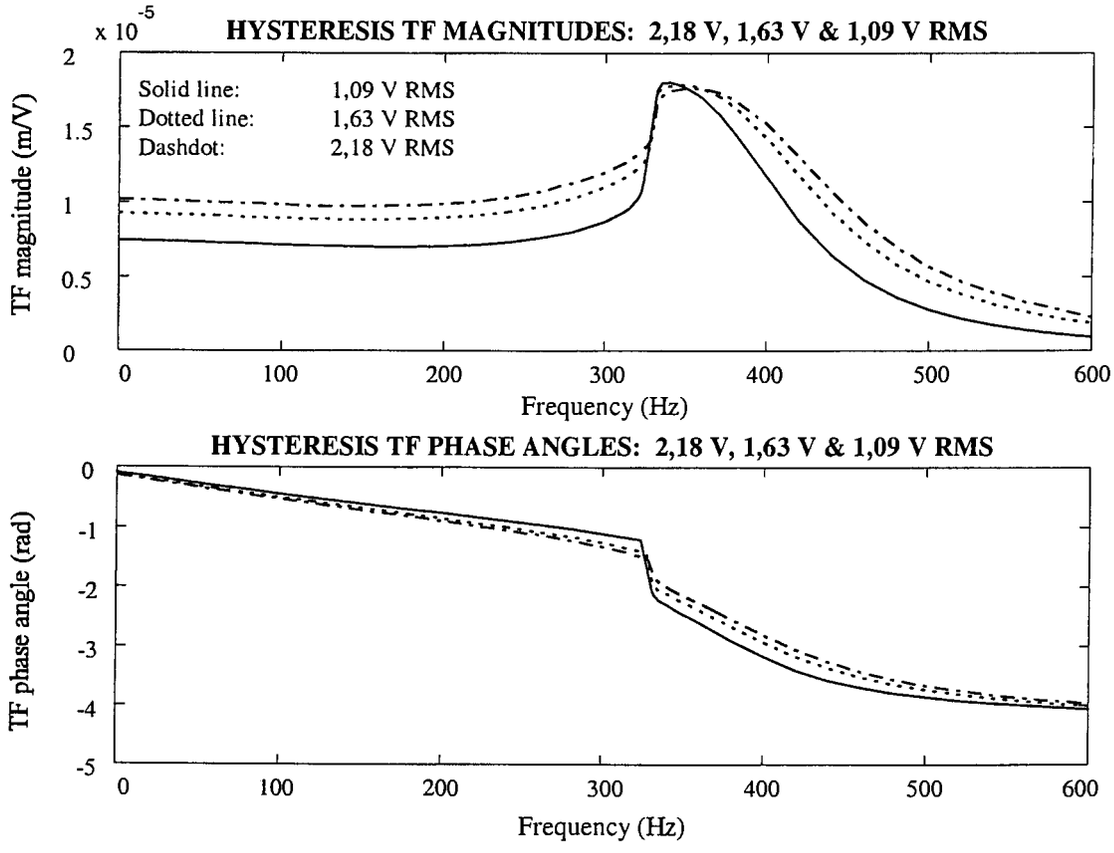

Figure 2.7.3.2: Actuator transfer functions for 2,18 V, 1,63 V and 1,09 V RMS inputs

It can be seen from figure 2.7.3.2 that input voltage magnitude has a significant effect on the characteristics of the Terfenol-D actuator. This can mainly be attributed to the effects of hysteresis. Furthermore, a typical softening characteristic is displayed.

To conclude section 2.7, the hysteresis damping model used in this section was derived from published quasi-static magnetostrictive and magnetization hysteresis loops, as given in section 2.3. These loops are currently the only source available for modelling damping.

High frequency effects on the hysteresis parameters are unknown at this stage. Experimentally measured damping may differ from modelled damping, as will its influence on measured dynamic characteristics. The latter will be experimentally determined in chapter 4, after which the dynamic parameters will be extracted form the test results, using linear identification techniques in chapter 5.

The next section, i.e. section 2.8, will be devoted to the analysis of the characteristics and behaviour of the LOS stabilization system, consisting of two Terfenol-D actuators, the optical instrument and the instrument support structure. The characteristics obtained in section 2.7.3 will be used to model the actuators and system.

2.8 Magnetostrictive LOS stabilization system model

The characteristics of the magnetostrictive LOS stabilization system are modelled in this section. The system consists of the two Terfenol-D actuators, the optical instrument and a support structure for the instrument. The model developed here forms a theoretical basis for open-loop system (plant), to be controlled in chapter 6, as well as to update system dynamic parameters in chapter 5.

A schematic layout of the system is shown and a mathematical model is developed. A beam model is used to analyze the characteristics of the instrument and support structure. Lumped mass, stiffness and damping models are used for the actuators. Actuator hysteresis is modelled using equivalent, linear viscous damping. The equation of motion is derived in modal coordinates.

A number of solution methods for the equation of motion, i.e. the exact separation of variables method, Galerkin, Finite Element (FE), Finite difference (FD) and Rayleigh-Ritz methods, are discussed and compared in short. The Rayleigh-Ritz method is selected as the most suitable solution technique and discussed in detail. Assumed mode shapes are selected and coupled mass, stiffness and damping matrices are obtained using energy methods. An eigenvalue analysis is carried out to obtain the normal mode shapes and natural frequencies.

The equation of motion, in modal form, is coupled to the coil current equation. Transfer functions between the coil input voltages and outputs, i.e. the vertical displacements at the sensor locations and the LOS angle of the system, are derived using state-space techniques. The magnitudes and phases of the frequency-domain transfer functions are shown graphically.

2.8.1 System layout and mathematical model

A schematic layout of the LOS stabilization system is shown in figure 2.8.1.1. The two actuators are mounted at the ends of the structure, between the base and structure. The actuator mass, stiffness, damping coefficient and force are respectively given by m_a, k_a, c_a and F_a. The actuators are soft in the vertical translational direction, but are relatively rigid in the rotational (pitching) direction. In order to allow angular motion of the instrument, the support structure is provided with flexures between the instrument and actuator attachment points.

The optical instrument material is steel. In the interest of saving mass, aluminium is used for the support structure. Aluminium spacers and an aluminium stiffener are provided to prevent bending of the instrument during excitation.

For the purpose of this study, a clamped-clamped beam with actuated supports is used to model the system characteristics and behaviour. Strictly speaking, two beams, each with its own material properties (flexural rigidity and mass per unit length), should be used to separately model the instrument and structure. However, to simplify the model, the assumption is made that the instrument and structure have a common neutral axis. This makes it possible to express the material properties of the individual components in terms of that of a single beam. Due to the presence of notches, spacers and a stiffener, the geometric properties of the beam vary along its length. The beam model is shown in figure 2.8.1.2.

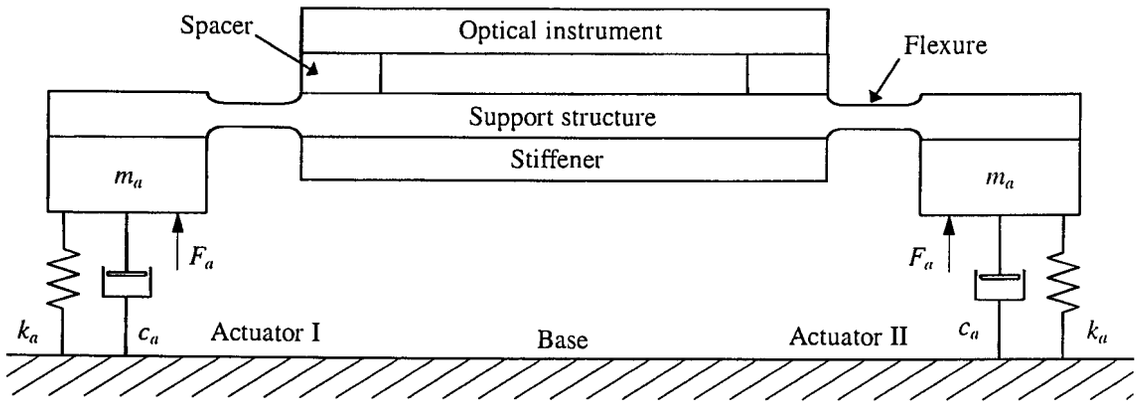

Figure 2.8.1.1: Schematic system layout

The length of the beam is l. The concentrated mass, stiffness, damping coefficient and force of actuator I are given by m_{a1}, k_{a1}, c_{a1} and F_{a1}, while those of actuator II are given by m_{a2}, k_{a2}, c_{a2} and F_{a2}. The output displacements of the two actuators are given by y_{a1} and y_{a2}.

The structural properties of the beam, i.e. density, cross-sectional area, Young's modulus and second moment of area, are respectively given by ρ_s, A_s, E_s and I_s. The properties vary with x, the distance from the left support. The LOS angle of the instrument is given by θ.

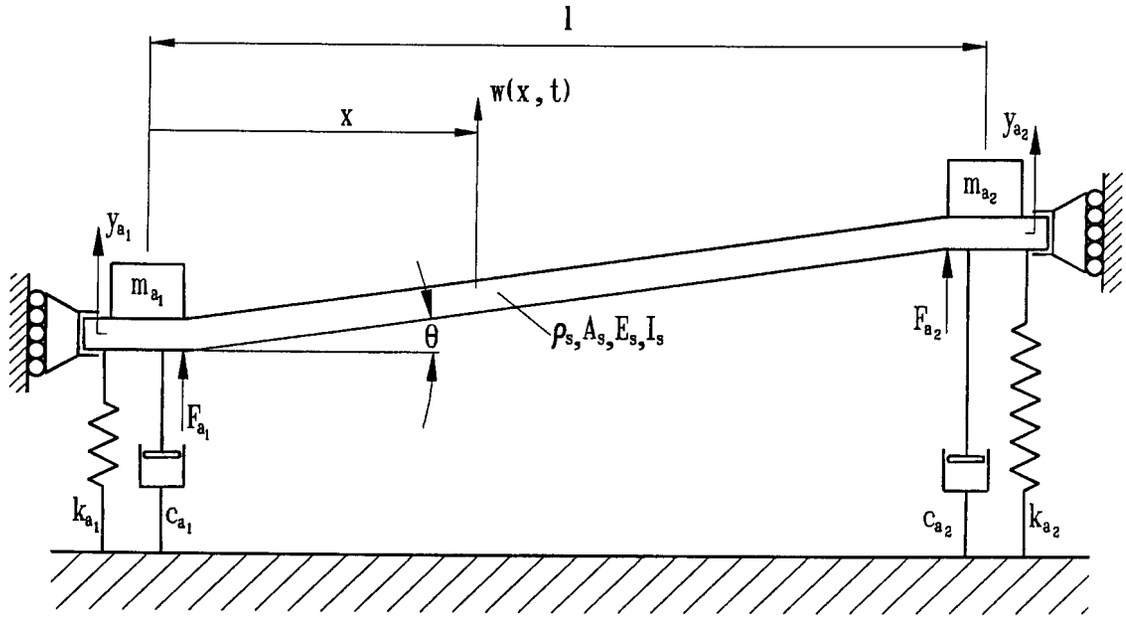

Figure 2.8.1.2: Beam model of optical instrument and support structure

The vertical, or transverse, displacement w at any point x and time t is:

$$w = w(x,t) \qquad \textbf{(2.8.1.1)}$$

The linear equation of motion of the beam is:

$$m\ddot{w} + c\dot{w} + kw = F \tag{2.8.1.2}$$

where m, c and k respectively represent the mass, damping coefficient and stiffness of the beam and the dot indicates differentiation with respect to t.

F is the excitation force at any point x and time t:

$$F = F(x,t) \tag{2.8.1.3}$$

For forces acting at the actuator attachment points only, i.e. at $x = 0$ and $x = l$, F in equation 2.8.1.3 can be written as:

$$F = \delta(0)F_{a1}(t) + \delta(l)F_{a2}(t) \tag{2.8.1.4}$$

where δ is the Dirac delta function, the value of which is one at the actuator attachment points, and zero between the actuators.

For beams with zero damping, the equation of motion is obtained by substitution of $c = 0$ into equation 2.8.1.2:

$$m\ddot{w} + kw = F \tag{2.8.1.5}$$

The equation of motion for an undamped beam, in terms of the material and geometric properties, is

$$\underbrace{\frac{\partial^2}{\partial t^2}(\rho_s A_s w)}_{mass\ \ term} + \underbrace{\frac{\partial^2}{\partial x^2}\left(E_s I_s \frac{\partial^2 w}{\partial x^2}\right)}_{stiffness\ \ term} = P \tag{2.8.1.6}$$

where ρ_s and E_s respectively represent the density and Young's modulus of the beam material at a point x on the beam:

$$E_s = E_s(x) \tag{2.8.1.7a}$$
$$\rho_s = \rho_s(x) \tag{2.8.1.7b}$$

A_s and I_s respectively represent the second moment of inertia and cross-sectional area of the beam at x:

$$I_s = I_s(x) \tag{2.8.1.8a}$$
$$A_s = A_s(x) \tag{2.8.1.8b}$$

The term $\rho_s A_s$ in equation 2.8.1.6 is the mass per unit length of the beam, while $E_s I_s$ is the flexural rigidity. P is the force per unit length, or distributed load acting on the structure at any point x and time t:

$$P = P(x,t) \tag{2.8.1.9}$$

P is the partial derivative of F with respect to x:

$$P = \frac{\partial F}{\partial x} \tag{2.8.1.10}$$

The equation describing static beam behaviour is obtained by omitting the inertia term in equation 2.8.1.6:

$$\frac{\partial^2}{\partial x^2}\left(E_s I_s \frac{\partial^2 w}{\partial x^2}\right) = P \tag{2.8.1.11}$$

For natural behaviour of the beam, the loading vector P in equation 2.8.1.6 is zero, in which case the equation of motion is

$$\underbrace{\frac{\partial^2}{\partial t^2}(\rho_s A_s w)}_{mass\ \ term} + \underbrace{\frac{\partial^2}{\partial x^2}\left(E_s I_s \frac{\partial^2 w}{\partial x^2}\right)}_{stiffness\ \ term} = 0 \tag{2.8.1.12}$$

Equations 2.8.1.6 and 2.8.1.12 must be solved to determine the forced and natural behaviour of the system. Possible solution methods are discussed in section 2.8.2, after which the most suitable method is selected and described in section 2.8.3.

2.8.2 Solution methods for beam equations of motion

The available methods of solving beam transverse equations of motion can broadly be divided into two groups, namely analytical methods and numerical methods [Rao, 1989]. A diagram, which classifies the methods of analysis, from Rao [1989], is shown in figure 2.8.2.1.

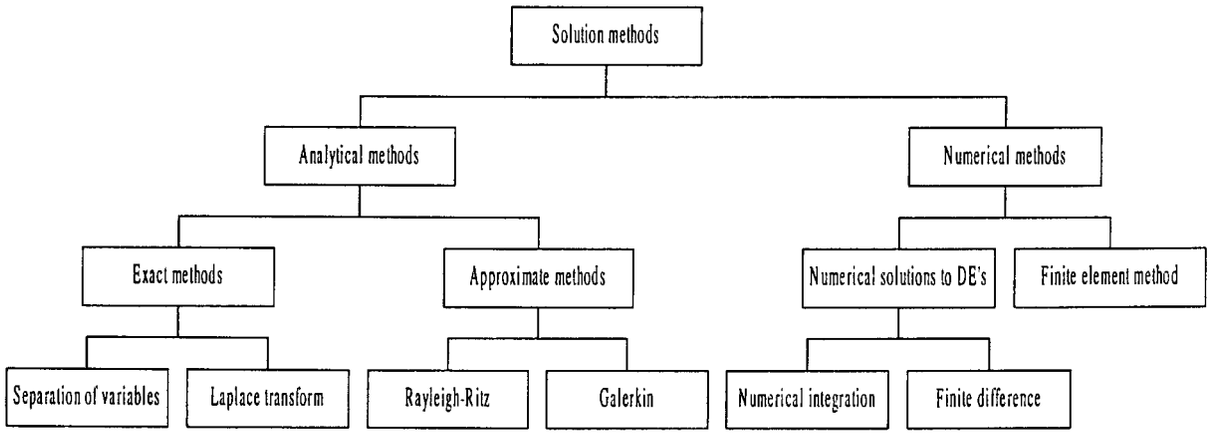

Figure 2.8.2.1: Solution methods for beam transverse equations of motion

Analytical methods include exact and approximate methods. Exact methods are, inter alia, the Laplace transform method and the separation of variables method, while the Rayleigh-Ritz and

Galerkin methods are approximate analytical methods. Two types of numerical methods exist, such as numerical solution of the equation of motion and the Finite Element Method (FEM). Two methods can be used to obtain numerical solutions of the equation of motion, i.e. numerical integration and the Finite Difference (FD) method.

A number of the methods, i.e. the exact separation of variables, Finite Difference, Finite Element, Galerkin and Rayleigh-Ritz methods are summarized by Rao [1989]. A short summary of the most important methods is given in the next few paragraphs.

Exact separation of variables method

The separation of variables method entails the separation of time and spatial variables in continuous systems such as beams, plates, shafts and rods, thereby simplifying system analysis. Parameters such as displacement, speed, acceleration, shear force and bending moment are written as products of separated spatial and time functions. The spatial functions for displacement, for instance, are typically the normal, or uncoupled, mode shapes, while the time functions are the modal amplitudes. In lateral beam vibrations, the normal mode shapes are one-dimensional functions of the spatial parameter x, while the amplitudes are functions of the time parameter t.

Consider equation 2.8.1.6. For constant E_s, I_s, ρ_s and A_s, the beam equation of motion is:

$$\underbrace{\rho_s A_s \frac{\partial^2 w}{\partial t^2}}_{\text{mass term}} + \underbrace{E_s I_s \frac{\partial^4 w}{\partial x^4}}_{\text{stiffness term}} = P \qquad \textbf{(2.8.2.1)}$$

Using separation of variables, the exact solution to equation 2.8.2.1 is expressed as:

$$w(x,t) = \sum_{i=1}^{\infty} \phi_i(x) q_i(t) \qquad \textbf{(2.8.2.2)}$$

where $\phi_i(x)$ is the i-th normal mode shape of the beam at a position x on the beam and $q_i(t)$ is the i-th modal amplitude at time t. The i-th normal mode shape is given by (see appendix L):

$$\phi_i(x) = A_i \cos \beta_i x + B_i \sin \beta_i x + C_i \cosh \beta_i x + D_i \sinh \beta_i x \qquad \textbf{(2.8.2.3)}$$

where A_i, B_i, C_i and D_i are constants determined by the boundary values and β_i is the i-th eigenvalue, given by:

$$\beta_i = \left(\frac{\rho_s A_s}{E_s I_s} \omega_i^2 \right)^{\frac{1}{4}} \qquad \textbf{(2.8.2.4)}$$

The values of β_i depend on the beam supports. Tabulated values of β_i for different beam support configurations, such as cantilever, simply-supported, clamped-clamped and clamped-free beams, are given by Harris [1988], Thomson [1993] and Tse et al [1978]. In most of these references, only the first four to six eigenvalues are given.

The advantage of the separation of variables method is its simplicity of use in continuous systems with constant material and geometric properties. The method is well-established in vibration theory and therefore forms the theoretical basis of most vibration analysis methods for continuous systems. The method allows the separation of spatial and time variables, thereby reducing the degree of mathematical complication. A single normal mode can for instance be analyzed in isolation of all the other modes. Furthermore, system displacement is simply obtained by adding the individual modal displacements.

However, for systems with varying material and geometric properties, application of the method becomes complicated. Secondly, the behaviour of an infinite number of modes may be difficult to describe mathematically. Thirdly, while relatively simple solutions exist for input forces such as impulse, step, ramp and steady-state harmonic functions, this may not be the case for wide-band random excitation. Alternative methods, such as the Rayleigh-Ritz, Galerkin, FD and FE methods must therefore be considered. These methods are described in short below.

The Rayleigh-Ritz method

The Rayleigh-Ritz method is an approximate method, which makes use of a finite number of assumed modes, to describe continuous system behaviour. The assumed mode shapes are combined linearly to form the normal mode shapes. The assumed mode shapes are selected in such a way as to satisfy all the boundary values of the problem. For the clamped-clamped beam with actuated supports, as used in this study, beam end displacements are equal to the actuator output displacements, while the beam end slopes are zero.

The stiffness, damping and inertia matrices of the assumed modes are calculated using energy methods. An eigenvalue problem is solved to determine the eigenvectors and eigenvalues. The normal mode shapes are the products of the assumed mode shapes and the eigenvectors.

The use of a finite number of modes implies that the resulting eigenvalues and normal mode shapes will not be exact. Generally, the higher the number of assumed modes, the more accurate the approximation will be, and vice versa. A practical rule is that, if n number of natural frequencies is required with an acceptable degree of accuracy, $2n$ number of assumed modes must be used [Clough & Penzien, 1982].

The advantages of the method are firstly that system behaviour can be expressed in terms of a finite number of modes. Secondly, material and geometrical properties need not be uniform. Thirdly, the relative contribution of each assumed mode to the normal modes can be obtained from the eigenvectors.

However, the method is not easily applied to systems with a large number of discontinuities, such as stepped beams. This type of system is more easily analyzed using the finite element method. The analysis of discontinuous structures using the Rayleigh-Ritz method, may require the division of the beam into piecewise continuous substructures. The displacement of each substructure is expressed in terms of its own modes, known as component modes. The displacement, slope, bending moment and shear force of each component must match those of its neighbouring components at the boundaries. This method is known as the component mode synthesis method, or substructure synthesis method. More detail about the method is

provided by Béliveau & Souci [1985], Benfield & Hruda [1971], Craig & Bampton [1968], Hintz [1975], Klein & Dowell [1974], Kubomura [1982], Kubomura [1987], Meirovitch [1990], Rubin [1975] and Thomson [1993].

The Galerkin method

Similar to the Rayleigh-Ritz method, a finite number of assumed modes are used which satisfy the boundary values of the beam. Due to the limited number of assumed modes, an error, or residual term, results in the equation of motion. The error is minimized by integrating the product of each mode shape and the residual term over the length of the beam and setting the result equal to zero. For n number of assumed modes, an n x n coefficient matrix is obtained in terms of the eigenvalues. The latter are calculated by setting the determinant of the coefficient matrix equal to zero. The resulting modes are orthogonal and modal superposition can be applied. The Galerkin method is described in more detail by Rao [1989].

The difference between the Rayleigh-Ritz and Galerkin methods is that the Galerkin method is a weighted residual method, while the Rayleigh-Ritz method is an energy method. The latter is fundamentally a better approach, therefore the Rayleigh-Ritz method is preferred to the Galerkin method for the purpose of this study.

The Finite Difference method

Contrary to the Rayleigh-Ritz and Galerkin methods, the FD method does not make use of assumed mode shapes to model continuous system behaviour. In the FD method, the stiffness and mass are defined at m number of discrete nodes along the beam. The partial derivatives of w with respect to x and t, in equation 2.8.2.1, are obtained by numerical differentiation. The central difference method is normally used for differentiation of w with respect to x. Boundary values are taken into account by adding discrete points left of actuator I and right of actuator II. The partial derivatives of w with respect to t can be obtained by either the forward difference method or the backward difference method.

The advantages of the method are that a finite number of nodes and time steps can be used to describe beam behaviour, thereby simplifying the problem. The disadvantages are firstly that the size of the eigenvalue problem is m, which can be large if a large number of nodes are used. Reducing m to decrease the size of the problem, can result in highly inaccurate eigenvalues. Secondly, while the method is relatively easily applied to solve the equation of motion of a uniform beam (equation 2.8.2.1), analyzing the behaviour of non-uniform beams, as described by equations 2.8.1.6 to 2.8.1.8, may be highly complicated.

The FD method is not as often used in vibration analyses as the Rayleigh-Ritz method and the FE method. An application of the FD method is the analysis of nonlinear, coupled three-dimensional fluid vibrations in tanks of arbitrary geometry [Van Schoor, 1989]. Application of the FD method to the analysis of vibrations in one-dimensional continuous systems, e.g. transverse vibrations in beams, is explained in more detail by Rao [1989]. Mathematical theory of the FD method is provided by Burden & Faires [1985], Chapra & Canale [1985], Conte & de Boor [1972] and Gerald & Wheatley [1984].

The Finite Element Method (FEM)

In the finite element method, the beam is divided into a finite, or discrete number of elements along the length of the beam. Four cubic displacement shape functions are written for each element. The shape functions are expressed in terms of the translational and rotational degrees-of-freedom (DOF's) at the element ends. The element mass (m_e) and stiffness (k_e) matrices are calculated using energy methods. The sizes of m_e and k_e are 4 x 4 each. The loading vector F for each shape function is obtained by integrating the product of the distributed loading vector and the shape function over its length, resulting in a 4 x 1 element loading vector. The FEM is in essence a Rayleigh-Ritz method applied to a beam element.

The m_e and k_e matrices of all the elements are assembled in order to obtain mass and stiffness matrices for the entire beam. This is done by prescribing equal element displacements at interfaces between neighbouring elements. Known DOF's of the beam are eliminated. In this study, the known DOF's are the beam end slopes, which are zero. Once the beam mass and stiffness matrices are known, an eigenvalue analysis is carried out to determine the normal mode shapes and natural frequencies.

The advantage of using FEM to solve a beam equation of motion is that the mass and stiffness matrices are sparse, thereby facilitating the eigenvalue analysis. Secondly, no prior knowledge is required to select the assumed modes. Thirdly, for a beam with a large number of discontinuities and varying material properties, FEM is easily applied to determine the natural and forced behaviour. A further advantage is that the same element shape functions can be used for all beam vibration problems. Contrary to the Rayleigh-Ritz method, a new set of shape functions is not required to solve a new problem.

A disadvantage of the FE method is that the size of the eigenvalue problem increases quadratically with the number of elements. Normally, for high accuracy, a large number of elements are required. The main disadvantage, however, is that no physical insight is provided by the method, since an element shape function does not give a global picture of what the normal mode shapes will eventually look like. The Rayleigh-Ritz method has a clear advantage in this regard, since the solution is defined in terms of the (global) assumed modes, which are used to calculate the normal modes. If the assumed mode shapes are carefully selected, only a small number of modes are required, resulting in a small eigenvalue problem.

Selection of the Rayleigh-Ritz method

In this section, the different methods discussed above are compared and the inapplicable methods are eliminated. The Rayleigh-Ritz method is selected as the most appropriate method to solve the beam equations of motion.

The exact method is extremely difficult to apply to the analysis of beams with varying geometry, and can therefore be eliminated. The Galerkin method, being a weighted residual method, is fundamentally not as good as the Rayleigh-Ritz method, which is an energy method. The Rayleigh-Ritz method is therefore preferred to the Galerkin method for this application. The disadvantage of the FD method is that a large number of nodes are required for a beam with varying geometry, resulting in a large eigenvalue problem. The FE method has the same disadvantage, i.e. a large eigenvalue problem for a beam with varying geometry.

The FE method is mainly ruled out because it fails to give physically interpretable normal mode shapes in terms of element shape functions.

Irrespective of its disadvantages, the Rayleigh-Ritz method is the most appropriate method for solving the equation of motion of the LOS stabilization system. Using physical insight, the assumed mode shapes can be carefully selected to satisfy the boundary values and to deal with discontinuities. The Rayleigh-Ritz method is discussed in detail in section 2.8.3.

2.8.3 Detailed discussion of the Rayleigh-Ritz method

The undamped equation of motion for natural behaviour of the beam shown in figure 2.8.1.2 is:

$$m\ddot{w}(x,t)+kw(x,t)=0 \qquad \textbf{(2.8.3.1)}$$

The displacement $w(x,t)$ is determined by the superposition of n number of normal, uncoupled modes:

$$w(x,t)=\sum_{i=1}^{n}\phi_i(x)q_i(t) \qquad \textbf{(2.8.3.2)}$$

where $\phi_i(x)$ is the i-th normal mode shape of the beam at a position x, $q_i(t)$ is the i-th modal amplitude at time t and n is the number of modes.

Equation 2.8.3.2 is written concisely in matrix form as:

$$w=\Phi q \qquad \textbf{(2.8.3.3)}$$

where Φ is the 1 x n row vector of normal mode shapes:

$$\Phi=\begin{Bmatrix}\phi_1(x) & \phi_2(x) & \cdots & \phi_i(x) & \phi_j(x) & \cdots & \phi_n(x)\end{Bmatrix} \qquad \textbf{(2.8.3.4)}$$

and q is the n x 1 column vector of normal mode amplitudes:

$$q=\begin{Bmatrix}q_1(t) & q_2(t) & \cdots & q_i(t) & q_j(t) & \cdots & q_n(t)\end{Bmatrix}^T \qquad \textbf{(2.8.3.5)}$$

The normal mode shapes $\phi_i(x)$ are currently unknown. In order to obtain the solution to equation 2.8.3.1, n number of assumed modes shapes $\psi_i(x)$ are chosen which satisfy the boundary conditions of the beam. The assumed mode shape vector Ψ is given by:

$$\Psi=\begin{Bmatrix}\psi_1(x) & \psi_2(x) & \cdots & \psi_i(x) & \psi_j(x) & \cdots & \psi_n(x)\end{Bmatrix} \qquad \textbf{(2.8.3.6)}$$

The size of Ψ is the same as that of Φ, i.e. 1 x n.

The boundary conditions of the beam shown in figure 2.8.1.2 are the same as those of a clamped-clamped beam with moving supports. For this type of beam, the boundary values are as follows: Beam displacement at x = 0 is equal to the output displacement of the left

The boundary conditions of the beam shown in figure 2.8.1.2 are the same as those of a clamped-clamped beam with moving supports. For this type of beam, the boundary values are as follows: Beam displacement at $x = 0$ is equal to the output displacement of the left actuator, while beam displacement at $x = l$ is equal to the output displacement of the right actuator. The slopes of the beam at both ends are zero.

Mathematically, these boundary conditions can be expressed as:

$$w(x_{a1},t) = y_{a1} \qquad \textbf{(2.8.3.7a)}$$
$$w(x_{a2},t) = y_{a2} \qquad \textbf{(2.8.3.7b)}$$
$$w'(0,t) = 0 \qquad \textbf{(2.8.3.7c)}$$
$$w'(l,t) = 0 \qquad \textbf{(2.8.3.7d)}$$

where x_{a1} and x_{a2} are the attachment points of the two actuators and y_{a1} and y_{a2} are the actuator output displacements. For actuators attached at the beam ends, equations 2.8.3.7a to 2.8.3.7d become:

$$w(0,t) = y_{a1} \qquad \textbf{(2.8.3.8a)}$$
$$w(l,t) = y_{a2} \qquad \textbf{(2.8.3.8b)}$$
$$w'(0,t) = 0 \qquad \textbf{(2.8.3.8c)}$$
$$w'(l,t) = 0 \qquad \textbf{(2.8.3.8d)}$$

Assumed mode shapes which satisfy the boundary conditions of the beam under discussion, are:

$$\psi_i(x) = \cos\left(\frac{i\pi x}{l}\right) \qquad \textbf{(2.8.3.9)}$$

The advantages of using the above mode shapes is that they are infinitely differentiable and easy to generate. The disadvantage is that an extremely high number of modes (larger than 100) are required to accurately describe flexure bending. The reason is that the flexures are situated close to the beam ends (see figure 2.8.1.1).

An alternative set of assumed modes, which describe flexure bending with a limited number of modes, can be used. The modes include five symmetric bending modes and four asymmetric bending modes, as well as a purely translational rigid body mode. The symmetric and asymmetric bending mode shapes are shown in figures 2.8.3.1 and 2.8.3.2 respectively. The disadvantage of using these mode shapes is that differentiation with respect to x, to obtain inflections, may be tedious, especially if polynomials are used to generate the mode shapes.

Note from figure 2.8.3.2, that two of the asymmetric mode shapes are almost identical. The two mode shapes differ only in the flexure, where quadratic bending is used for the one mode and quartic bending for the other. Both these modes are rigid between the flexures.

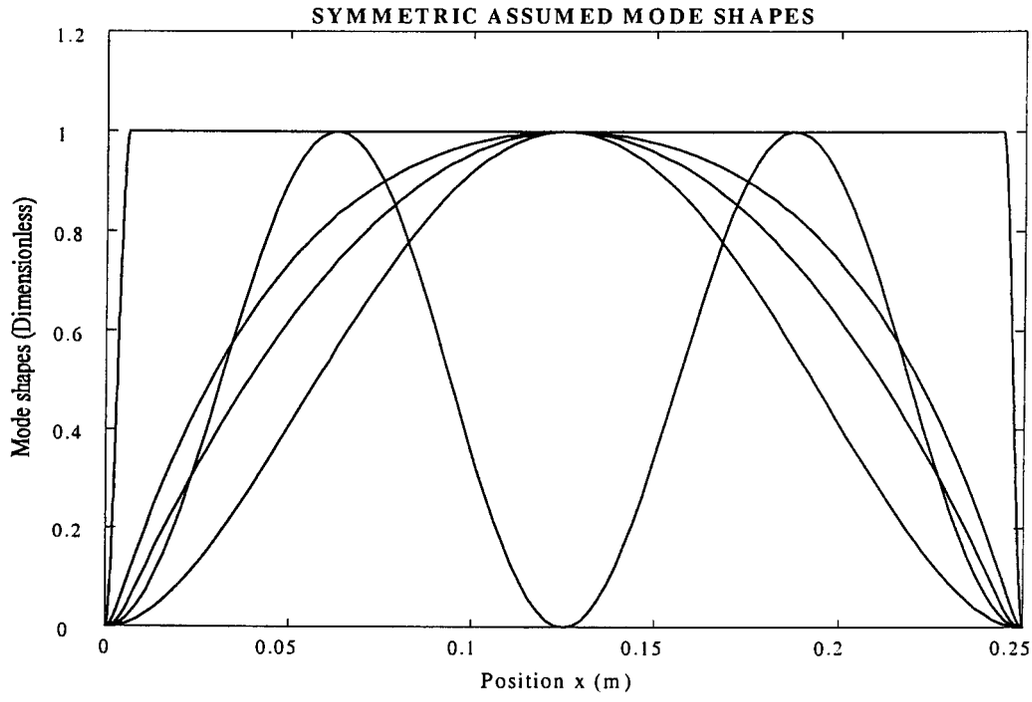

Figure 2.8.3.1: Symmetric assumed mode shapes for beam model

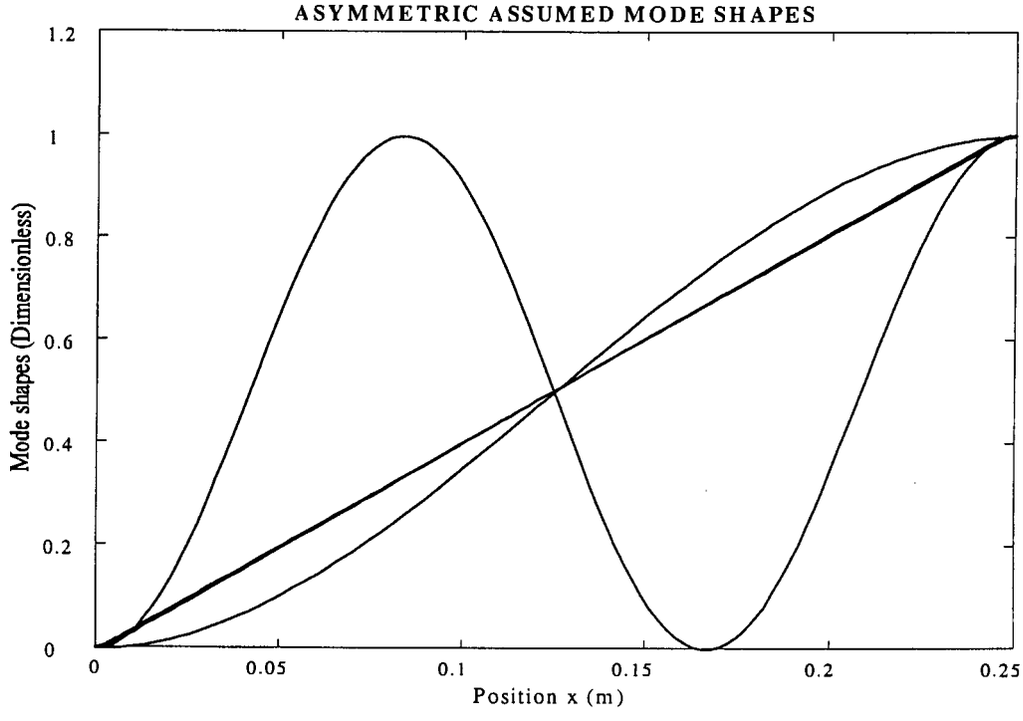

Figure 2.8.3.2: Asymmetric assumed mode shapes for beam model

The modal distributed mass and stiffness matrices of the beam, for the assumed modes, are:

$$M_b = \int_{x=0}^{x=l} \rho_s(x) A_s(x) \psi_i(x) \psi_j(x) dx \qquad \textbf{(2.8.3.10a)}$$

$$K_b = \int_{x=0}^{x=l} E_s(x) I_s(x) \psi_i''(x) \psi_j''(x) dx \qquad \textbf{(2.8.3.10b)}$$

where ψ_i and ψ_j are the i-th and j-th assumed mode shapes respectively and the prime denotes partial differentiation with respect to x.

M_b is the distributed mass matrix and K_b is the distributed stiffness matrix.

If the assumed mode shapes ψ are equal to the normal mode shapes ϕ, M_b and K_b will be diagonal matrices and the modes will be uncoupled. Generally, assumed modes of a beam with varying geometric and material properties will be coupled, therefore M_b and K_b will not be diagonal. If all the elements of the stiffness matrix are non-zero, the beam is said to be statically, or elastically coupled. If all the elements of the mass matrix are non-zero, the beam is dynamically, or inertia coupled.

An imbalance mass is usually required to bring about both static and dynamic coupling. In practice, static and dynamic coupling is obtained if the stiffnesses of the two actuators differ slightly and if a sensor is placed close to one actuator.

The concentrated masses and stiffnesses of the actuators can be included in the model. The contribution of the actuators to the modal mass and stiffness matrices is:

$$M_a = \Psi^T(x_a) m_a \Psi(x_a) \qquad \textbf{(2.8.3.11a)}$$

$$K_a = \Psi^T(x_a) k_a \Psi(x_a) \qquad \textbf{(2.8.3.11b)}$$

where m_a and k_a are the actuator masses and stiffnesses respectively and $\Psi(x_a)$ is the assumed mode vector at the actuator attachment points x_a.

The modal mass matrix is the sum of the distributed mass and the concentrated mass, while the modal stiffness matrix is the sum of the distributed stiffness and the concentrated stiffness:

$$M = M_b + M_a \qquad \textbf{(2.8.3.12a)}$$

$$K = K_b + K_a \qquad \textbf{(2.8.3.12b)}$$

The natural frequencies and normal mode shapes of the beam are determined by solving the following eigenvalue equation:

$$(K - M\Omega^2)U = 0 \qquad \textbf{(2.8.3.13)}$$

where Ω^2 is a diagonal matrix containing the eigenvalues and U is a square matrix containing the eigenvectors. The eigenvalues are the values of Ω^2 for which

$$\left|K - M\Omega^2\right| = 0 \qquad \textbf{(2.8.3.14)}$$

The natural frequency f_i of the i-th normal mode is:

$$f_i = \frac{1}{2\pi}\Omega_{ii} \qquad \textbf{(2.8.3.15)}$$

where Ω_{ii} is the i-th diagonal element of the matrix Ω containing the natural frequencies of the beam.

The normal mode shapes are the product of the assumed mode shape vector and U:

$$\Phi = \Psi U \qquad \textbf{(2.8.3.16)}$$

The mode shapes obtained by means of equation 2.8.3.16 are real.

The uncoupled, normal mode mass and stiffness matrices are:

$$M^* = U^T M U \qquad \textbf{(2.8.3.17a)}$$
$$K^* = U^T K U \qquad \textbf{(2.8.3.17b)}$$

The equation of motion of the beam, in terms of the uncoupled, normal coordinates $\{q\}$, are:

$$M^*\ddot{q} + K^* q = 0 \qquad \textbf{(2.8.3.18)}$$

Equation 2.8.3.18 gives the undamped beam equation of motion. The equation of motion of a damped beam is also required, because the two Terfenol-D actuators, which serve as beam supports, are hysteretically damped (see section 2.7). Hysteresis damping can be modelled by means of equivalent viscous damping (see section 2.3). The inclusion of viscous damping in the Rayleigh-Ritz model is discussed in the next section, after which hysteresis damping is expressed in terms of equivalent viscous damping.

Inclusion of viscous damping in the Rayleigh-Ritz model of the beam

The equation of motion for natural behaviour of a viscous damped beam, in normal coordinates, is:

$$M^*\ddot{q} + C^*\dot{q} + K^* q = 0 \qquad \textbf{(2.8.3.19)}$$

where C^* is the uncoupled damping matrix, given by:

$$C^* = \int_{x=0}^{x=l} c(x)\phi_i(x)\phi_j(x)dx \qquad \textbf{(2.8.3.20)}$$

C^* is also known as the orthogonal, classical, modal or proportional damping matrix [Craig, 1981].

For uncoupled damped modes, it is required that C^* be a diagonal matrix. To make this possible, the normal mode shapes must simultaneously uncouple the mass, stiffness and damping matrices. Uncoupling of the mass and stiffness matrices was achieved by solving the

undamped eigenvalue problem as given in equation 2.8.3.13. The mode shapes thus obtained do however not give a diagonal damping matrix. If the undamped mode shapes are substituted into equation 2.8.3.20, C^* will contain non-zero, off-diagonal terms, resulting in coupled mode shapes.

A diagonal C^* matrix can be obtained in a number of ways. The first is to use Rayleigh damping, which is a particular form of proportional damping. In Rayleigh damping, the damping matrix C is directly proportional to both the coupled mass and stiffness matrices:

$$C = \alpha M + \beta K \tag{2.8.3.21}$$

where M and K are respectively given by equations 2.8.3.10a and 2.8.3.10b. C is the coupled damping matrix, given by:

$$C = \int_{x=0}^{x=l} c(x)\psi_i(x)\psi_j(x)dx \tag{2.8.3.22}$$

α and β are determined from known damping factors of the first two normal mode shapes. The damping factors of the higher modes are then expressed in terms of α and β. Rayleigh damping is described in more detail by Craig [1981].

The advantage of using Rayleigh-damping is that a diagonal damping matrix is easily obtained. The disadvantage is that the uncoupled modal damping factors must be known in advance. In this chapter, the uncoupled damping matrix is unknown and must be derived from actuator damping parameters.

The second method gives proportional damping with specified damping factors for a given number of modes [Craig, 1981]. The damping matrix C, from Craig [1981], is:

$$C = \left(M\Phi M^{*-1}\right)C^*\left(M^{*-1}\Phi^T M\right) \tag{2.8.3.23}$$

Determining the damping matrix using equation 2.8.3.23 is even simpler than using Rayleigh damping, if the uncoupled modal damping matrix C^* is known in advance. However, as with Rayleigh-damping, C^* is unknown for the beam vibration problem under discussion.

The third, and preferred method, is to write equation 2.8.3.19 in state variable form and to obtain the eigenvalues of the coefficient matrix, which contain the uncoupled damping factors. The assumption made here is that damping does not change the undamped normal mode shapes. This assumption is only acceptable for low damping, which gives an insignificant shift in natural frequency (for example, a damping factor of 10% lowers the natural frequency by as little as 0,5%).

The state variable form of equation 2.8.3.19 is:

$$\begin{Bmatrix} \dot{q} \\ \ddot{q} \end{Bmatrix} = -\begin{bmatrix} M^* & 0 \\ C^* & M^* \end{bmatrix}^{-1}\begin{bmatrix} 0 & -M^* \\ K^* & 0 \end{bmatrix}\begin{Bmatrix} q \\ \dot{q} \end{Bmatrix} \tag{2.8.3.24}$$

where M^*, K^* and C^* are respectively given by equations 2.8.3.17a, 2.8.3.17b and 2.8.3.20. In equation 2.8.3.24, M^* and K^* are diagonal, but C^* is not.

The eigenvalues are determined by solving the $2n$ x $2n$ eigenvalue problem:

$$|sI - A| = 0 \tag{2.8.3.25}$$

where A is the coefficient matrix given by:

$$A = \begin{bmatrix} M^* & 0 \\ C^* & M^* \end{bmatrix}^{-1} \begin{bmatrix} 0 & -M^* \\ K^* & 0 \end{bmatrix} \tag{2.8.3.26}$$

The i-th eigenvalue s_i is given by:

$$s_i = -\alpha_i \pm j\Omega_{di} \tag{2.8.3.27}$$

where α_i is the real part of the i-th eigenvalue and Ω_{di} is the imaginary part, which is the i-th damped natural frequency:

$$\alpha_i = \zeta_i \Omega_{ii} \tag{2.8.3.28a}$$

$$\Omega_{di} = \Omega_{ii}\left(1 - \zeta_i^2\right)^{\frac{1}{2}} \tag{2.8.3.28b}$$

The i-th modal damping factor ζ_i is

$$\zeta_i = \frac{\alpha_i}{\left(\alpha_i^2 + \Omega_{di}^2\right)^{\frac{1}{2}}} \tag{2.8.3.29}$$

The i-th diagonal element of the uncoupled C^* matrix is given by:

$$C_{ii}^* = 2\zeta_i M_{ii}^* \Omega_{ii} \tag{2.8.3.30}$$

The procedure described above gives the normal, uncoupled viscous damping matrix. The matrix can also be derived for a beam excited by actuators with hysteresis damping. This is done in short in the following section.

Rayleigh-Ritz model of beam excited by actuators with hysteresis damping

It was shown in section 2.7 that the Terfenol-D actuators display hysteresis damping. These hysteresis effects must be included in the model, since the transfer function between the coil input voltages and the LOS angle of the optical instrument are damping-dependent. The most convenient way of including hysteresis in the model is to derive a diagonal, linear viscous damping matrix for the beam, the elements of which are the natural mode damping coefficients.

The assumption made here is that all the damping in the system is provided by the actuators. Since material and joint damping in the beam are unknown in the modelling stage, these effects will be excluded here. In chapter 4, the transfer functions of the system will be measured,

after which the damping factors, including all the damping effects, will be extracted in chapter 5.

Recall from equation 2.3.15 that the relationship between the actuator viscous damping coefficient c_a, stiffness k_a, dimensionless loss factor η_a and frequency ω is:

$$c_a = \frac{k_a \eta_a}{\omega} \tag{2.8.3.31}$$

Rewriting equation 2.8.3.31 gives:

$$\omega c_a = k_a \eta_a \tag{2.8.3.32}$$

where ωc_a is the dynamic dissipative stiffness of the actuator. For hysteresis damping, the term $k_a \eta_a$ is constant for all frequencies, since c_a varies hyperbolically with frequency (see also figure 2.3.7).

The modal dissipative stiffness of the beam, in terms of that of the actuators, is given by:

$$\Omega C^* = \Phi^T(x_a) k_a \eta_a \Phi(x_a) \tag{2.8.3.33}$$

where C^* is the coupled n x n modal matrix and Ω is a diagonal matrix containing the undamped angular natural frequencies of the beam. $\Phi(x_a)$ is the undamped normal mode vector at the actuator attachment points.

In order to uncouple the damping matrix, the equation of motion 2.8.3.19 is first premultiplied by Ω:

$$\Omega M^* \ddot{q} + \Omega C^* \dot{q} + \Omega K^* q = 0 \tag{2.8.3.34}$$

Equation 2.8.3.34 is subsequently written in state-variable form as:

$$\begin{Bmatrix} \dot{q} \\ \ddot{q} \end{Bmatrix} = -\begin{bmatrix} \Omega M^* & 0 \\ \Omega C^* & \Omega M^* \end{bmatrix}^{-1} \begin{bmatrix} 0 & -\Omega M^* \\ \Omega K^* & 0 \end{bmatrix} \begin{Bmatrix} q \\ \dot{q} \end{Bmatrix} \tag{2.8.3.35}$$

where ΩC^* is given by equation 2.8.3.33.

The eigenvalues of the beam are the values of s for which:

$$|sI - A| = 0 \tag{2.8.3.36}$$

where A is the coefficient matrix:

$$A = \begin{bmatrix} \Omega M^* & 0 \\ \Omega C^* & M^* \end{bmatrix}^{-1} \begin{bmatrix} 0 & -\Omega M^* \\ \Omega K^* & 0 \end{bmatrix} \tag{2.8.3.37}$$

From the eigenvalues, the uncoupled damping coefficients can be obtained using the procedure set out in equations 2.8.3.27 to 2.8.3.30.

The Rayleigh-Ritz model developed in section 2.8.3 will be used in section 2.8.4 to obtain the natural frequencies and normal mode shapes of the system.

2.8.4 Natural frequencies, normal mode shapes and modal damping factors

The natural frequencies, normal mode shapes and modal damping factors of the system are calculated in this section. The actuator parameters are given, together with the beam mass per unit length and flexural rigidity. The first ten natural frequencies are calculated and tabled and the first four normal mode shapes are shown. The mode shapes and natural frequencies are discussed. Modal damping factors and coefficients for the first three natural frequencies are calculated.

The Terfenol-D actuator parameters, from section 2.7.3, are given in table 2.8.4.1. The mass per unit length and structural rigidity of the optical instrument, support structure and stiffener are shown in figures 2.8.4.1 and 2.8.4.2 respectively.

Table 2.8.4.1: Terfenol-D actuator parameters

Parameter	Symbol	Value
Concentrated mass	m_a	0,15 kg
Stiffness	k_a	$6{,}5.10^5$ N/m
Dynamic dissipative stiffness	$k_a\eta_a$	13076.2π N/m

It can be seen from figure 2.8.4.2 that the flexural rigidity between the instrument attachment points is approximately 10^6 times of that in the middle of the flexures. It can therefore be expected that the natural frequencies, where flexure bending dominates, will be considerably lower than those where bending between the flexures dominates.

The coupled mass and stiffness matrices are calculated from equations 2.8.3.10 to 2.8.3.12. The assumed modes are as given in section 2.8.3. Only dynamic coupling is considered. The eigenvalue problem, as given in equation 2.8.3.13, is solved for Ω and U. The undamped natural frequencies and normal mode shapes are calculated from equations 2.8.3.15 and 2.8.3.16 respectively. The calculated natural frequencies for the first ten normal modes are given in Table 2.8.4.2.

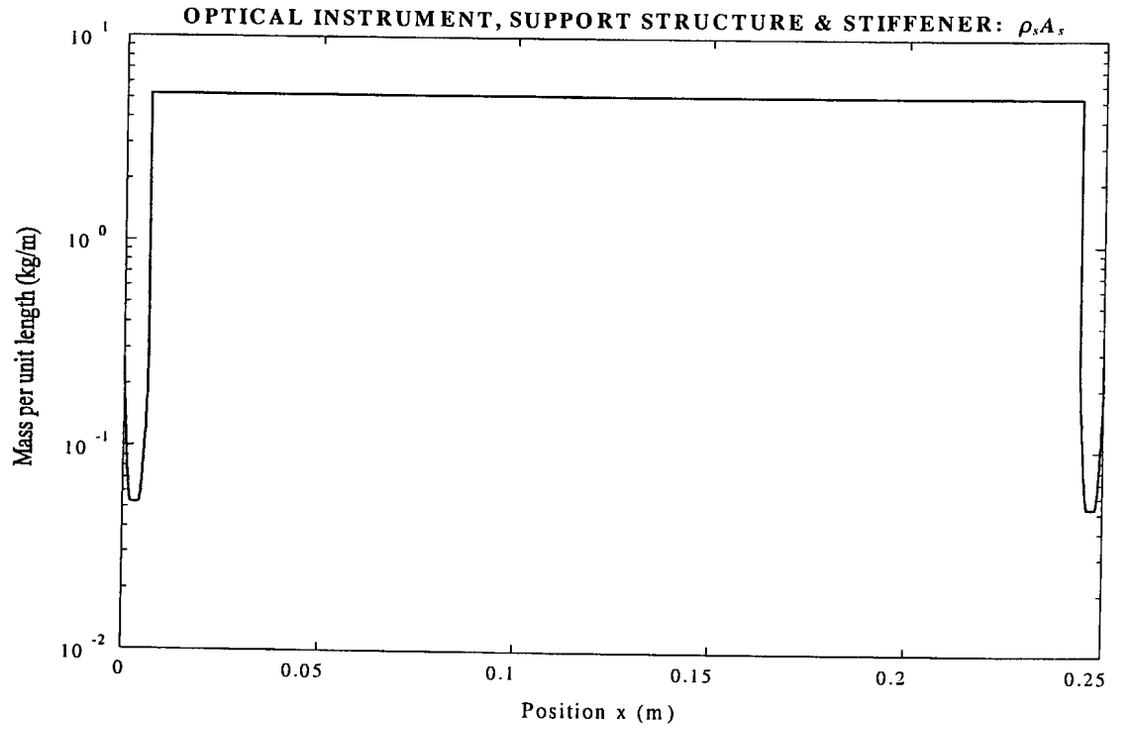

Figure 2.8.4.1: **Mass per unit length of optical instrument, support structure and stiffener**

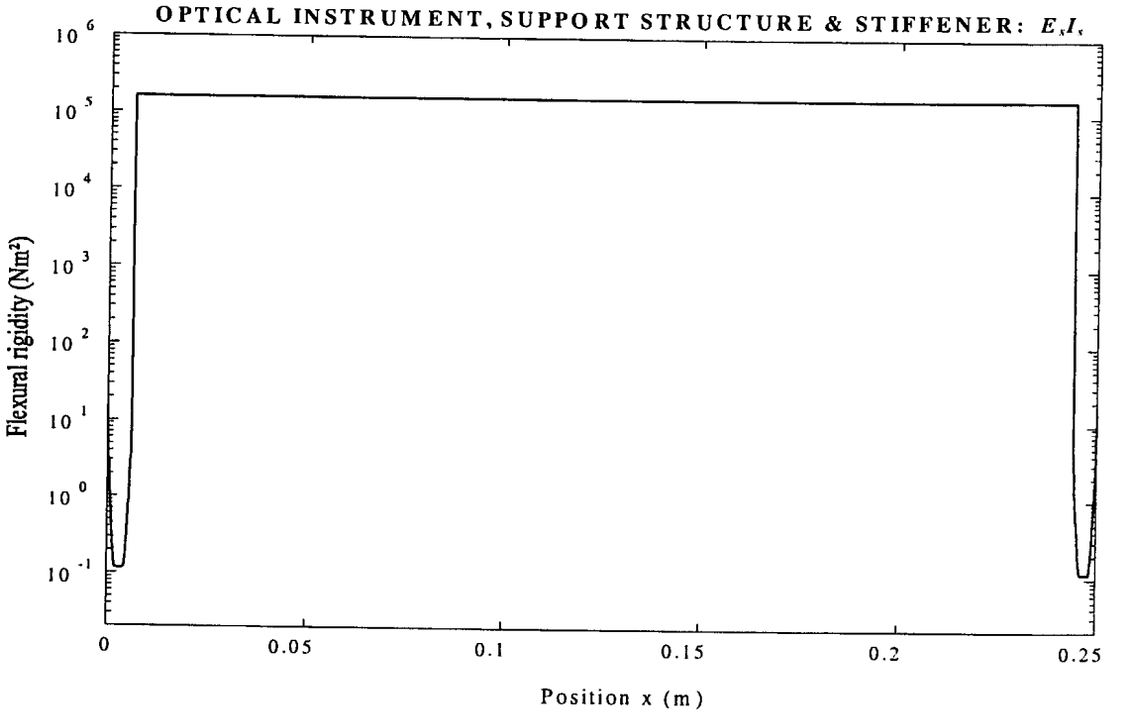

Figure 2.8.4.2: **Flexural rigidity of optical instrument, support structure and stiffener**

Table 2.8.4.2: Natural frequencies for first ten normal modes

Mode number	Natural frequency (Hz)
1	145,81
2	218,97
3	4 625,2
4	6 266,3
5	12 242
6	30 847
7	59 881
8	156 860
9	259 300
10	710 430

Modal stiffness and mass are calculated from equations 2.8.3.17a and 2.8.3.17b. Modal dissipative stiffness is calculated from equation 2.8.3.33. The state coefficient matrix, as given by equation 2.8.3.37, is calculated and the eigenvalue problem in equation 2.8.3.36 is solved. Modal damping factors and coefficients are calculated from equations 2.8.3.29 and 2.8.3.30. The normal mode mass, stiffness and damping matrices, for the first three normal modes, are given below, while the damping factors are shown in table 2.8.4.3.

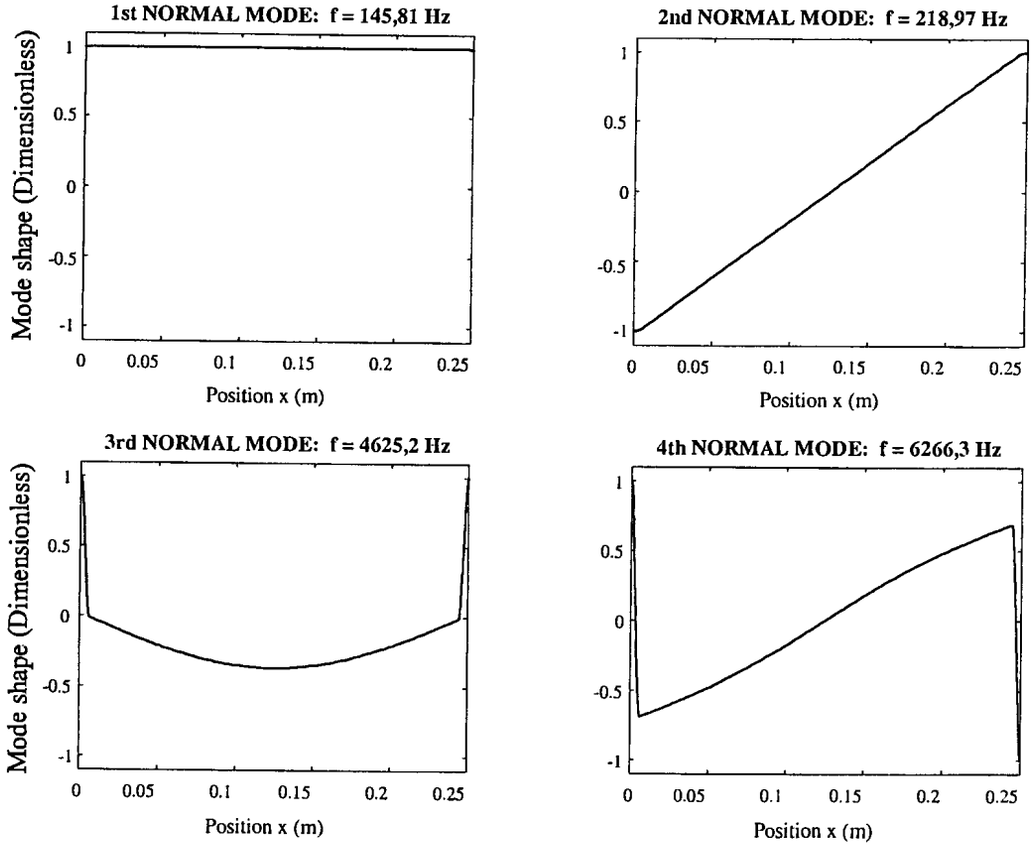

Figure 2.8.4.3: First four normal mode shapes of support structure

The normal mode mass, stiffness and damping matrices are:

$$M^* = \begin{bmatrix} 1{,}538 & 0 & 0 \\ 0 & 0{,}699 & 0 \\ 0 & 0 & 0{,}387 \end{bmatrix} kg \qquad \textbf{(2.8.4.1a)}$$

$$K^* = \begin{bmatrix} 1{,}291.10^6 & 0 & 0 \\ 0 & 1{,}323.10^6 & 0 \\ 0 & 0 & 3{,}269.10^8 \end{bmatrix} N/m \qquad \textbf{(2.8.4.1b)}$$

$$C^* = \begin{bmatrix} 177{,}43 & 0 & 0 \\ 0 & 119{,}43 & 0 \\ 0 & 0 & 5{,}65 \end{bmatrix} Ns/m \qquad \textbf{(2.8.4.1c)}$$

Table 2.8.4.3: Damping factors for first three normal modes

Mode number	Natural frequency (Hz)	Damping factor (%)
1	145,81	6,3
2	218,97	6,21
3	4625,2	0,025

It can be seen from table 2.8.4.3 that the damping factors are relatively low. The assumption made in section 2.8.3 that normal mode damping can be analyzed using the undamped normal modes, without significant distortion of the mode shapes, is therefore valid.

2.8.5 Forced behaviour of the LOS stabilization system

The forced linear equation of motion of the system, from equation 2.8.3.19, is:

$$M^*\ddot{q} + C^*\dot{q} + K^*q = Q \qquad \textbf{(2.8.5.1)}$$

where M^*, C^* and K^* are normal mode mass, damping and stiffness matrices respectively and Q is the modal excitation force vector, given by:

$$Q = \int_{x=0}^{x=l} \Phi^T(x) F(x,t) dx \qquad \textbf{(2.8.5.2)}$$

F is the distributed force vector as given by equation 2.8.1.3.

In more concise matrix form, equation 2.8.5.2 can be written as:

$$Q = \Phi^T F \tag{2.8.5.3}$$

The system state-space equations for forced behaviour are fully derived in appendix M. The equations are written in the following familiar form:

$$\dot{x} = Ax + Bu \tag{2.8.5.4a}$$
$$y = Cx + Du \tag{2.8.5.4b}$$

where:

$$x = \left\{ \{q\} \quad \{\dot{q}\} \quad \{I_1 \quad I_2\}^T \right\}^T \tag{2.8.5.5a}$$
$$u = \{V_1 \quad V_2\}^T \tag{2.8.5.5b}$$
$$y = \{w_1 \quad w_2 \quad \theta\}^T \tag{2.8.5.5c}$$

$$A = \begin{bmatrix} 0 & I & 0 \\ -\Omega^2 & -2Z\Omega & \dfrac{A_T E N d^H}{G l_T} M^{*-1} \left[\Phi^T(0) \quad \Phi^T(l) \right] \\ 0 & -\dfrac{A_T E N d^\sigma}{G l_T L_0} \begin{bmatrix} \Phi(0) \\ \Phi(l) \end{bmatrix} & -\dfrac{R_c}{L_0} \begin{bmatrix} 1 & 0 \\ 0 & 1 \end{bmatrix} \end{bmatrix} \tag{2.8.5.6a}$$

$$B = \begin{bmatrix} 0 & 0 \\ 0 & 0 \\ \dfrac{1}{L_0} \begin{bmatrix} 1 & 0 \\ 0 & 1 \end{bmatrix} \end{bmatrix} \tag{2.8.5.6b}$$

$$C = \begin{bmatrix} \{\Phi(x_1)\} & \{0\} & \{0 \quad 0\} \\ \{\Phi(x_2)\} & \{0\} & \{0 \quad 0\} \\ \left\{ \dfrac{1}{l} \left(\Phi(x_2) - \Phi(x_1) \right) \right\} & \{0\} & \{0 \quad 0\} \end{bmatrix} \tag{2.8.5.6c}$$

$$D = \{0 \quad 0\} \tag{2.8.5.6d}$$

The system transfer functions, which are the ratios between the outputs and inputs, are obtained by means of equation 2.5.2.1. The transfer function $G_{kl}(s)$ for the k-th input and l-th output, is:

$$G_{kl}(s) = \frac{y_l}{u_k} = C_{row\,l}\left[sI - A\right]^{-1} B_{column\,k} + D_{column\,k} \qquad \textbf{(2.8.5.7)}$$

The desired transfer functions of the system, for the inputs and outputs in equations 2.8.5.5b and 2.8.5.5c, are:

$$G_{11}(s) = \frac{W_1(s)}{V_1(s)} \qquad \textbf{(2.8.5.8a)}$$

$$G_{12}(s) = \frac{W_2(s)}{V_1(s)} \qquad \textbf{(2.8.5.8b)}$$

$$G_{13}(s) = \frac{\Theta(s)}{V_1(s)} \qquad \textbf{(2.8.5.8c)}$$

$$G_{23}(s) = \frac{\Theta(s)}{V_2(s)} \qquad \textbf{(2.8.5.8d)}$$

where $W_k(s)$ and $V_l(s)$ respectively represent the Laplace-transform of the k-th displacement output and l-th coil voltage input, while $\Theta(s)$ is the Laplace-transformed LOS output angle of the optical instrument.

For the sake of convenience, G_{11} is called the "parallel" *TF*, i.e. the *TF* for an input at actuator I and an output at instrument attachment point I. Assuming equal actuator characteristics, the same *TF* will be obtained for an input at actuator II and an output at instrument attachment point II, i.e.:

$$G_{22}(s) = G_{11}(s) \qquad \textbf{(2.8.5.9)}$$

G_{12} is called the "crisscross" *TF*, i.e. for an input at actuator I and an output at instrument attachment point II. G_{21}, for an input at actuator II and an output at instrument attachment point I, is:

$$G_{21}(s) = G_{12}(s) \qquad \textbf{(2.8.5.10)}$$

The above *TF*'s, in terms of the state and output matrices, are:

$$G_{11}(s) = C_{row\,1}\left[sI - A\right]^{-1} B_{column\,1} \qquad \textbf{(2.8.5.11a)}$$

$$G_{12}(s) = C_{row\,2}\left[sI - A\right]^{-1} B_{column\,1} \qquad \textbf{(2.8.5.11b)}$$

$$G_{13}(s) = C_{row\,3}\left[sI - A\right]^{-1} B_{column\,1} \qquad \textbf{(2.8.5.11c)}$$

$$G_{23}(s) = C_{row\,3}\left[sI - A\right]^{-1} B_{column\,2} \qquad \textbf{(2.8.5.11d)}$$

The transfer functions G_{11}, G_{12} and G_{23} are calculated below. The positions of the actuators are at the beam ends, i.e. at $x = 0$ and $x = l$. Positions of the instrument attachment points are:

$$x_1 = 0{,}006\ m \qquad \textbf{(2.8.5.12a)}$$

$$x_2 = 0{,}244\ m \qquad \textbf{(2.8.5.12b)}$$

The first three normal modes are used. The natural frequencies and damping factors are as in table 2.8.4.3. The normal mode mass matrix is as given in equation 2.8.4.1a. The values of d^H, μ^σ and L_0 are obtained from the actuator simulation results as given in section 2.7.3, for a frequency corresponding to the second normal mode of the undamped system, i.e. 218,97 Hz. This is the first natural frequency for angular excitation of the optical instrument (see figure 2.8.4.3). At this frequency, d^H and μ^σ are $8{,}14.10^{-9}$ m/A and $4{,}71.10^{-6}$ Tm/A respectively, while L_0 is $8{,}7.10^{-4}$ H.

The Terfenol-D piezomagnetic cross-coupling constant d^σ and Young's modulus E, from section 2.7.3, are $1{,}09.10^{-8}$ m/A and 23,46 GPa respectively. The rest of the actuator parameters, i.e. l_T, A_T, N, R_c, are as given in table 2.7.3.1.

The *TF's* are obtained by application of equations 2.8.5.11a, 2.8.5.11b and 2.8.5.11d. The *TF's* are of the form:

$$G_{kl}(s) = \frac{P(s)}{Q(s)} = \frac{\sum_{i=0}^{i=5} p_i s^i}{\sum_{j=0}^{j=8} q_j s^j} \qquad \textbf{(2.8.5.13)}$$

Note that, as was the case with the actuator model developed in section 2.5, the relative degree-of-freedom of the *TF*, i.e. the difference between the numerator and denominator polynomial orders is 3. The coefficients for the different *TF's* are given in table 2.8.5.1. The denominator coefficients are the same for all the *TF's*.

Table 2.8.5.1: *TF* numerator and denominator polynomial coefficients

Transfer function:	G_{11}	G_{12}	G_{23}
p_0	$1{,}5675.10^{23}$	$2{,}9397.10^{21}$	$6{,}1524.10^{23}$
p_1	$9{,}3771.10^{19}$	$-2{,}2232.10^{18}$	$3{,}8398.10^{20}$
p_2	$1{,}3882.10^{17}$	$-5{,}0367.10^{16}$	$7{,}5677.10^{17}$
p_3	$3{,}6558.10^{13}$	$-1{,}3525.10^{13}$	$2{,}0033.10^{14}$
p_4	$1{,}6154.10^{8}$	$-6{,}3107.10^{7}$	$8{,}9857.10^{8}$
p_5	$4{,}2246.10^{4}$	$-1{,}6733.10^{5}$	$2{,}3591.10^{5}$
q_0	$1{,}8162.10^{28}$	$1{,}8162.10^{28}$	$1{,}8162.10^{28}$
q_1	$2{,}1747.10^{25}$	$2{,}1747.10^{25}$	$2{,}1747.10^{25}$
q_2	$3{,}8878.10^{22}$	$3{,}8878.10^{22}$	$3{,}8878.10^{22}$
q_3	$2{,}7594.10^{19}$	$2{,}7594.10^{19}$	$2{,}7594.10^{19}$
q_4	$1{,}7394.10^{16}$	$1{,}7394.10^{16}$	$1{,}7394.10^{16}$
q_5	$6{,}4991.10^{12}$	$6{,}4991.10^{12}$	$6{,}4991.10^{12}$
q_6	$8{,}6782.10^{8}$	$8{,}6782.10^{8}$	$8{,}6782.10^{8}$
q_7	7658,7	7658,7	7658,7
q_8	1	1	1

The frequency-domain transfer functions are obtained by substitution of s with $j\omega$ in equations 2.8.5.11a to 2.8.5.11d. As is the case with the actuator transfer functions (see section 2.7), the system ω-domain transfer functions are complex, with frequency-dependent magnitudes and phase angles. The "parallel", "crisscross" and optical instrument LOS angle transfer functions, for a frequency band of 0 Hz to 400 Hz, are shown graphically in figures 2.8.5.1 to 2.8.5.3.

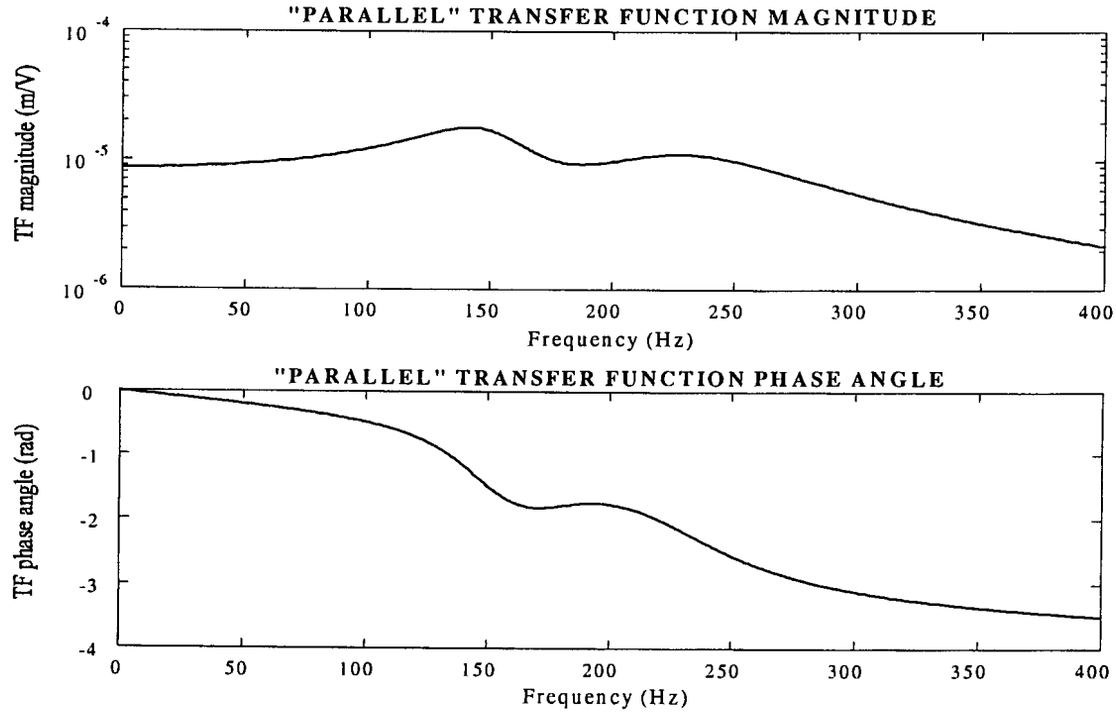

Figure 2.8.5.1: System *TF* magnitude for "parallel" excitation and measurement

A special case arises if the coil input voltages V_1 and V_2 are 180° out-of-phase, i.e.:

$$V_2 = -V_1 \qquad \textbf{(2.8.5.14)}$$

In this case, the magnitude of the transfer function G_{23} is twice that shown in figure 2.8.5.3. The excited DOF is purely rotational and no translation is possible.

This concludes the simulation of the LOS stabilization system. The *TF's* derived and calculated above, will be used as design inputs in chapter 3 and will be experimentally measured in chapter 4. Thereafter, in chapter 5, the state-space and *TF* parameters will be extracted from the measured *TF's* and the model will be updated.

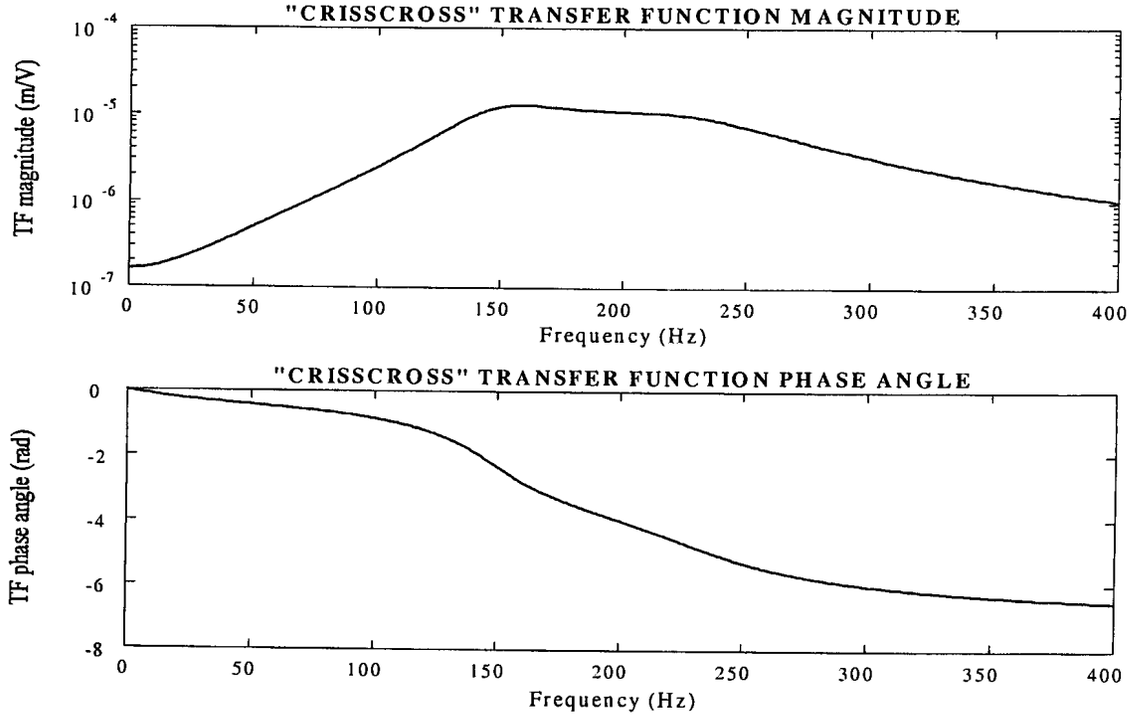

Figure 2.8.5.2: System *TF* magnitude for "crisscross" excitation and measurement

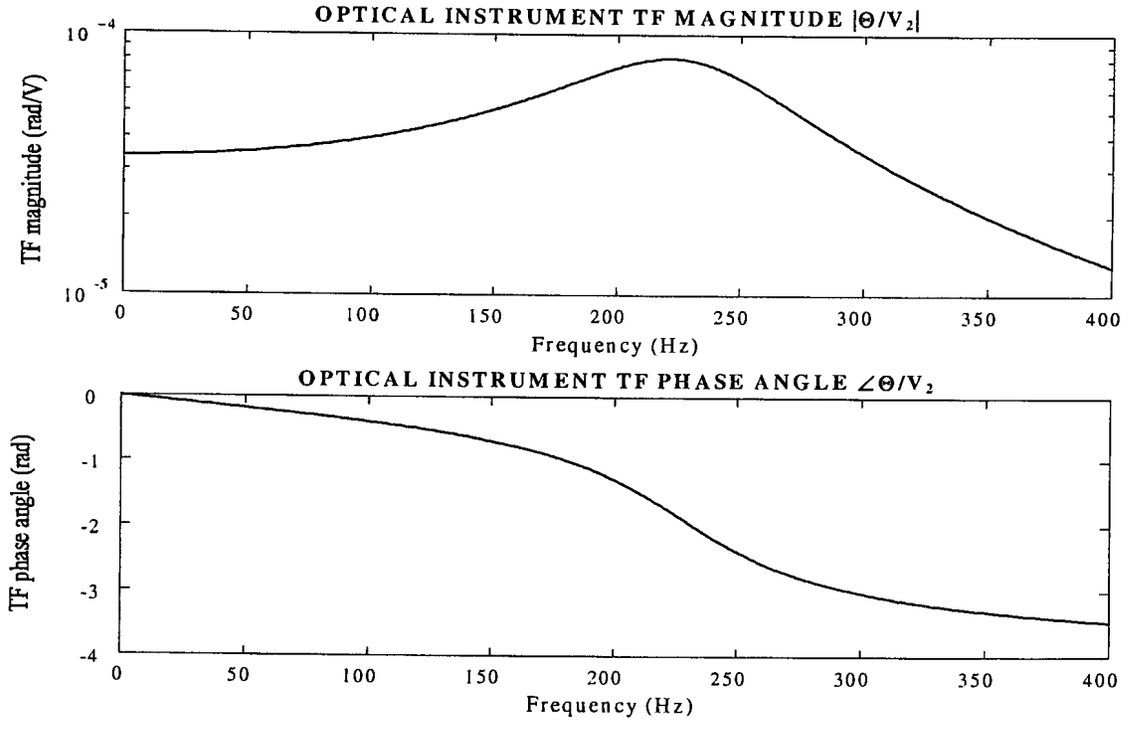

Figure 2.8.5.3: System LOS angle per unit input voltage

2.9 Summary of chapter 2 and preview of chapter 3

The magnetostrictive and magnetization characteristics of Terfenol-D were modelled in section 2.2. The characteristics were linearized and the strain constant, Young's modulus, piezomagnetic cross-coupling constant and permeability were derived from graphs published in literature. The effects of hysteresis on the strain constant and permeability were investigated in section 2.3. It was shown that hysteresis has a significant influence on both these parameters.

A Terfenol-D actuator was modelled in section 2.4. The nonlinear and linear equations of motion and coil current equations were expressed in terms of the magnetostrictive, magnetization, actuator and coil dynamic parameters. The equations of motion were coupled to the coil current equation in section 2.5, where an actuator state-space model was developed. Linear s- and ω-domain transfer functions were derived from the state-space model. The natural vibration behaviour of an actuator was covered in section 2.6 and the coupling effects of the coil current equation and the equation of motion on the eigenvalues, were indicated.

Actuator behaviour was simulated in section 2.7. The linear dynamic parameters were calculated for different input levels. A beam model was developed for the optical instrument and its support structure in section 2.8, which was coupled to the linear actuator model. An uncoupled modal equation of motion was derived. The natural frequencies and mode shapes of the system were calculated, using the Rayleigh-Ritz method, and shown graphically. The coil current equations were coupled to the equation of motion in state-space and the system transfer functions were obtained in the s- and ω-domains.

In chapter 3, the theory developed in chapter 2, together with the base disturbance parameters, will be used as inputs to design the Terfenol-D actuators and LOS stabilization system. The parameters required to reject the disturbance, such as actuator stroke length, system natural frequency, bandwidth, coil resistance to inductance ratio and input voltage, will be determined.

Chapter 3
Design and manufacture of magnetostrictive LOS stabilization system

3.1 Background

The design and manufacture of the magnetostrictive LOS stabilization system, consisting of two Terfenol-D actuators and a support structure for the optical instrument, are described in this chapter. The design inputs are given, i.e. the maximum allowable LOS angle, the frequency band and spectrum of the disturbance, the mass of the optical instrument and the maximum available voltage of the power source. These inputs are used to determine the required system performance parameters, namely the actuator stroke length and displacement gain factor, mechanical prestress in the Terfenol-D rods, system natural frequency, coil resistance to inductance ratio, bias voltage and amplitude.

Once the performance parameters have been determined, design concepts are generated, evaluated and compared. The principle of operation, performance parameters, advantages and disadvantages of each concept are discussed. The most suitable concept, on which the design will be based, is selected. A detailed design of the system and its components follows, including the necessary mathematical equations, graphs, component parameters, material specifications and assembly and detail drawings. In order to ensure system safety and reliability, a number of critical parameters, such as the buckling force and buckling frequency of the rods and critical eddy current frequency, are checked. The manufacturing and assembly procedures of the system are described.

The actuator and system design and manufacture are covered in detail in the following sections: Section 3.2 gives the design inputs, which are employed in section 3.3 to determine the system performance parameters. The design concepts are generated and compared in section 3.4 and the most suitable concept is selected. A detailed design of the actuators and system follows in section 3.5. Detail and assembly drawings are given in section 3.6. The design checks are covered in section 3.7 and 3.8. Section 3.9 describes the manufacturing procedure, and finally, chapter 3 is summarized and chapter 4 is previewed in section 3.10.

3.2 Magnetostrictive actuator and system design input parameters

This section gives the design input parameters of the actuators and system. The maximum allowable LOS angle, frequency band and spectrum of the disturbance, the mass of the optical instrument and its support structure, and the available voltage of the power source, are given. These parameters are required to calculate the system performance factors, such as the actuator stroke length and output force, system natural frequency, resistance to inductance ratio of the coils and the system bandwidth.

The different inputs influence the design as follows: The maximum allowable LOS angle and base angular disturbance determine the actuator output stroke length. The angular acceleration of the base and the mass of the optical instrument determine the required actuator

output force. The disturbance frequency bandwidth determines the resistance to inductance ratio of the coils, natural frequency and stabilization system bandwidth. The available voltage of the power source determines the maximum coil input voltage.

The base disturbance angular acceleration and displacement frequency spectra are shown in figure 3.2.1.

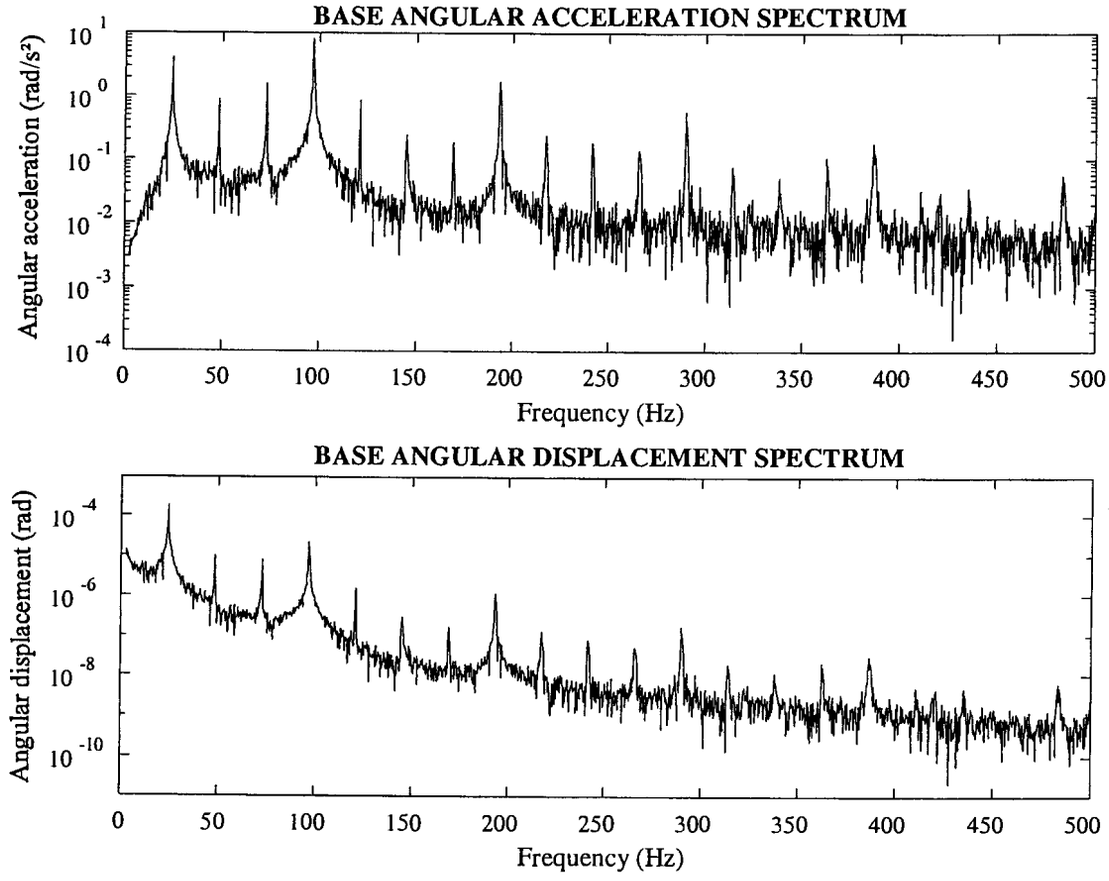

Figure 3.2.1: Base angular acceleration and displacement frequency spectra

The maximum allowable LOS angular displacement and acceleration of the optical instrument are 0,1 mrad peak-to-peak (p-p) and 5,37 rad/s^2 respectively. The maximum and RMS angular displacements of the disturbance are 0,7 mrad p-p and 1,81.10^{-4} rad respectively, while the maximum and RMS angular accelerations of the disturbance are 39,48 rad/s^2 p-p and 9,12 rad/s^2 respectively. The attenuation factor, which is the ratio of the difference between the base and instrument angular displacements, to the base angular displacement, is 85%.

The crest factor, or peak-to-RMS ratio of the disturbance displacement, is 2,17. The base disturbance bandwidth is 2,5 Hz to 500 Hz. The dominant frequency of the base angular acceleration signal is 96,75 Hz, while that of the base angular displacement is 24 Hz. The mass of the optical instrument and its support structure is 1,24 kg. The maximum available voltage of the source is 28 V.

The disturbance bandwidth deserv detail here. The purpose of the LOS stabilization system is to limit the instrument angular displacement to a value of 0,1 mrad, which is considerably lower than that of the disturbance, i.e. 0,7 mrad. This poses a problem, as the LOS angle of the instrument will be difficult to measure accurately due to output noise, which is aggravated by the presence of high frequencies in the disturbance signal. A sample frequency of five to ten times the maximum disturbance frequency is normally required for accurate measurement. For the disturbance under consideration, the maximum frequency is 500 Hz (see figure 3.2.1), therefore a sample frequency of 2,5 kHz to 5 kHz will be required.

In order to limit the influence of noise, it will be desirable to reduce the sample frequency to a more convenient value of 1 kHz. However, this measure will imply that disturbance frequencies above 100 Hz will have to be ignored and that the energy in the signal above 100 Hz will be unaccounted for. Since the bulk of the energy (91%) is concentrated below 100 Hz, limiting the disturbance band to 100 Hz is justifiable. Therefore, in this study, the maximum disturbance frequency will be limited to 100 Hz.

For the sake of completeness, all the actuator and system design input parameters are summarized in table 3.2.1.

Table 3.2.1: Magnetostrictive actuator and system design input parameters

Maximum allowable LOS angular displacement	0,1 mrad p-p
Maximum allowable LOS angular acceleration	5,37 rad/s^2 p-p
Maximum angular displacement of base disturbance	0,7 mrad p-p
Maximum angular acceleration of base disturbance	39,48 rad/s^2 p-p
RMS angular displacement of base disturbance	0,181 mrad
RMS angular acceleration of base disturbance	9,12 rad/s^2
Base disturbance displacement crest factor	2,17
Attenuation factor	85%
Percentage energy in disturbance below 100 Hz	91%
Base disturbance bandwidth	2,5 Hz to 100 Hz
Dominant base angular acceleration frequency	96,75 Hz
Dominant base angular displacement frequency	24 Hz
Length of optical instrument	250 mm
Mass of optical instrument and support structure	1,24 kg
Available voltage of power source	28 V

In the next section, the above design input parameters will be used to determine the actuator and system performance criteria.

3.3 Terfenol-D LOS stabilization system performance parameters

The system performance parameters required to reject the base disturbance, are determined in this section. These parameters will be used in section 3.5 to do a detailed system design. The parameters are the actuator stroke length and output force, coil resistance to inductance ratio and system natural frequency and bandwidth. The system design inputs, which were given in section 3.2, are used to calculate the performance parameters.

The actuator stroke length is determined from the maximum disturbance angle, maximum allowable LOS angle of the optical instrument and instrument length. The actuator output force is determined from the actuator displacements. The system frequency bandwidth, natural frequency and coil resistance-to-inductance ratio are determined from the disturbance frequency bandwidth.

Actuator stroke length

A sketch of the base and instrument angular displacements, and actuator stroke lengths and forces, is shown in figure 3.3.1. The instrument length is l. The angular displacement of the base is given by θ_b, while that of the instrument is given by θ. The stroke lengths of actuators I and II are respectively given by y_{a1} and y_{a2}. The force outputs of actuators I and II are F_{a1} and F_{a2} respectively. The moment acting on the instrument, due the actuator forces, is T.

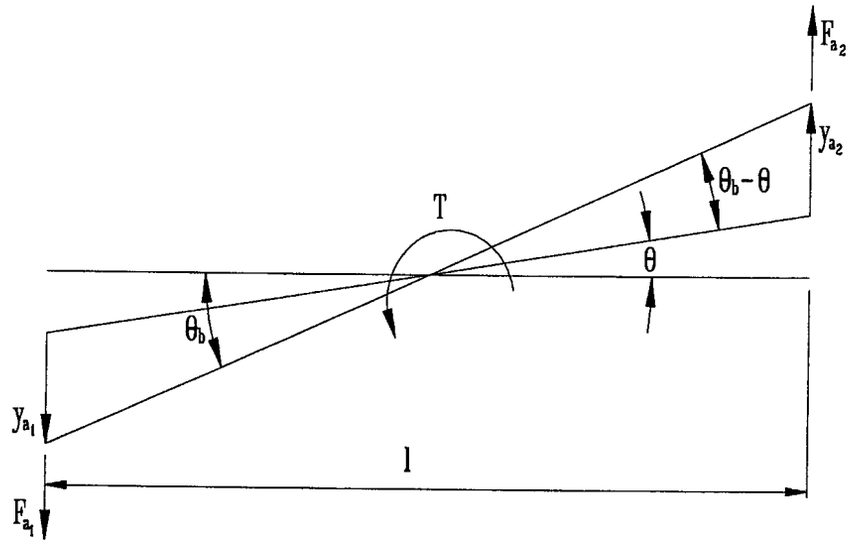

Figure 3.3.1: Base and instrument displacements and actuator stroke lengths and forces

The actuator stroke lengths y_{a1} and y_{a2} can be expressed as follows in terms of l, θ_b and θ:

$$y_{a1} = y_{a2} = \frac{l}{2}(\theta_b - \theta) \qquad \textbf{(3.3.1)}$$

The numerical values of l, θ_b and θ, from table 3.2.1, are:

$$l = 0{,}25 \text{ m} \quad \textbf{(3.3.2a)}$$

$$\theta_b = 0{,}7.10^{-3} \text{ rad} \quad \textbf{(3.3.2b)}$$

$$\theta = 0{,}1.10^{-3} \text{ rad} \quad \textbf{(3.3.2c)}$$

By substitution of Equations 3.3.2a to 3.3.2c into equation 3.3.1, the required stroke lengths of the two actuators are:

$$y_{a1} = y_{a2} = 75.10^{-6} \text{ m} \quad \textbf{(3.3.3)}$$

Actuator force

From Newton's 2nd law, actuator force can be expressed as follows:

$$F_a = \frac{m\omega^2 y_a}{2} \quad \textbf{(3.3.4)}$$

where F_a is peak-to-peak output force per actuator, m is system concentrated mass, ω is excitation frequency and y_a is actuator stroke length. The concentrated mass depends on the particular normal mode of the support structure and optical instrument that has to be excited. For angular motion, m is the modal mass of the first angular normal mode, i.e. 0,699 kg (see equation 2.8.4.1a):

$$m = M_{22} = 0{,}699 \text{ kg} \quad \textbf{(3.3.5)}$$

The excitation frequency is the maximum frequency of the disturbance band, i.e. 628,3 rad/s (corresponding to a frequency of 100 Hz - see table 3.2.1):

$$\omega = 628 \text{ rad/s} \quad \textbf{(3.3.6)}$$

From equation 3.3.3, y_a is 75.10^{-6} m. Substitution of equations 3.3.3, 3.3.5 and 3.3.6 into equation 3.3.4, gives:

$$F_a = 10{,}35 \text{ N} \quad \textbf{(3.3.7)}$$

Note that the actuator force given in equation 3.3.7 is the *external* force required by each actuator and does not include Terfenol-D rod or displacement gain mechanism stiffness. Rod and gain mechanism stiffness will be included in the detailed design in section 3.5.1.

System bandwidth

The disturbance rejection bandwidth (BW) of the system can be defined as the frequency where the magnitude of the TF is 70,7% of its DC value [Kuo, 1982]. The rejection BW thus defined is also known as the -3dB bandwidth. In order to reject the disturbance over the entire disturbance band, the BW must be at least as wide as the disturbance band. In section 3.2, the disturbance band was given as 100 Hz, therefore a disturbance rejection band of at least 100 Hz is required.

The rejection band depends on a number of system parameters, such as the natural frequencies, damping factors and coil R_o/L_o ratios. In an SDOF system, if the coupling effects of the coils are ignored, the –3dB bandwidth (BW) only depends on the natural frequency and damping factor. The bandwidth of an SDOF system, in terms of f_n and ζ, is:

$$BW = f_n g(\zeta) \tag{3.3.8}$$

where $g(\zeta)$ is:

$$g(\zeta) = \left[\left(1-2\zeta^2\right)+\sqrt{4\zeta^4-4\zeta^2+2}\right]^{0,5} \tag{3.3.9}$$

$g(\zeta)$ for damping factors of 0 to 1, from Kuo [1982], is given in table 3.3.1.

Table 3.3.1: $g(\zeta)$ for ζ ranging from 0 to 1 [Kuo, 1982]

Damping factor ζ	$g(\zeta)$
0,0	1,5538
0,1	1,5428
0,2	1,5096
0,3	1,4537
0,4	1,3745
0,5	1,2720
0,6	1,1482
0,7	1,0100
0,8	0,8709
0,9	0,7461
1,0	0,6436

From equation 3.3.8, it can be seen that BW is directly proportional to f_n, while, from table 3.3.1, it can be seen that BW decreases with an increase in ζ. It can further be seen that BW is strongly dependent on ζ. As damping is a parameter which is difficult to design into a system without any experimentally determined values, it is necessary to adopt a safe strategy in the system design.

One approach is to use the damping factor which will give the narrowest bandwidth, i.e. $\zeta = 1$. For this value of ζ, the value of g, from table 3.3.1, is 0,6436, and the bandwidth, from equation 3.3.8, is $0{,}6436 f_n$. For a desired system bandwidth of 100 Hz, the required natural

frequency, for $\zeta = 1$, is 155 Hz. However, if this approach is taken in the design of an actuator, the stiffness will be too high and excessive coil power may be required to give the desired stroke length.

Another approach is to ignore the influence of damping on the *BW* altogether and to use a *BW* of $\sqrt{2}$ times the natural frequency. At this frequency, the *TF* magnitude is equal to the DC magnitude and is damping independent. By taking this approach, the natural frequency required to give a bandwidth of 100 Hz, is 70,7 Hz. Note that this natural frequency gives a narrower bandwidth than the –3dB bandwidth, since the transfer function magnitude is 100% of that at DC, and not 70,7% as is the case with the –3dB bandwidth.

The above approaches can be successfully applied to the design of SDOF systems. However, the system under consideration is MDOF (see section 2.8), which requires a different design approach. The *TF* of an MDOF system may display an anti-resonance frequency, which is slightly larger than the lowest natural frequency. Depending on damping, the *TF* magnitude may show a sharp drop at frequencies above resonance, in which case the bandwidth may, for all practical purposes, be limited to the lowest natural frequency. As an example, consider a system whose zeroes z and poles p are:

$$z = -5 \pm j.628$$
$$p = \begin{Bmatrix} -5 \pm j.600 \\ -500 \pm j.1571 \\ -628 \end{Bmatrix} \qquad \textbf{(3.3.10)}$$

The magnitude and phase of the system are shown in figure 3.3.2. The lowest natural frequency is 95,4 Hz, while the anti-resonance frequency is 100,1 Hz. The bandwidth is 97,8 Hz, which is only 2,5% higher than the lowest natural frequency.

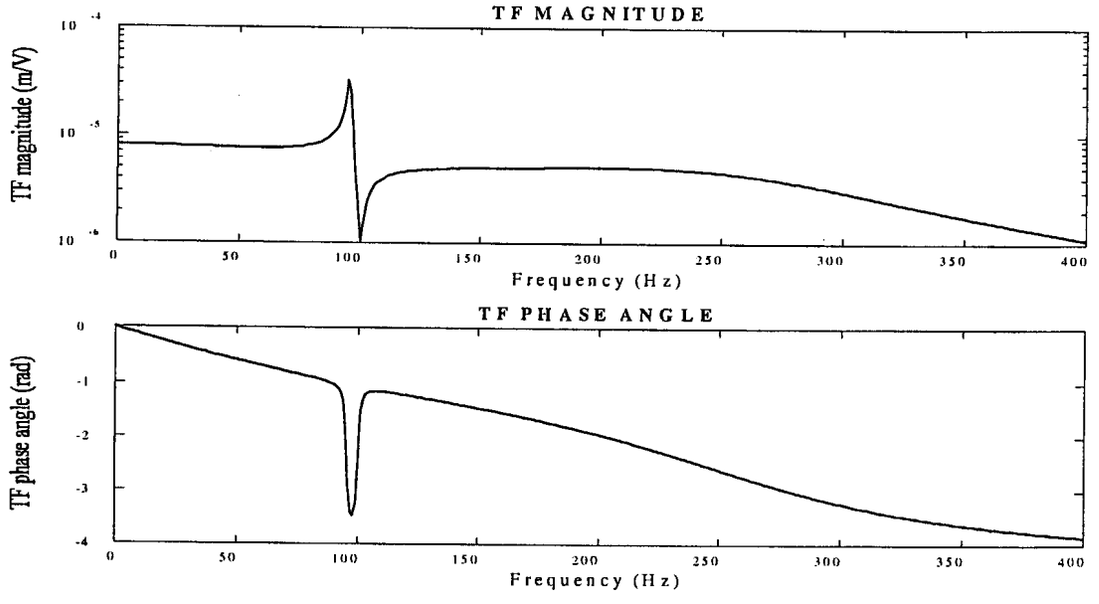

Figure 3.3.2: Transfer function of an MDOF system with a bandwidth close to f_n

Although the simulated *TF* of the system does not display an anti-resonance frequency (see figure 2.8.5.3), the dynamic and magnetostrictive parameters used in the simulations may differ from the true parameters. The differences may be attributed to phenomena such as hysteresis. The true parameters will be obtained from measured *TF's* in chapter 5. Until the true parameters are known, it will be assumed that the system may have an anti-resonance frequency close to the natural frequency. As a safety precaution, the system will be designed to have a natural frequency of at least 100 Hz. If the system has an anti-resonance frequency close to the natural frequency, it will be outside the isolation bandwidth.

Coil resistance to inductance ratio

The coil resistance to inductance ratio (R_c/L_0) determines the real poles of the system *TF* (see sections 2.4, 2.5 and 2.8). In order to ensure a bandwidth of at least 100 Hz, the real poles (and R_c/L_0 ratio) must be at least 100 Hz. If the R_c/L_0 ratio is lower than 100 Hz, the field versus coil voltage *TF* may drop below -3dB inside the disturbance band. This may result in insufficient isolation at the higher end of the band and may require excessive coil power to correct. In this design, in order to ensure a *BW* of at least 100 Hz, a coil R_c/L_0 ratio of at least 100 Hz is required.

Summary of required system parameters

For the sake of completeness, the required system performance parameters, as discussed above, are summarized in table 3.3.2.

Table 3.3.2: LOS stabilization system performance parameters

Performance parameter	Parameter value
Actuator stroke length	75.10^{-6} m
Actuator output force	10,35 N
Disturbance rejection bandwidth	2,5 Hz to 100 Hz
System natural frequency	≥ 100 Hz
Coil resistance to inductance ratio	≥ 100 Hz

The above parameters will be used in section 3.5 to do a detailed design of the actuators and system. Before that can be done, it is necessary to suggest and compare a number of possible design concepts in section 3.4. The concepts are discussed and evaluated and the most suitable concept is selected.

3.4 Magnetostrictive LOS stabilization system design concepts

This section discusses the possible system design concepts. The need for a displacement gain mechanism, magnetic biasing and mechanical biasing is motivated. A number methods to achieve the desired actuator gain, bias field and bias stress in the Terfenol-D rod are presented. The different concepts are compared on the basis of principle of operation, effective range of operation, advantages and disadvantages. Mathematical equations, graphs and tables are supplied to explain the principle of operation of each concept. The most suitable concepts are motivated and selected. These concepts are incorporated into an actuator and system design concept.

The stroke length of a magnetostrictive actuator depends on the strain in the active rod and the rod length. The maximum strain in the rod depends on the saturation strain of the particular material at a given prestress. Terfenol-D, which is a highly magnetostrictive material, can produce "giant" magnetostrictive strains of up to 2000 $\mu\varepsilon$. However, this strain is attainable at the cost of high compressive prestresses and large field strengths, which are not desirable for design purposes. Large field strengths are inefficient in terms of energy consumption, while high compressive stresses may be unpractical to achieve and may lead to rod buckling.

The other factor which determines the actuator stroke length, i.e. the rod length, is unfortunately also limited. In order to produce feasible actuator stroke lengths, a rod with an unrealistic length may be required, which will lead to an actuator of unpractical proportions. Furthermore, as is the case with high compressive prestresses, unduly long rods will also be prone to buckling. It is therefore clear that both the strain in the rod and the rod length limit the actuator stroke length to practically achievable values.

One method of achieving an actuator with the desired stroke length, is to implement a displacement gain mechanism, which "multiplies" the elongation of the rod with a dimensionless displacement gain factor. The gain mechanism may operate on pneumatic, hydraulic or purely mechanical principles. The advantage of a displacement gain mechanism is an increase in stroke length without the need of high fields or stresses. The actuator can be operated more efficiently in the linear range of its strain versus field characteristic, without having to force the field into the saturation range.

Unfortunately, there is also a disadvantage to the use of a gain mechanism, namely that the actuator output force is decreased by a factor equal to the displacement gain factor (see equation 2.4.7). Irrespective of this disadvantage, each of the actuators which will be used in this study will be equipped with a gain mechanism, since it is the only practical means of obtaining the desired stroke length.

In section 2.2 it was shown that Terfenol-D would produce a positive strain if subjected to a positive field. Terfenol-D will however, like other magnetostrictive materials, also produce a positive strain if a negative field is induced, as shown in figure 3.4.1. This characteristic is known as a symmetric characteristic. The disadvantage of a symmetric characteristic is that the strain amplitude is smaller for a given field amplitude than is the case with an asymmetric characteristic. This point is explained in the following example.

Consider the Terfenol-D strain versus field characteristic shown in figure 3.4.1. For a field with a zero mean (point a) and an amplitude of 40 kA/m, the maximum field is 40 kA/m and the minimum field is –40 kA/m. The strain which corresponds with the maximum field is 800 $\mu\varepsilon$ (point b). The strain which corresponds with the minimum field is also 800 $\mu\varepsilon$ (point c). It can be seen that the maximum available strain for a field with an amplitude of 40 kA/m and a zero mean, is 800 $\mu\varepsilon$. The strain versus field characteristic in the above example is symmetric.

Next, consider a field with a mean of 40 kA/m (point b), with the same amplitude as before, i.e. 40 kA/m. The maximum field will be 80 kA/m and the minimum field will be 0 kA/m. The minimum strain will be zero (point a), while the maximum strain will be 1300 $\mu\varepsilon$ (point d). This strain versus field characteristic is asymmetric. It is clear from figure 3.4.1 that the maximum strain in the asymmetric case is approximately 63% higher than in the symmetric case.

The above technique of improving the maximum strain is known as magnetic biasing. Due to the advantage illustrated in the above example, magnetic biasing will be applied in this study to obtain the maximum available strain in the Terfenol-D rod.

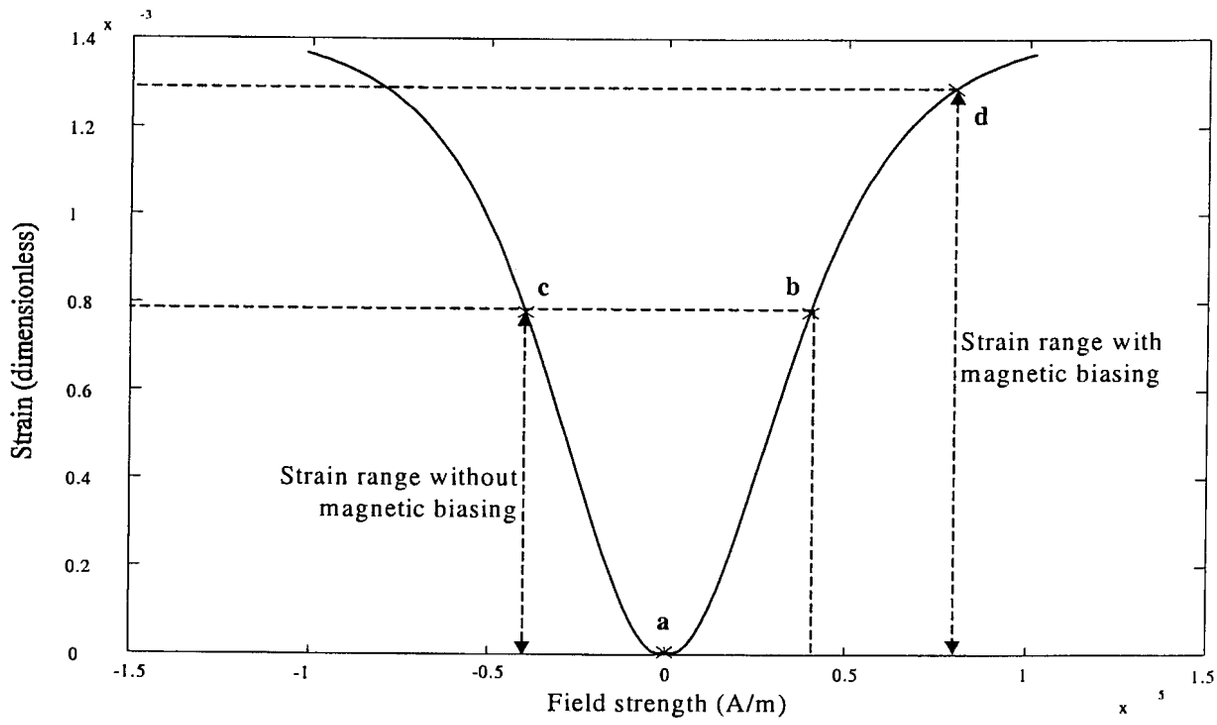

Figure 3.4.1: Magnetostrictive strain versus magnetic field strength for two bias fields

Mechanical biasing, or prestressing, of a Terfenol-D rod is required for two reasons. In the first place, larger saturation strains can be achieved. Figure 3.4.2 illustrates the effect of two compressive prestresses, i.e. 6,9 MPa and 17,9 MPa, on the magnetostrictive strain of Terfenol-D. At a field strength of 100 kA/m, the strain for a prestress of 6,9 MPa is approximately 1200 $\mu\varepsilon$, while for a prestress of 17,9 MPa, the strain is approximately

1400 $\mu\varepsilon$. It can be seen that a prestress can be used to good effect to increase the magnetostrictive strain in the rod. Secondly, Terfenol-D is soft in tension and must therefore always be under compression. The tensile strength of Terfenol-D is only 28 MPa, while the compressive strength is 700 MPa [Butler, 1988].

There are however, also disadvantages in prestressing the rod. The first is that higher compressive prestresses require larger field strengths to produce the same strain. For instance, to produce a strain of 750 $\mu\varepsilon$ at a prestress of 6,9 MPa, a field strength of approximately 20 kA/m is required, while a field strength of approximately 45 kA/m is required to produce the same strain at a prestress of 17,9 MPa (see figure 3.4.2). This problem can be solved by means of magnetic biasing, where, for instance, a permanent magnet is used to provide the desired bias field.

The second disadvantage, which has already been mentioned, is the danger of buckling. Buckling can be avoided by applying moderate prestresses, which do not exceed the buckling load of the rod, but at the same time, are ample to significantly increase the saturation strain. Mechanical biasing will be used in this study to improve the saturation strain of the rod.

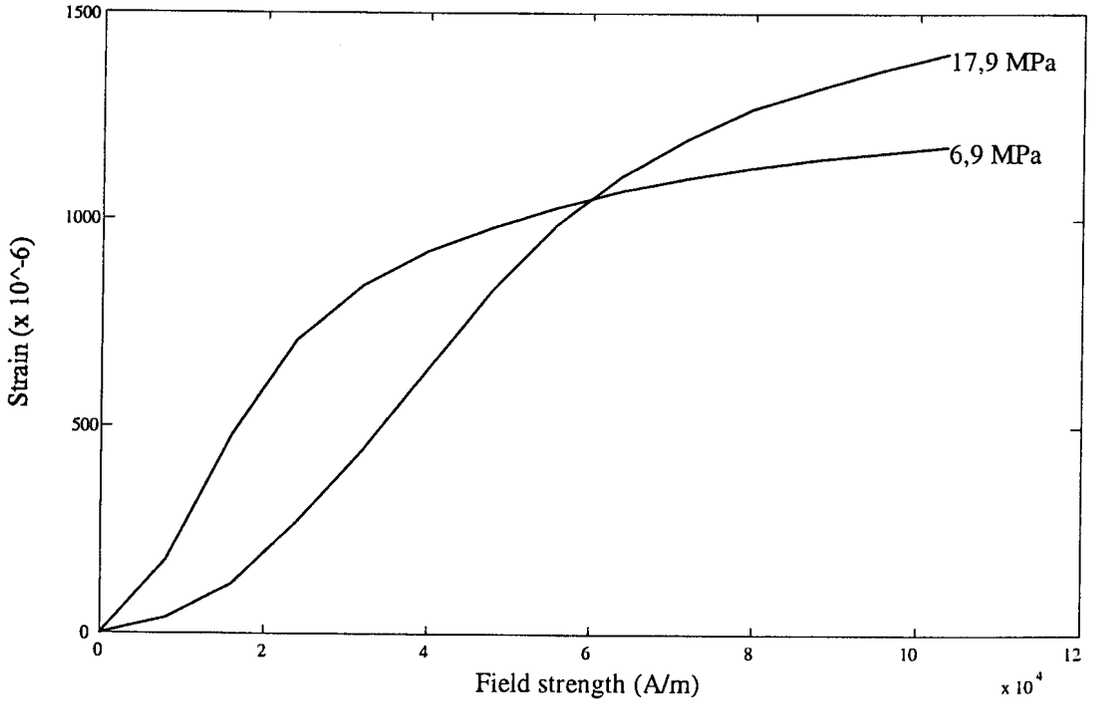

Figure 3.4.2: Terfenol-D strain versus field strength for two compressive prestresses

Section 3.4 is organized as follows: In section 3.4.1, different methods that can be used to obtain the desired actuator gain, are discussed. Bias field and bias stress concepts are covered in sections 3.4.2 and 3.4.3 respectively. The actuator and LOS stabilization system design concepts are presented in section 3.4.4.

3.4.1 Actuator gain concepts

Four methods of achieving the desired actuator displacement gain factor are presented in this section. The first method, which is also the simplest, works on the principle of resonance. A mechanical spring connects the actuator with the optical instrument. If the actuator is operated at frequencies in the vicinity of the natural frequency of the mechanism, a considerable displacement gain can be achieved.

A second method of increasing the output displacement of the actuator, is to make use of a hydraulic gain mechanism. The optical instrument is supported by a hydraulic piston with a cross-sectional area which is smaller than that of the Terfenol-D rod. During excitation, the displacement of the piston will be larger than that of the rod, thereby extending the output displacement of the actuator. The gain factor equals the ratio of the rod area to the piston area.

A third method of obtaining a displacement gain is to utilize the change in dimensions of a structure with unique geometric properties, such as an elliptical structure. The Terfenol-D rod is mounted along the major axis of the ellipse. During excitation, the length of the major axis will increase and the length of the minor axis will decrease. The gain factor is the ratio of the decrease in the length of the minor axis to the increase in the length of the major axis.

The fourth and last gain concept works on the same principle as the elliptical structure mentioned above, but the elliptical shape is replaced with an octagonal shape. The sides of the octagon are relatively hard in comparison with the corners, which act as flexures. During excitation, the corners deflect and allow the dimensions of the octagon to change. The length of the structure is increased while the height is decreased. The gain factor is the ratio of the decrease in height of the octagon, to the increase in length. The four concepts will be discussed in more detail in the following paragraphs.

Resonance spring gain mechanism

A mechanical model of a resonance spring gain mechanism is shown in figure 3.4.1.1. m_s is the concentrated mass of the optical instrument and its support structure, while m_a is the concentrated mass of the actuator. x_b represents the base disturbance displacement, while x_a is the displacement of the actuator mass, which is also the deformation of the Terfenol-D rod. x_s is the displacement of the instrument. k_a is the stiffness of the actuator, and F_m is the magnetostrictive force in the rod. k_{spr} is the stiffness of the gain spring and c represents the damping coefficient of the gain mechanism.

The principle of operation of the mechanism is as follows: The force F_m acts on the mass m_a, whose displacement x_a is resisted by the elastic stiffness k_a of the rod. The displacement of the mass is transmitted to the optical instrument through the spring k_{spr}. At low excitation frequencies, the instrument displacement will not be significantly larger than that of the mass. As the frequency is increased, x_s will exceed x_a, and the effect will increase with frequency.

The maximum amplification, or gain, will be achieved in the vicinity of the natural frequency of the system. At frequencies above the natural frequency, the gain will start to decrease and

eventually, at high frequencies, the displacement of the instrument will be smaller than that of the mass. This method is more effective if the damping is low.

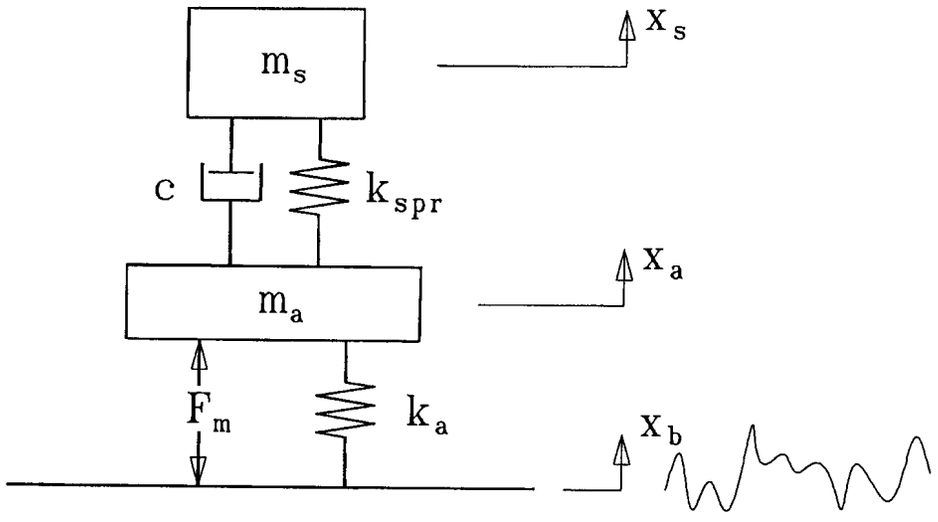

Figure 3.4.1.1: Resonance spring gain mechanism

The displacement gain factor is the ratio of the displacement x_s, of the mass to the displacement x_a, of the rod:

$$G = \frac{x_s}{x_a} \tag{3.4.1.1}$$

G can be derived in terms of the mechanical properties of the gain mechanism and the excitation frequency. The assumption is made that the natural frequency of the gain mechanism and instrument is significantly lower than that of the Terfenol-D rod and actuator mass:

$$\frac{k_{spr}}{m_s} << \frac{k_a}{m_a} \tag{3.4.1.2}$$

The derivation is not done here, but can be found in standard textbooks on vibration theory, such as Tse et al [1978]. The gain factor is given by:

$$G = \sqrt{\frac{1+\left(2\zeta_G \frac{\omega}{\omega_G}\right)^2}{\left(1-\left(\frac{\omega}{\omega_G}\right)^2\right)^2 + \left(2\zeta_G \frac{\omega}{\omega_G}\right)^2}} \tag{3.4.1.3}$$

where ω is the angular excitation frequency and ζ_G is the damping factor of the gain

mechanism:

$$\zeta_G = \frac{c}{2\sqrt{k_{spr} m_s}} \qquad \textbf{(3.4.1.4a)}$$

ω_G is the natural frequency of the gain mechanism:

$$\omega_G = \sqrt{\frac{k_{spr}}{m_s}} \qquad \textbf{(3.4.1.4b)}$$

The gain factor is shown graphically in figure 3.4.1.2. The frequency-dependence of the gain, natural frequency, desired gain and gain band are indicated on the graph.

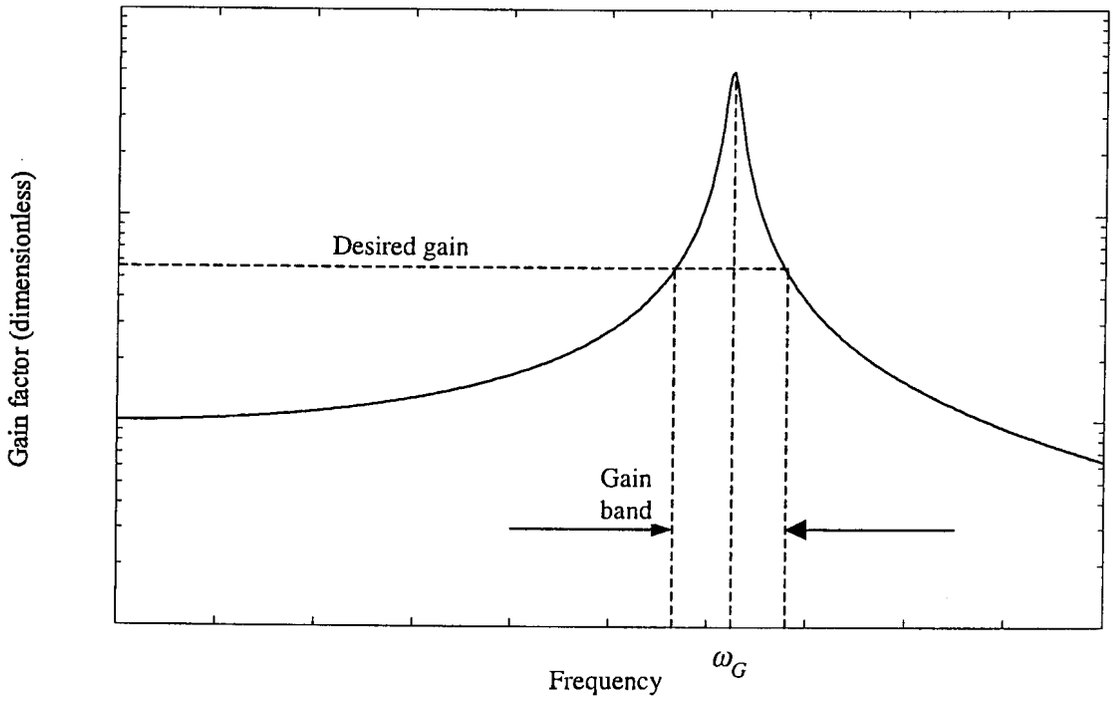

Figure 3.4.1.2: Resonance spring displacement gain factor versus frequency

The advantage of the resonance gain mechanism is its simplicity. This is due to the fact that only a spring is needed to accomplish a gain. However, the disadvantage is that a significant gain can only be achieved in the vicinity of the natural frequency, in a relatively narrow frequency band. This type of gain mechanism is very limited and cannot be used in the stabilization system of the optical instrument, since the disturbance is wide-band (2,5 Hz to 100 Hz - see section 3.2). A second disadvantage is that the gain is not constant, which will complicate closed-loop control of the line of sight of the optical instrument.

Due to these shortcomings, the resonance gain mechanism concept will have to be ruled out and alternative mechanisms, which are independent of the excitation frequency, will have to be considered. One such mechanism is a hydraulic gain mechanism, which will be discussed next.

Hydraulic gain mechanism

The principle of operation of a hydraulic gain mechanism is described in this section. A mathematical expression for the displacement gain factor is derived in terms of the dimensional parameters of the actuator. The effect of fluid compressibility on actuator stiffness, natural frequency and the output displacement to input coil voltage transfer function is given. The advantages and disadvantages of a hydraulic gain mechanism are mentioned.

A hydraulically gained actuator is shown in figure 3.4.1.3. The actuator consists of a Terfenol-D rod, a piston, which supports the mass of the optical instrument, and hydraulic fluid, which fills the space between the rod and the piston. The actuator is mounted on a moving base. The cross-sectional area of the rod is A and that of the piston is A_p. The piston cross-sectional area is smaller than the rod cross-sectional area. The displacement of the rod is x_a and that of the optical instrument is x_s. The base displacement is x_b.

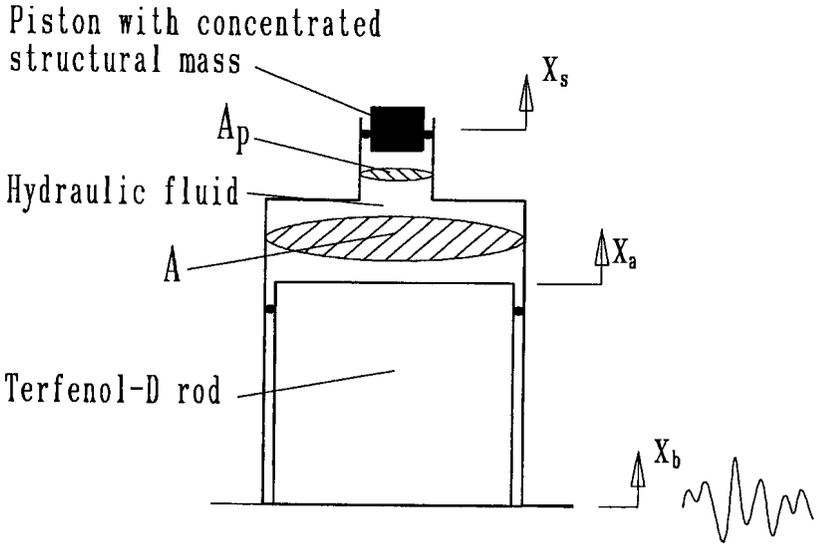

Figure 3.4.1.3: Actuator with hydraulic gain mechanism

The hydraulic gain mechanism works as follows: During excitation, a strain is produced in the rod, which displaces the hydraulic fluid and lifts the piston. The piston displacement is larger than that of the rod, thereby extending the output displacement or stroke length of the actuator. The displacement gain factor depends on cross-sectional area of the rod and the cross-sectional area of the piston. A mathematical expression for the gain factor is derived below.

The volume of fluid v_r displaced during excitation is the product of the rod cross-sectional area and the rod displacement:

$$v_r = Ax_a \tag{3.4.1.5}$$

The volume of fluid v_p which displaces the piston is the product of the piston cross-sectional area and the piston displacement:

$$v_p = A_p x_s \tag{3.4.1.6}$$

Assuming incompressibilty of the hydraulic fluid, the volume of fluid displaced by the rod equals the volume of fluid which displaces the piston:

$$v_p = v_r \tag{3.4.1.7}$$

Substitution of equations 3.4.1.5 and 3.4.1.6 into equation 3.4.1.7 gives:

$$Ax_a = A_p x_s \tag{3.4.1.8}$$

The displacement gain factor is the ratio of the piston displacement to the rod displacement:

$$G = \frac{x_s}{x_a} \tag{3.4.1.9}$$

By substitution of equation 3.4.1.8 into equation 3.4.1.9, the gain factor can be expressed as the ratio of the rod cross-sectional area to the piston cross-sectional area:

$$G = \frac{A}{A_p} \tag{3.4.1.10}$$

It is clear from equation 3.4.1.10 that the gain factor only depends on the cross-sectional areas of the rod and piston. Since both these areas are constant, the gain factor is also constant. If the hydraulic gain mechanism is compared with the resonance gain mechanism, it can be seen that the most important advantage of the hydraulic gain mechanism is a displacement gain factor which is independent of the excitation frequency, and whose operation does not depend on resonance.

In the derivation of equation 3.4.1.10, the assumption was made that the hydraulic fluid is incompressible. However, all hydraulic fluids exhibit a certain degree of compressibility, which will "soften" the actuator by introducing a resilience between the rod and the piston. This resilience will reduce the natural frequency of the actuator and will therefore alter the voltage input to displacement output transfer function (*TF*) of the actuator. The compressibility effect will differ from fluid to fluid, and will increase if the excitation is of such a nature that evaporation, or cavitation, of the fluid takes place.

Fluid compressibility is normally described by means of a bulk modulus [Schwarzenbach & Gill, 1986] and [Ashby & Pinches, 1989]. The bulk modulus can in turn be used to obtain an equivalent spring stiffness of the fluid, which facilitates the derivation of the *TF*. The bulk

modulus is defined below, and the equivalent stiffness, *TF* and actuator natural frequency are given. The *TF* of a compressible fluid is compared with that of an incompressible fluid. The derivation of the *TF* will not be done here, but is given in appendix N.

The bulk modulus can be defined as the ratio of the change in pressure, to the change in volume per unit volume:

$$K_B = \frac{\Delta P}{\left(\frac{\Delta V}{V}\right)} \tag{3.4.1.11}$$

where K_B is the bulk modulus, ΔP is the change in pressure, V is volume and ΔV is the change in volume.

The equivalent fluid stiffness k_{fluid} is given by:

$$k_{fluid} = \frac{A^2 K_B}{V_{ref}} \tag{3.4.1.12}$$

where V_{ref} is the reference volume.

The complex Laplace-domain *TF* of the actuator is:

$$\frac{X_s(s)}{V(s)} = \frac{\frac{\alpha}{\beta}\frac{AENd^H}{m_s(G-1)l_T L_0}}{s^3 + \frac{1}{\beta}\frac{R_c}{L_0}s^2 + \left[\alpha\frac{AE}{m_s G(G-1)l_T} + \frac{\alpha^2}{\beta}\left(\frac{AEN}{l_T}\right)^2 \frac{d^\sigma d^H}{m_s G(G-1)L_0}\right]s + \frac{\alpha}{\beta}\frac{AE}{m_s G(G-1)l_T}\frac{R_c}{L_0}} \tag{3.4.1.13}$$

where E is Young's Modulus of Terfenol-D, N is the number of coil turns, m_s is the concentrated mass of the optical instrument and its support structure, l_T is the length of the Terfenol-D rod, L_0 is the clamped coil inductance, R_c is the coil resistance, d^H is the strain constant and d^σ is the piezomagnetic cross-coupling constant. α and β are dimensionless parameters given by:

$$\alpha = \frac{k_{fluid}}{k_{fluid} + \frac{AE}{l_T}} \tag{3.4.1.14a}$$

$$\beta = 1 + \left(1 - \frac{k_{fluid}}{k_{fluid} + \frac{AE}{l_T}}\right)\frac{AENd^H}{l_T}\frac{Nd^\sigma}{L_0} \tag{3.4.1.14b}$$

For the sake of conciseness, the *TF* can be written in the following general form:

$$TF = \frac{P(s)}{Q(s)} = \frac{p_2 s^2 + p_1 s + p_0}{s^3 + q_2 s^2 + q_1 s + q_0} \qquad \textbf{(3.4.1.15)}$$

where the polynomial coefficients of $P(s)$ and $Q(s)$ are given in table 3.4.1.1. For comparison purposes, the polynomial coefficients for an incompressible hydraulic gain mechanism are also given.

Table 3.4.1.1: *TF* polynomial coefficients for magnetostrictive actuator with compressible and incompressible hydraulic gain mechanisms

Gain mechanism:	**Incompressible**	**Compressible**
Coefficient		
p_0	$\frac{AENd^H}{m_s(G-1)l_T L_0}$	$\frac{\alpha}{\beta}\frac{AENd^H}{m_s(G-1)l_T L_0}$
p_1	0	0
p_2	0	0
q_0	$\frac{AE}{m_s G(G-1)l_T}\frac{R_c}{L_0}$	$\frac{\alpha}{\beta}\frac{AE}{m_s G(G-1)l_T}\frac{R_c}{L_0}$
q_1	$\frac{AE}{m_s G(G-1)l_T}+\left(\frac{AEN}{l_T}\right)^2\frac{d^\sigma d^H}{m_s G(G-1)L_0}$	$\alpha\frac{AE}{m_s G(G-1)l_T}+\frac{\alpha^2}{\beta}\left(\frac{AEN}{l_T}\right)^2\frac{d^\sigma d^H}{m_s G(G-1)L_0}$
q_2	$\frac{R_c}{L_0}$	$\frac{1}{\beta}\frac{R_c}{L_0}$

The natural frequency ω_{nc} of a Terfenol-D actuator with a compressible hydraulic gain mechanism is:

$$\omega_{nc} = \sqrt{\alpha\frac{AE}{m_s G(G-1)l_T}} \qquad \textbf{(3.4.1.16a)}$$

whereas the natural frequency ω_{ni} of an actuator with an incompressible hydraulic gain mechanism is:

$$\omega_{ni} = \sqrt{\frac{AE}{m_s G(G-1)l_T}} \qquad \textbf{(3.4.1.16b)}$$

If equations 3.4.1.16a and 3.4.1.16b are compared, it can be seen that the compressibility of the fluid reduces the natural frequency with a factor $\sqrt{\alpha}$.

The advantage of a hydraulic gain mechanism, i.e. a constant factor gain over a wide frequency range, has already been mentioned. The disadvantages are as follows: In the first place, proper sealing at the contact surface between the cylinder and piston is essential.

Improper sealing may cause leaks, resulting in fluid losses and infiltration of air into the fluid chamber. The presence of air in the fluid will significantly reduce actuator output. Furthermore, maintenance will have to be done periodically to check the condition of the seals. The actuator will therefore have to be dismantled from time to time, resulting in lost operation time.

The hydraulic gain mechanism will not be considered for the magnetostrictive actuators used in this study. A gain mechanism which is not plagued by fluid leaks, sealing problems or costly maintenance, will be discussed in the next section. The gain mechanism makes use of the change in dimensions of an elliptical structure, mounted around the Terfenol-D rod.

Elliptical gain mechanism

A gain mechanism in the form of an elliptically-shaped structure is described in this section. Its principle of operation is explained. The gain factor is derived in terms of the elongation of the Terfenol-D rod and the lengths of the major and minor axes of the ellipse. The application, advantages and disadvantages of this type of gain mechanism are mentioned in short.

An elliptical gain mechanism is shown in figure 3.4.1.4. An elliptical structure is horizontally mounted on a moving base with a vertical displacement of x_b. The optical instrument is attached to the top of the structure, and the Terfenol-D actuator is mounted along the major axis of the ellipse. The mass and displacement of the instrument are m_s and x_s respectively. The length of the major axis of the ellipse is b, while that of the minor axis is a. The elongation of the Terfenol-D rod is $2\Delta b$ and the output displacement of the mechanism is $2\Delta a$.

The principle of operation of the mechanism is as follows: During excitation, the major axis of the ellipse is extended to a length $b+\Delta b$, while at the same time, the minor axis is shortened to a length of $a-\Delta a$. Due to the fact that the minor axis is shorter than the major axis, Δa is larger than Δb. The gain factor G is the ratio of Δa to Δb, and depends on the dimensional properties of the undeformed shape, i.e. a and b. An increase in the ratio of b to a leads to an increase in G. In order to obtain the gain factor for a gain mechanism with given dimensional properties, an equation which relates G to a and b is sought. This relationship is derived in appendix P.

A number of assumptions must be made in the derivation. Firstly, it is assumed that during excitation, the gain mechanism is not distorted, in other words the profile always stays elliptical. A second assumption is that the strain in the structure of the gain mechanism is zero, therefore the perimeter of the ellipse stays constant.

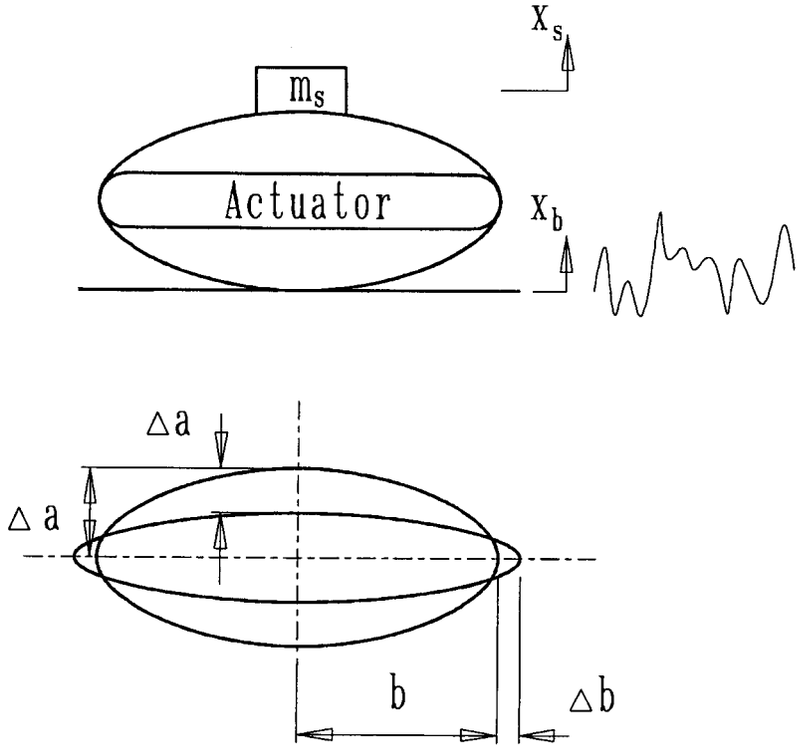

Figure 3.4.1.4: Elliptical gain mechanism

The gain factor is given by:

$$G = \frac{a - \sqrt{a^2 - 2b\Delta b + (\Delta b)^2}}{\Delta b} \qquad \textbf{(3.4.1.17)}$$

It can be seen from equation 3.4.1.17 that the gain factor depends on the dimensions a and b of the undeformed elliptical structure, as well as on the elongation Δb of the Terfenol-D rod. As was the case with the hydraulic actuator, which was discussed in the previous section, the gain factor is independent of excitation frequency. The elliptical gain mechanism has further advantages over the hydraulic gain mechanism, namely that it does not require periodic maintenance it is not plagued by fluid leaks.

One disadvantage of the elliptical structure, however, is that the elliptical shape is difficult to manufacture. Furthermore, it may be difficult to attach the gain mechanism to the optical instrument and to the base. In order to facilitate attachment of the gain mechanism, it will have to be flattened to a certain extent at the top and bottom.

The application of this method of obtaining a displacement gain also deserves mentioning. The method is mainly used by the Swedish Navy for underwater detection at high frequency. The gain factor is enhanced by exciting the structure at resonance, and the resulting gain is the combined effect of the geometric gain factor of the ellipse and the resonance spring gain described before.

This method of accomplishing an actuator displacement gain will not be considered any further in this study because of the manufacturing and installation problems described above. In order to overcome these problems, an octagonal flexural gain mechanism which operates on the same principle as the elliptical structure, but which is easier to manufacture, is recommended. This gain concept is discussed next.

Octagonal flexural gain mechanism

The principle of operation of an octagonal flexural gain mechanism is described in this section. The displacement gain factor is expressed in terms of the geometric properties of the mechanism by means of two methods, i.e. an exact method and an approximate method. The exact method expresses the gain in terms of the Terfenol-D rod length, strain in the rod, and the length and initial slope angle of the slanted sides of the octagon. The approximate method expresses the gain in terms of the initial angle of the slanted sides only.

The gain factor versus initial slope angle is shown graphically. The advantages and disadvantages of the octagonal flexural gain mechanism are discussed, and this method of accomplishing a displacement gain is selected for the LOS stabilization of the optical instrument.

A Terfenol-D actuator with an octagonal flexural gain mechanism is shown in figure 3.4.1.5. The mechanism consists of two horizontal beams, one at the top and one at the bottom, two vertical beams at the ends of the rod and four slanted beams which connect the horizontal beams with the vertical beams. During excitation, the eight corners of the mechanism, which are relatively soft in comparison with the beams, act as flexures to allow simultaneous changes in the length and height of the octagon. The horizontal beam at the bottom serves to attach the actuator to the base, while the horizontal beam at the top serves to attach the actuator to the optical instrument.

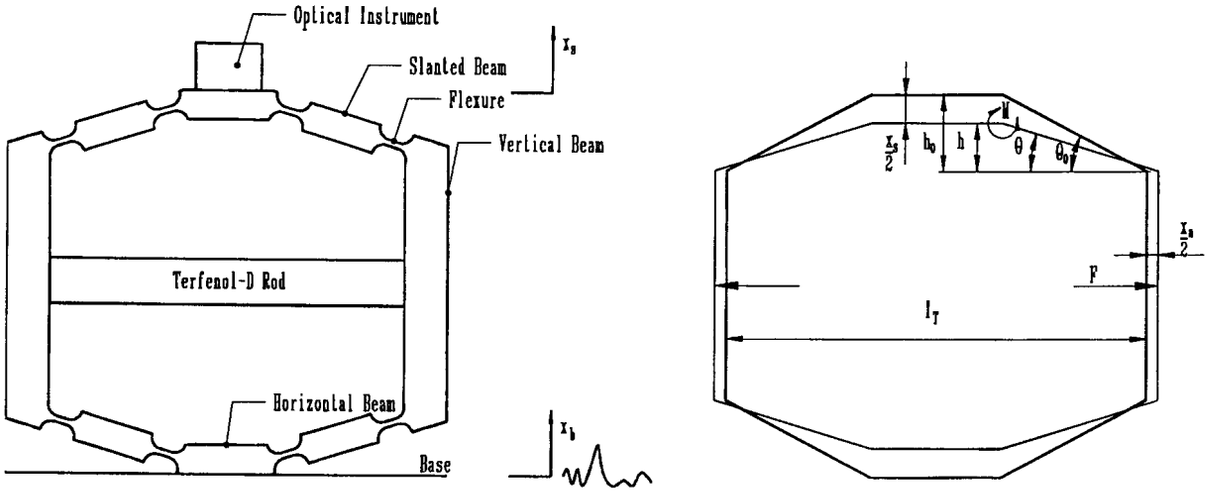

Figure 3.4.1.5: Octagonal flexural gain mechanism

The initial length of the Terfenol-D rod is l_T. The length of each slanted beam is r and the initial slope angle and height of the beam are θ_0 and h_0 respectively. The principle of operation of the gain mechanism is as follows: During excitation, a strain ε is produced in the rod, which generates a force F in the rod and extends the length of the mechanism by x_a. The force causes a bending moment M in the flexures, which tilts the slanted beam from an initial slope angle of θ_0 to a final slope angle of θ. The height of the slanted beam is reduced from an initial height h_0 to a final height h, which causes a vertical displacement x_s at the optical instrument. A displacement gain is brought about if x_s exceeds x_a.

An exact equation, which expresses the gain in terms of ε, l_T, r and θ_0, is derived in appendix Q. An alternative approximate equation, which expresses the gain in terms of θ_0 only, is also derived in the appendix. The gain factors obtained with the two methods are compared and it is shown that the gain depends strongly on θ_0, while ε, l_T and r have an insignificant effect.

The exact equation for the gain factor, in terms of r, θ_0, ε and l_T, is:

$$G = 2\frac{r\sin\theta_0 - \sqrt{r^2 - \left(r\cos\theta_0 + \frac{\varepsilon l_T}{2}\right)^2}}{\varepsilon l_T} \qquad \textbf{(3.4.1.18)}$$

The approximate equation for the gain factor, in terms of θ_0, is:

$$G = \cot\theta_0 \qquad \textbf{(3.4.1.19)}$$

The approximate gain factor is acceptably accurate for initial angles ranging from 5° to 35°, i.e. for gains ranging from 1,7 to 11,4 (see appendix Q). It can be concluded that, for the above range of θ_0, the gain depends strongly on θ_0, but is relatively insensitive to l_T, ε and r. The approximate gain factor, for slanted beam angles ranging from 5° to 30°, is shown in figure 3.4.1.6.

It has been shown above that the desired gain can be achieved by means of an octagonal flexural gain mechanism. The gain can be expressed in terms of the geometric properties of the octagon, using simple mathematical equations. As was the case with the elliptical structure discussed in the previous section, the gain factor is independent of the excitation frequency, as long as the system is not excited in the vicinity of one of its natural frequencies. This mechanism can therefore be designed to give an almost constant gain over a wide frequency band.

The octagonal gain mechanism is not plagued by the problems associated with the manufacture and installation of the ellipse because the sides are straight, thereby facilitating attachment of the actuator to the instrument and base. Due to the advantages just mentioned, the above method of achieving the desired gain will be employed in the design of the two Terfenol-D actuators.

However, there are also disadvantages that deserve to be addressed. One disadvantage is that the mechanism can only transmit and amplify motion through bending at the flexures. The latter will have to be very soft in order not to absorb too much actuator power. To this end, the flexures will have to be relatively thin, which could weaken the structure and lead to failure. Special attention will be paid to this problem during the detail design stage, which will be discussed in section 3.5.

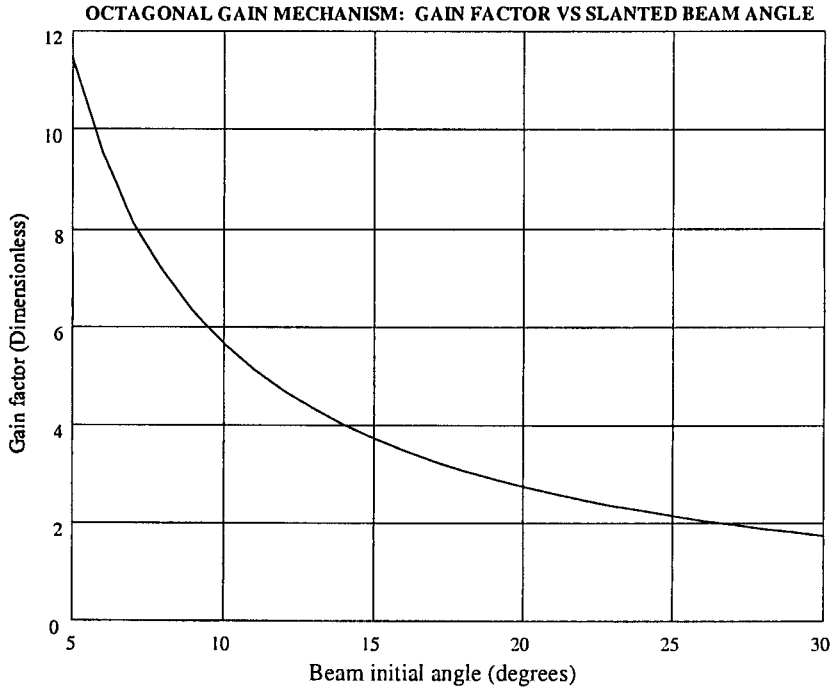

Figure 3.4.1.6: Gain factor versus initial angle of the slanted beam

This concludes the actuator gain mechanism concepts. Different concepts of achieving bias fields are discussed in section 3.4.2.

3.4.2 Magnetic biasing concepts

Two methods can be used to accomplish magnetic biasing. In the first method, a permanent magnet is used to induce a permanent bias field in the rod. This method is appropriately known as permanent magnet biasing. In the second method, an external current or voltage source is connected to the coil, to induce a field in the rod. The DC field is not permanent and will only be applied as long as the source is connected to the coil. This method is known as electromagnetic biasing. The two biasing methods will be discussed in short below.

Permanent magnet field biasing

Permanent magnet field biasing of a Terfenol-D rod is described in this section. The concept is shown diagrammatically. The principle of operation of permanent magnet biasing and its effect on dynamic excitation of the coil are explained. A number of permanent magnet materials are mentioned and their compositions and coercivities are tabled. The design philosophy of permanent magnet biasing is discussed and the necessary design equations are derived. The advantages and disadvantages of permanent magnet biasing are given.

A permanent magnet biasing concept is shown schematically in figure 3.4.2.1. A field coil is mounted concentrically around a Terfenol-D rod. The coil is connected to an AC voltage source, which induces an AC field in the rod. A permanent magnet, which induces a DC field

in the rod, is mounted concentrically around the coil. End caps are mounted at the rod ends to close the path of magnetic flux through the rod (see also figure 2.4.1). An air gap exists between the magnet and end caps. The force produced by the rod, due to the field, is F_r.

The DC field induced by the magnet biases the field in the rod. When the AC field is superimposed on the bias field, a fluctuating strain, with a displaced DC component, is produced. A positive strain results if a positive field is applied, while a negative strain results if a negative field is applied. This is known as the so-called "two-way effect" (see also figure 3.4.1).

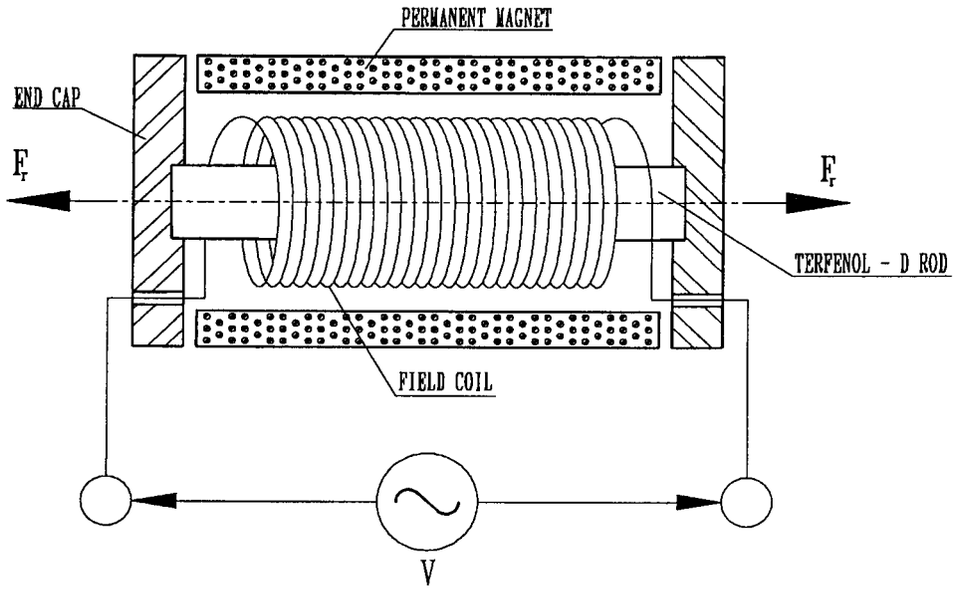

Figure 3.4.2.1: Permanent magnet field biasing of a Terfenol-D rod

The maximum field H_{max} is given by:

$$H_{max} = H_b + H_A \tag{3.4.2.1}$$

where H_b is the bias field and H_A is the amplitude of the AC component of the field.

The minimum field H_{min} is given by:

$$H_{min} = H_b - H_A \tag{3.4.2.2}$$

In order to ensure positive fields during excitation, the bias field must be equal to or larger than the field amplitude.

The maximum strain is the strain that corresponds with the maximum field at a given constant mechanical stress, i.e.:

$$\varepsilon_{max} = \varepsilon(H_b + H_A)\big|_{\sigma=const} \tag{3.4.2.3}$$

The minimum strain is the strain that corresponds with the minimum field at a given constant stress:

$$\varepsilon_{\min} = \varepsilon(H_b - H_A)\big|_{\sigma=const} \qquad \textbf{(3.4.2.4)}$$

As an example, consider a field with a bias component of 50 kA/m and a harmonic AC component of 50 kA/m excited at a frequency of 1 Hz. The stress is –12 MPa. The field is shown graphically in figure 3.4.2.2. The maximum field is 100 kA/m, while the minimum field is 0 kA/m. The maximum strain, from equation 2.3.1 and table 2.3.1 (for the dehysterized characteristic), is 1003 $\mu\varepsilon$, while the minimum strain is 0 $\mu\varepsilon$.

If the permanent magnet is removed and only the AC field is applied, the bias field will be zero. Irrespective of the direction of the field, a positive strain will result (the so-called "one-way effect"). This will considerably reduce the strain in the rod, and consequently, also the actuator output stroke length. Repeating the analysis for the above example, with $H_b = 0$ in equations 3.4.2.3 and 3.4.2.4, the maximum and minimum fields will be 50 kA/m and –50 kA/m respectively. The maximum strain of 572 $\mu\varepsilon$ will occur at both 50 kA/m and –50 kA/m, while the minimum strain will be 0 $\mu\varepsilon$. The maximum strain, if compared with that achieved with a bias field of 50 kA/m, is approximately 43% lower.

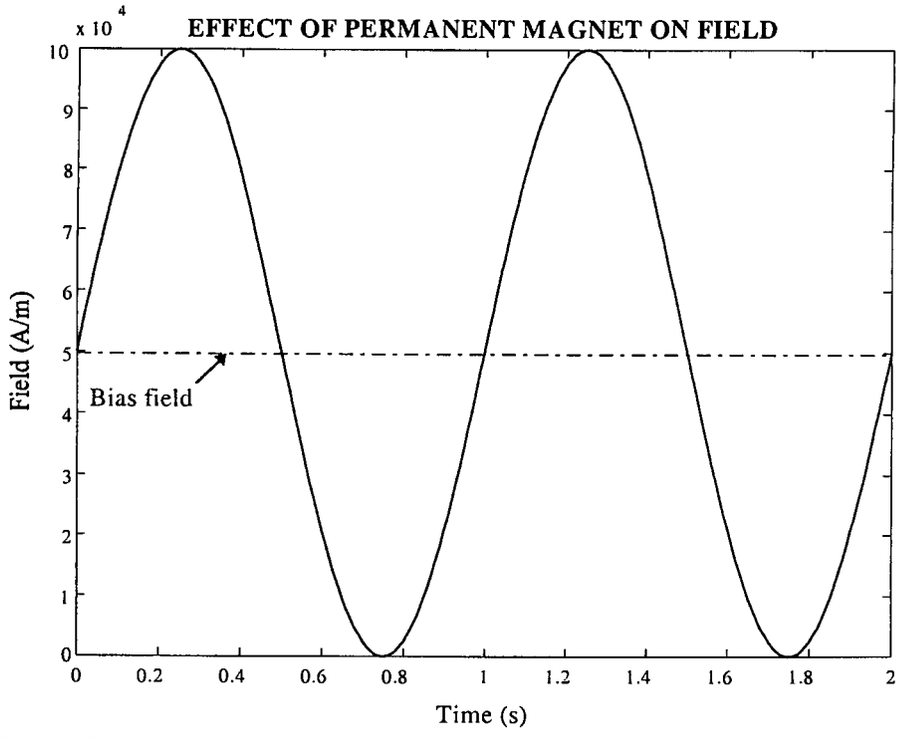

Figure 3.4.2.2: Effect of permanent magnet on field strength

Permanent magnets are generally made of hard magnetic materials with high intrinsic coercivities. The coercivity of a magnetic material is its ability to resist demagnetization. Traditionally, magnetic materials with coercivities above 10 kA/m have been known as hard magnetic materials [Jiles, 1991].

However, modern permanent magnet materials display coercivities two orders of magnitude larger than this. Samarium-cobalt, with a coercivity of 696 kA/m, has been a very popular permanent magnet material since 1967. More recently, in 1984, neodymium-iron-boron was introduced, with a coercivity of almost twice that of samarium-cobalt. The coercivities of various permanent magnet materials and their composition, from Jiles [1991], are given in table 3.4.2.1.

Table 3.4.2.1 Compositions and coercivities of various permanent magnet materials [Jiles, 1991]

Material	Composition	Coercivity (kA/m)
Steel	99% Fe,1% C	4,00
36 Co Steel	36% Co, 3,75% W, 5,75% Cr, 0,8% C	18,25
Alnico 2	12% Al, 26% Ni, 3% Cu, 63% Fe	52,00
Alnico 5	8% Al, 15% Ni, 24% Co, 3% Cu, 50% Fe	57,60
Alnico DG	8% Al, 15% Ni, 24% Co, 3% Cu, 50% Fe	56,00
Ba Ferrite	$BaO_6Fe_2O_3$	192,00
PtCo	77% Pt, 23% Co	344,00
Remalloy	12% Co, 17% Mo, 71% Fe	18,40
Vicalloy	13% V, 52% Co, 35% Fe	36,00
Samarium-cobalt	$SmCo_5$	696,00
Neodymium-iron-boron	$Nd_2Fe_{14}B$	1120,00

The goal of permanent magnet design is to obtain the magnet volume, which will give the desired bias field in the rod. The magnet volume V_m, in terms of the bias field, rod, magnet and air gap parameters, from appendix R, is given by:

$$V_m = \frac{B_T(H_b)A_T}{B_m H_m}\left(H_b l_T - \frac{B_T(H_b)A_T l_g}{\mu_0 A_g}\right) \qquad \textbf{(3.4.2.5)}$$

For a cylindrical magnet, the volume, in terms of the dimensional parameters, is:

$$V_m = \frac{\pi}{4}\left(d_o^2 - d_i^2\right)l_m \qquad \textbf{(3.4.2.6)}$$

where d_i and d_o are the magnet inner and outer diameters respectively.

Equations 3.4.2.5 and 3.4.2.6 provide the most important design equations for permanent magnet biasing of the Terfenol-D rod. In equation 3.4.2.5, the term B_mH_m is known as the magnet energy. Magnets are normally designed in such a way that the product of B_mH_m is a maximum [McCaig & Clegg, 1987].

The advantage of permanent magnet biasing is a considerable reduction in the required coil current, coil input voltage and power. The field supplied by the external source only requires an AC component, while the DC component is supplied by the permanent magnet.

However, there are also disadvantages to this method of magnetic biasing. The permanent magnet may become demagnetized if exposed to high fields and high temperatures. Even if used at relatively low temperatures, demagnetization may occur with time. The process can be retarded by using a permanent magnet with a high coercivity, but these materials are relatively expensive. Due to the high cost, permanent magnet biasing will not be considered in this study. An alternative magnetic biasing method, i.e. electromagnetic biasing, will be discussed in the next section.

Electromagnetic field biasing

This section discusses magnetic biasing of a Terfenol-D rod by means of an electromagnetic field. The concept is shown and the principle of operation is discussed. Equations for the coil current, voltage and power are given in terms of the bias field, field amplitude and excitation frequency. The power requirement of electromagnetic biasing is compared with that of permanent magnet biasing. The advantages and disadvantages of electromagnetic biasing are discussed. Electromagnetic biasing is motivated and selected as the most suitable magnetic biasing concept for this study.

An electromagnetic field biasing concept is shown in figure 3.4.2.3. A Terfenol-D rod is mounted concentrically inside a field coil, which is connected to an external voltage source with a voltage V. The end caps act as couplers to close the magnetic flux path (see also figure 2.4.1). The voltage source induces a field, which contains both the AC and bias (DC) fields, in the rod. The bias field is only present as long as the external source is connected to the coil. The force produced by the rod, due to the applied field, is F_r.

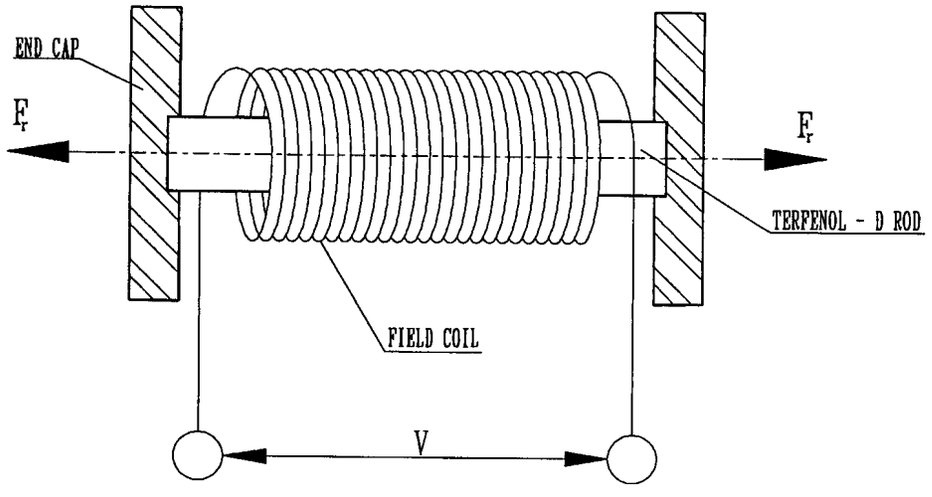

Figure 3.4.2.3: Electromagnetic field biasing of a Terfenol-D rod

The coil input current required to give the desired field in the rod, from equation 2.4.4, is:

$$I = \frac{l_T}{N} H \tag{3.4.2.7}$$

where I is the coil current, l_T is the rod length, N is the number of coil turns and H is the strength of the magnetic field in the rod. The coil impedance Z is given by:

$$Z = \sqrt{R_c^2 + \omega^2 L_0^2} \tag{3.4.2.8}$$

where R_c is the coil resistance, L_0 is the clamped inductance of the coil and ω is the angular excitation frequency. The voltage V supplied to the coil is the product of the coil impedance Z and the coil current I:

$$V = ZI \tag{3.4.2.9}$$

Substitution of equations 3.4.2.7 and 3.4.2.8 into equation 3.4.2.9 gives the coil voltage as follows in terms of the field:

$$V = \frac{l_T}{N} \sqrt{R_c^2 + \omega^2 L_0^2} H \tag{3.4.2.10}$$

The coil power is the product of the coil voltage and the coil current:

$$P = VI \tag{3.4.2.11}$$

The maximum coil current, voltage and power, from appendix S, are expressed as follows:

$$I_{\max} = \frac{l_T}{N}(H_b + H_A) \tag{3.4.2.12a}$$

$$V_{\max} = \frac{l_T}{N} \sqrt{R_c^2 + \omega^2 L_0^2}(H_b + H_A) \tag{3.4.2.12b}$$

$$P_{\max} = \left(\frac{l_T}{N}\right)^2 \sqrt{R_c^2 + \omega^2 L_0^2}(H_b + H_A)^2 \tag{3.4.2.12c}$$

Equations 3.4.2.12 give the relationships between the most important coil performance parameters for electromagnetic field biasing.

Equations 3.4.2.12 can also be used to compare the performance of a permanent magnet biased field with that of an electromagnetically biased field.

For permanent magnet biasing, the DC component of the field induced by the coil is zero, in

which case equations 3.4.2.12 become:

$$I_{\max} = \frac{l_T}{N} H_A \tag{3.4.2.13a}$$

$$V_{\max} = \frac{l_T}{N} \sqrt{R_c^2 + \omega^2 L_0^2}\, H_A \tag{3.4.2.13b}$$

$$P_{\max} = \left(\frac{l_T}{N}\right)^2 \sqrt{R_c^2 + \omega^2 L_0^2}\, H_A^2 \tag{3.4.2.13c}$$

The difference $\Delta P_{\max}$ between the maximum coil power for an electromagnetically biased field and that for a permanent magnet biased field, by subtracting equation 3.4.2.13c from equation 3.4.2.12c, is:

$$\Delta P_{\max} = \left(\frac{l_T}{N}\right)^2 \sqrt{R_c^2 + \omega^2 L_0^2}\left(H_b^2 + 2H_b H_A\right) \tag{3.4.2.14}$$

It can be seen from equation 3.4.2.14 that the difference between the maximum coil power for electromagnetic field biasing and that for permanent magnet field biasing, increases with bias field.

The advantage of electromagnetic field biasing is a substantial saving in the cost of a permanent magnet. As was mentioned in the previous section, the cost of permanent magnet materials, such as samarium cobalt, is high. Another advantage of electromagnetic biasing is simplicity of construction of the actuator. Both DC and AC components of the field are supplied by the coil, therefore a permanent magnet is not required and can be omitted. This further reduces actuator size and mass.

The disadvantage of electromagnetic field biasing is power consumption, as indicated in equation 3.4.2.14. Although an initial cost saving can be effected by using electromagnetic biasing, the running cost of this biasing method will be higher. However, since the aim of this study is to build and test a technology demonstrator, the high initial cost of a permanent magnet cannot be justified, therefore electromagnetic biasing will be used.

This concludes the discussion on magnetic biasing. A number of mechanical biasing techniques will be investigated in section 3.4.3 and the most suitable concept will be motivated and selected.

3.4.3 Mechanical biasing concepts

Mechanical biasing, or prestressing, of a Terfenol-D rod, is discussed in this section. A motivation for mechanical biasing is given, and the principle of operation is explained. Two methods of achieving mechanical biasing, i.e. by means of Belleville springs and coil springs, are discussed. The parameters which determine the characteristics of each spring type are mentioned, and the force versus deflection characteristic of each spring type is given mathematically and graphically. The advantages and disadvantages of each spring type are discussed and the use of coil springs is motivated.

It was shown in section 3.4 that a Terfenol-D rod subjected to a compressive prestress, will give higher saturation strains than an unstressed rod. The advantage of applying a compressive prestress to the rod is a larger rod strain and therefore a longer actuator stroke length for the same peak-to-peak magnetic field.

Mechanical prestressing of a Terfenol-D rod is shown schematically in figure 3.4.3.1. A prestress is brought about by a compressive force F_b acting at the ends of the rod. The end caps aid in distributing the stress uniformly over the rod cross-sectional area, denoted by A_T.

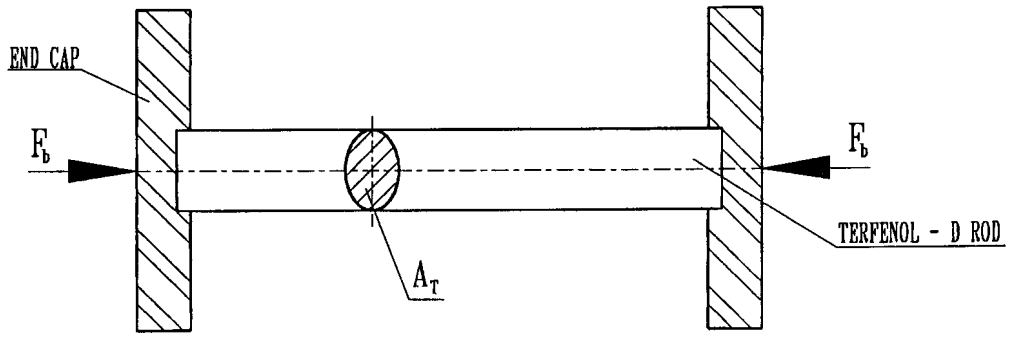

Figure 3.4.3.1: Mechanical prestressing of a Terfenol-D rod

The prestress σ_b is the ratio of the spring force F_b to the cross-sectional area A_T of the rod:

$$\sigma_b = \frac{F_b}{A_T} \qquad \textbf{(3.4.3.1)}$$

Practically, a prestress can be accomplished by using a mechanical spring, which exerts a force on the rod via an end cap (see figure 3.4.3.2). The prestress depends on the force versus deflection characteristic of the spring, initial spring deflection and rod cross-sectional area. In order to provide a relatively constant prestress during excitation, the initial deflection of the spring must be relatively large in comparison with the magnetostrictive deformation of the rod.

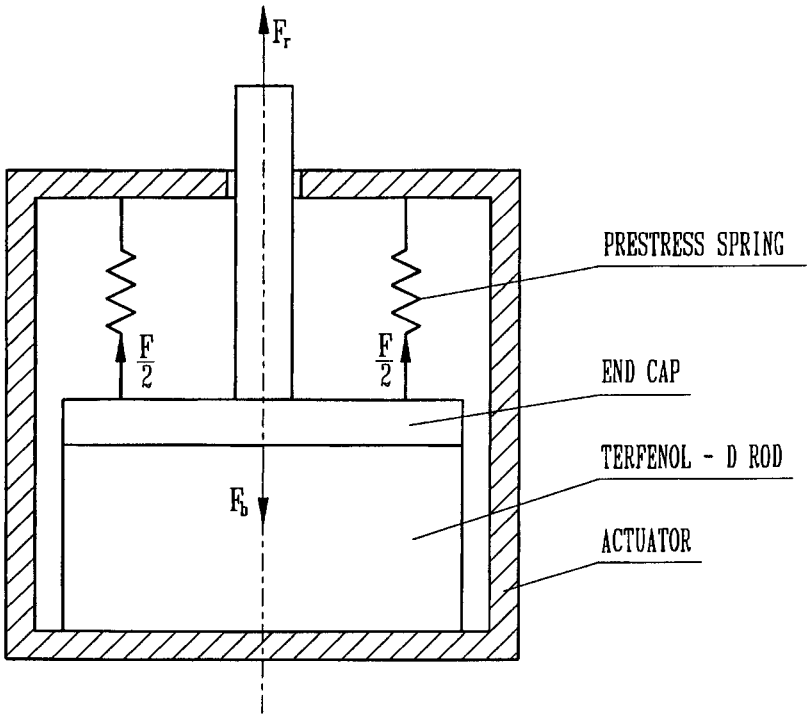

Figure 3.4.3.2: Prestressing by means of a mechanical spring

The spring force F is a function of the initial deflection x_i of the spring:

$$F = F(x_i) \tag{3.4.3.2}$$

The bias force acting on the rod is equal to the spring force:

$$F_b = F \tag{3.4.3.3}$$

Rod prestress can be enhanced by gaining the spring force. This can for instance be accomplished by using a displacement gain mechanism, as was discussed in section 3.4.1. The advantage is that the desired prestress can be achieved by using a relatively soft spring. For a gain factor of G, rod prestress, in terms of spring force, is given by:

$$F_b = GF \tag{3.4.3.4}$$

Two spring types, which can be considered for mechanical biasing, are Belleville springs (or Belleville washers) and coil springs. The two spring types are discussed in short below. The dimensional parameters, force versus deflection characteristics, advantages and disadvantages of each spring type are given. Belleville washers are discussed first, followed by a discussion of coil springs.

Mechanical biasing with Belleville springs

A Belleville spring is shown in figure 3.4.3.3. The spring has the shape of a shallow conical disc, or washer, with a hole in the centre. The conical angle is α. The outer diameter of the washer is D_e and the diameter of the hole is D_i. The thickness of the spring is t, the free height is h and the total height is H. The applied axial compressive force is F and the spring deflection is x.

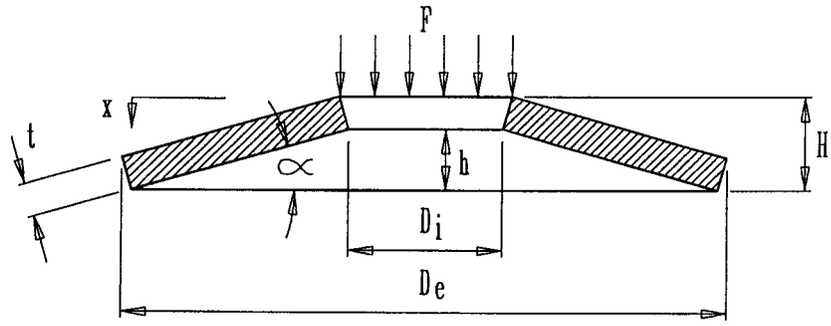

Figure 3.4.3.3: Diagrammatic representation of a Belleville spring

The force versus deflection characteristic is given as follows by Roark & Young [1983]:

$$F = \frac{4E}{\left(1-\nu^2\right)MD_i^{\,2}}\left[\left(h-x\right)\left(h-\frac{x}{2}\right)t+t^3\right]x \qquad \textbf{(3.4.3.5)}$$

where E and ν are Young's modulus and Poissons' ratio of the spring material and M is a dimensionless constant which depends on the ratio of the outer diameter of the spring to the hole diameter. M can be conveniently described by the following approximate empirical equation, which was obtained by interpolation from data supplied by Roark & Young [1983]:

$$M \approx 0{,}8196 - \frac{0{,}8516}{\left(D_e/D_i\right)^{2{,}7}} \qquad \textbf{(3.4.3.6)}$$

As can be seen from equation 3.4.3.5, spring force is a cubic function of deflection. The parameters E, ν, M and D_i are constant for a given spring, while t, h and x are variables, which determine the shape of the characteristic. The influence of t and h on the characteristics of two Belleville washers is illustrated in figure 3.4.3.4. Both springs have an outer diameter of 10 mm, a hole diameter of 3,2 mm and a thickness of 0,3 mm. The free height to thickness ratio of the first spring is 1,435 and that of the second spring is 1,167. The maximum deflection is 1 mm in both cases.

A high degree of nonlinearity is displayed by both spring characteristics. The differences in the two characteristics are the following: The force curve of spring I initially rises more sharply than that of spring II. However, for deflections between 0,3 mm and 0,6 mm, the force curve of spring I displays a region of zero gradient, or constant force, while the slope of the force curve of spring II shows an increasing trend. For deflections larger than 0,5 mm, the

compressive force of spring II exceeds that of spring I. At the maximum deflection of 1 mm, the maximum compressive force of spring I is 460 N, while that of spring II is 660 N.

Figure 3.4.3.4 highlights the most important advantage of a Belleville spring, i.e. that a constant force versus deflection characteristic can be obtained over a reasonably wide deflection range by proper selection of the *h/t* ratio. This feature makes the spring particularly desirable for maintaining a constant prestress in the Terfenol-D rod.

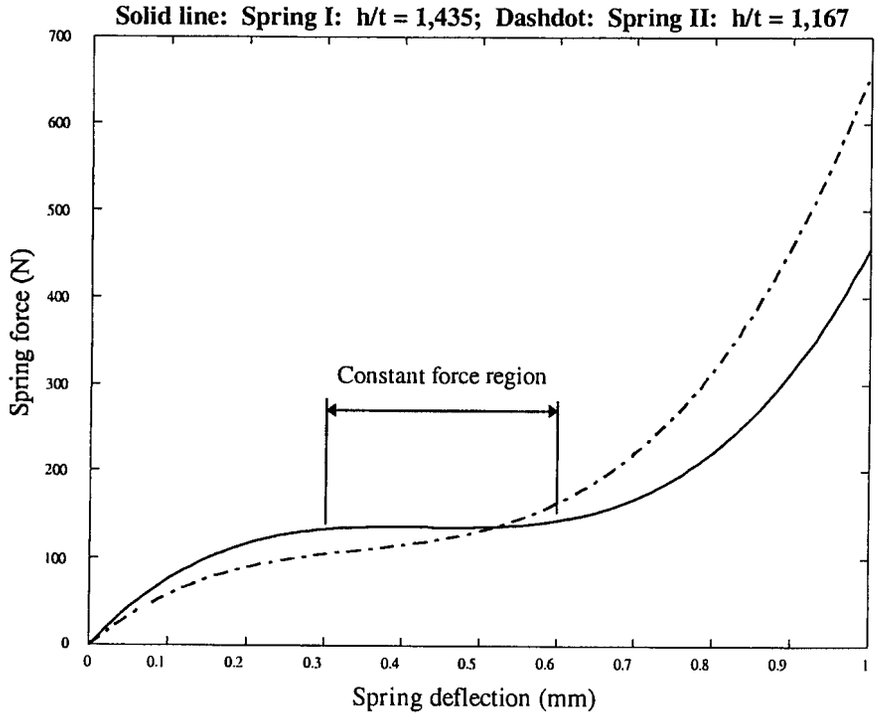

Figure 3.4.3.4: Spring force versus deflection characteristics of two Belleville springs

Belleville springs have a number of disadvantages: In the first place, due to their low height, Belleville springs are relatively stiff in comparison with other spring types. In order to reduce stiffness, a number of springs must be stacked. This leads to another problem, i.e. that during dynamic excitation, friction forces act at contact surfaces between the springs, which may cause hysteresis losses in the actuator output displacement. The problem can be overcome by lubricating the springs, but this will have to be done periodically in order to replenish the lubricant and to keep the springs clean.

A second disadvantage of using a conical spring for this application, is its nonlinearity. It was shown in chapter 2 that, due to magnetostrictive and magnetization saturation and hysteresis, Terfenol-D is a material which displays a high degree of nonlinearity in its static and dynamic behaviour. During characterization tests, it may be difficult to isolate material nonlinearities from spring nonlinearities. Lastly, depending on the *h/t* ratio, Belleville springs may become unstable at large deflections and may snap through.

For the abovementioned reasons, Belleville springs will not be considered for mechanical biasing. Coil springs are a feasible alternative. The characteristics, advantages and disadvantages of a coil spring will be discussed next.

Mechanical biasing with coil springs

Mechanical biasing of a Terfenol-D rod by means of a coil spring is described in this section. The spring parameters are given and the spring stiffness and spring wire shear stress are described in terms of the material and dimensional properties. The advantages and disadvantages of this spring type are mentioned. The coil spring is selected as the most suitable spring for mechanical biasing of the rod.

A diagrammatical representation of a coil spring is shown in figure 3.4.3.5. The outer diameter of the spring is D_e and the pitch circle diameter (PCD) is D. The change in the PCD during compression is ΔD. The free length is l_f and the compressed length is l_c. The wire diameter is d. The applied compressive force is F and the deflection is x.

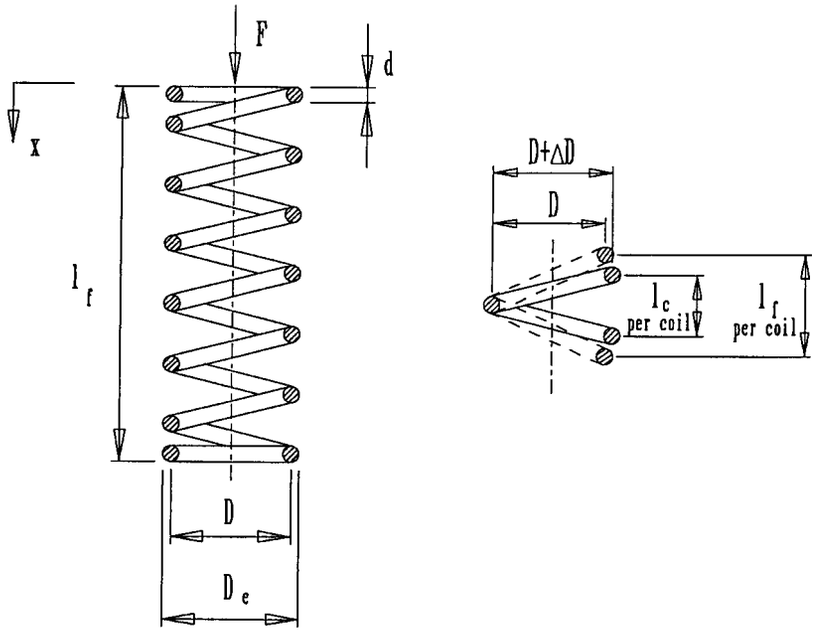

Figure 3.4.3.5: Diagrammatical representation of a coil spring

Two important coil spring parameters are the spring stiffness and spring wire shear stress. Equations for the spring characteristic and shear stress in terms of the spring material properties, dimensional parameters and type of coil ends, will be given in the following paragraphs. It will be shown that the characteristic of a coil spring is weakly nonlinear, but can, for this application, be assumed as linear.

Spring free length l_f can be expressed as follows in terms of the wire diameter d, total number of coils N_t and maximum deflection x_{max}:

$$l_f = dN_t + x_{max} \tag{3.4.3.7}$$

Rod prestress σ_b in terms of rod cross-sectional area A_T and compressive force in the rod F_b, is given by equation 3.4.3.1. F_b, in terms of spring force F and gain factor G, is given by equation 3.4.3.4. F, in terms of spring deflection x, is given by equation 3.4.3.2. For a spring with a linear characteristic, F is given by:

$$F = kx \tag{3.4.3.8}$$

where k is the spring stiffness, given as follows by the SAE Spring Design Manual [1990]:

$$k = \frac{G_s d^4}{8D^3 N_a} \tag{3.4.3.9}$$

In equation 3.4.3.9, G_s is the spring material shear stress modulus and N_a is the number of active coils. The latter is determined by the total number of coils N_t, and the type of spring end. The relationship between N_t and N_a is:

$$N_a = N_t - N_e \tag{3.4.3.10}$$

where N_e is the number of inactive coils. Values of N_e for different spring ends, from Shigley [1977], are given in table 3.4.3.1.

Table 3.4.3.1: N_e for different spring end types [Shigley, 1977]

Type of spring end	N_e
Plain end	0,5
Plain and ground end	1,0
Squared end	1,0
Squared and ground end	2,0

It can be seen from equation 3.4.3.9 that k is directly proportional to G_s, directly proportional to d^4, inversely proportional to D^3 and inversely proportional to N_a. Since these parameters are constant for a given spring, the stiffness is also constant.

Equations 3.4.3.8 to 3.4.3.10 are valid for a linear spring characteristic. However, a coil spring displays a weakly nonlinear characteristic, which can be attributed to a change in coil diameter during compression (see figure 3.4.3.5). The relative change in diameter $\Delta D/D$ can be described as a function of the spring pitch p, spring diameter D, wire diameter d and a dimensionless factor α which accounts for the degree of constraint from unwinding during

compression:

$$\frac{\Delta D}{D} = \alpha f(p, d, D) \tag{3.4.3.11}$$

For a spring which is constrained from unwinding, α and f are respectively given as:

$$\alpha = 0{,}05 \tag{3.4.3.12a}$$

$$f = \frac{p^2 - d^2}{D^2} \tag{3.4.3.12b}$$

where p is the pitch, given by:

$$p = \frac{l_f}{N_t} \tag{3.4.3.13}$$

When one or both ends of the spring are free to unwind without friction, α and f are given by:

$$\alpha = 0{,}1 \tag{3.4.3.14a}$$

$$f = \frac{p^2 - 0{,}8pd - 0{,}2d^2}{D^2} \tag{3.4.3.14b}$$

Equations 3.4.3.12 and 3.4.3.14 are valid for a spring whose deflection corresponds with the maximum spring deflection. However, due to the relatively small elongation of the Terfenol-D rod, the spring deflection and accompanying change in diameter will be insignificant. For this application, spring stiffness can therefore be considered as constant.

Apart from spring stiffness, another important parameter, which must be considered in the selection of a suitable spring type for mechanical biasing of the Terfenol-D rod, is stress. If a compressive force is applied to a coil spring, the coil wire is subjected to a shear stress. The shear stress depends on the spring PCD, wire diameter, applied force and spring index.

The shear stress τ_c is given by:

$$\tau_c = K_w \tau \tag{3.4.3.15}$$

where τ is given by:

$$\tau = \frac{8}{\pi}\frac{FD}{d^3} \tag{3.4.3.16}$$

K_w is the Wahl shear stress correction factor, given by:

$$K_w = \frac{4C-1}{4C-4} + \frac{0{,}615}{C} \qquad \textbf{(3.4.3.17)}$$

where C is the spring index, which is the ratio of the PCD to the wire diameter:

$$C = \frac{D}{d} \qquad \textbf{(3.4.3.18)}$$

Combination of equations 3.4.3.15 to 3.4.3.18, gives the shear stress as follows in terms of applied force, spring PCD and wire diameter:

$$\tau_c = \frac{D}{d}\left[\frac{4\left(\frac{D}{d}\right)-1}{4\left(\frac{D}{d}\right)-4} + \frac{0{,}615}{\left(\frac{D}{d}\right)}\right]\frac{8F}{\pi d^2} \qquad \textbf{(3.4.3.19)}$$

The main advantage of using a coil spring for mechanical biasing is its almost constant spring stiffness, as discussed above. A further advantage is that coil springs needn't be stacked to give the correct stiffness, as is required with Belleville springs. The problem of mechanical hysteresis can therefore be eliminated. Coil springs can be designed to give the desired stiffness by selecting the correct PCD, wire thickness and number of active coils (see equation 3.4.3.9).

The disadvantages of coil springs are twofold. In the first place, coil springs operate at high shear stresses, even during normal use. If exposed to high loads for long periods, coil springs tend to yield slowly and fail to maintain a constant force.

Secondly, coil springs may buckle under large compressive forces. This problem can however be overcome by a using a spring with a low free length to PCD ratio and by making use of fixed ends, instead of hinged ends. According to the SAE Spring Design Manual [1990], a free length to PCD (l_f/D) ratio of less than 5,2 is required for unconditional buckling stability of a spring with fixed ends. By comparison, a coil spring with hinged ends will be unconditionally stable if the free length to PCD ratio is less than 2,6.

In spite of the shortcomings of coil springs, this spring type is preferred to Belleville springs for mechanical biasing of the Terfenol-D rods. The advantages of coil springs outweigh the disadvantages. Spring life can be extended by designing more conservatively in order to reduce shear stresses, while the buckling problem is easily solved using a relatively low l_f/D ratio.

The concepts discussed in sections 3.4.1 to 3.4.3 can be combined to create a design concept for the actuators and LOS stabilization system. Section 3.4.4 will cover the actuator and system design concept.

3.4.4 Terfenol-D actuator and LOS stabilization system design concept

The Terfenol-D actuator and LOS stabilization system design concepts are described in this section. The Terfenol-D rods, gain mechanism, coils and prestress springs are combined into a unit to generate an actuator design concept. The concept is shown diagrammatically. A design concept for the support structure is also shown. The actuator and support structure concepts are combined to generate a system design concept.

An actuator design concept is shown in figure 3.4.4.1. The actuator consists of two Terfenol-D rods, a coil wound around each rod, two springs, four end caps, a gain mechanism, two bolts and nuts and a centrepiece. The coils induce a field in the rods, while the springs provide mechanical biasing in the form of compressive prestressing of the rods. The gain mechanism extends the elongation of the rods to provide the desired actuator stroke length, and also acts as a magnetic coupler to close the path of magnetic flux through the rods. The end caps serve as mechanical couplings between the rods and the gain mechanism, and locate the rods relative to the gain mechanism.

The bolts act as an additional measure to adjust the prestress in the rods and to complement the springs. The nuts lock the bolts to the gain mechanism to take up any free play in the actuator. The centrepiece provides a support for the rods and prestress springs.

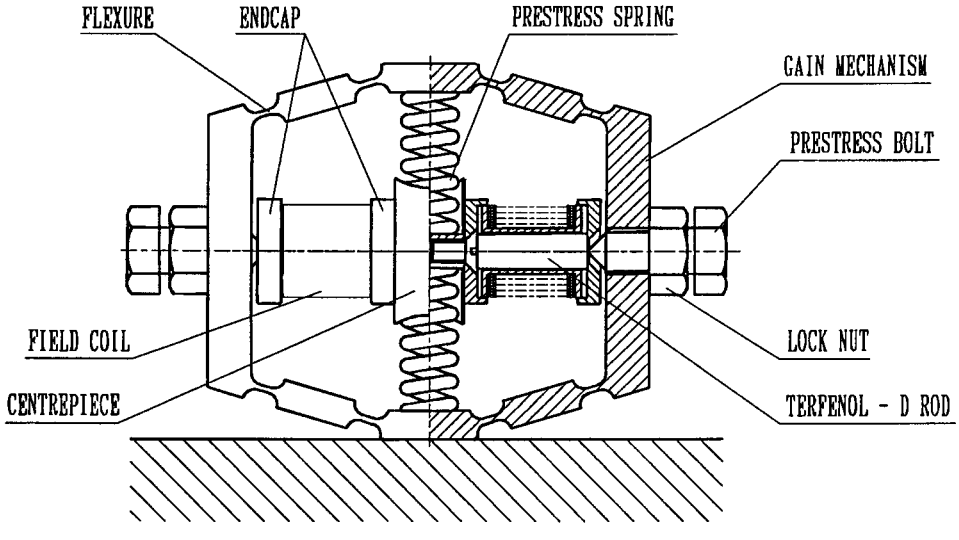

Figure 3.4.4.1: Terfenol-D actuator design concept

The actuator concept described above is used to generate a concept for the LOS stabilization system. The system is shown diagrammatically in figure 3.4.4.2. The system consists of two actuators, the optical instrument and its support structure. The support structure is soft at the actuator attachment points to allow easy bending, thereby making angular motion of the optical instrument possible. The actuators are mounted at the ends of the support structure to achieve the highest possible angular moment on the optical instrument.

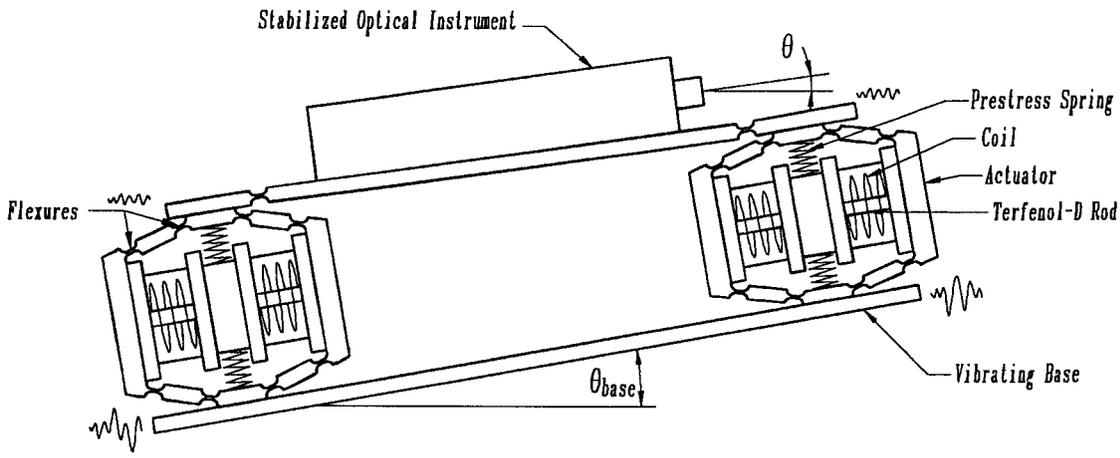

Figure 3.4.4.2: Terfenol-D LOS stabilization system design concept

This concludes the design concepts. A detailed design of the system and all its components will be done in section 3.5. The concept generated in this section will form the basis of the design.

3.5 Detailed design of the Terfenol-D actuators and stabilization system

A detailed design of the Terfenol-D actuators and optical instrument support structure is done in this section. The Terfenol-D rod length and diameter, rod strain and elongation, actuator displacement gain factor, gain mechanism stiffness and maximum stress are determined. The finite element method is used to determine the design parameters of the gain mechansim and support structure. The field coils and prestress springs are designed. Design theory is given and practical design aspects are addressed. Design parameters and geometries are calculated, tabled and shown graphically.

Gain mechanism design, including the calculation of the Terfenol-D rod length and diameter, rod elongation and strain, actuator displacement gain factor, gain mechanism stiffness and maximum stress are determined in section 3.5.1. The field coils and prestress springs are designed in sections 3.5.2 and 3.5.3 respectively. The support structure is designed in section 3.5.4.

3.5.1 Detailed design of the Terfenol-D actuators

Design of the Terfenol-D actuators is described in detail in this section. The required Terfenol-D rod length, diameter and cross-sectional area are calculated. The necessary mathematical equations are given and practical aspects to be taken into account, are discussed. Suitable actuator gain factor and rod length are selected, using the simulated and required stroke lengths and rod strain. Rod diameter is calculated from the strain, gain factor and required output force. Gain mechanism geometry, maximum mechanism stress, mechanism stiffness and mechanism deflection profile are determined. A first order calculation of the

required slanted beam angle is done, followed by a more comprehensive finite element calculation. Actuator parameters are tabled.

Rod length, diameter and actuator gain factor

The mathematical relationship between actuator output stroke length, displacement gain factor and rod elongation, is:

$$y_a = Gx_r \tag{3.5.1.1}$$

where y_a is output stroke length, G is gain factor and x_r is rod elongation. Rod elongation is the product of the strain in the rod and rod length:

$$x_r = \varepsilon l_T \tag{3.5.1.2}$$

where ε is rodstrain and l_T is rod length. Substitution of equation 3.5.1.2 into equation 3.5.1.1 gives the actuator output displacement in terms of the gain factor, rod length and strain in the rod:

$$y_a = Gl_T\varepsilon \tag{3.5.1.3}$$

from which:

$$Gl_T = \frac{y_a}{\varepsilon} \tag{3.5.1.4}$$

Equation 3.5.1.4 will be used to determine the gain factor and strain.

Comparison between simulated and required stroke length and strain

The simulated (quasi-static) stroke length, from table 2.7.3.2, is:

$$y_{a\max} = 178{,}5\,\mu m \tag{3.5.1.5}$$

The maximum strain corresponding to the above actuator stroke length is:

$$\varepsilon_{\max} = 944\,\mu\varepsilon \tag{3.5.1.6}$$

The stroke length and strain obtained with the simulations can be compared with those required to reject the disturbance. The required stroke length, from table 3.3.2, is:

$$y_a = 75\mu m \tag{3.5.1.7}$$

If equations 3.5.1.5 and 3.5.1.7 are compared, it can be seen that the required stroke length is considerably shorter (approximately 60%) than the simulated stroke length. The latter was

obtained with a gain factor of 5,4, which was arbitrarily selected for the simulations (see table 2.7.3.1).

The simulated value of the maximum rod strain, i.e. 944 $\mu\varepsilon$, is acceptable since it is in the linear region of the strain versus field characteristic (see figure 3.4.1). For this strain, saturation nonlinearities can, for all practical purposes, be neglected. A maximum strain of 944 $\mu\varepsilon$ is therefore a feasible value and will be used in the design calculations that follow. If a higher maximum strain is allowed, magnetostrictive saturation may be encountered. On the other hand, if strain is limited to a lower value, excessive rod length may be required. This may lead to rod buckling, especially if compressive prestresses are applied to enhance saturation strain.

Practical aspects to be considered in the selection of rod length and gain

Practical factors to be taken into account in selecting a suitable rod length and gain are as follows. From equation 3.5.1.4, it can be seen that, the shorter the rod, the higher the required gain for the same stroke length and strain. Higher gains have the advantage that lower coil input voltages are required to produce the desired actuator stroke length. However, higher gains lower the natural frequency (see equations 2.4.22 and 2.4.23). If the natural frequency is too low, the system isolation band may be too narrow to reject the disturbance.

Another disadvantage of a high gain is that it may be practically impossible to achieve. The reason is as follows: In order to make a high gain possible, a low slanted beam angle is required (see figure 3.4.1.6). A lower limit must however be placed on the slanted beam angle. If the angle is decreased below a certain value, which depends on the gain and flexure geometry, rod length and strain, the flexures will start to stretch, instead of bend. This will have an adverse effect on actuator output displacement.

For the purpose of assembling the actuators, the rods must be recessed in the end caps. The recessed parts of the rods are not exposed to the magnetic field and do not contribute to the actuator force. Additional rod length, known as the passive length, is required for this purpose. Furthermore, spools are required for winding the coils around the rods. Spool end thickness will inevitably add to the passive length. The danger of excessive passive length is that it may contribute to rod buckling and must therefore be limited as much as is practically possible.

Gain mechanism stiffness must be taken into account. In the simulations described in chapter 2, an ideal gain mechanism, i.e. with zero stiffness, was assumed. However, it is to be expected that the flexures of the octagonal gain mechanism (see figure 3.4.1.5) will not be ideal, i.e. their stiffness will not be zero. Flexure stiffness will add to actuator stiffness. Since actuator output displacement is inversely proportional to stiffness for the same field strength, output displacement will be reduced. In order to compensate for the reduction in displacement, the gain factor must be increased.

A last factor to be taken into account, is the cost of Terfenol-D rods. The manufacturer of the Tefenol-D rods, i.e. Etrema, prices rods per 25 mm length. To save cost, rod lengths must preferably be limited to 25 mm each.

Rod length and gain factor selection procedure

The procedure for obtaining rod length and gain factor is as follows: The values of y_a and ε_{max} in equations 3.5.1.6 and 3.5.1.7 are substituted into equation 3.5.1.4. A number of feasible rod lengths are arbitrarily selected, for which the corresponding gains are calculated. A rod length, with its corresponding gain, is subsequently decided upon. The resulting gain is adjusted to allow for gain mechanism stiffness. Rod length is adjusted to allow for recessing of rod ends in the end caps. (Passive length required for coil spool thickness will be addressed in the detailed coil design in section 3.5.2).

Substitution of equations 3.5.1.6 and 3.5.1.7 into equation 3.5.1.4 gives:

$$Gl_T = 0{,}0794 \text{ m} \qquad \textbf{(3.5.1.8)}$$

A number of arbitrarily selected rod lengths and corresponding gain factors, which satisfy equation 3.5.1.8, are given in table 3.5.1.1.

Table 3.5.1.1: Gain factors for selected rod lengths

Rod length l_T (m)	Gain factor G (Dimensionless)
0,025	3,18
0,030	2,65
0,035	2,27
0,040	1,99
0,045	1,76

A rod length of 35 mm, or 0,035 m, was used in the simulations in sections 2.7 and 2.8. For this rod length, the corresponding gain factor, from table 3.5.1.1, is 2,27. This gain factor will however be insufficient, since the effect of gain mechanism stiffness is not taken into account. To accommodate the reduction in output displacement, the gain factor must be increased. The percentage increase will depend on the ratio of gain mechanism stiffness to rod stiffness. Gain mechanism stiffness is unknown at this stage. It is assumed that the ratio of gain mechanism stiffness to rod stiffness will be approximately 20%. Consequently, the gain factor as given in table 3.5.1.1 is increased by approximately 20%, i.e. from 2,27 to 2,7. Therefore, the gain G is 2,7:

$$G = 2{,}7 \qquad \textbf{(3.5.1.9)}$$

Rod elongation x_r, from equation 3.5.1.1, for a gain factor of 2,7 and an actuator output displacement of 75.10^{-6} m, is:

$$x_r = 27{,}8.10^{-6} \text{ m} \qquad \textbf{(3.5.1.10)}$$

Passive rod length can be limited to 0,75 mm per rod end. The total length of the two rods, recessing included, is therefore 38 mm:

$$l_T = 38 \text{ mm} \tag{3.5.1.11}$$

The length l_r per rod, for two rods, is 19 mm:

$$l_r = 19 \text{ mm} \tag{3.5.1.12}$$

Selection of rod diameter and calculation of rod cross-sectional area

The relationship between actuator output force F_a, rod cross-sectional area A_T, rod strain ε and Youngs modulus E, is given by:

$$F_a = \frac{A_T E \varepsilon}{G} \tag{3.5.1.13}$$

from which A_T is obtained as:

$$A_T = \frac{G F_a}{E \varepsilon} \tag{3.5.1.14}$$

Young' modulus of Terfenol-D can vary from 16 GPa to 56 GPa (see figure 2.2.1.4). The average value of E, from table 2.7.3.2, is 23,46 GPa. It can be seen from equation 3.5.1.14 that the lowest E-value will give the highest cross-sectional area for the same strain, force and gain factor. In the interest of design safety, the lowest E-value, i.e. 16 GPa, is used to calculate A_T. For a gain factor of 2,7 (from equation 3.5.1.9), actuator force of 10,35 N (from table 3.3.2), Young's modulus of 16 GPa and strain of 944 $\mu\varepsilon$ (from equation 3.5.1.6), the rod cross-sectional area is:

$$A_T = 1{,}85.10^{-6} \text{ m}^2 \tag{3.5.1.15}$$

Rod cross-sectional area, in terms of rod diameter, is given by:

$$A_T = \frac{\pi}{4} d_T^2 \tag{3.5.1.16}$$

From equation 3.5.1.16, rod diameter is obtained as follows in terms of cross-sectional area:

$$d_T = \sqrt{\frac{4A_T}{\pi}} \tag{3.5.1.17}$$

The rod diameter d_T, which will give the required cross-sectional area in equation 3.5.1.15, is:

$$d_T = 1{,}53 \text{ mm} \tag{3.5.1.18}$$

The rod diameter in equation 3.5.1.18 is the minimum diameter that will give the required actuator output force. However, rods with this diameter are not produced by the manufacturer, Etrema. The smallest rod diameter produced, is 5 mm. During the time of actuator manufacture, the only available rod diameter was 6 mm. Therefore, the diameter of the Terfenol-D rods used in the actuators, is 6 mm:

$$d_T = 6 \text{ mm} \tag{3.5.1.19}$$

The cross-sectional area of the 6 mm rods, from equation 3.5.1.16, is:

$$A_T = 2{,}827.10^{-5} \text{ m}^2 \tag{3.5.1.20}$$

Actuator output force, for the above rod cross-sectional area, a strain of 944 $\mu\varepsilon$, Young's modulus of 16 GPa and gain of 2,7, from equation 3.5.1.13, is:

$$F_a = 158{,}2 \text{ N} \tag{3.5.1.21}$$

It can be seen that the actuator force is approximately 15 times higher than required (see equation 3.3.7). This is due to the fact that the rod diameter is approximately 4 times the required diameter.

Calculation of gain mechanism deflection, stiffness, stress and geometry

A concept of an octagonal gain mechanism was shown in figure 3.4.1.5. The gain mechanism geometry, deflection, stiffness and stresses are calculated in this section. To facilitate the calculation procedure, a mechanical model of the gain mechanism is used. The calculations are done in two stages. A 1st order calculation of the slanted beam angle is done, using a simple beam and hinge model. The assumptions made in the calculation are given. Shortcomings of the method are mentioned and the use of a more accurate and sophisticated finite element (FE) method is motivated. Calculation of the slanted beam angle is repeated using the FE method. The 1st order calculation of the slanted beam angle is used as an aid to determine gain mechanism geometry. Stresses and gain mechanism stiffness are calculated.

In order to do a first order calculation of the slanted beam angle, a simplified quarter model of the gain mechanism is used. The model consists of three beams, i.e. a horizontal beam, slanted beam and vertical beam, connected with hinges. The assumption is made that the beams are rigid and the hinges are frictionless.

The quarter model is shown in figure 3.5.1.1. The slanted beam length is r and its initial horizontal slope angle, before deflection, is θ_0. The force in the rod if F_r, the rod length is l and its elongation is x_r. The actuator output deflection is y_a.

The gain factor G is the ratio between y_a and x_r:

$$G = \frac{y_a}{x_r} \tag{3.5.1.22}$$

The relationship between the initial slanted beam angle and displacement gain factor is given by the following equation (see also equation 3.4.1.19):

$$G = \cot\theta_0 \tag{3.5.1.23}$$

For a given value of G, θ_0 can be obtained from equation 3.5.1.23 as:

$$\theta_0 = \cot^{-1}(G) \tag{3.5.1.24}$$

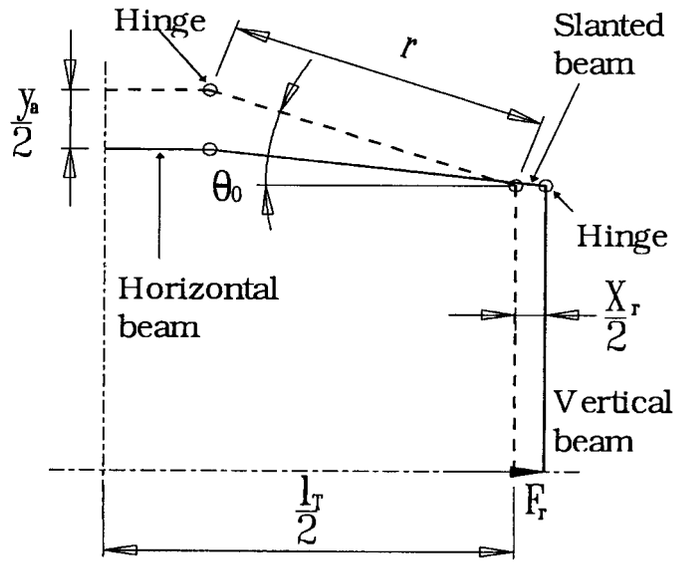

Figure 3.5.1.1: Octagonal gain mechanism beam and hinge quarter model

For a given gain factor of 2,7, the required slanted beam angle, from equation 3.5.1.24, is:

$$\theta_0 = 20{,}3° \tag{3.5.1.25}$$

The assumptions for which equation 3.5.1.25 is valid, are not realistic, since it is practically impossible to obtain zero flexure thickness and infinite beam thickness between flexures. A practically implementable gain mechanism will have beams and flexures with finite thickness, the flexures being considerably thinner than the beams. Consequently, the mechanism will bend in the flexures and slightly in the beams.

The bending profile is mathematically complicated to evaluate, since it will not only depend on mechanism geometry, but also on mechanism forces and displacements. The prestress spring force and rod elongation will cause stresses in the mechanism. These stresses will be higher in the flexures than in the beams. Furthermore, stress concentrations will be present at connecting points between flexures and beams. The 1st order method used above cannot be used to calculate stresses. A more powerful method, which takes the effects of geometry, forces and stress concentrations into account, is required. The finite element method (FEM) is used for this purpose. FEM calculation of the gain mechanism parameters is discussed below.

FEM calculation of gain, gain mechanism deflection profile, stiffness and stresses

The displacement gain factor, gain mechanism deflection profile, stiffness and maximum stress are calculated in this section, using the FE method. The method is applied iteratively to calculate the above parameters. In order to limit computational complexity, the analysis is carried out on a quarter model of the mechanism.

The method is applied as follows. An initial gain mechanism geometry is generated using the slanted beam angle obtained in equation 3.5.1.25. An element grid is generated. Mechanism boundary values are specified and material properties are given. Prestress spring and rod forces are applied and the deflection profile is calculated. The gain factor, which is the ratio between output displacement and rod end displacement, is calculated. Gain stiffness, which is the ratio between rod force and rod end displacement, is calculated. Maximum stress is calculated.

Calculated values of gain factor, mechanism stiffness and stresses are analyzed. If the stiffness is too high, flexure length is increased. If the gain factor is too low, the slanted beam angle is decreased. If stresses are too high, either flexure width or notch radius is increased. The procedure is repeated until the calculated parameters correspond with the required parameters.

Final gain mechanism geometry is shown in figure 3.5.1.2. The length of the slanted beam is 24,66 mm and its horizontal slope angle is 17°. The lengths and widths of the flexures are 2 mm and 1 mm respectively. The notch radii are 2 mm each. The thickness of the mechanism is 20 mm (not shown). Horizontal beam length is 14 mm and its width is 5mm. Vertical beam length and width are 46,87 mm and 7,5 mm respectively.

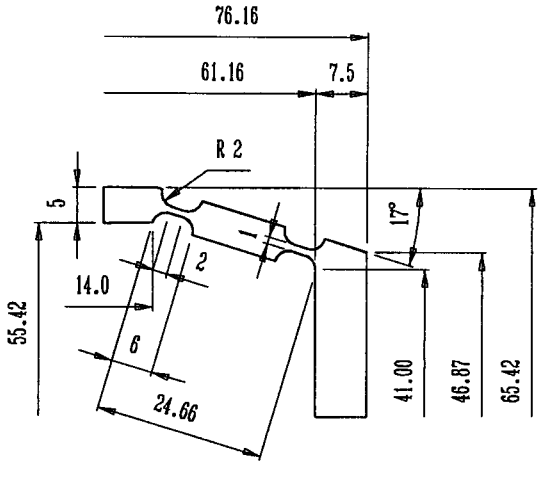

Figure 3.5.1.2: Gain mechanism quarter model geometry

The element grid is shown in figure 3.5.1.3. The number of elements, per quarter of the gain mechanism, is 624. Two-dimensional quadrangular elements are used. Mechanism boundary values are as shown in figure 3.5.1.3. Material is mild steel, with a Young's modulus of 210 GPa and a Poissons ratio of 0,29.

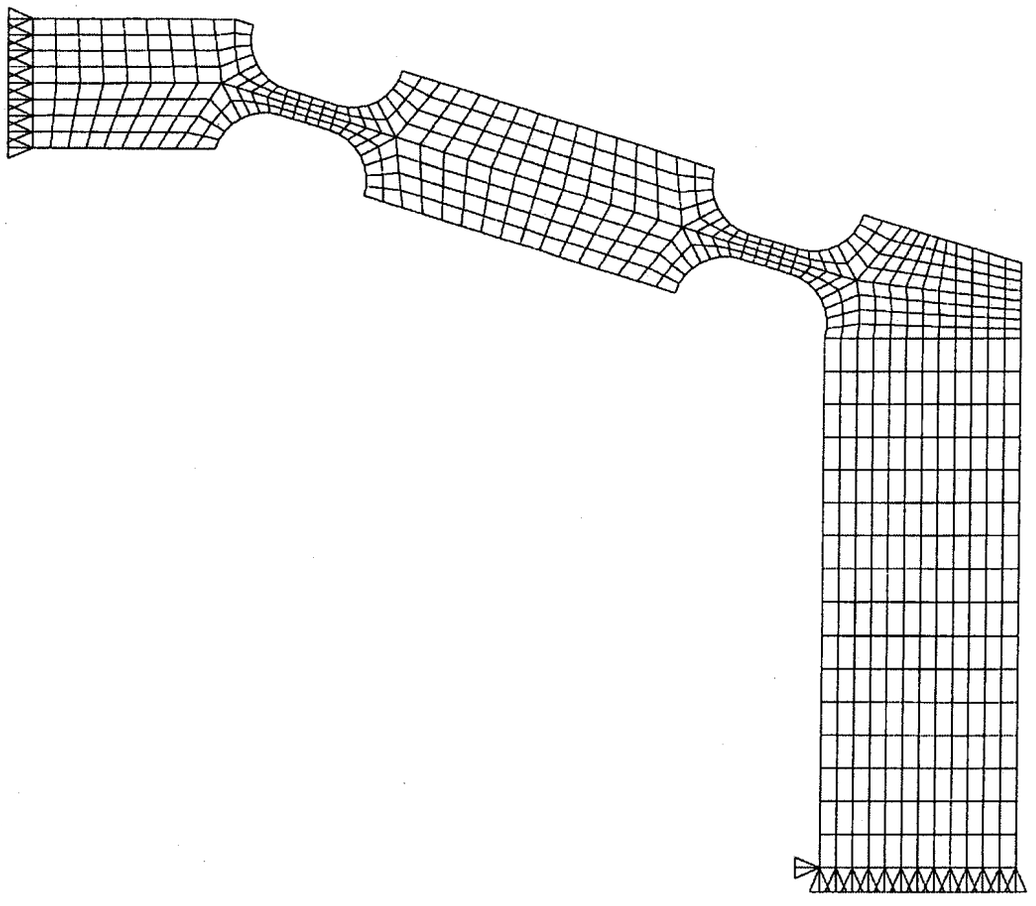

Figure 3.5.1.3: Gain mechanism quarter model finite element grid

The input forces and displacements applied to the gain mechanism are the prestress spring force and rod elongation. Spring force F is given by:

$$F = \frac{\sigma_b A_T}{G} \qquad \textbf{(3.5.1.26)}$$

where σ_b is the prestress, A_T is the rod cross-sectional area and G is the gain. For a gain of 2,7, rod cross-sectional area of $2{,}827.10^{-5}m^2$ and compressive prestress of 12 MPa, F is 125,66 N. The force acting on the quarter model is half the spring force:

$$\frac{F}{2} = 62{,}83 \text{ N} \qquad \textbf{(3.5.1.27)}$$

Rod elongation x_r, from equation 3.5.1.10 is $27{,}8.10^{-6}$ m. For the quarter model, the maximum horizontal displacement is half the rod elongation:

$$\frac{x_r}{2} = 13{,}9.10^{-6} \text{ m} \qquad \textbf{(3.5.1.28)}$$

A linear analysis is carried out to obtain the deflection shape, gain factor, maximum stress and gain stiffness. Gain mechanism stiffness is calculated as a percentage of rod stiffness. Both prestress spring force and rod elongation inputs are applied to calculate maximum stress, while only rod elongation is applied to calculate gain factor.

The deflection profile of the quarter model is shown in figure 3.5.1.4. The calculated parameters are given in table 3.5.1.2. For the sake of completeness, all the actuator parameters determined in section 3.5.1, are included.

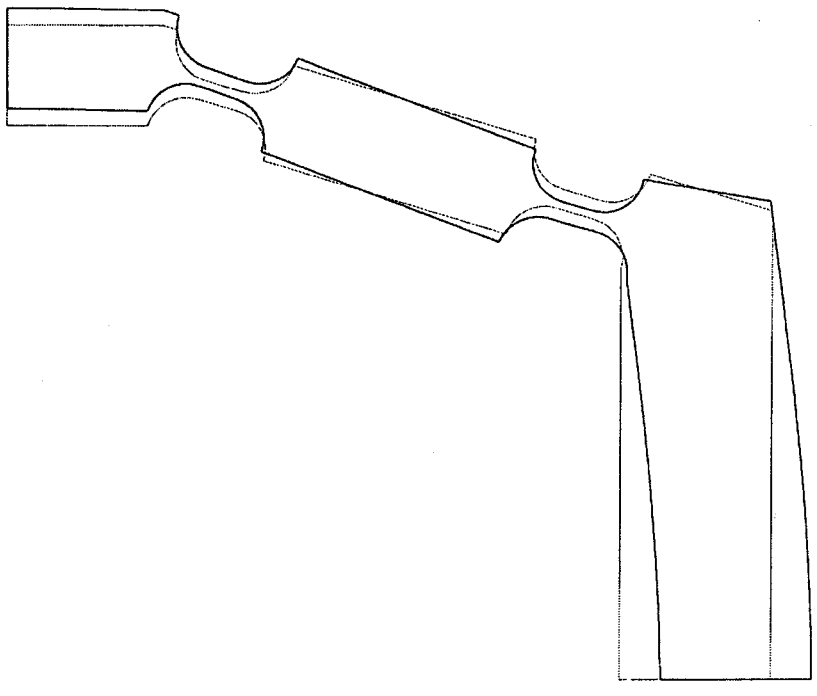

Figure 3.5.1.4: Gain mechanism deflection profile

Table 3.5.1.2: Terfenol-D actuator parameters

Parameter	Value
Terfenol-D rod length (total)	38 mm
Rod length (per rod)	19 mm
Rod diameter	6 mm
Rod cross-sectional area	$2{,}827.10^{-5}$ m^2
Rod elongation (total)	27,8 μm
Rod stiffness	$17{,}46.10^{6}$ N/m
Actuator stroke length	75 μm
Actuator gain factor	2,7
Actuator output force	158,2 N
Mechanism slanted beam angle	17°
Mechanism maximum stress	80,95 MPa
Mechanism stiffness	$3{,}28.10^{6}$ N/m
Ratio of mechanism stiffness to rod stiffness	18,8%

This concludes the gain mechanism design. Field coil design is covered in section 3.5.2.

3.5.2 Detailed design of field coils

The design of the field coils is described in detail in this section. Design input parameters are given, followed by all the required mathematical relationships. Practical design aspects are discussed. Coil parameters are calculated and tabled. Coil current, voltage and power versus frequency are shown graphically.

The given coil parameters are the Terfenol-D rod diameter, length and strain, actuator output force and stroke length, E, d^{σ}, d^{H} and μ^{σ} of Terfenol-D, coil bandwidth and maximum available input voltage. The input parameters, from sections 2.7, 2.8, 3.3 and 3.5.1 are summarized in table 3.5.2.1.

A parameter which is of particular importance in coil design, is μ^{σ}, since it, inter alia, determines the R_c/L_0 ratio. The higher μ^{σ}, the lower R_c/L_0. The value of μ^{σ} obtained from the simulations is 4,71 μTm/A (see section 2.8.5). This value of μ^{σ} includes the effects of hysteresis. This value is however considerably lower than the value of 11,6 μTm/A given by Butler [1988]. It is unknown whether the latter value includes hysteresis effects, but it is a safer value to use for design purposes, since it will give a lower R_c/L_0 ratio. In the interest of coil design safety, a μ^{σ} value of 11,6 μTm/A will be used.

Table 3.5.2.1: Coil design input parameters

Parameter	Value
Rod diameter	6 mm
Rod length (total)	38 mm
Actuator output force	158,2 N
Actuator stroke length	75 μm
Rod strain	944 $\mu\varepsilon$
Coil bandwidth	≥ 100 Hz
E of Terfenol-D	23,46 GPa
d^{σ} of Terfenol-D	$1{,}09.10^{-8}$ m/A
d^{H} of Terfenol-D	$8{,}14.10^{-9}$ m/A
μ^{σ} of Terfenol-D	$1{,}16.10^{-5}$ Tm/A
Maximum available coil voltage	28 V

Mathematical relationships required for coil design

The number of coil turns per layer n_c depends on the active rod length l_a and coated wire thickness d_{wc}. The relationship between n_c, l_a and d_{wc} is:

$$l_a = n_c d_{wc} \tag{3.5.2.1}$$

The coated wire thickness is the thickness of the bare copper wire plus the thickness of the coating:

$$d_{wc} = d_w + 2t_c \tag{3.5.2.2}$$

where d_w is the thickness of the bare wire and t_c is the coating thickness.

The number of coil turns N is given by:

$$N = n_c n_l \tag{3.5.2.3}$$

where n_c is the number of turns per layer and n_l is the number of layers.

The coil wire length l_c is given by:

$$l_c = \pi N D_c \tag{3.5.2.4}$$

where D_c is the arithmetic mean of the coil inner and outer diameters d_i and d_o:

$$D_c = \frac{d_i + d_o}{2} \tag{3.5.2.5}$$

The difference between the inner and outer diameters, in terms of n_l and d_{wc}, is:

$$d_o - d_i = 2n_l d_{wc} \tag{3.5.2.6}$$

The coil packing factor *pf*, which is the ratio of the packed volume of the coil, to the available volume, is given by:

$$pf = \frac{\pi N d_{wc}^2}{2(d_o - d_i)l_a} \tag{3.5.2.7}$$

The wire cross-sectional area A_w is:

$$A_w = \frac{\pi}{4} d_w^2 \tag{3.5.2.8}$$

The coil resistance R_c is given by:

$$R_c = \frac{\rho_c l_c}{A_w} \tag{3.5.2.9}$$

where ρ_c is the wire material resistivity.

R_c can be written as follows in terms of ρ_c, N, D_c and A_w:

$$R_c = \pi \frac{\rho_c N D_c}{A_w} \tag{3.5.2.10}$$

The rod cross-sectional area A_T is:

$$A_T = \frac{\pi}{4} d_T^2 \tag{3.5.2.11}$$

where d_T is the rod diameter.

The free inductance L_f is:

$$L_f = \frac{\mu^\sigma A_T N^2}{l_a} \tag{3.5.2.12}$$

where μ^σ is the free permeability of Terfenol-D.

The clamped inductance L_0 is:

$$L_0 = L_f\left[1-(cf)^2\right] \tag{3.5.2.13}$$

where cf is the coupling factor given by:

$$cf = \sqrt{\frac{Ed^{\sigma}d^{H}}{\mu^{\sigma}}} \tag{3.5.2.14}$$

L_0, in terms of the rod, coil and Terfenol-D magnetostrictive and magnetization parameters, is:

$$L_0 = \frac{\mu^{\sigma}A_T N^2}{l_a}\left(1-\frac{Ed^{\sigma}d^{H}}{\mu^{\sigma}}\right) \tag{3.5.2.15}$$

The −3dB bandwidth BW of the coil is given by:

$$BW = \frac{1}{2\pi}\frac{R_c}{L_0} \tag{3.5.2.16}$$

where R_c/L_0 is the coil resistance to inductance ratio.

The frequency-dependent coil impedance Z_c is:

$$Z_c = \sqrt{R_c^2 + \omega^2 L_0^2} \tag{3.5.2.17}$$

where ω is the angular frequency, given in terms of frequency f as:

$$\omega = 2\pi f \tag{3.5.2.18}$$

The coil phase angle φ between voltage and current is:

$$\varphi = \tan^{-1}\left(\frac{\omega L_0}{R_c}\right) \tag{3.5.2.19}$$

The field H, current I, voltage V and power P, for a biased harmonic field, are respectively given by:

$$H = H_b + H_A \sin \omega t \tag{3.5.2.20a}$$

$$I = \frac{l_a}{N}\left(H_b + H_A \sin \omega t\right) \tag{3.5.2.20b}$$

$$V = \frac{l_a}{N}\left[R_c H_b + Z_c H_A \sin\left(\omega t + \varphi\right)\right] \tag{3.5.2.20c}$$

$$P = \left(\frac{l_a}{N}\right)^2 \left[R_c H_b + Z_c H_A \sin\left(\omega t + \varphi\right)\right]\left[H_b + H_A \sin \omega t\right] \tag{3.5.2.20d}$$

The maximum field H_{max}, from equation 3.4.2.1, is:

$$H_{max} = H_b + H_A \tag{3.5.2.21}$$

The maximum current I_{max} is:

$$I_{max} = \frac{l_a}{N}\left(H_b + H_A\right) \tag{3.5.2.22}$$

The maximum input voltage V_{max} is:

$$V_{max} = \frac{l_a}{N}\left[R_c H_b + Z_c H_A \sin\left(\omega t_v + \varphi\right)\right] \tag{3.5.2.23}$$

where t_v is given by:

$$t_v = \frac{1}{\omega}\left[\left(2n+1\right)\frac{\pi}{2} - \varphi\right]; \quad n = 0, 2, 4, \ldots \tag{3.5.2.24}$$

The maximum power P_{max} is:

$$P_{max} = \left(\frac{l_a}{N}\right)^2 \left[R_c H_b + Z_c H_A \sin\left(\omega t_p + \varphi\right)\right]\left[H_b + H_A \sin \omega t_p\right] \tag{3.5.2.25}$$

where t_p is given by the roots of the following equation:

$$\frac{\cos \omega t_p}{Z_c \cos\left(\omega t_p + \varphi\right)} + \frac{H_b + H_A \sin \omega t_p}{R_c H_b + Z_c H_A \sin\left(\omega t_p + \varphi\right)} = 0 \tag{3.5.2.26}$$

Values of t_p which give minima of P are rejected.

The maximum rod strain ε_{max} is:

$$\varepsilon_{max} = \varepsilon(H_b) + d^H H_A \tag{3.5.2.27}$$

The minimum rod strain ε_{min} is:

$$\varepsilon_{min} = \varepsilon(H_b) - d^H H_A \tag{3.5.2.28}$$

The actuator static force F_a is:

$$F_a = \frac{A_T E}{G}(\varepsilon_{max} - \varepsilon_{min}) \tag{3.5.2.29}$$

The actuator static stroke length y_a is:

$$y_a = Gl_a(\varepsilon_{max} - \varepsilon_{min}) \tag{3.5.2.30}$$

Equations 3.5.2.1 to 3.5.2.30 give the most important equations required to calculate the coil parameters. Before the calculations can be done, a number practical coil aspects, which will have a significant influence on the design, are addressed. This is done in the next section.

Practical coil design aspects

Practical aspects to be considered in coil design, include factors such as passive rod length, space consumed by spools, packing methods and their influence on space utilization and magnetic saturation, the influence of coil impedance on amplifier output power, the influence of number of windings on coil frequency bandwidth, available wire diameters and insulation coating thickness. Each of these aspects, together with their respective influences on coil design, will be discussed in short below.

In order to allow ample space for coil spools and recessing of the rods in the end caps, the active rod length will be shorter than the total rod length. If 20% of the rod length is allowed for spools and recessing, 80% of the total rod length will be usable. From table 3.5.2.1, the total rod length is 38 mm. The usable, or active rod length, is therefore 30,4 mm.

The coil inner diameter must exceed the rod diameter, plus the spool thickness and free space between the spool and rod, to prevent sticking of the rod. The assumption is made that spool thickness and free space will take up no more than 40% of the rod diameter. The rod diameter, from table 3.5.2.1, is 6 mm. The coil inner diameter is therefore selected as 8,4 mm.

Coil packing methods include parallel and staggered packing. The two packing methods are shown diagrammatically in figures 3.5.2.1 and 3.5.2.2.

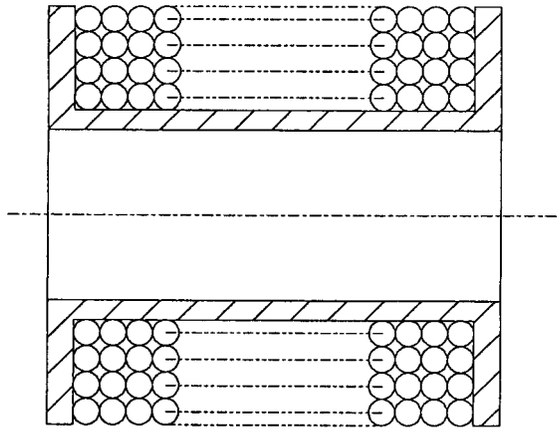

Figure 3.5.2.1: Parallel packing of a field coil

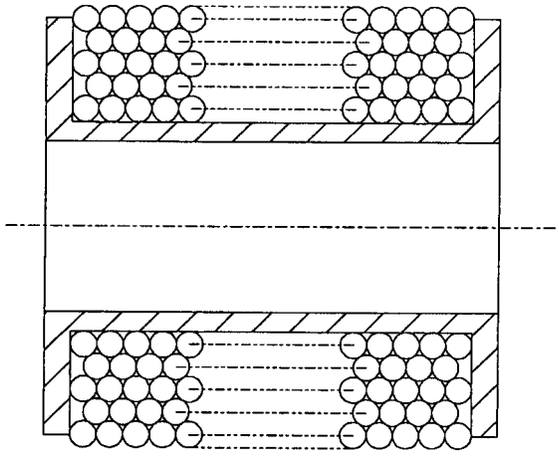

Figure 3.5.2.2: Staggered packing of a field coil

It can be seen from the above figures, that staggered packing gives better utilization of available coil space than parallel packing. However, a coil with staggered packing is more difficult to wind than a coil with parallel packing. During winding, a constant stress must be maintained in the wire, else the coil may deform as shown in figure 3.5.2.3. The consequence is that the centre of the Terfenol-D rod may be exposed to a larger field than the ends and may therefore magnetically saturate at relatively low coil currents. To avoid uneven fields, parallel packing will be used for the field coils in this study.

An important factor to be considered in coil design, is coil impedance. The coil impedance must be matched to that of the output circuit of an amplifier, which will be used to amplify the signal generator output voltage. If the impedance is too low, coil current and power will be excessive, resulting in clipping of the voltage signal and possible amplifier damage.

Amplifier output circuits are normally matched to electromagnetic field coils, such as audio loudspeaker coils, with impedances of 4Ω or 8Ω. For the same field and active rod length, an 8Ω coil will consume less power than a 4Ω coil. The impedance of the coils used in this study, will be 4Ω per actuator (at an excitation frequency of 100 Hz). The reason is that the field

biasing method that will be used in this study, is electromagnetic (see section 3.4.2). For electromagnetic biasing, both the bias and AC components of the field must be supplied by the power source. However, for future production models, field biasing will be done with permanent magnets, in which case only the AC component of the field will be required, thereby significantly reducing input power.

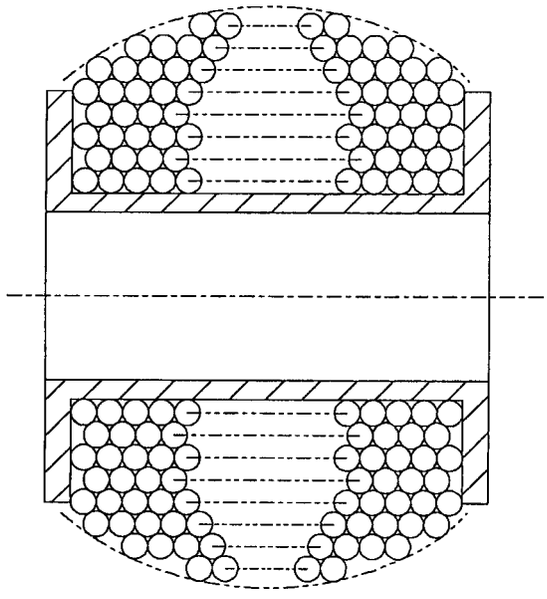

Figure 3.5.2.3: Possible coil deformation with staggered packing

Another important coil design parameter is the resistance to inductance ratio (R_c/L_0), which determines coil bandwidth (see equation 3.5.2.16). An R_c/L_0 ratio of at least 100 Hz is required to ensure that the coil produce sufficient field in the rod over the entire isolation bendwidth. As a safety precaution, the R_c/L_0 ratio is chosen 50% higher than the maximum frequency of the isolation band, i.e. 150 Hz. This is done to allow for possible variations in dynamic and material parameters, e.g. permeability, which is difficult to model, due to phenomena such as hysteresis (see section 2.3).

Impedance and resistance to inductance ratio are determined by the following factors (see equations 3.5.2.10, 3.5.2.15 and 3.5.2.17: ρ_c, N, D_c, A_w, l_a, μ^σ, E, d^σ and d^H. The active rod length l_a and the magnetostrictive and magnetization parameters μ^σ, E, d^σ and d^H have already been determined. Parameters which remain to be determined, are wire resistivity and cross-sectional area, number of windings and coil diameter.

Coil wire resistivity depends on the wire material. Copper, with a resistivity of $1{,}7.10^{-8}$ Ωm [Bartkowiak, 1973] and [Sears & Zemansky, 1975] is often used in electromagnetic field coils and will also be used in this study.

Wire cross-sectional area depends on the wire diameter. A vast number of wire diameters can be considered, three of which are 0,511 mm (for AWG 24), 0,644 mm (for AWG 22), and 0,4 mm (for "API 2"). The cross-sectional areas of the different wires are given in table 3.5.2.2. The wire with the smallest cross-sectional area, i.e. "API 2", is selected, since it will

give the highest R_c/L_0 ratio for the same length. The insulation coating thickness of "API 2" is 0,035 mm.

Table 3.5.2.2: Coil wire diameters and cross-sectional areas

Wire	Diameter (mm)	Cross-sectional area (mm^2)
"API 2"	0,4	0,126
AWG 24	0,511	0,205
AWG 22	0,644	0,326

For the selected wire diameter, the number of windings, which will give the required impedance and R_c/L_0 ratio, is calculated. From the number of windings, the coil PCD, inner and outer diameters can be determined. To systematize the design, a stepwise procedure, using equations 3.5.2.1 to 3.5.2.30, is given below.

Coil design procedure

A stepwise design procedure to calculate the required coil parameters, is as follows:

Step I: For the selected d_w, A_w is calculated, using equation 3.5.2.8.

Step II: For E, d^H, d^σ and μ^σ, as given in table 3.5.2.1, cf is calculated, using equation 3.5.2.14.

Step III: For a BW of 150 Hz and Z_c of 4 Ω at 100 Hz, equations 3.5.2.16 and 3.5.2.17 are simultaneously solved for R_c and L_0.

Step IV: With L_0 and cf, L_f is calculated, using equation 3.5.2.13.

Step V: With L_f, μ^σ and A_T, N is calculated, using equation 3.5.2.12.

Step VI: With R_c, ρ_c and A_w, l_c is calculated, using equation 3.5.2.9.

Step VII: With l_c and N, D_c is calculated using equation 3.5.2.4.

Step VIII: With l_a, d_w and t_c, n_c is calculated, using equations 3.5.2.1 and 3.5.2.2.

Step IX: With N and n_c, n_l is calculated, using equation 3.5.2.3.

Step X: With n_l, d_{wc} and D_c, equations 3.5.2.5 and 3.5.2.6 are simultaneously solved for d_i and d_o.

Step XI: With N, d_{wc}, d_i, d_o and l_a, pf is calculated, using equation 3.5.2.7.

Step XII: With H_b and H_A, I, V and P are calculated for a number of frequencies in the band ranging from 0 Hz to 333 Hz, using equations 3.5.2.22 to 3.5.2.26.

Step XIII: Actuator output force F_a is checked, using equation 3.5.2.29. F_a must be at least 158,2 N.

Step XIV: Actuator output displacement y_a is checked, using equation 3.5.2.30. y_a must be at least 75 μm.

Step XV: Coil input voltage V is checked: It must be smaller than the maximum available source voltage of 28 V.

Coil parameters

The coil parameters are calculated using the procedure set out in steps I to XV. The parameters are given in table 3.5.2.3. It can be seen from table 3.5.2.3 that the bias voltage of 8,8 V compares favourably with the bias voltage of 8,75 V used for the simulations (see table 2.7.3.1). The bias field of 56,13 kA/m is approximately 12% larger than the bias field used for the simulations. The actuator output force is 47% higher than required. This is due to the fact that the value of Young's modulus of Terfenol-D used for the coil design (23,46 GPa) is 47% higher than the value used for the gain mechanism design (16 GPa).

Table 3.5.2.3: Magnetostrictive actuator coil parameters

Parameter	Value
Inner diameter	8,4 mm
Outer diameter	16,2 mm
Pitch circle diameter (PCD)	12,3 mm
Number of spools per actuator	2
Coil length per spool (50% of rod active length)	15,2 mm
Total wire length	24,4 m
Wire diameter, excluding coating	0,4 mm
Wire coating thickness	0,035 mm
Wire material resistivity	$1{,}7.10^{-8}$ Ωm
Number of windings per layer, per spool	35
Number of layers per spool	9, plus 10 windings
Total number of windings	640
Packing factor	78,5%
Free inductance	4,27 mH
Clamped inductance	3,50 mH
Coupling factor	42%
Resistance to (clamped) inductance ratio	150 Hz
Resistance	3,3 Ω
Impedance at 100 Hz	4,0 Ω
Bias field	56,13 kA/m
Field amplitude (constant)	56,13 kA/m
Maximum field	112,3 kA/m
Bias current	2,67 A
Current amplitude	2,67 A
Maximum current	5,33 A
Bias voltage	8,8 V
Maximum static Terfenol-D rod strain	944 $\mu\varepsilon$
Actuator static force (p-p)	232 N
Actuator static stroke length	75 μm

Coil current, voltage and power versus frequency curves, are shown in figure 3.5.2.4. For comparison purposes, the curves for electromagnetic and permanent field biasing are shown on the same scale.

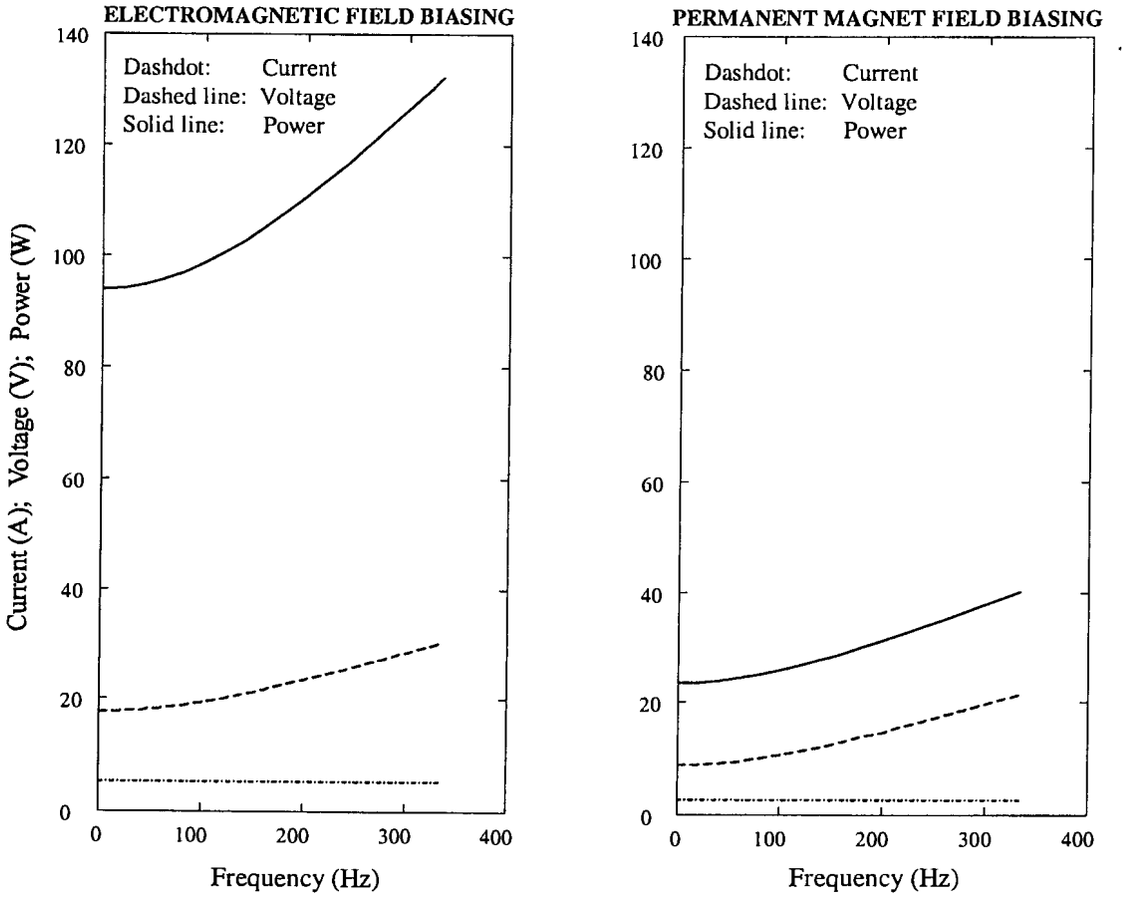

Figure 3.5.2.4: Coil current, voltage and power

Current, voltage and power at 0,01 Hz (quasi-static), 100 Hz (maximum frequency of disturbance band), 150 Hz (coil cutoff frequency) and 333 Hz (system cutoff frequency) are given in table 3.5.2.4.

From figure 3.5.2.4 and table 3.5.2.4, it can be seen that biasing method has a significant influence on current, voltage and power. Electromagnetic field biasing consumes significantly more power than permanent magnet biasing. However, irrespective of its high power consumption, electromagnetic biasing will be used in this study to avoid the high cost of permanent magnets.

Table 3.5.2.4: Current, voltage and power for two biasing methods

Frequency (Hz):		**0,01**	**100**	**150**	**333**
Comment:		Quasi-static	Disturbance BW	Coil BW	System BW
Electromagnetic biasing:	Current (A)	5,33	5,33	5,33	5,33
	Voltage (V)	17,6	19,4	21,2	30,2
	Power (W)	93,8	98,7	104,1	132,3
Permanent magnet biasing:	Current (A)	2,67	2,67	2,67	2,67
	Voltage (V)	8,8	10,6	12,4	21,4
	Power (W)	23,5	25,8	28,3	40,3

This concludes the detailed design of the field coils. A detailed design of the prestress springs follows in section 3.5.3.

3.5.3 Detailed design of prestress springs

A detailed design of the mechanical bias (prestress) springs is done in this section. Spring design input parameters, i.e. required Terfenol-D rod prestress, rod cross-sectional area, actuator gain factor, available space and wire material shear modulus are given. A stepwise design procedure, using the equations given in section 3.4.3, is presented. The spring parameters are calculated and tabled.

The spring design input parameters are given in table 3.5.3.1.

Table 3.5.3.1: Prestress spring design input parameters

Parameter	**Symbol**	**Value**
Terfenol-D rod compressive prestress	σ_b	12 MPa
Rod cross-sectional area	A_T	$2{,}83.10^{-5}$ m^2
Actuator gain factor	G	2,7
Available space (compressed length)	l_c	20,8 mm
Wire shear stress modulus (for steel)	G_s	79,3 GPa

A stepwise spring design procedure is as follows:

Step I: A spring diameter (D) and wire thickness (d) are arbitrarily selected. A number of available wire diameters, from 0,15 mm to 5,39 mm, are considered. For this spring, a diameter of 7,6 mm and wire thickness of 2,3 mm, are selected.

Step II: A nominal spring deflection x of 1,4 mm (approximately 20 times actuator output displacement) is selected. The maximum deflection x_{max} is selected as 3 times nominal deflection, i.e. 4,2 mm.

Step III: The spring end type, i.e. squared and ground (this end type simplifies spring attachment), is selected. From table 3.4.3.1, N_e for this end type is 2,0.

Step IV: With σ_b and A_T known, F_b is calculated, using equation 3.4.3.1.

Step V: With F_b and G known, F is calculated, using equation 3.4.3.4.

Step VI: With F and x known, k is calculated, using equation 3.4.3.8.

Step VII: With G_s, D, d and k known, N_a is calculated, using equation 3.4.3.9.

Step VIII: With N_a and N_e known, N_t is calculated, using equation 3.4.3.10.

Step IX: With d, N_t and x_{max} known, l_f is calculated, using equation 3.4.3.7.

Step X: With l_f and N_t known, p is calculated, using equation 3.4.3.13.

Step XI: With l_f and D known, l_f/D is calculated.

Step XII: With p, D and d known, $\Delta D/D$ is calculated, using equations 3.4.3.11 and 3.4.3.12.

Step XIII: With D and d known, C is calculated, using equation 3.4.3.18.

Step XIV: With C known, K_w is calculated, using equation 3.4.3.17.

Step XV: With D, d and F known, τ_c is calculated, using equation 3.4.3.19.

Spring parameters are calculated using the procedure as set out in steps I to XV above. The parameters are summarized in table 3.5.3.2.

Table 3.5.3.2: Actuator prestress spring design parameters

Number of springs per actuator	2
Type of spring	Coil spring
Spring force (per spring)	125,6 N
Spring stiffness (per spring)	90 kN/m
Spring nominal deflection	1,4 mm
Total number of coils per spring	9
Number of active coils per spring	7
Spring mean diameter (PCD)	7,6 mm
Wire diameter	2,3 mm
Spring index	3,3
Spring solid length	20,8 mm
Spring free length	25 mm
Spring pitch	2,76 mm
Spring maximum outer diameter	9,6 mm
Wahl shear stress correction factor	1,51
Wire shear stress	302 MPa
Spring free length to PCD ratio	3,3
Type of spring end	Squared and ground
End condition	Fixed
	Constrained from unwinding

This concludes the detailed design of the coil springs and of the actuator. Design of the support structure is described in the next section.

3.5.4 Support structure design

Support structure design is described in this section. Structure geometry is shown. The finite element method is used to calculate the deflection profile and maximum Von Mises stress. Material properties and the input displacement at an actuator attachment point are given. The finite element grid and deflection profile are shown. It is shown that the maximum Von Mises stress is relatively low.

The support structure geometry is shown in figure 3.5.4.1 and its finite element grid is shown in figure 3.5.4.2. A total number of 624 two-dimensional quadrangular elements are used. A fine grid, as shown in figure 3.5.4.3, is used for the flexures.

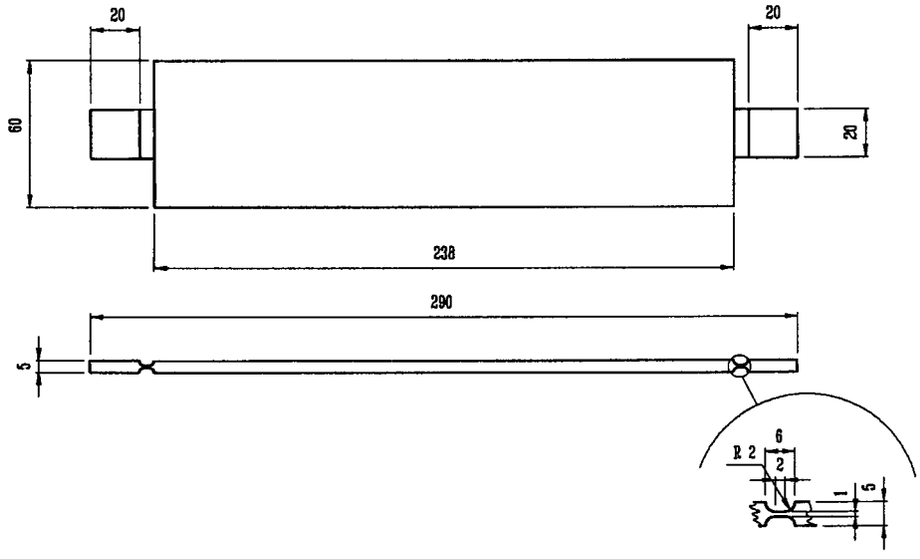

Figure 3.5.4.1: Support structure geometry

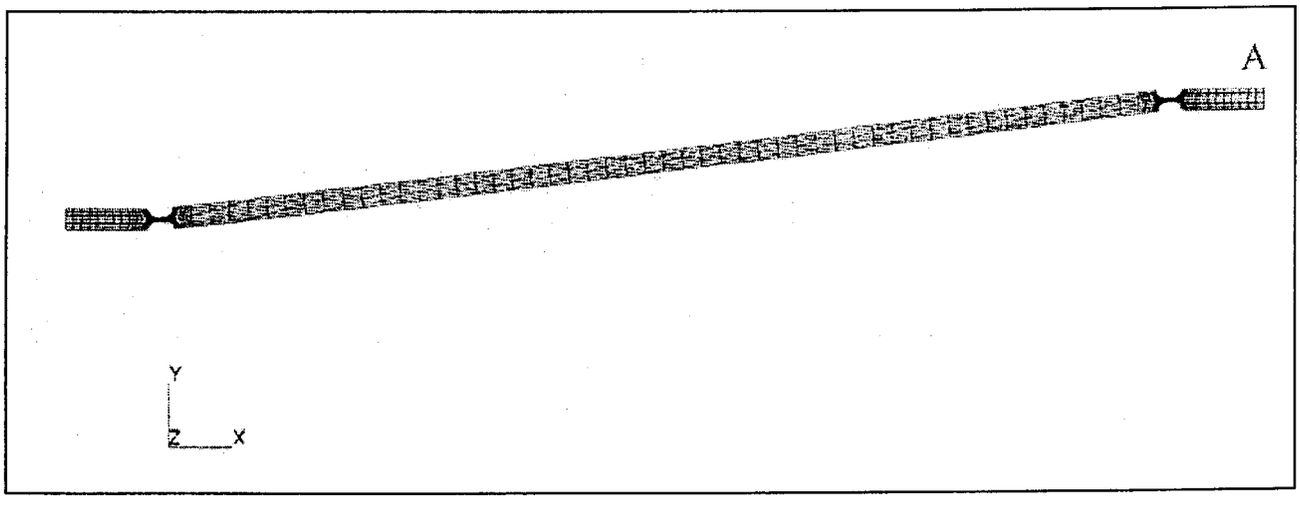

Figure 3.5.4.2: Support structure finite element grid

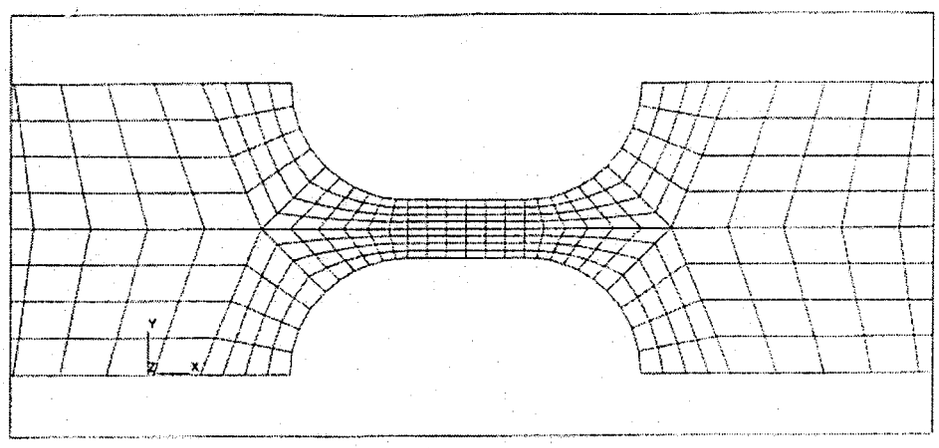

Figure 3.5.4.3: Flexure finite element grid

Support structure material is aluminium grade 7075, which has a Young's modulus of 71 GPa and Poissons ratio of 0,33. The maximum deflection of the structure, which is twice the displacement of a single actuator, i.e. 150 μm, occurs at the right hand actuator attachment point (point A in figure 3.5.4.2). The maximum calculated Von Mises stress, which occurs at the centre of the flexure, is 16,3 MPa. This stress is relatively low. The structure deflection profile is shown on the finite element grid in figure 3.5.4.2.

This concludes the design calculations, practical design aspects and design parameters of the most important system components. Detailed and assembly drawings are shown in the next section.

3.6 System assembly drawing and component detail drawings

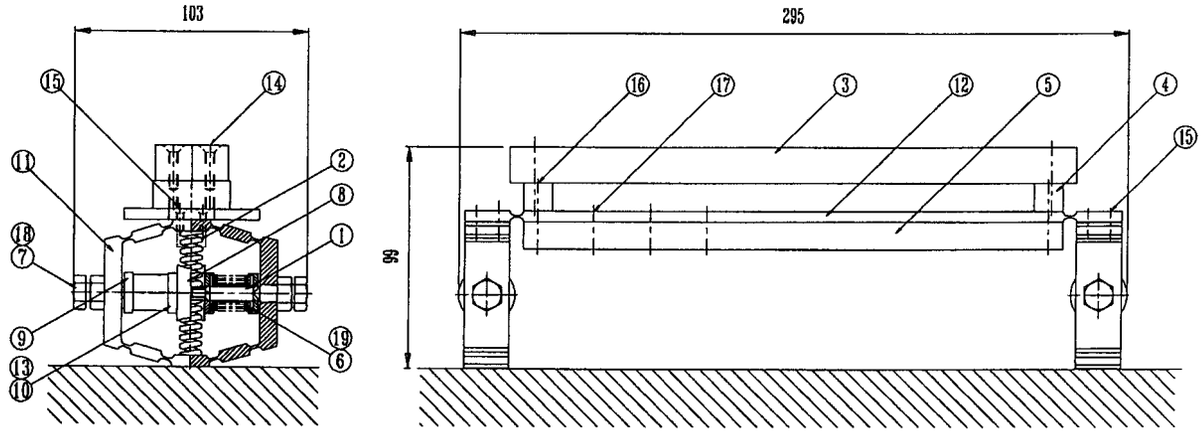

ITEM	QUANTITY	DESCRIPTION	MATERIAL
19	AR	SPOOL WIRE ϕ 0.4	COPPER
18	4	LOCK NUT	EN8
17	4	CSK HEAD SCREW M4 X 15	EN8
16	2	CSK HEAD SCREW M4 X 25	EN8
15	6	CSK HEAD SCREW M4 X 10	EN8
14	4	CSK HEAD SCREW M4 X 20	EN8
13	4	CSK HEAD SCREW M4 X 6	EN8
12	1	SUPPORT STRUCTURE	ALUMINIUM 7075
11	2	GAIN MECHANISM	EN8
10	4	ENDCAP 1	EN8
9	4	ENDCAP	EN8
8	2	CENTREPIECE	EN8
7	4	PRESTRESS BOLT	HIGH TENSILE STEEL
6	4	COIL SPOOL	TEFLON
5	1	STIFFENER	ALUMINIUM
4	2	SPACER	ALUMINIUM
3	1	DUMMY LOAD	EN8
2	4	COMPRESSION PRESTRESS SPRING	SPRING STEEL
1	4	ROD	TEKTRONIX-D

OPTICAL INSTRUMENT LOS STABILIZATION SYSTEM

Figure 3.6.1: System assembly drawing

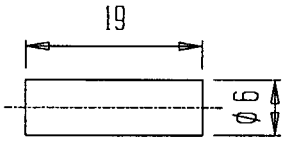

ITEM 1
ROD
MATL.: TERFENOL - D

Figure 3.6.2: Item 1: Terfenol-D rod

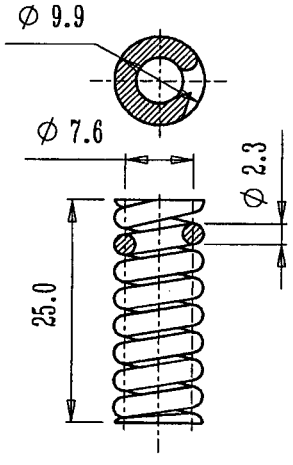

ITEM 2
PRESTRESS SPRING
MATL.: SPRING STEEL

Figure 3.6.3: Item 2: Prestress spring

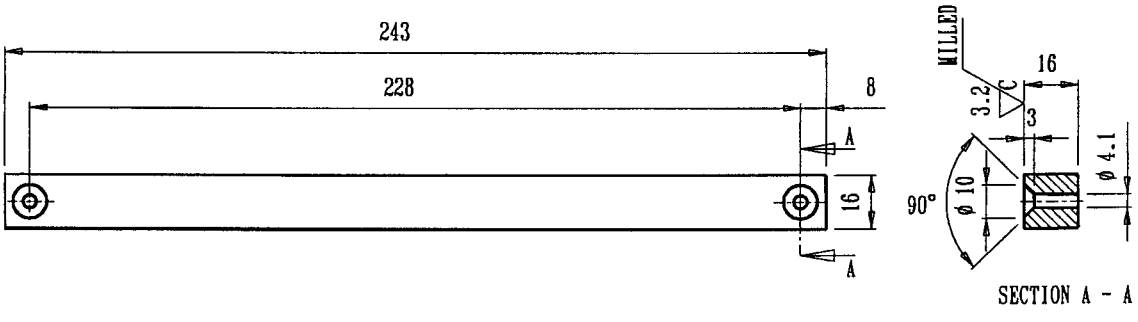

ITEM 3
DUMMY LOAD
MATL.: EN8

Figure 3.6.4: Item 3: Dummy load

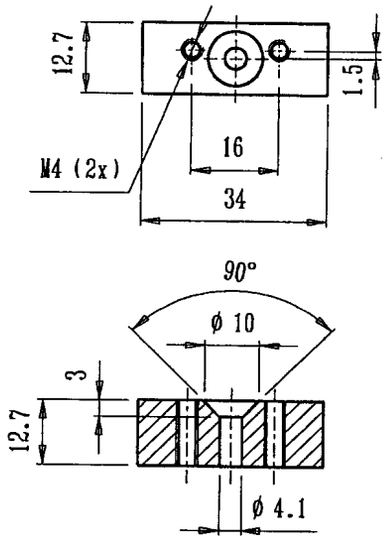

ITEM 4
SPACER
MATL.: ALUMINIUM

Figure 3.6.5: Item 4: Spacer

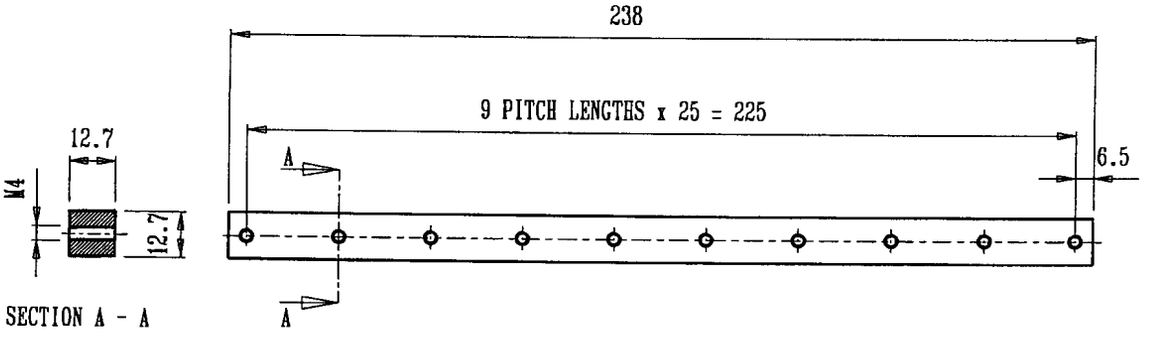

ITEM 5
STIFFENER
MATL.: ALUMINIUM

Figure 3.6.6: Item 5: Stiffener

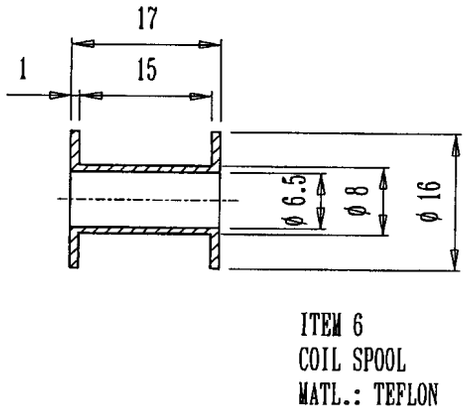

Figure 3.6.7: Item 6: Coil spool

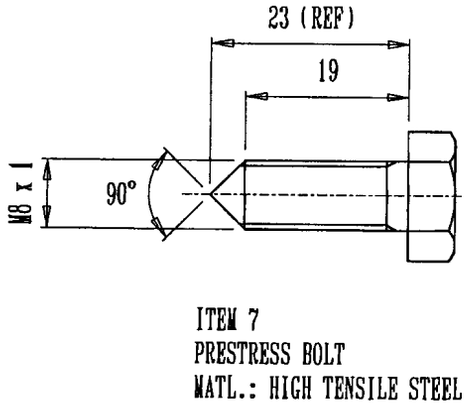

Figure 3.6.8: Item 7: Prestress bolt

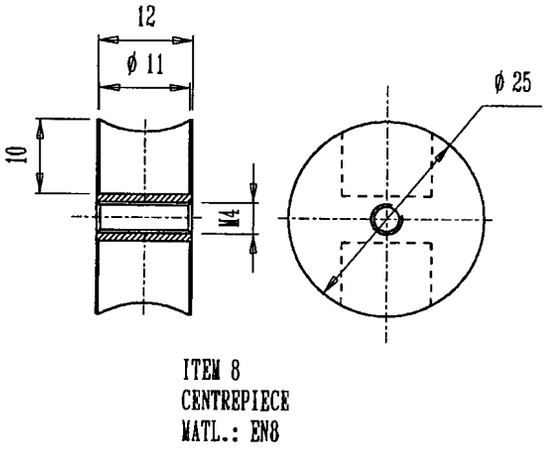

Figure 3.6.9: Item 8: Centrepiece

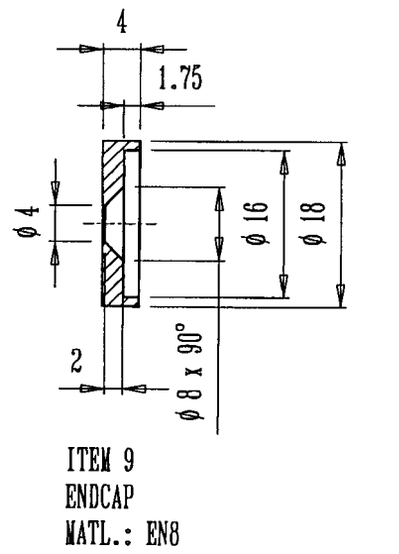

Figure 3.6.10: Item 9: Endcap

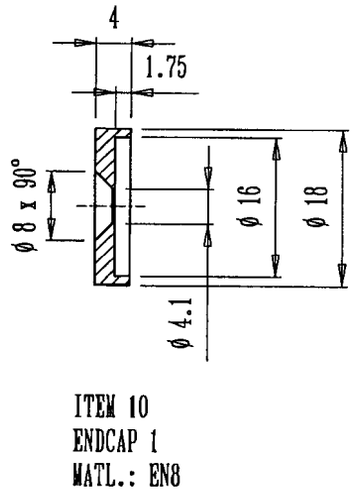

Figure 3.6.11: Item 10: Endcap 1

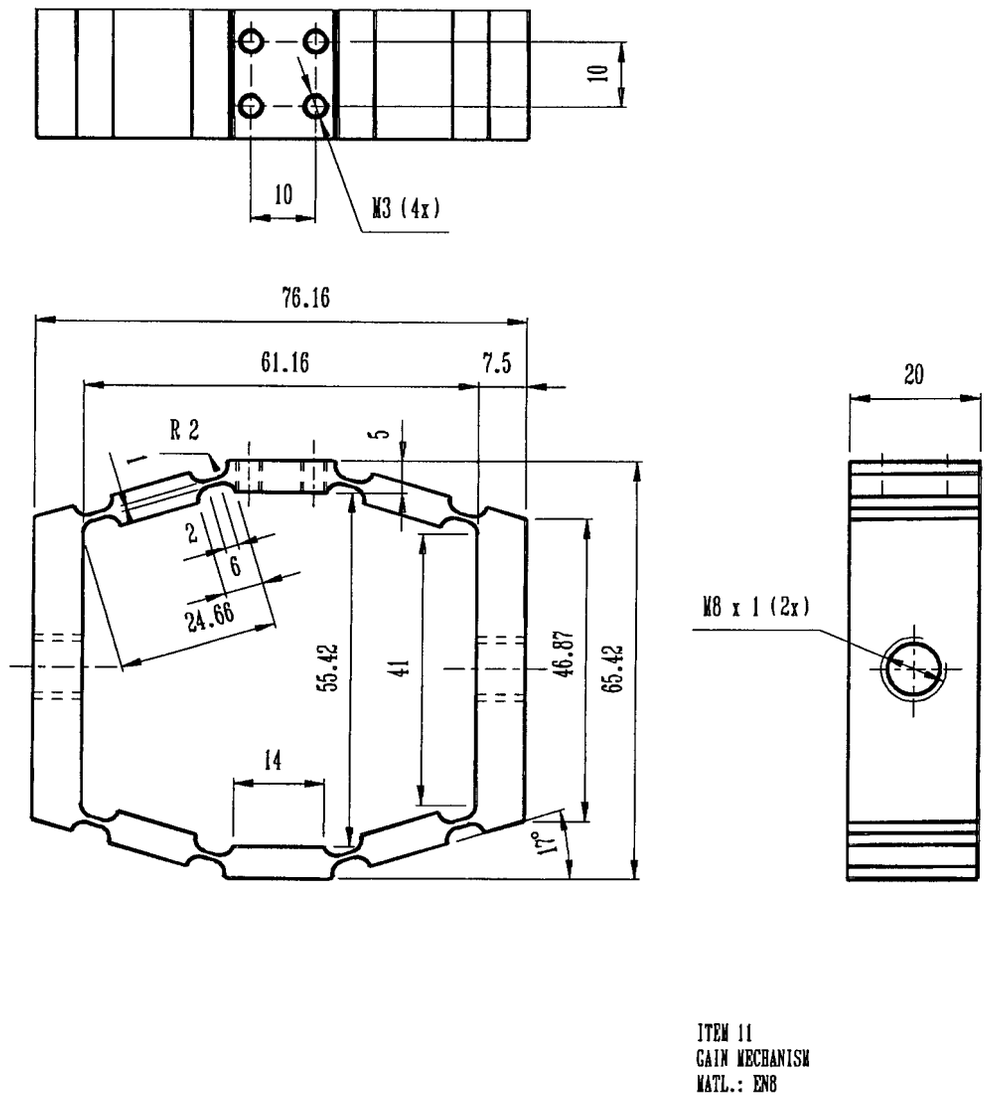

Figure 3.6.12: Item 11: Gain mechanism

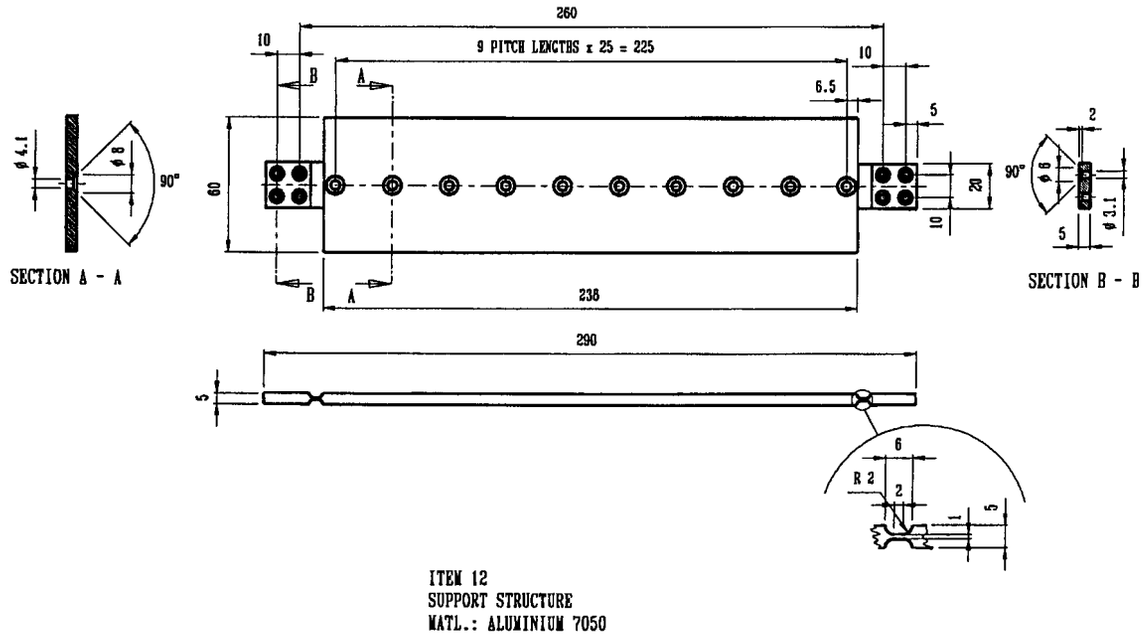

Figure 3.6.13: Item 12: Support structure

3.7 Design safety checks

A number of design safety checks are described in this section. The checks are required to ensure that the actuator and system design is safe. The checks comprise investigations into static and dynamic buckling of the Terfenol-D rods. Buckling criteria are defined. The static buckling load on the rods is calculated and compared with the crtical compressive load. The natural frequency of the rods is calculated and compared with the maximum frequency of the disturbance band. Static buckling is investigated in section 3.7.1, while dynamic buckling is investigated in section 3.7.2.

3.7.1 Static buckling of the Terfenol-D rods

It was mentioned in section 2.2 that the saturation strain of Terfenol-D can be greatly enhanced by subjecting the material to a compressive prestress. The prestress is also known as the bias stress. Generally, the larger the prestress, the larger the saturation strain. The practical implication of applying a prestress is that the desired elongation of a Terfenol-D rod with a given length can be obtained with smaller magnetic field amplitudes, thereby reducing the energy input into the coil.

The disadvantage, however, is that excessively large prestresses can cause the rods to buckle. The designer of a Terfenol-D actuator must therefore ensure that the prestress is sufficient to produce the desired saturation strain, but at the same time, the stress must be brought about by a compressive load which will not exceed the critical buckling load of the rod.

The static compressive and buckling loads of the rods are calculated in this section. A conservative approach is followed in the calculation of the loads. The factors which influence the buckling load

are discussed. It will be shown that the compressive load is well below the critical buckling load and that the actuator design is safe as far as static buckling of the rods is concerned.

Consider a Terfenol-D rod which is subjected to a static compressive load, as shown in figure 3.7.1.1. The compressive load is F_b. The cross-sectional area of the rod is given by A_T. The load is distributed over the entire cross-sectional area of the rod by means of two end caps, one at each end of the rod.

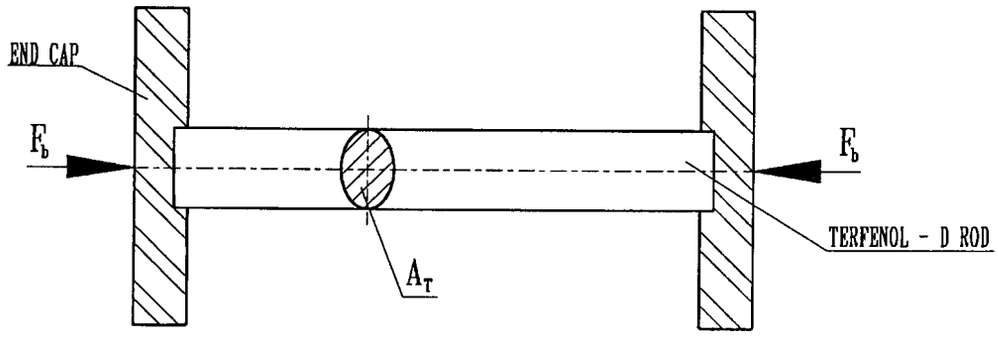

Figure 3.7.1.1 Compressive load acting on a Terfenol-D rod

The maximum compressive load acting on the rod is the product of the maximum stress in the rod and the cross-sectional area of the rod:

$$F_b = \sigma_{max} A_T \qquad \textbf{(3.7.1.1)}$$

where σ_{max} the maximum stress. The maximum stress is the sum of the compressive prestress and the stress amplitude:

$$\sigma_{max} = \sigma_b + \sigma_A \qquad \textbf{(3.7.1.2)}$$

where σ_b is the compressive prestress and σ_A is the stress amplitude. The stress amplitude is limited by the prestress: Since the tensile strength of Terfenol-D is relatively low in comparison with its compressive stress [Butler, 1988], it is essential to maintain a compressive stress in the rod under all circumstances. Therefore, the maximum allowable stress amplitude is equal to the prestress:

$$\sigma_A = \sigma_b \qquad \textbf{(3.7.1.3)}$$

Substitution of equation 3.7.1.3 into equation 3.7.1.2 gives:

$$\sigma_{max} = 2\sigma_b \qquad \textbf{(3.7.1.4)}$$

Finally, the compressive load on the rod is obtained in terms of the prestress by substitution of equation 3.7.1.4 into equation 3.7.1.1:

$$F_b = 2\sigma_b A_T \qquad \textbf{(3.7.1.5)}$$

The critical load F_{cr} is given as follows by Shigley [1977]:

$$F_{cr} = A_T \frac{n\pi^2 E}{(l_T/r_G)^2} \tag{3.7.1.6}$$

where n is the end condition constant of the rod, E is Young's modulus of Terfenol-D and r_G is the radius of gyration of the rod cross-section. Equation 3.7.1.6 is also known as the Euler equation, or the Euler column formula [Shigley, 1977].

For a rod with a round cross-section, as is used in this study, the radius of gyration is:

$$r_G = \frac{d_T}{4} \tag{3.7.1.7}$$

where d_T is the rod diameter. Substitution of equation 3.7.1.7 into equation 3.7.1.6 gives the critical load as follows in terms of the rod diameter:

$$F_{cr} = A_T \frac{n\pi^2 E}{(4l_T/d_T)^2} \tag{3.7.1.8}$$

The rod end condition constant n depends on the attachment method of the rods. Possible end conditions which can be considered for this analysis include fixed-free, rounded-rounded, fixed-rounded and fixed-fixed conditions. Theoretical values of n vary from 0,25 for fixed-free columns to 4 for fixed-fixed columns. However, practice has shown that, in the cases of fixed-rounded and fixed-fixed columns, it is difficult, if not impossible, to fix the column ends in such a way that the theoretical values apply. Instead, a more realistic practical value of 1,2 is recommended for both these cases. For the sake of completeness, the theoretical and recommended values of n for the abovementioned four rod end conditions, from Shigley [1977], are given in table 3.7.1.1.

Table 3.7.1.1: Theoretical and recommended n-values for different rod end conditions [Shigley, 1977]

End condition	Theoretical value of n	Recommended value of n
Fixed-free	0,25	0,25
Rounded-rounded	1,00	1,00
Fixed-rounded	2,00	1,20
Fixed-fixed	4,00	1,20

The applicable end condition for the Terfenol-D rod is a debatable point. If it is assumed that the rod is fully supported by the actuator structure, the buckling analysis can be based on fixed-fixed ends, in which case the recommended end condition constant will be 1,2. If, however, cognisance is taken of the fact that during compression, the rod may not be perfectly straight and the load surfaces at the ends of the rod may not be parallel, the assumption can be made that a fixed-free end condition applies, for which n is 0,25. The latter end condition will yield a lower critical load, resulting in a more conservative design. For the purpose of this analysis, an end condition constant of 0,25 will be used.

The compressive load on the rod and the critical buckling load are subsequently calculated and compared. Numerical values for the rod length, diameter and cross-sectional area, the prestress, Young's modulus and end condition constant are obtained from previous sections and substituted into the applicable equations. From section 3.5, the total rod length is 0,038 m, the rod diameter is 0,006 m and the rod cross-sectional area is $2{,}827.10^{-5}$ m^2:

$$l_T = 0{,}038 \text{ m} \quad \textbf{(3.7.1.9a)}$$

$$d_T = 0{,}006 \text{ m} \quad \textbf{(3.7.1.9b)}$$

$$A_T = 2{,}827.10^{5} \text{ m}^2 \quad \textbf{(3.7.1.9c)}$$

The prestress, from section 2.7, is 12.10^6 Pa:

$$\sigma_b = 12.10^6 \text{ Pa} \quad \textbf{(3.7.1.10)}$$

Young's modulus can vary from approximately 16 GPa to 56 GPa (see section 2.2, figure 2.2.1.4). Taking a conservative approach, the lowest value of 16 GPa is used:

$$E = 16.10^9 \text{ Pa} \quad \textbf{(3.7.1.11)}$$

The end condition constant, from the above discussion, is 0,25:

$$n = 0{,}25 \quad \textbf{(3.7.1.12)}$$

By subsitution of equations 3.7.1.9c and 3.7.1.10 into equation 3.7.1.5, the maximum compressive load is:

$$F_b = 339{,}3 \text{ N} \quad \textbf{(3.7.1.13)}$$

By substitution of equations 3.7.1.9a to 3.7.1.9c, 3.7.1.11 and 3.7.1.12 into equation 3.7.1.8, the critical buckling load of the rod is:

$$F_{cr} = 1739 \text{ N} \quad \textbf{(3.7.1.14)}$$

By comparison of equations 3.7.1.13 and 3.7.1.14, the maximum compressive load on the rod is considerably lower than the critical buckling load. The conclusion can therefore be drawn that the actuator design is safe as far as static buckling of the rods is concerned.

This concludes the static buckling analysis of the Terfenol-D rods. A dynamic buckling analysis is carried out in the next section.

3.7.2 Dynamic buckling of the Terfenol-D rods

The possibility of dynamic buckling of the Terfenol-D rods is investigated in this section. A buckling criterion is defined. The rods are modelled as transversely vibrating beams with distributed mass and stiffness. The centerpiece, end caps and coils are modelled as a concentrated mass, attached at the centre of the beam. The concentrated mass is included in the beam mass by means of an equivalent density of the rod material. Two beam end conditions, i.e. clamped-clamped and simply supported, are considered. In order to ensure a conservative design, buckling is investigated for the end condition which gives the lowest fundamental natural frequency.

The effect of compressive prestress on the natural frequency of the rods is added. The fundamental natural frequency is calculated and compared with the maximum frequency of the disturbance band. It is shown that the fundamental natural frequency is significantly higher than the maximum disturbance frequency.

Static buckling of the rods was investigated in the previous section. It was shown that buckling would occur if the applied static load exceeded the critical buckling load. The dynamic buckling analysis of the rods differs from the static buckling analysis in the sense that, during dynamic excitation, the rods can buckle due to transverse resonance, as well as the axial compressive forces acting on the rods. Resonance will normally occur at the transverse natural frequencies of the rods. The fundamental natural frequency is of particular importance in the investigation.

The natural frequency depends on the distributed stiffness and inertia of the rods, concentrated mass of the coils, compressive prestress in the rods and rigidity of the joints between the rods and end caps. For the purpose of the dynamic buckling analysis, it is necessary to model the rods, coils and centrepiece with equivalent mechanical elements. The rods are modelled as a transversely vibrating beam and the coils and centrepiece are modelled as a concentrated mass attached at the beam centre. Two rod end models are considered, i.e. simply supported ends and clamped-clamped ends. Prestress is modelled by means of an axial load acting at the beam ends.

In order to design conservatively, the end condition which gives the lower fundamental natural frequency, will be used in the model. Since beams with simply-supported ends have lower natural frequencies than beams with clamped-clamped ends for the same stiffness and mass distributions, the simply-supported beam end model will be used.

The fundamental natural frequency of a simply-supported beam with a concentrated mass at the centre, and which is subjected to an axial force acting at the beam ends, is derived in appendix T. The frequency is given by:

$$f_1 = \frac{1}{2\pi}\sqrt{\left(\frac{\pi}{l_T}\right)^4 \frac{EI}{\rho\left(1+2m_c/\rho A_T l_T\right)A_T} - \left(\frac{\pi}{l_T}\right)^2 \frac{F_b}{\rho\left(1+2m_c/\rho A_T l_T\right)A_T}} \qquad \textbf{(3.7.2.1)}$$

Calculation of the fundamental transverse natural frequency of the rods is done by substitution of numerical values for the rod length, Young's Modulus and density of the rod material, cross-sectional area and second moment of area of the rod, concentrated mass of the coils, centrepiece and end cap, as well as the compressive force acting on the rod, into equation 3.7.2.1.

The density of the beam material, i.e. Terfenol-D, is 9250 kg/m^3 [Butler, 1988]:

$$\rho = 9250 \text{ kg/m}^3 \quad \textbf{(3.7.2.2)}$$

The calculated mass of the coils is 16 g each, while those of the centrepiece and end caps are 34 g and 12 g each:

$$m_{coil} = 0{,}016 \text{ kg} \quad \textbf{(3.7.2.3a)}$$
$$m_{centrepiece} = 0{,}034 \text{ kg} \quad \textbf{(3.7.2.3b)}$$
$$m_{end\,cap} = 0{,}012 \text{ kg} \quad \textbf{(3.7.2.3c)}$$

The concentrated mass attached at the centre of the beam, is the sum of the masses of the two coils, centrepiece and two end caps:

$$m_c = 2m_{coil} + m_{centrepiece} + 2m_{end\,cap} \quad \textbf{(3.7.2.4)}$$

By substitution of equations 3.7.2.3 into equation 3.7.2.4, m_c is:

$$m_c = 0{,}09 \text{ kg} \quad \textbf{(3.7.2.5)}$$

The beam length, diameter and cross-sectional area are 38 mm, 6 mm and 2,827.10^{-5} m^2 respectively:

$$l_T = 0{,}038 \text{ m} \quad \textbf{(3.7.2.6a)}$$
$$d_T = 0{,}006 \text{ m} \quad \textbf{(3.7.2.6b)}$$
$$A_T = 2{,}827.10^{-5} \text{ m}^2 \quad \textbf{(3.7.2.6c)}$$

Young's modulus of the beam material, i.e. Terfenol-D, is 16 GPa (see equation 3.7.1.11):

$$E = 16.10^9 \text{ Pa} \quad \textbf{(3.7.2.7)}$$

The second moment of area of the beam cross-section is:

$$I = \frac{\pi d_T^4}{64} \quad \textbf{(3.7.2.8)}$$

Substitution of equation 3.7.2.6b into equation 3.7.2.8 gives the second moment of area of the rods as:

$$I = 6{,}362.10^{-11} \text{ m}^4 \quad \textbf{(3.7.2.9)}$$

The maximum axial compressive force acting on the beam is 339,3 N (see equation 3.7.1.13):

$$F_b = 339{,}3 \text{ N} \qquad \textbf{(3.7.2.10)}$$

The fundamental natural frequency of the beam is obtained by substitution of equations 3.7.2.2, 3.7.2.5, 3.7.2.6a, 3.7.2.6c, 3.7.2.7, 3.7.2.8 and 3.7.2.10, into equation 3.7.2.1:

$$f_1 = 478{,}8 \text{ Hz} \qquad \textbf{(3.7.2.11)}$$

If the effect of the compressive force is neglected, the fundamental natural frequency is:

$$f_1 = 490{,}9 \text{ Hz} \qquad \textbf{(3.7.2.12)}$$

If equations 3.7.2.11 and 3.7.2.12 are compared, it can be seen that the axial force reduces the fundamental natural frequency by approximately 2,5%.

From equation 3.7.2.11, the fundamental transverse natural frequency of the rods is 478,8 Hz. The maximum frequency of the disturbance band is 100 Hz. Seeing that the natural frequency is considerably higher than the maximum frequency of the disturbance band, it can be concluded that the rods will not buckle during dynamic excitation.

In the next section, the effects of eddy currents on inductance losses in the rods will be investigated.

3.8 Investigation of eddy current losses in the Terfenol-D Rods

The effects of eddy current losses in the Terfenol-D rods are investigated in this section. The investigation is motivated. The complex eddy current loss factor is defined and expressed in terms of Kelvin functions of the crtical frequency ratio. Series expansions for the loss factor are also given. The critical eddy current frequency is expressed in terms of the material resistivity, rod diameter and clamped permeability. In the interest of simplifying the design, an equation which gives the critical frequency in terms of the rod diameter only, is presented and shown graphically. This equation is used to indicate that the critical frequency is well above the maximum frequency of the disturbance.

When a dynamic field is induced in the Terfenol-D rods, a circulating eddy current is caused in the rods. The eddy current produces a magnetic field which opposes the induced field, thereby reducing the effective permeability and inductance [Butler, 1988]. Eddy current losses become significant when the actuator is operated at frequencies above the critical eddy current frequency. The losses are expressed in terms of a dimensionless loss factor, called the eddy current loss factor. The critical frequency depends on the resistivity and clamped permeability of Terfenol-D, as well as on the rod diameter. The effective permeability, critical frequency and eddy current loss factor are discussed in short below.

The effective permeability is the product of the clamped permeability and the loss factor:

$$\mu_{eff} = \chi \mu_0 \tag{3.8.1}$$

where μ_{eff} is the effective permeability, χ is the eddy current loss factor and μ_0 is the clamped permeability.

The clamped permeability can be expressed mathematically as:

$$\mu_0 = \mu^{\sigma}\left[1-(cf)^2\right] \tag{3.8.2}$$

where μ^{σ} is the free permeability and cf is the coupling factor.

Free permeability is the partial derivative of the magnetic flux density with respect to the applied magnetic field at a constant mechanical stress (see equation 2.2.2.4):

$$\mu^{\sigma} = \left.\frac{\partial B(\sigma, H)}{\partial H}\right|_{\sigma=const} \tag{3.8.3}$$

where B is flux density, σ is stress and H is field strength.

The coupling factor, from equation 3.5.2.14, is given by:

$$cf = \sqrt{\frac{Ed^{\sigma}d^{H}}{\mu^{\sigma}}} \tag{3.8.4}$$

where E is Young's modulus, d^{σ} is the piezomagnetic cross-coupling constant and d^{H} is the strain constant.

The critical frequency f_{cr}, according to Butler [1988], is:

$$f_{cr} = \frac{2\rho_T}{\pi \mu_0 {d_T}^2} \tag{3.8.5}$$

where ρ_T is the resistivity and d_T is the rod diameter. The resistivity and clamped permeability are material properties, while the diameter is a property of the rod. It can be seen from equation 3.8.5 that the critical frequency is directly proportional to resistivity, inversely proportional to clamped permeability and inversely proportional to diameter squared.

The frequency ratio p is the dimensionless ratio of the excitation frequency to the critical eddy current frequency:

$$p = \frac{f}{f_{cr}} \tag{3.8.6}$$

The eddy current loss factor is a complex dimensionless factor given by:

$$\chi = \chi_r - j\chi_i \tag{3.8.7}$$

where χ_r and χ_i respectively represent the real part and imaginary part of the loss factor. χ_r and χ_i can be expressed as follows in terms of ber and bei Kelvin functions of the frequency ratio and their derivatives [Butler & Lizza, 1987]:

$$\chi_r = \frac{2}{\sqrt{p}} \frac{\left(ber\sqrt{p}\right)\left(bei'\sqrt{p}\right) - \left(bei\sqrt{p}\right)\left(ber'\sqrt{p}\right)}{ber^2\sqrt{p} + bei^2\sqrt{p}} \tag{3.8.8a}$$

$$\chi_i = \frac{2}{\sqrt{p}} \frac{\left(ber\sqrt{p}\right)\left(ber'\sqrt{p}\right) + \left(bei\sqrt{p}\right)\left(bei'\sqrt{p}\right)}{ber^2\sqrt{p} + bei^2\sqrt{p}} \tag{3.8.8b}$$

where the prime denotes differentiation with respect to p.

For design purposes, especially as far as the selection of a suitable rod diameter is concerned, equations 3.8.8 may be difficult to apply. The reason is that the ber and bei functions of p and their derivatives are relatively complicated to evaluate.

In order to facilitate the evaluation of the functions, Butler & Lizza [1987] developed the following infinite series expansions for χ_r and χ_i:

$$\chi_r = \sum_{q=0}^{\infty} \frac{(p/4)^{2q}}{\left[(q!)^2(2q+1)!\right]} \Bigg/ \sum_{q=0}^{\infty} \frac{(p/4)^{2q}}{\left[(q!)^2(2q)!\right]} \tag{3.8.9a}$$

$$\chi_i = \frac{2}{p} \sum_{q=0}^{\infty} \frac{(p/4)^{2q}\,2q}{\left[(q!)^2(2q)!\right]} \Bigg/ \sum_{q=0}^{\infty} \frac{(p/4)^{2q}}{\left[(q!)^2(2q)!\right]} \tag{3.8.9b}$$

Equations 3.8.9a and 3.8.9b provide a simple calculation method for the real and imaginary parts of the complex loss factor in terms of the frequency ratio. Although the series are infinite, truncation of the series can be applied, albeit at the cost of accuracy. Accuracy will depend on the frequency ratio and the number of terms retained in the series expansion.

Equation 3.8.5 expresses the critical frequency in terms of the resistivity, clamped permeability and rod diameter. For design purposes, calculation of the critical frequency can be simplifed by expressing it in terms of the rod diameter only. This is done by substitution of known numerical values of the material parameters, i.e. the resistivity and clamped permeability, into equation 3.8.5. The resistivity of Terfenol-D is given as follows by Butler & Lizza [1987] and Butler [1988]:

$$\rho_T = 600.10^{-9}\ \Omega\text{m} \tag{3.8.10}$$

The clamped permeability is given by Butler [1988] as:

$$\mu_0 = 5{,}56.10^{-6} \text{ Tm/A} \tag{3.8.11}$$

By substitution of equations 3.8.10 and 3.8.11 into equation 3.8.5, the following empirical equation for the critical frequency in terms of the rod diameter results:

$$f_{cr} = \frac{0{,}06871}{d_T^2} \tag{3.8.12}$$

where d_T is the rod diameter in metres.

For the rod diameter in millimetres, equation 3.8.12 becomes:

$$f_{cr} = \frac{68710}{d_T^2} \tag{3.8.13}$$

Equation 3.8.13 shows that the critical frequency is inversely proportional to the diameter squared. Therefore, the larger the diameter, the lower the critical frequency. A similar equation, in Imperial units, has been derived by Butler [1988]. For the purpose of convenience, a graphical depiction of equation 3.8.13 is shown in figure 3.8.1. The high-loss and low-loss regions are indicated on the graph.

The critical eddy current frequency for the rod diameter used in this study can now be calculated and compared with the maximum frequency of the disturbance band. The rod diameter, from section 3.5, is 6 mm:

$$d_T = 6 \text{ mm} \tag{3.8.14}$$

By substitution of equation 3.8.14 into equation 3.8.13, the critical frequency is:

$$f_{cr} = 1909 \text{ Hz} \tag{3.8.15}$$

The maximum frequency of the disturbance band is 100 Hz (see table 3.2.1). If this frequency is compared with f_{cr}, it can be seen that the critical frequency is well above the disturbance band. The conclusion that can be drawn from the above analysis is that eddy current losses are insignificant in the disturbance band, and can be ignored in this study. As far as eddy current losses are concerned, the selected rod diameter of 6 mm is therefore suitable for installation in the actuators.

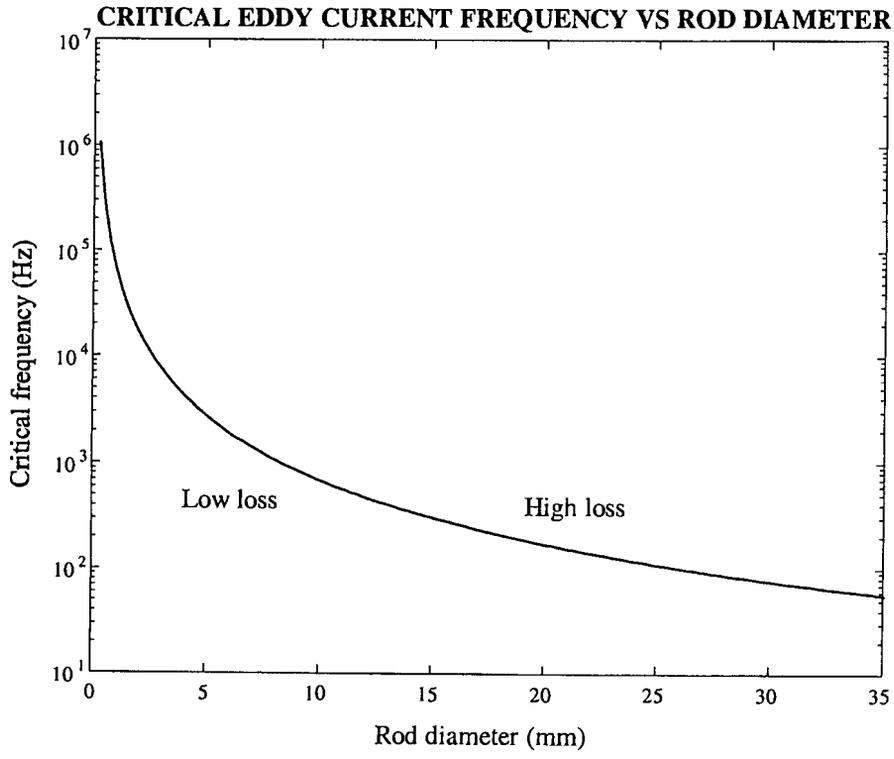

Figure 3.8.1: Terfenol-D critical eddy current frequency versus rod diameter [Butler, 1988]

In the next section, manufacturing and assembly procedures of the actuators and LOS stabilization system are described.

3.9 Terfenol-D actuator and system manufacturing and assembly procedures

A description of the actuator and support structure manufacturing procedures is given in this section. Assembly procedures of the actuators and system are described in short.

The four Terfenol-D rods are bought from the manufacturer, i.e. Etrema Products Inc., Ames Iowa. The actuator gain mechanisms are manufactured from 20 mm thick mild steel sheets. The holes for the prestress bolts are drilled and tapped, after which the mechanisms are cut out, using the wire erosion technique. The mild steel centrepiece and end caps are turned on a lathe. Prestress bolts are tapered on a lathe to aid in locating the end caps. The prestress springs are manufactured from spring steel by a spring manufacturer. Teflon spools for the field coils are turned on a lathe, after which coil wire is wound around the spools on a lathe. Epoxy is used to bond the turns and layers toggether. The coil wire length and number of turns are checked and coil resistance is measured.

The inner end caps are attached to the centrepieces with screws. The two rods of each actuator are placed inside the coils and centred inside the recesses in the end caps. The rods, coils, end caps and centrepiece are placed inside the gain mechanisms and centred. The

prestress bolts and nuts are fastened lightly and the prestress springs are fitted. (At this stage rod prestress is uncontrolled, since it cannot be measured. Prestress adjustment will be described in more detail in chapter 4).

The support structure for the optical instument is milled from 7075 high strength, aircraft quality aluminium. A numerically controlled milling machine is used. The stiffener is milled from commercial quality aluminium. The stiffener is clamped to the support structure and the holes for the connecting screws are drilled. The "dummy" load representing the optical instrument is milled from mild steel strips. The spacers between the support structure and "dummy" load are milled from commercial quality aluminium. The spacers are clamped between the support structure and "dummy" load and the holes for the connecting screws are drilled.

The support structure, stiffener, spacers and dummy load are assembled using screw joints. The actuators are attached to the support structure with screw joints. Assembly drawings of the actuator and system are shown in section 3.6.

3.10 Summary of chapter 3 and preview of chapter 4

The design and manufacture of the Terfenol-D actuators and the LOS stabilization system were discussed in detail in chapter 3. The design inputs were given and were used to obtain the actuator and system performance parameters. A number of design concepts were generated and compared and the most suitable concepts for a gain mechanism, magnetic field biasing and mechanical biasing were selected. These concepts were incorporated into an actuator design concept and a system design concept. A detailed design of all the actuator and system components was done. The design was checked for static and dynamic buckling of the rods and eddy current losses. The manufacturing and assembly procedures of the actuators and system were described.

Experimental testing of the actuators and system will be covered in chapter 4. The purpose of the tests is twofold: In the first place, the system characteristics, such as the stroke length of the actuators and system bandwidth must be measured to establish whether the design meets the requirements. Secondly, the accuracy of the model developed in chapter 2, must be evaluated. The modelled dynamic characteristics will be compared with the experimentally measured characteristics. Differences between modelled and measured characteristics will be explained and recommendations towards updating of the model will be made.

The following aspects of the experimental tests are covered in chapter 4. The test specimens, i.e. the two Terfenol-D actuators and LOS stabilization system, are discussed in short. The modelled characteristics, as well as the design parameters and dimensions of the system, are used to write a test specification. The test setup and apparatus are discussed and the tests are designed. The test procedures for the quasi-static and dynamic tests are spelt out. Post-processing of the test results is done. The test results are compared with the modelled results and reasons for differences between the modelled and experimental results are given.